Universidade de Aveiro Departamento de Física
2006

Nuno João de Oliveira e Silva

Estudos magnéticos e estruturais em nanopartículas de óxidos de ferro em matrizes híbridas

Structural and magnetic studies on iron oxide nanoparticles in hybrid matrices

Universidade de Aveiro Departamento de Física
2006

Nuno João de Oliveira e Silva

Structural and magnetic studies on iron oxide nanoparticles in hybrid matrices

Dissertação apresentada à Universidade de Aveiro para cumprimento dos requisitos necessários à obtenção do grau de Doutor em Física, realizada sob a orientação científica do Prof. Doutor Vítor Brás de Sequeira Amaral, Professor Associado do Departamento de Física da Universidade de Aveiro, e do Prof. Doutor Luís António Dias Carlos, Professor Catedrático do Departamento de Física da Universidade de Aveiro.

o júri

Presidente

Doutor Carlos de Pascoal Neto
Professor Catedrático do Departamento de Química da Universidade de Aveiro

Doutora Maria Margarida da Fonseca Beja Godinho
Professora Catedrática da Faculdade de Ciências da Universidade de Lisboa

Doutor Luís António Ferreira Martins Dias Carlos
Professor Catedrático do Departamento de Física da Universidade de Aveiro

Doutora Verónica Cortés de Zea Bermudez
Professora Associada da Universidade de Trás-Os-Montes e Alto Douro

Doutor Vítor Brás de Sequeira Amaral
Professor Associado com Agregação do Departamento de Física da Universidade de Aveiro

Doutor Manuel Almeida Valente
Professor Associado do Departamento de Física da Universidade de Aveiro

Doutor Fernando Palacio Parada
Professor de Investigação da Universidad de Zaragoza, Espanha

agradecimentos

O texto a seguir apresentado enquadra-se nos projectos "géis com propriedades ópticas, magnéticas e electroquímicas inovadoras, desenvolvido numa colaboração entre a Universidade de Trás-os-Montes e Alto Douro e o Departamento de Física e CICECO (Centro de Investigação em Materiais Cerâmicos e Compósitos) da Universidade de Aveiro, apoiados pela FCT (POCTI/1999/CTM/33653), a quem quero agradecer. A disponibilidade pessoal para a realização este trabalho foi possível graças a uma bolsa concedida pela FCT, durante estes últimos quatro anos, pela qual estou agradecido.
Estou profundamente grato aos meus orientadores, Prof. Doutor Vítor Amaral e Prof. Doutor Luís Carlos, por um continuado empenho, disponibilidade pessoal, apoio e discussões assíduas, pela confiança, entusiasmo e exemplo transmitidos e por todas as oportunidades oferecidas durante este trabalho. Quero agradecer à Sílvia Nunes e à Prof. Doutora Verónica de Zea Bermudez a síntese dos materiais, a simpatia no acolhimento em Vila Real e disponibilidade nas discussões sobre o processo sol-gel, FTIR e DSC. Agradeço ao Prof. Doutor Masaki Mito e aos membros do seu grupo que me receberam no Kyushu Institute of Technology e foram um exemplo da profunda gentileza nipónica. Quero agradecer aos investigadores do Institute for Rock Magnetism e em particular à Doutora Thelma Berquó, o acolhimento, disponibilidade pessoal e dos recursos existentes. Quero agradecer a todos os que me receberam e acolheram no Instituo de Ciencia de Materiales de Aragón em Saragoça, em particular à Ainhoa Urtizberea, Doutor Angel Millan, Prof. Doutor Fernando Luís, Prof. Doutor Júlio Fernandez e Prof. Doutor Fernando Palácio. Agradeço também ao Benito Rodríguez-González e ao Prof. Doutor Luís Liz-Marzán do Departamento de Química Física da Universidade de Vigo pela realização de um excelente trabalho de TEM. Expresso o meu agradecimento à Doutora Paula Soares e à Doutora Rosário Soares pela disponibilidade pessoal na realização e discussão dos difractogramas de raios-X. Expresso também o meu agradecimento ao Doutor Lianshe Fu pela disponibilidade na realização de sucessivas séries de amostras. Ao Instituto de Física e Materiais da Universidade do Porto, IFIMUP, e em particular ao Doutor João Pedro Araújo, agradeço a possibilidade de realização das medidas magnéticas. Lembro aqui também os bons momentos e discussões com os meus colegas de grupo e de laboratório em particular António Moreira dos Santos, Armandina Lopes, Fábio Figueiras, João Amaral, Mário Reis e Sérgio Pereira. A todos os que me acompanharam até aqui, aos meus professores do conservatório, aos meus amigos, à minha família, à minha irmã e aos meus pais.

palavras-chave

nanopartículas magnéticas, superparamagnetismo, óxidos de Ferro, antiferromagnetismo, ferrimagnetismo, híbridos orgânicos-inorgânicos

resumo

Este trabalho aborda algumas propriedades magnéticas e estruturais de nanopartículas de óxidos e óxidos-hidróxidos de ferro crescidos em matrizes híbridas orgânicas-inorgânicas. As matrizes híbridas, denominadas di-ureasils e obtidas pelo processo sol-gel, são compostas por uma rede siliciosa ligada covalentemente por pontes ureia a cadeias orgânicas de diferente peso molecular. A estrutura local dos di-ureasils não dopados está modelada como grupos de domínios siliciosos com dimensões nanométricas, estruturalmente correlacionados no seio de uma matriz rica em polímero. Neste trabalho mostra-se que os di-ureasils permitem o crescimento controlado de óxidos e óxidos-hidróxidos de ferro, incluindo a magnetite, maguemite, oxihidroxinitrato de ferro e ferrihidrite. O crescimento das nanopartículas de ferrihidrite dá-se em condições ácidas à superfície dos domínios siliciosos, junto aos grupos carbonilo, que funcionam como pontos de nucleação. Desse modo dá-se uma nucleação heterogénea, onde o tamanho das nanopartículas depende da concentração de ferro (entre 1 e 6% em massa), sendo a concentração de partículas constante. As propriedades magnéticas das nanopartículas de ferrihidrite revelam a existência de interacções antiferromagnéticas e de momentos descompensados. A contribuição destas duas componentes nas curvas de magnetização em função do campo magnético pode ser separada usando um método aqui proposto, o que permite um adequado estudo da evolução do momento magnético com a temperatura. O estudo das propriedades magnéticas dinâmicas das partículas de ferrihidrite, através de susceptibilidade ac, medidas de relaxação e medidas de efeito Mossbauer, permitiu estudar a evolução das interacções dipolares em função da concentração de ferro, bem como determinar a distribuição de barreiras de energia de anisotropia no caso em que essas interacções são desprezáveis. É apresentado um novo método para comparação desta distribuição com a distribuição de tamanhos, que permitiu concluir que os momentos magnéticos descompensados estão aleatoriamente distribuídos em volume. Usando baixas concentrações de água, foi possível crescer fases de oxihidroxinitrato de ferro com diferentes graus de cristalinidade, sendo algumas precursoras da ferrihidrite (como observado noutros trabalhos) e sendo outras novas fases. O crescimento de nanopartículas de maguemite e magnetite acontece após incorporação de iões de Fe^{2+} e Fe^{3+} seguidos de tratamento básico e térmico. Estes sistemas apresentam propriedades magnéticas típicas de nanopartículas superparamagnéticas sem interacções dipolares. As propriedades magnéticas dependem criticamente da existência de grupos isocianato livres, que actuarão como pontos de nucleação.

keywords

magnetic nanoparticles, superparamagnetism, iron oxides, antiferromagnetism, ferrimagnetism, organic-inorganic hybrids

abstract

The present work focus on the structure and the magnetic properties of iron oxide and iron oxide hydroxide nanoparticles grown in organic-inorganic hybrids. The sol-gel derived matrix, termed di-ureasils, is a siliceous network to which oligopolyoxyethilene chains with different molecular weight are grafted by means of urea cross-links. The di-ureasils local structure was modelled as groups of nanometric siloxane correlated domains embedded in a polymeric-rich media. In this thesis, the controlled growth of ferrihydrite, iron(III) oxyhydroxynitrate phases, maghemite and magnetite in di-ureasils is demonstrated. Ferrihydrite nanoparticles are formed at low pH on the siliceous surface, where the carbonyl groups act as nucleation points. This implies an heterogeneous nucleation, where the nanoparticles size depend on the amount of iron (in the 1 to 6% wt range) and the nanoparticles concentration is constant. The ferrihydrite nanoparticles have antiferromagnetic and uncompensated/canted moments, responsible for linear and saturation components in the dependence of the magnetization with field, respectively. These components can be separated by a new method here presented and an accurate dependence of the magnetic moment with temperature determined. The dynamic magnetic properties of ferrihydrite were studied by ac susceptibility, relaxation and Mossbauer measurements. These studies allowed the determination of the evolution of the dipolar interactions with the iron content and the determination of the anisotropy energy barrier distribution in cases where such interactions are negligible. Comparing the energy barrier distribution with the size distribution allowed to conclude that the uncompensated moments are randomly distributed in volume. This conclusion is based on a new method here presented, that uses distributions to investigate the power law relation between physical quantities. Antiferromagnetic iron(III) oxyhydroxynitrate phases with different degrees of crystallinity are formed when using low water concentrations in the sol-gel process. Some of these are precursors of ferrihydrite, as previously found in literature, but others constitute new phases. Maghemite and magnetite nanoparticles can be grown inside di-ureasils after the incorporation of Fe^{2+} and Fe^{3+} ions, followed by basic and thermal treatment. The magnetic properties show the existence of non-interacting superparamagnetic nanoparticles. Evidence for the possibility of tuning the magnetic properties of the system by allowing the existence of free isocyanate groups acting as nucleation sites was found.

Vale mais a pena ver uma cousa sempre pela primeira vez que conhecê-la,
Porque conhecer é como nunca ter visto pela primeira vez,
E nunca ter visto pela primeira vez é só ter ouvido contar.

Alberto Caeiro, em Poemas Inconclusivos, 1919

Contents

1 Introduction **5**

1.1 Description of the thesis . . . 5
1.2 Organic-inorganic hybrids . . . 6
1.2.1 Classification . . . 6
1.2.2 Synthesis . . . 7
1.2.3 The sol-gel process . . . 7
1.2.4 Applications . . . 11
1.2.5 The di-ureasils . . . 12
1.3 Iron-oxides . . . 15
1.3.1 Ferrihydrite . . . 16
1.3.2 Iron oxyhydroxynitrates . . . 22
1.3.3 Magnetite . . . 23
1.3.4 Maghemite . . . 26
1.4 Magnetic nanoparticles in nanocomposites . . . 27
1.4.1 Synthesis . . . 27
1.4.2 Applications . . . 28

2 Magnetic properties of nanoparticles **31**

2.1 General considerations . . . 31
2.2 Superparamagnetism . . . 32
2.2.1 General theory . . . 32
2.2.2 Deviations to superparamagnetism . . . 34
2.3 Magnetization under an applied field above T_B . . . 35
2.3.1 The Langevin law . . . 35
2.3.2 Effect of anisotropy . . . 35
2.3.3 Effect of distributions . . . 38
2.3.4 Effect of inter-particle interactions . . . 40
2.3.5 Surface effects and disorder . . . 42
2.4 Magnetization under an applied field below T_B . . . 43
2.4.1 The Stoner-Wohlfarth model . . . 43

2.4.2 Deviations from the canonic behavior . . . 43
2.4.3 The field and volume dependence of H_C . . . 44
2.5 Ac and dc susceptibility . . . 45
2.5.1 Non interacting systems . . . 45
2.5.2 Effect of interactions . . . 49
2.6 Magnetic relaxation . . . 53
2.7 Antiferromagnetic systems . . . 55
2.7.1 Bulk antiferromagnetic systems . . . 55
2.7.2 Antiferromagnetic nanoparticles . . . 55
2.7.3 Magnetization under an applied field in the $T_B < T < T_N$ range . . . 56
2.7.4 Magnetization under an applied field below T_B . . . 58
2.7.5 Susceptibility . . . 59
2.7.6 Thermoinduced effect . . . 60
2.8 Ferrimagnetic systems . . . 61
2.8.1 Bulk ferrimagnetic systems . . . 61
2.8.2 Nanoparticle ferrimagnetic systems . . . 62
2.9 Mössbauer spectroscopy . . . 64
2.9.1 Background and experimental technique . . . 64
2.9.2 Application to iron-based nanoparticles . . . 66
2.10 Magnetic property experimental techniques . . . 67
2.10.1 Dc measurements . . . 68
2.10.2 Ac measurements . . . 68

3 Ferrihydrite/hybrid matrix nanocomposites 71
3.1 Overview . . . 71
3.2 Synthesis . . . 71
3.3 Structural properties . . . 72
3.3.1 XRD and SAXS . . . 72
3.3.2 TEM and STEM/EDS studies . . . 75
3.3.3 FT-IR spectroscopy . . . 81
3.3.4 NMR spectroscopy . . . 82
3.4 Magnetic properties . . . 84
3.4.1 Dc susceptibiliy . . . 84
3.4.2 Ac susceptibility . . . 89
3.4.3 Magnetic relaxation measurements $M(t, T)$ . . . 90
3.4.4 Mössbauer spectroscopy . . . 92
3.4.5 Influence of the iron concentration: dipolar interactions . . . 94
3.4.6 $M(H, T)$ measurements . . . 97

3.5 Influence of the chains' length and synthesis procedure in the formation of ferrihydrite: d-U(2000) vs d-U(900) . . . 105
3.5.1 XRD . . . 105
3.5.2 FT-IR spectroscopy . . . 106
3.5.3 NMR spectroscopy . . . 107
3.5.4 Magnetic properties . . . 108
3.5.5 Influence of chains' length and synthesis procedure: conclusions . . . 112
3.6 Summary . . . 113

4 Magnetic studies in ferritin and ferrihydrite nanoparticles 115
4.1 Overview . . . 115
4.2 Description of the samples . . . 115
4.3 M(H,T) analysis: the scaling method . . . 116
4.3.1 Description of the method and application to ferritin . . . 116
4.3.2 Application to ferrihydrite/hybrid matrix nanocomposites . . . 120
4.3.3 Comparison between scaling method and fitting results . . . 120
4.4 Relation between size, anisotropy energy and moment investigated by distributions . . . 123
4.4.1 Relation between lognormal distributed physical quantities . . . 124
4.4.2 Size and energy distributions . . . 126
4.4.3 Size and moment distributions . . . 128
4.5 Summary . . . 129

5 Iron oxyhydroxynitrate/hybrid matrix composites 131
5.1 Overview . . . 131
5.2 Low crystalline iron oxyhydroxynitrates . . . 131
5.2.1 Synthesis . . . 131
5.2.2 XRD . . . 132
5.2.3 Ac susceptibility . . . 134
5.3 Crystalline Iron oxyhydroxynitrate . . . 135
5.3.1 Synthesis . . . 135
5.3.2 XRD . . . 136
5.3.3 SEM . . . 136
5.3.4 Magnetic properties . . . 137
5.3.5 Mössbauer spectroscopy . . . 138
5.4 Summary . . . 139

6 Maghemite and magnetite/hybrid matrix nanocomposites 141
6.1 Overview . . . 141
6.2 Synthesis . . . 141

6.2.1 Maghemite . . . 142
6.2.2 Magnetite . . . 143
6.3 XRD . . . 143
6.4 Ac susceptibiliy . . . 144
6.4.1 Maghemite . . . 144
6.4.2 Magnetite . . . 144
6.5 M(H,T) measurements . . . 146
6.5.1 Maghemite . . . 146
6.5.2 Magnetite . . . 146
6.6 Influence of the isocyanate groups in the formation of maghemite . . . 148
6.6.1 Dc susceptibility . . . 148
6.7 Summary . . . 150

7 Conclusions **153**
7.1 Summary and conclusions . . . 153
7.2 Future perspectives . . . 156

Appendices **157**

A MatLab routine for moment distributed Langevin M(H,T) fit **159**
A.1 Routine LagFitLNdes . . . 159
A.2 Sub-routine LagFitLNdessub . . . 161

B TEM and STEM/EDS images **165**

C List of samples/measurements **169**

Bibliography **171**

Chapter 1

Introduction

1.1 Description of the thesis

This thesis reports work made on the relation between structure and magnetic properties of iron oxide and iron oxide-hydroxide nanoparticles formed within organic-inorganic hybrid matrices. This constitutes a small part of the effort being developed in the investigation groups of Prof. Verónica de Zea Bermudez, Prof. Fernando Palácio, Prof. Luis Carlos and Prof. Vítor Amaral, concerning the development of organic-inorganic matrices and polymers for optical and magnetic applications. In the last years, these groups have developed the synthesis of organic-inorganic matrices based on urea crosslinks, and the synthesis of several iron oxide and iron oxide-hydroxide nanoparticles in polyvinilpyridine (PVP). Structure characterization techniques commonly used in these materials include X-ray diffraction, small-angle X-ray scattering, electron microscopy, Fourier-transformed infra-red and Raman spectroscopy and nuclear magnetic resonance. Characterization techniques used to study the magnetic properties of these materials include the determination of magnetization as a function of temperature, field and frequency. Another part of the work being developed in these groups concerns application of magnetic nanoparticles in medicine, in particular applications in hyperthermia devices.

Based on this know-how, this work aimed the adaptation of the synthesis routes applied in the growth of nanoparticles in PVP to produce nanoparticles in organic-inorganic matrices, and the structural and magnetic characterization of the produced materials. Effort was also made on relating structure and magnetism and on modeling the magnetic properties of the studied materials. The modeling consists on studying the influence of magnetic moment distribution on the nanoparticles magnetization and the relation between size, anisotropy energy and magnetic moment based on their distributions.

The first chapter of the thesis comprises a description of the organic-inorganic hybrids and an overview on the iron oxide and iron oxide-hydroxide nanoparticles. In chapter 2 we describe the magnetic properties of nanoparticles, based in the framework of superpara-

magnetism. Then we present chapters devoted to a nanoparticle/organic-inorganic hybrid composite, where their synthesis and characterization are discussed. Chapter 3 describes the study made on composites with ferrihydrite nanoparticles, chapter 5 describes oxyhydroxinitrate nanocomposites, while chapter 6 describes maghemite and magnetite nanocomposites. We also present a more detailed study on the relation between structure and magnetism of ferritin and ferrihydrite nanoparticles in chapter 4. The last chapter includes the main conclusions of the work and future expectations for the field.

1.2 Organic-inorganic hybrids

In the present context, hybrids are defined as organic-inorganic or bio-mineral systems, where at least one of the components is present in the nanometer scale [1]. The combination of both organic and inorganic components has made accessible materials with tuned properties between those characteristic of organic and inorganic materials [2]. For instance, inorganic materials offer the potential for a wide range of electronic, magnetic and dielectric properties, mechanical hardness, and thermal hydrolytic stability. On the other hand, organic molecules can provide high fluorescence efficiency, large polarizability, plastic mechanical properties, ease of processing, and structural diversity [3]. Beyond the characteristic properties of the organic and inorganic components, new properties arise, due to the synergy resulting from the organic-inorganic interface, due to multi-scale order and due to the reduced size of the components.

1.2.1 Classification

The nature of the organic-inorganic interface is a key point for the design of hybrids and has been used to classify hybrids. In class I hybrids, organic and inorganic components are linked by weak interactions (in terms of orbital overlap), while in class II hybrids organic and inorganic components are linked by covalent bonds [2]. Weak interactions include hydrogen, van der Waals and electrostatic bonding. Class II hybrids are mainly based on the hydrolytic stability of the Si-C bond. In the last years, new hybrid materials that combine weak and strong interactions have emerged. This combination is responsible for hierarchically structured hybrids, that present complexity. Complex behavior is not necessarily associated to the atomic structure, but is mainly due to the orderly assembly of all or part of its constituents.

Examples of class I hybrids are organic dyes and biomolecules incorporated in porous sol-gel matrices [4, 5, 6]. The guest molecules are physically dissolved together with the precursors of the inorganic host or introduced to the sol state so that they become entrapped in the final material (see Sec. 1.2.3 for details about the sol-gel process). There is a great number of precursors based on the stability of the Si-C bond and therefore there are many examples of class II hybrids [1, 2]. The covalent bonding enables one to enlarge the in-

corporated amount of the organic ingredients, comparing to class I hybrids. An important example of hierarchically structured hybrids are silsesquioxanes of the type RO_3-Si-R'-Si-O_3R, where R and R' are organic groups, and organosilanes R'-Si-X_3, where X=OR or Cl. Different architectures with well-defined morphologies at the macroscopic scale can be obtained. Examples include bilayered lamellar structures [7, 8, 9, 10, 11], two-dimensional (2D) hexagonal structures [10], twisted helical fibres with controlled handedness [12], hollow tubes and spheres [13], and ladder-like superstructures [11]. In these hybrids, the basic structural units are covalently-linked organic-inorganic monomers and the multi-level structure is induced by phase separation. This has an entropic contribution, and an enthalpic contribution due to weak interactions (hydrogen bonding, hydrophobic interactions, $\pi - \pi$ interactions) between the R' organic spacers. A recent example of a self-structured lamellar organic-inorganic hybrid (named mono-amidosil) was reported by Carlos el al. [14]. In mono-amidosil, luminescence is not just governed by a microscopic mechanism with a characteristic time associated to independent entities, but by correlated processes occurring at larger length scales, due to the multi-scale structure.

1.2.2 Synthesis

There are different chemical pathways to design an hybrid material [2, 15], schematically represented in Fig. 1.1. Paths A_1 and A_2 correspond to the conventional sol-gel route and are presented with some more detail in Sec. 1.2.3. Path A_3 leads to the obtention of crystalline hybrid materials (hybrid metal organic frameworks) by hydrothermal synthesis, using polar solvents and organic templates. In path C, the inorganic component grows inside a pre-structured self-assembled organic template, which allows the control of organization and texturing of the final hybrid. Path B is similar to C, but involves the use of pre-formed inorganic clusters, that are used as nanobuilding blocks. These nanobuilding blocks can also be capped and connected by organic molecules, that act as ligands and spaces (path B). The use of these blocks allows a better definition of the inorganic components and include objects like clusters, nanoparticles or nanolayered compounds. Path D is a combination between strategies used in paths A, B, and C, allowing the construction of hierarchically organized materials inspired by those observed in natural systems [15]. It is important to note that all these pathways correspond to processing at mild conditions, in particular low temperatures, using the concept of "*chimie douce*" [15]. At the same time, the materials are formed starting from molecules, in a "bottom-up" approach.

1.2.3 The sol-gel process

The sol-gel process allows the synthesis of organic-inorganic materials (depicted as paths A_1 and A_2 in Fig. 1.1) as well as inorganic materials. Materials are obtained in the form of monoliths, films, fibers, and particles. The sol-gel process includes the polymerization of

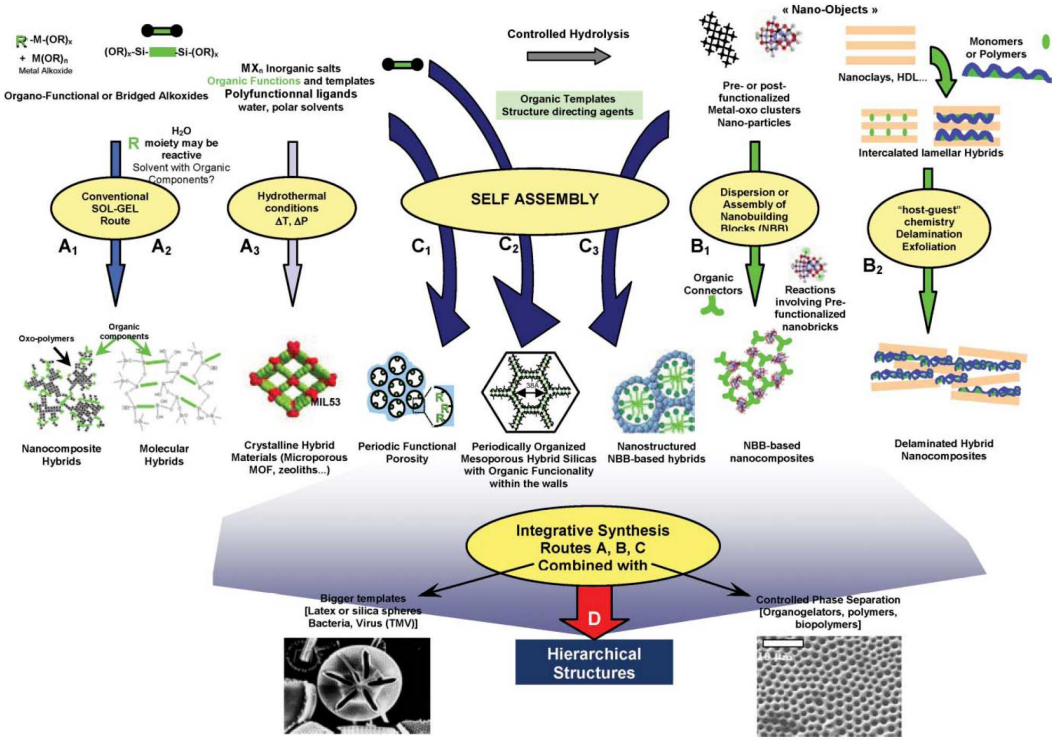

Figure 1.1: Different paths for the synthesis of hybrid materials. Path A corresponds to conventional sol-gel routs; path B involves the assembly of inorganic nanobuilding blocks *via* organic molecules; path C involve the use of organic and inorganic templates; and path D corresponds to combination of the previous routes (from Ref. [15]).

molecular precursors, the obtention of a sol, the gelification of the sol, and the evaporation of the solvent [16]. A sol is defined as a colloidal dispersion of particles with dimensions between 1 and 200 nm. A gel is a solid composed of at least two phases, often a liquid embedded in a 3-dimensional porous phase.

Steps of the sol-gel process

The sol-gel process starts with a solution containing the molecular precursors, water, an alcohol, and a catalyst (see, for instance Ref. [16]). Molecular precursors include metal salts, alkoxides or organically modified alkoxides. The latter are often used in the synthesis of organic-inorganic hybrids. In this solution, the precursors are hydrolyzed and condensed, leading to the formation of the sol. The next step depends on the desired form of the final material. To obtain a monolith or a powder the sol is casted into a mould. Films are obtained by spin- or dip-coating. As the hydrolysis and condensation proceed, the viscosity of the gel increases up to the gelation point. At this point, fibers can be obtained by extrusion. The gel is then aged during a period of time that can range from hours to several days. During the aging, the hydrolysis and condensation reactions are still occurring. The liquid phase

is then removed from aged gel in the drying stage. In the case of the production of films and monoliths, this stage is critical, since the material may crack. This can be controlled, for instance, by evaporating in hypercritical conditions, at which the solid-liquid interface is avoided. The dried gel may be subject of a thermal treatment, to remove porosity.

Chemical reactions

The basic reactions of the sol-gel process are the hydrolysis and condensation of molecular precursors (see, for instance Ref. [16]). In the case of organic-inorganic hybrids reactions may also include the polymerization of the organic component. The hydrolysis of an organically modified alkoxide may be written as:

$$\text{R'}_n\text{M(OR)}_{m-n} + \text{H}_2\text{O} \rightleftharpoons \text{R'}_n\text{M(OR)}_{m-n-1}\text{(OH)}+\text{ROH} \tag{1.1}$$

where OR is the alkoxy group and R' the non-hydrolyzable organic group. This is an equilibrium reaction, where the reverse path of hydrolysis, esterification, may also occur. Further reactions may include molecules with OH groups that can react with OR or other OH groups leading to the formation of larger molecules. These are condensation reactions. The direct paths of the following reactions illustrate the formation of dimers:

$$\begin{aligned} \text{R'}_n\text{M(OR)}_{m-n} + \text{R'}_n\text{M(OR)}_{m-n-1}\text{(OH)} &\rightleftharpoons \\ \text{R'}_n\text{(OR)}_{m-n-1}\text{M-O-M(OR)}_{m-n-1}\text{R'}+\text{ROH} & \end{aligned} \tag{1.2}$$

$$\begin{aligned} \text{R'}_n\text{M(OR)}_{m-n-1}\text{(OH)} + \text{R'}_n\text{M(OR)}_{m-n-1}\text{(OH)} &\rightleftharpoons \\ \text{R'}_n\text{(OR)}_{m-n-1}\text{M-O-M(OR)}_{m-n-1}\text{R'}+\text{H}_2\text{O} & \end{aligned} \tag{1.3}$$

With time, condensation involves the formation of larger molecules.

In alternative, water may replaced by a carboxylic acids, such as acetic or valeric acid. The alkoxide is then condensed by a solvolysis route, instead of the hydrolysis one. At present, the mechanism of carboxylic acid solvolysis is not totally clear, although a two-step reaction mechanism was proposed by Pope and Mackenzie [17]. An example of solvolysis is acetic acid solvolysis, that may involve the following reactions:

$$\begin{aligned} \text{R'}_n\text{M(OR)}_{m-n} + \text{AcOH} &\rightleftharpoons \\ \text{R'}_n\text{M(OR)}_{m-n-1}\text{-OAc} + \text{ROH} & \end{aligned} \tag{1.4}$$

$$\text{ROH} + \text{AcOH} \rightleftharpoons \text{ROAc} + \text{H}_2\text{O} \tag{1.5}$$

$$\text{R'}_n\text{M(OR)}_{m-n-1}\text{-OAc} + \text{ROH} \rightleftharpoons \text{R'}_n\text{M(OR)}_{m-n-1}\text{-OH} + \text{ROAc} \tag{1.6}$$

$$\begin{aligned} &\text{R'}_n\text{M(OR)}_{m-n-1}\text{-OAc} + \text{R'}_n\text{M(OR)}_{m-n-1}\text{-OR} \rightleftharpoons \\ &\quad \text{R'}_n\text{M(OR)}_{m-n-1}\text{-O-M(OR)}_{m-n-1}\text{R'}_n + \text{ROAc} \end{aligned} \tag{1.7}$$

These possibilities have been demonstrated by spectroscopic techniques [18]. As seen in the above equations, in acetic acid solvolysis there are several different intermediate routes to obtain the final material: reaction 1.4 is a prerequisite of the remaining reactions, while reaction 1.6 corresponds to the creation of reactive R'M$(OR)_{m-n-1}$-OH species. Reaction 1.7 leads directly to the hybrid formation.

Influence of the synthesis conditions

The monomers (alkoxides) functionality, f, is defined as the number of links that it may establish, i. e. $m - n$ in the example given in Eq. 1.2. Materials obtained from monomers with $f = 2$ have a chained structure, while those obtained from monomers with $f = 3$ may have branched or 2-dimensional structures. Materials obtained from monomers with $f = 4$ with have more or less complex 3-dimensional structures [19]. Sol-gel derived structures are often fractal. For mass fractals, the relation between mass and radius is:

$$M \propto r^{D_f} \tag{1.8}$$

with $D_f < 3$ being the fractal dimension. Surface fractals have a similar relation between surface and radius:

$$S \propto r^{D_s} \tag{1.9}$$

with $D_S > 2$ being the surface fractal dimension. The fractal structures arise from the low reversibility of the processes expressed in Eqs. 1.2 and 1.3: once formed, a chemical linkage has low probability of being broken. Therefore, linkages are formed randomly and far from equilibrium conditions [19].

Hydrolysis and condensation proceed faster and are more complete when using catalysts. These can be acids or bases. Acid-catalyzed hydrolysis with low H_2O/M(OR) ratios produces weakly branched structures, while base-catalyzed hydrolysis with large H_2O/M(OR) ratios produces highly branched structures [19]. Any "complication" in the R group (i. e. larger or more branched groups) retards the hydrolysis rate. This is particularly severe in the case of branched groups. In the case where M is Si and R' is CH_3, Schmidt et al. [20] have demonstrated that the substitution of CH_3 groups by OR groups (i. e. the increase of n) increases the rate of hydrolysis in the case of acid catalysis, and decreases it in the case of basic catalysis. The increase of the H_2O/M(OR) ratio promotes hydrolysis, according to Eq. 1.1. At the same time, a H_2O/M(OR) ratio below the stoichiometric value promotes the alcohol producing condensation (Eq. 1.2), while a ratio above the stoichiometric value promotes the water producing condensation (Eq. 1.3). Hydrolysis is facilitated in the presence of

homogenizing agents, such as alcohols, dioxane, tetrahydrofuran (THF) and acetone. This is particularly important in the case of bulky R ligands. Important characteristics of the solvents are polarity and the availability of labile protons [19]. As one might expect, polar solvents which hydrogen bond to hydroxyl or hydronium ions reduce the catalytic activity under basic and acidic conditions, respectively.

1.2.4 Applications

The design an application of materials where organic and inorganic materials are mixed together at small scale is an old challenge. One of the most ancient examples is the "Maya blue", a man-made pigment, where natural blue indigo molecules are encapsulated within the channels of a clay mineral (palygorskite) [21]. This is an organic–inorganic hybrid of the 8^{th} century that combines the color of the organic pigment and the resistance of the inorganic host. Nowadays, successful commercial hybrid organic–inorganic materials have been part of manufacturing technology since the 1950s. Examples are thin-film and coating materials, as zinc-rich organic paints [22].

In general, applications of organic-inorganic hybrids exploit different properties as i) mechanical properties in abrasion resistant coatings, ii) barrier properties in corrosion protection of metals and reduction of permeability of polymeric sheets, iii) passive optical properties in decorative and functional coatings for glasses, iv) active optical properties in the development of photoactive coatings and systems, and v) electrical properties in antistatic films and ionic conductors [23].

Concerning i) exploiting mechanical properties, hard poly(methylsiloxane)s and related silica containing coating materials have been used in improving the wear and abrasion resistance of engineering plastics, e. g. on top of headlights of cars made from polycarbonate (PC) or side windows in buses made from poly(methyl methacrylate) (PMMA) [23]. In current automotive finish technology, coloration is provided in a pigmented base coat. A clear scratch-resistant overcoat is applied, which must not only satisfy optical and mechanical requirements, but must provide protection from environmental factors such as UV and chemical attack [22]. Other coating applications include films deposited on top of polymeric lenses by wet chemical techniques. Developments on polymer lenses due to hybrids include antireflective and hydrophobic "easy-to-clean" technology [23].

Barrier properties ii) are due to the fact that some molecules and metal ions have low solubility and diffusion rates in hybrid coatings. Therefore, hybrids may be used to protect metals from corrosion. Similar barrier effects occur in the case of oxygen, water and flavors [23]. The barrier, mechanical and transparency properties made the combination of an hybrid composite and a fluoropolymer the best solution in coating the Last Judgement panel of the St. Vitus Cathedral, Prague [24].

A traditional aspect of passive optical applications iii) is the coloration of glasses via

hybrid coatings. Organic dyes can be dissolved in the respective sols, and colored coatings are obtained by spraying the sol onto the glass. The adhesion is due to the presence of SiOH groups on the glass surfaces, which can react with their counterparts in the hybrid materials. Dye-doped transparent hybrid sol-gel coatings are also in use on cathode ray tubes to improve color TV image resolution [23]. A recent development has exploited the porous nature of silica-based sol-gel thin films to impart antireflective properties to architectural glasses. The porosity gradient leads to a corresponding gradient of the refractive index, thereby increasing the visible light transmissivity of the glass substrate to very high values (>99%) [23].

Exploiting active optical properties iv) include nonlinear optically active materials, photoelectrochemical cells based on a chelating metal-complex dye and doped TiO_2 nanoparticles, and luminescing hybrids doped with rare earth metal ions or quantum dots. As an example, light emitting diodes (LEDs) based on organic–inorganic perovskites are considered very attractive [3] . These organic-inorganic LEDs, combine the efficient fluorescence of organic molecules with the templating and electronic band-structure tunability of metal halide sheets.

Concerning electrical properties v), advantage can be taken from the highly isolating properties of hybrids. Typically specific bulk electrical resistivities are of the order of $10^{13} - 10^{16}$ Ωcm. In hybrids, this insulating behavior is combined with the high adhesion to various surfaces (via Si-OH groups) and with the possibility to use conventional photoresist technologies to form microstructural patterns. These properties are the basis for the use of hybrids as passivation and dielectric layers in microelectronic applications [23]. At the same time, pure methylsilsesquioxanes have dielectric constants in the range of 2.9–3.2 at 60 Hz and have become the starting-point compositions for interlayer dielectrics of interest for microelectronic features below 0.18 μm. Approaches for reducing the dielectric constant below 2.9 include mesoporous and composite versions [23].

1.2.5 The di-ureasils

Di-ureasils are organic-inorganic hybrids composed of a siliceous backbone, covalently linked to both ends of polyoxyethylene (POE) chains by means of urea linkages [25]. The POE chains may have different average molecular weights (M_w), corresponding to different average chain lengths. M_w may range between 230 and 2000 mol/g. Di-ureasils are often termed d-U(M_w), where U designates the urea linkages. The presence of the siliceous backbone promotes improved mechanical and thermal properties, compared to POE systems.

Di-ureasils can be doped with different ions, in particular rare-earth salts [26] and complexes [27], and alkaline ion salts [28], to tune luminescence and ionic conductivity, respectively. Concerning luminescence, it is possible to obtain white light emission [29] and to tune the emission color, by changing the salt concentration, and the excitation wavelength [26]. The absorption spectra of the undoped matrix can be tuned using metallic nanoparticles (in particular Ag and Au) with different shapes and concentrations [30]. More recently,

di-ureasils were successfully doped with zirconium (IV) n-propoxide and methacryloxipropyltrimethoxysilane in order to be used in integrated optics, as planar waveguides [31].

Synthesis

The synthesis of the di-ureasils is schematically represented in Fig. 1.2. The first step is the preparation of the organically modified alkoxide precursor. This involves the formation of urea linkages between the terminal NH_2 groups of a doubly functional amine (α, ω-diamine poly(oxyethylene-*co*-oxypropylene)) and the isocyanate group of an alkoxysilane precursor (3- isocyanatepropyltriethoxysilane, ICPTES, Fluka) in THF (Merck) at room temperature (RT)[25]. The doubly functional amine may have different M_w, being commercially available from Fluka as Jeffamine ED-2001®, Jeffamine ED-900® and Jeffamine ED-600®, (M_w=2000, 900 and 600). The second step is the hydrolysis and condensation of the hybrid precursor, by adding it to a mixture of ethanol and water (molar proportion ICPTES/CH_3CH_2OH/H_2O=1:4:1.5). The resulting mixture is then stirred in a sealed flask for a few minutes at RT and then casted into a mould. The mould is then transferred to an oven at ca. 40°C for a period of 7 days. The sample is then aged for 3 weeks at ca. 40°C to form mechanically stable films.

Di-ureasils may also be obtained by a carboxylic acid solvolysis route [32]. In the first step, acetic acid attacks the ethoxy groups bonded to the silicon atom (C_2H_5OSi-), forming an ester (CH_3COOSi-). During the second step, this ester reacts with ethanol, producing ethyl acetate ($CH_3COOC_2H_5$) and Si-OH groups. Then, the condensation of two Si-OH groups, or one Si-OH group and one ethanol molecule, yields the Si-O-Si network. This was recently confirmed by Lianos et al. for the acetic acid solvolysis of poly(propylene oxide)/siloxane hybrids in the presence of ethanol using infrared measurements [33]. However, Lianos et al. reported that the pure acetic acid solvolysis of di-ureasil precursors is a very slow process, especially when the reaction is operated in a dry N_2 atmosphere [18]. Therefore, residual water contained in ethanol and water from moisture (in the case of synthesis operated in air) also participate in the hydrolysis and condensation of the hybrid precursor.

Local structure

The local structure of the di-ureasils was modeled based on X-ray diffraction (XRD) [34, 32], small-angle X-ray scattering [35, 36], ^{29}Si and ^{13}C nuclear magnetic resonance [37, 32], infrared and Raman spectroscopy [25], and photoluminescence spectroscopy [34, 36]. The di-ureasils are composed of siliceous domains embedded in a polymeric-rich matrix. The siliceous domains are spatially correlated at an average distance that depends on the polymer length [35]. The characteristic size of the siliceous domains is $R_g = 0.5$ nm. These domains are mainly composed of Si atoms with T^2 and T^3 environments. T^2 corresponds to R'Si$(OSi)_2(OH)$ sites, while T^3 are R'Si$(OSi)_3$ sites. The degree of condensation of the

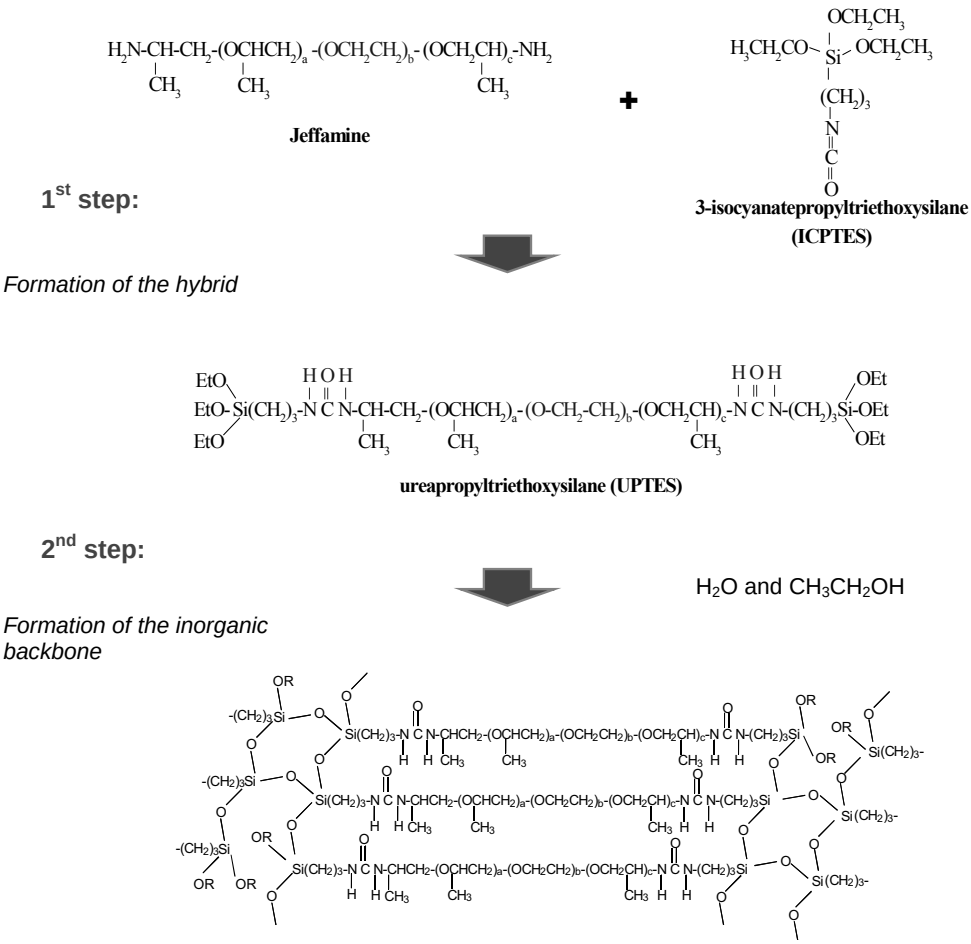

Figure 1.2: Synthesis of the undoped di-ureasils [25]. All Jeffamine® have $a + c = 2.5$, while $b = 40.5$, 15.5 and 8.5 for M_w= 2000, 900 and 600, respectively.

siliceous domains can be defined as: $c = (1/3)T_1 + (1/2)T_2 + (1/3)T_3$, and in di-ureasils ranges from 96 to 76 %, as M_w varies from 600 to 2000 g/mol [37].

1.3 Iron-oxides

Iron oxides are widespread in nature. As a consequence, they are present in many aspects of daily life and are subject of interest in different fields, including Geology, Mineralogy, Physics, Chemistry, Biology and Medicine [38]. There are 16 known iron oxides, hydroxides and oxide-hydroxides. Some iron oxides have also small amounts of anions, as Cl^-, SO_4^{2-}, CO_3^{2-} and NO_3^-. Among these 16 iron oxides are 5 polymorphs of FeOOH and four of Fe_2O_3. Some properties of the iron oxides are summarized in Tab. 1.1.

Table 1.1: Selected properties of the iron oxides, according to Ref.[38]

mineral name	Goethite	Akaganéite	Schwertmannite
chemical formula	α-FeOOH	β-FeOOH	$Fe_8O_8(OH)_6SO_4$
structure	orthorhombic	monoclinic	tetragonal
cell dimensions (nm)	$a = 0.9956$	$a = 1.0546$	$a = 1.065$
	$b = 0.30215$	$b = 0.3031$	$c = 0.604$
	$c = 0.4608$	$b = 1.0483$	
		$\beta = 90.63°$	
Formula units per unit cell, Z	4	8	2
Density (g/cm^3)	4.26		≈ 3.8
Color	yellow-brown	yellow-brown	orange-brown
Type of magnetism	antiferromag.	antiferromag.	antiferromag.
Transition temperature (K)	400	290	

.

Ferrihydrite	Hematite	Magnetite	Maghemite
$Fe_5HO_8{\cdot}4H_2O$ [39]			
$Fe_5(O_4H_3)_3$ [40]	α-Fe_2O_3	Fe_3O_4	β-Fe_2O_3
$Fe_2O_3{\cdot}2FeOOH\ {\cdot}4H_2O$ [41]			
hexagonal	rhombohedral	cubic	cubic or
	hexagonal		tetragonal
(see Sec. 1.3.1)	$a = 0.50356$	$a = 0.8396$	$a = 0.83474$
	$c = 1.37489$		
4	6	8	8
3.96	5.26	5.18	4.87
red-brown	red	black	reddish-brown
antiferromag.	weakly ferromag.	ferrimagnetism	ferrimagnetism [1]
300	956	850	820-986

The structure of the iron oxides is based on close packed arrays of anions. The usual arrangements are the hexagonal and cubic close packing of sheets of anions (hcp and ccp, respectively). The interstices are twice the number of anions and since the charge of the iron ions (Fe^{2+} and/or Fe^{3+}) is less than the double of the oxygen ions charge, only a portion of

the interstices are filled. This opens the possibility of different cation arrangements and thus polymorph iron oxide phases [38].

The most common basic structural units of iron oxides are the $Fe(O)_6$ and $Fe(O)_3(OH)_3$ octahedra. These basic units can be linked by corners, edges, faces or combinations of these linkages. The average Fe-Fe distance depends on the units linkages, as shown in Fig. 1.3. The

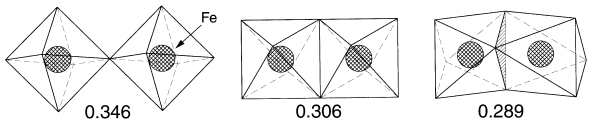

Figure 1.3: Typical Fe-Fe distances (in nm) for the different octahedra linkages (from Ref. [38]).

type of interaction between Fe ions on adjacent sites depends mainly on the Fe oxidation state and Fe-O-Fe angle. This interaction is electrostatic super-exchange interaction and proceeds via O^{2-} or OH^- ligands. The exchange interaction occurs between the unpaired electrons in the e_g orbitals of the Fe^{3+} ions and the electrons on the p orbitals of the O^{2-} ions. The intensity of the exchange interaction depends on the Fe-O-Fe angle and Fe-O bond length, as listed in Tab. 1.2 [38].

Table 1.2: Exchange interactions in the iron oxides (accordingly to Ref. [38]).

ion pair	Fe-O-Fe bond angle	Type of interaction
Fe^{3+}- Fe^{3+}	90°	weak antiferromag.
	120°	strong antiferromag.
Fe^{2+}- Fe^{2+}	90°	weak antiferromag.
	120-180°	strong antiferromag.

1.3.1 Ferrihydrite

Ferrihydrite is a poorly ordered iron oxide that typically forms after rapid hydrolysis of iron at low pH and low temperatures. The importance of ferrihydrite in the environmental iron cycle and in the metallurgy process triggered the interest of the scientific community. Ferrihydrite is present in cold-water springs, recent bottom sediments of some lakes and soils, as Hawaii basalt crusts, Spodosols, and loesses [42]. Ferrihydrite is also part of the iron cycle in living organisms. In fact, ferritin is a protein where Fe^{3+} is stored as ferrihydrite [43] (see details is Sec. 1.3.1).

Synthesis

In aqueous solution, ferrihydrite is often the first product of the hydrolysis of iron(III) salts. Standard synthesis to produce around 5 g of 6-line ferrihydrite starts with 2 L of distilled water at 75°C in which 20 g of unhydrolyzed crystals of $Fe(NO_3)_3 \cdot 9H_2O$ are dissolved with rapid stirring. The solution is putted at 75°C for 10-12 min, where it changes from gold to reddish brown, indicating the formation of Fe hydroxy-polymers. The solution is then rapidly cooled by plunging into ice water and transferred to a dialysis bag during at least 3 days. The freeze-dried suspension corresponds to ferrihydrite [38]. A method to produce 10 g of 2-line ferrihydrite starts by adding 330 ml of KOH to 500 mL of 0.1 M $Fe(NO_3)_3$ solution. The pH should be between 7 and 8. The suspension is then centrifuged, dialyzed and freeze-dried [38].

Ferrihydrite may be further converted to the thermodynamically more stable hematite or goethite, by aging, changing the pH and/or the temperature [42]. In fact, ferrihydrite is considered an important precursor for iron oxide formation in various natural environments. The transformation to hematite and goethite occurs by competing mechanisms. Factors as the degree of ordering of ferrihydrite, pH and temperature affect the goethite/hematite ratio. The formation of hematite involves a combination of aggregation-dehydration-rearrangement processes requiring water. The formation of goethite involves dissolution of ferrihydrite followed by crystallization of goethite in bulk solution. A scheme of the possible transformation pathways of ferrihydrite and other common iron oxides is shown in Fig. 1.4.

Structure

Ferrihydrite is characterized by high dispersion, small particle size, and poor crystallinity [42]. In fact, the x-ray diffraction (XRD) patterns of ferrihydrite show 2 or 6-8 reflections as the structural order increases. Ferrihydrites are usually termed according to the number of XRD reflections, i. e., 2-lines or 6-lines ferrihydrite. It was shown that not only these two ferrihydrites exist but several with different number of peaks, that decrease systematically as the rate of Fe^{3+} hydrolysis increase [44]. Typical ferrihydrite XRD pattern and transmission electron microscopy (TEM) image are shown in Fig. 1.5. TEM images of ferrihydrite powders usually show spherical particles with sizes between 4 and 6 nm. High resolution TEM images (HRTEM) show single crystals with a hexagonal outline [45].

There is not a broad agreement about the crystal structure of the ferrihydrites with different number of XRD reflections, in particular if they have the same structure but different crystallinity or if they have different structures [42]. The structure of 6-line ferrihydrite itself has been a matter of debate. The first model was given by Towe and Bradley in 1967 [39]. According to this model, the structure of ferrihydrite is a defective hematite structure, i. e., an hcp array of anions with vacant Fe^{3+} sites and considerable amount of water. Contemporary models include the one of Eggleton and Fitzpatrick [46], based on double-

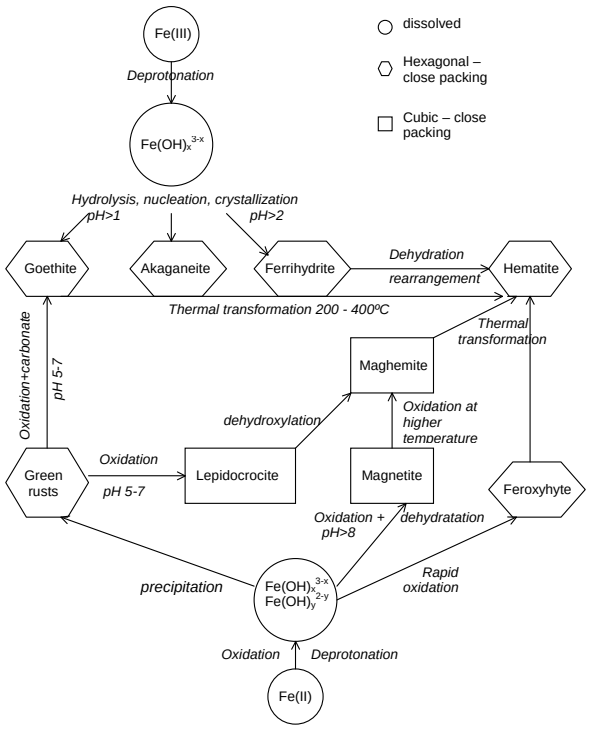

Figure 1.4: Schematic representation of formation and transformation pathways of common iron oxides together with the approximate transformation conditions (from ref. [38]).

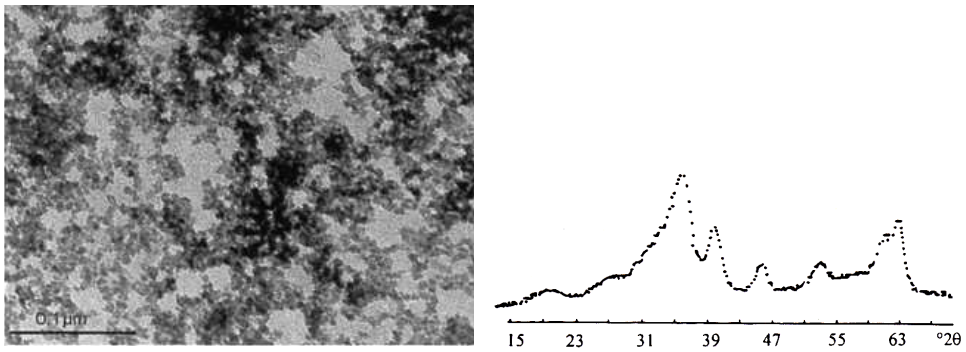

(a) (b)

Figure 1.5: Typical Ferrihydrite TEM image [38] and XRD pattern (Cu K_α) [42].

hexagonal close packing of oxygens $ABAC$. In this model, two sheets of anions have Fe ions in octahedral positions and the following two sheets have Fe ions in mixed octahedral and tetrahedral positions with 2:5 ratio. However, the existence of tetrahedral positions is not consistent with EXAFS [47] and Mössbauer spectroscopy results [48].

Based on EXAFS and XRD studies, Drits and co-workers proposed that 6-line ferrihydrite contains three intergrown components [49]: defect-free, defective, and ultra dispersed 1-2 nm

hematite. The defective-free component consists of $ABACA...$ anion close packing, where the Fe ions are at octahedral sites with 50% occupancy (Fig. 1.6). The unit cell is hexagonal (space group P31c) with $a = 0.296$ nm and $c = 0.949$ nm. The defective component has ABA and ACA structural fragments, with the Fe ions identically ordered within each fragment. The unit cell is hexagonal (space group P3) with $a = 0.5126$ nm and $c = 4.70$ nm.

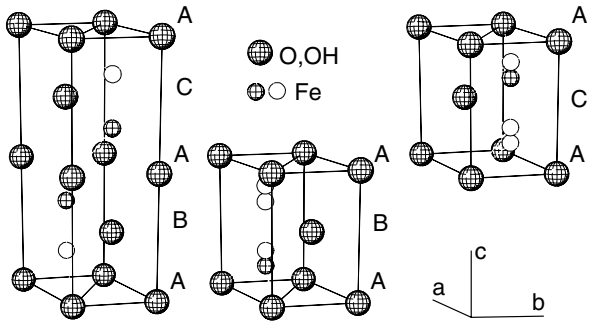

Figure 1.6: Ferrihydrite structure proposed by Drits et al. [49, 50].

The Drits model for 6-line ferrihydrite was further confirmed by neutron diffraction [50]. However, it was not necessary to assume the presence of ultra dispersed hematite. The presence of such phase may therefore depend on the synthesis conditions. The neutron diffraction studies revealed the existence of defect-free and defective phases with 1:1 ratio.

Magnetic properties

The magnetic properties of the iron oxides, including ferrihydrite are often characterized by Mössbauer spectroscopy and magnetometry. Ferrihydrite has antiferromagnetic interactions and the spins are ordered below temperatures of the order of 330 K [50]. In contrast to bulk antiferromagnetic systems, ferrihydrite nanoparticles have uncompensated and canted spins that give a net magnetic moment. This moment is able to fluctuate across the anisotropy barrier above a characteristic temperature, usually called T_B. This temperature depends on the magnetic moment, on the particles size, on the anisotropy energy, on the interparticle interactions, and on the characteristic time of the measurement. T_B is usually between 10 and 100 K (see details about T_B and superparamagnetism in Sec. 2.2). Below T_B, the magnetization curves of ferrihydrite show hysteresis. Typical coercive fields are of the order of tens-hundreds of Oe. When the samples are cooled from $T > T_B$ to $T < T_B$ in the presence of a magnetic field the hysteresis cycles are shifted in the field axis [51]. This has been interpreted as an exchange bias phenomena [52, 53], resulting from an interaction between an antiferromagnetic core and the uncompensated moments [51]. Above T_B, the magnetization curves show linear and saturation components, associated to the antiferromagnetic Fe atoms and to the uncompensated/canted atoms, respectively.

Mössbauer spectroscopy of ferrihydrite varies according to the crystalline order and purity of the particles. Below T_B, the Mössbauer spectra show a sextet, with a hyperfine field, $B_{hf} \approx 400 - 500$ kOe, quadrupole splitting of -0.06 mm/s, and isomer shift of 0.25 mm/s (6-line ferrihydrite at 4.2 K) [38]. As the temperature crosses T_B a doublet appears, superimposed to the sextet. T_B associated to Mössbauer measurements is usually defined as the temperature where the intensity of the doublet is equal to the one of the sextet. As an example, the evolution of the Mössbauer spectra with temperature of ferrihydrite nanoparticles artificially grown inside apoferritin protein is show in Fig. 1.7 [54]. The contribution of the doublet and sextet are show in continuous lines.

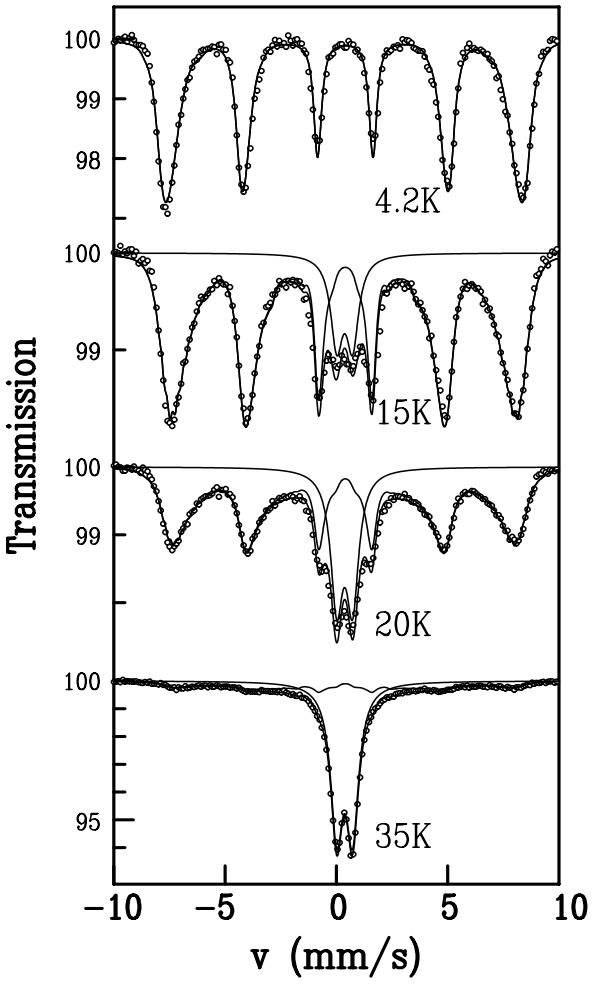

Figure 1.7: ^{57}Fe Mössbauer absorption spectra at different temperatures of ferrihydrite nanoparticles with 4 nm diam. artificially reconstructed in apoferritin protein (from ref. [54].)

The hyperfine splitting that occurs at low temperatures increases the resolution, concerning the analysis of both crystallographic and magnetic states of ferrihydrite. This resolution is further increased by the application of an external magnetic field [48]. Pankhurst and Pol-

lard [48] analyzed the high-field Mössbauer spectra of 2- and 6-line ferrihydrite and concluded that tetrahedral Fe ions are not significantly present in neither of the structures. The spectra of 2-line ferrihydrite obtained at different applied fields up to 90 kOe are well fitted to a model of two sublattice ferrimagnetism. The spectra of 6-line ferrihydrite recorded in similar conditions can be fitted to a simple two sublattice antiferromagnetism model [48]. The 2-line ferrihydrite nanoparticles used in this study are smaller and less crystalline than the 6-line ferrihydrite nanoparticles, which might be the reason for the observed ferrimagnetism [48].

The existence of antiferromagnetic order in 6-line ferrihydrite is further confirmed by neutron diffraction data [50]. The evolution of the (002) magnetic reflection with temperature in a ferrihydrite powder with about 2.8 nm diameter nanoparticles allow the estimation of the Néel temperature: 330 ±20 K (see Fig. 1.8). Moreover, the magnetic moment per Fe ion estimated by Rietveld analyzes is 3.2 μ_B at 5 K [50].

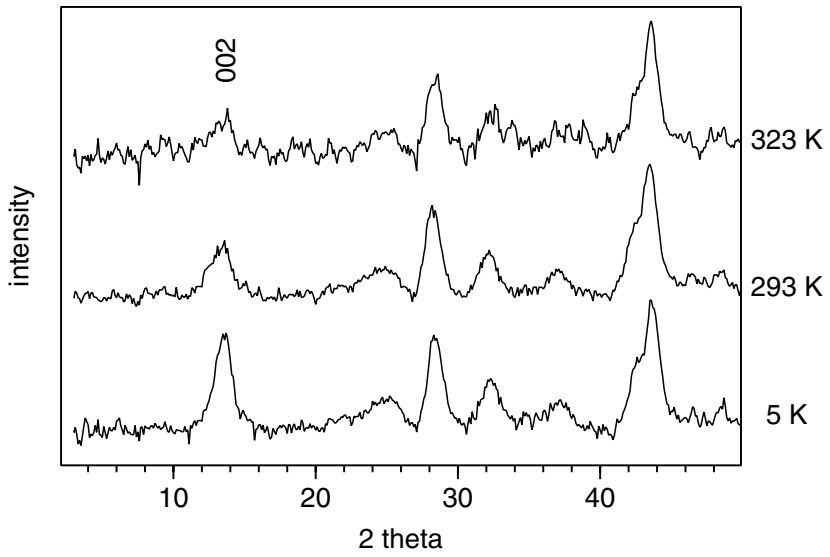

Figure 1.8: Neutron diffraction patterns of 6-line ferrihydrite (from Ref. [50]).

Ferrihydrite in ferritin [43]

Horse spleen ferritin consists of a hollow spherical shell, composed of 24 protein subunits surrounding a core of ferrihydrite (Fig. 1.9). The diameter of the cavity is of the order of 7-8 nm. This implies an upper limit of 4500 Fe ions stored within the protein as ferrihydrite. Ferritin is used by organisms to avoid the precipitation of toxic solid iron phases and is part of the homeostatic iron control. The structure and magnetic properties of ferritin from vertebrate, invertebrate, and bacterial sources are different. Vertebrate (human) ferritin cores are single-crystals, while invertebrate (limpet) ferritin are less crystalline, with domains of the order of 3-5 nm, and bacteria ferritin have lamella-like structures with short-range order (1-2

nm). As a consequence, T_B of human ferritin is about 40 K, while in limpet ferritin is ∼20 K and bacterial ferritin is ∼ 4 K. Factors governing these structural changes include the rate of Fe^{2+} oxidation on entry into the protein shell and subsequent mechanisms of growth. The growth of the ferrihydrite core depends on local redox and pH conditions, ionic concentrations and binding sites. For instance, the growth of single crystals in mammalian ferritin indicates that nucleation occurs in one location, where oxidation of Fe^{2+} occurs. These binding sites may result from clustering of glutamate (carboxylic) residues, that create the necessary Fe^{3+} density to act as the nucleation zone.

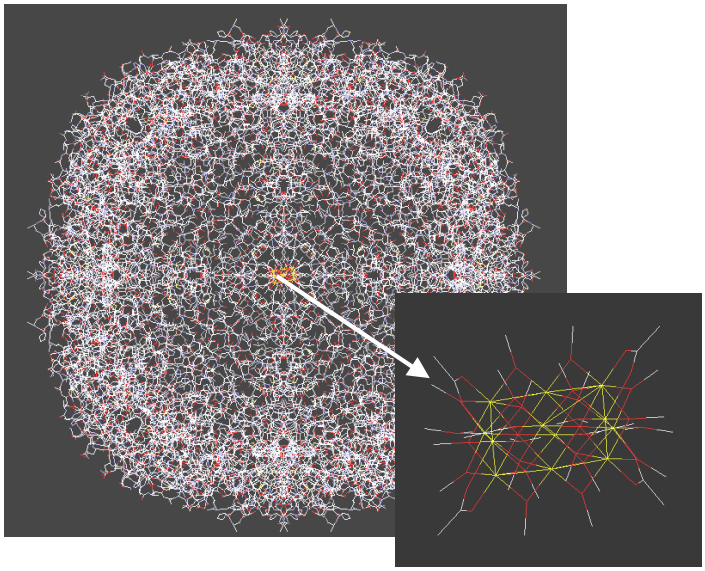

Figure 1.9: Scheme of the chemical bonds on ferritin. The protein shell is depicted in white. Inset show a zoom over the ferrihyidrite-like core (from http://wunmr.wustl.edu/EduDev/LabTutorials/Ferritin/FerritinTutorial.html).

1.3.2 Iron oxyhydroxynitrates

As described in Sec. 1.3.1, the formation of ferrihydrite processes *via* hydrolysis of iron nitrate solutions. This hydrolysis involves different and more or less ordered intermediate products, generally designated by iron oxyhydroxynitrates [44].

Rose and co-workers [55] have studied the evolution of basic-treated iron(III) nitrate solutions (medium/high rate of hydrolysis) with time. They have concluded that the process involves the formation of oligomers in a chaotic way. The size of the oligomers increase with time but growth does not follow a defined pathway. In the early stages the oligomers are dimers, composed of Fe octahedra sharing one edge and a small fraction of trimers formed by double-corner sharing of a Fe octahedron with a dimer. These basic units link to each other leading to the formation of linear aggregates. Further aging leads to the aggregation of other Fe octahedron to the dimers and trimers or the aggregation between dimers, dimers-trimers,

and trimers. The evolution of the oligomers with time depend on the amount of base present in the initial solution. For higher base concentrations the structural units are larger (more than three Fe octahedra) and the aggregates are more branched.

At very low rate of hydrolysis (i. e. pH<3) it is possible to obtain different ordered precursors in the process of transformation of iron nitrate salt to 6-line ferrihydrite. One of these precursors was obtained by freeze-drying iron nitrate solutions after 12 min at 80°C [56, 44]. This phase, Fe(III) oxyhydroxynitrate, contains ca. 15 wt% NO_3. Both XRD patterns and Mössbauer spectra are similar to those of the Fe(III) oxyhydroxysulfate phase (schwertmannite) (Fig. 1.10). On the other hand, there are apparent differences between the XRD pattern and Mössbauer spectra of Fe(III) oxyhydroxynitrate and 6-lines ferrihydrite: the intensity of the double peak between $d = 0.14 - 0.15$ nm is reversed comparing to ferrihydrite and the shoulder present at $d \approx 0.26$nm in ferrihydrite is absent in the Fe(III) oxyhydroxynitrate (arrows in Fig. 1.10a.). At 4 K, the magnetically ordered state of Fe(III) oxyhydroxynitrate indicates a B_{hf} ranging between 450 and 460 kOe, against 490–500 kOe for the 6-line ferrihydrite. At the same time, the spectra of both oxyhydroxides show a second, weaker component (arrows in Fig. 1.10b.) with a somewhat higher B_{hf}, which is absent in ferrihydrite [44].

Bigham et al. [57] suggested that schwertmannite has a defect akaganéite structure (see Fig. 1.11). The structure would therefore consist of four double rows of $Fe_3(OH)_3$ octahedra which form a square tunnel with NO_3^- ions inside. Based on the similarity between the XRD pattern and Mössbauer spectra of schwertmannite and Fe(III) oxyhydroxynitrate, Schwertmann et al. [56] have proposed a similar defect akaganéite structure for the nitrate-based oxide.

A different iron oxide hydroxide nitrate phase was first reported by López Delgado and co-workers [58]. This oxide is quite crystalline and does not constitute an intermediate product of ferrihydrite. The synthesis of this phase involves the preparation of a 8 N solution of iron(III) nitrate and urea, the aging of this solution at 63°C during one week. After this the precipitated is filtered, washed with water, ethanol and acetone and dried in vacuum. The precipitate has a red-orange color. The structure of this iron oxide hydroxide nitrate phase has been solved *ab initio* by X-ray powder diffraction data, collected with a conventional Co x-ray source [59]. The symmetry is monoclinic (Pc) and the cell parameters (in nm) are $a = 0.30844(6)$, $b = 0.9508(2)$, $c = 0.9993(3)$ and $\beta = 91.01°$. The magnetic properties of this phase were not yet reported.

1.3.3 Magnetite

Magnetite (Fe_3O_4) is a well known black ferrimagnetic mineral, containing Fe^{2+} and Fe^{3+} ions in an inverse spinel structure. Magnetite and titanomagnetite are responsible for the spontaneous magnetization of rocks. Magnetite is also present in bacteria, where it is

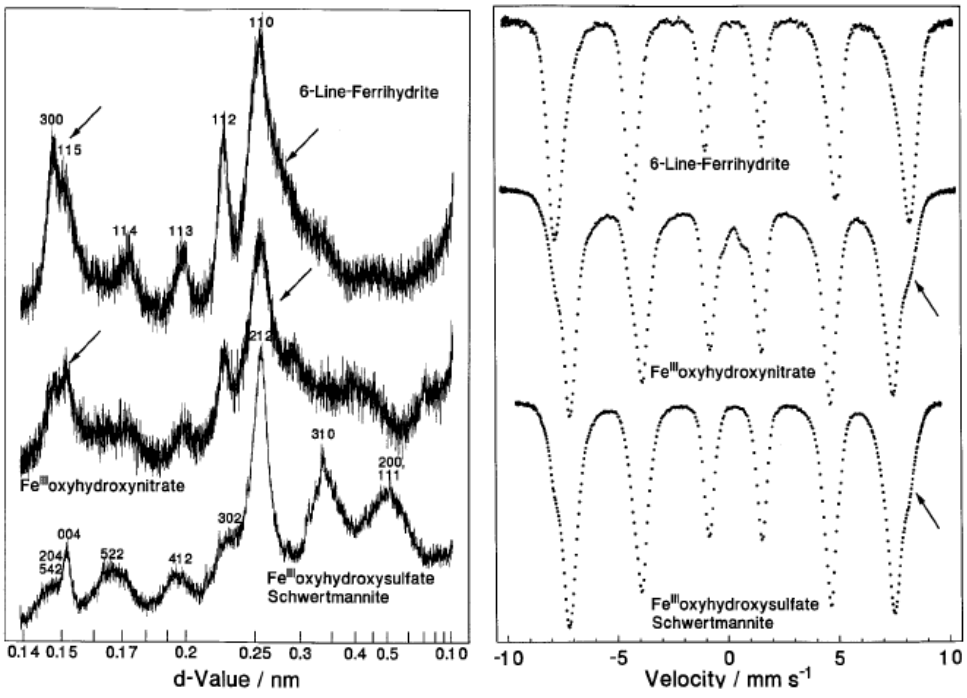

(a) (b)

Figure 1.10: XRD pattern (a) and Mössbauer spectra (b) of Fe(III) oxyhydroxynitrate, Fe(III) oxyhydroxysulfate phase (schwertmannite) and 6-line ferrihydrite (from Ref. [44]).

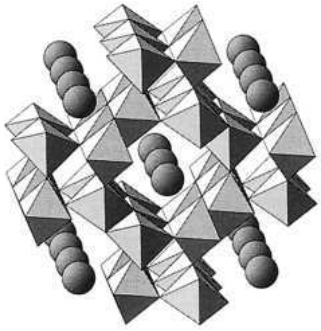

Figure 1.11: Structure of akaganéite and schwertmannite also proposed for Fe(III) oxyhydroxynitrate [44]. Spheres represent Cl^- or SO_4^{2-} ions for akaganéite and schwertmannite, respectively.

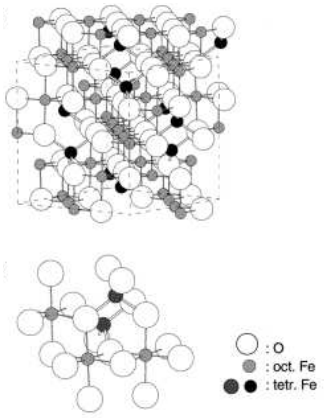

Figure 1.12: Structure of magnetite, with the unit cell outlined (dotted line) and zoom over a portion of unit cell, highlighting octahedral and tetrahedral coordination.

synthesized in the form of discrete crystallographically orientated inclusions. These inclusions are aligned in chains, which are used by bacteria as compass to find oxygen-depleted zones at sediment-water interface of freshwater and marine environments, near the poles [43].

Synthesis

There are several methods to produce magnetite, that can be found in Ref. [38]. One of these methods is based on the reaction between a 0.3 M solution of Fe^{2+} sulphate and a solution containing 3.33 M KOH and 0.27 M KNO_3 in the proportion 2.3 to 1, at 90 °C, for 60 min, under N_2 atmosphere. The solutions should also be outgassed with N_2 before use. The formation of other iron oxides can be further prevented by adding hydrazine of metallic Fe.

Structure

Magnetite was one of the first minerals being studied by XRD. The structure is that of an inverse spinel, whose formula can be written as Fe(III)[Fe(II) Fe(III)]O_4. Octahedral sites are occupied by both Fe^{3+} and Fe^{2+} ions, whereas tetrahedral sites are occupied by Fe^{3+} ions. Magnetite has a face-centered cubic unit cell, based on 32 O^{2-} ions, regularly cubic close packed along the [111] direction (Fig. 1.12). Magnetite is frequently non-stoichiometric, in which case it has a cation deficient Fe^{3+} sublattice. [38]

Magnetic properties

Magnetite is ferrimagnetic up to about $T_C = 850$ K. The exchange constants between tetrahedral and octahedral sites, between two octahedral sites, and between two tetrahedral sites are $J_{TO} = -28$ K, $J_{OO} = -18$ K and $J_{TT} = 3$ K [38]. Thus, TO antiferromagnetic interactions prevail. The ferrimagnetism arises since the magnitude of the spins in the octahedral sites is different from that of the tetrahedral sites. Magnetite presents a transition temperature around 118 K, the Verwey transition temperature T_V, usually associated to charge ordering of the Fe^{3+} and Fe^{2+} ions of the octahedral cites. Above T_V, the electrons of the Fe ions are thermally delocalized, which confers high conductivity to magnetite. Magnetite has cubic anisotropy and the preferred direction is [111]. The saturation magnetization of bulk magnetite is about 80 emu/g [38].

The Mössbauer spectrum of magnetite for $T > T_C$ consists of one broad line which can be resolved into a component for the tetrahedral cubic sites and a quadrupole split doublet for the octahedral sites. For temperatures between T_C and T_V, the Mössbauer spectrum consists of two sextets, corresponding to the tetrahedral ($B_{hf} = 492$ kOe) and octahedral sites ($B_{hf} = 461$ kOe). Below T_V, the Mössbauer spectra of magnetite have split components from each valence and crystallographic site [38].

1.3.4 Maghemite

Maghemite (γ-Fe_2O_3) is a red-brown ferrimagnetic iron oxide, with a cation deficient magnetite structure. It occurs in soils as a weathering product of magnetite. It can also occur as a product of heating of other iron oxides [38].

Synthesis

Maghemite can be obtained by thermal treatment of other oxides: lepidocrocite or magnetite in oxidation conditions (250°C for 2 or 5 hours, respectively) or heating of goethite or ferrihydrite in air at 450°C for 2 hours in the presence of an organic material. Maghemite can also be obtained by oxidation of Fe^{2+}/Fe^{3+} solutions at pH=7 or oxidation of Fe^{2+} solutions in air, sodium iodate or nitrate and a complexing agent as pyridine [38].

Structure

Maghemite has a structure similar to that of magnetite. However, it has no (or almost no) Fe^{2+} ions. The change in the oxidation state is compensated by cation vacancies. The unit cell contains 32 O^{2-} ions, $21 + 1/3$ Fe^{3+} ions and $2 + 1/3$ vacancies. Eight of the Fe^{3+} ions occupy all tetrahedral sites, while the others are randomly distributed over the octahedral sites. The maghemite formula can be written as $Fe_8[Fe_{13.3}\square_{2.67}]O_{32}$. A series of maghemite/magnetite solid solutions, with different Fe^{2+} concentrations can be obtained. Some maghemite systems, obtained by phase transformations *via* goethite, hematite and magnetite have a tetragonal unit cell [38].

Magnetic properties

Maghemite is ferrimagnetic up to the temperature at which transforms to hematite, i. e. 700-800 K. The transition temperature is estimated to be between 820 and 990 K [38]. The magnetic structure consists on two sublattices corresponding to the Fe located on tetrahedral and octahedral sites. The nearest neighbor exchange constants of maghemite are not determined. However, they are considered to be similar to those of $NiFe_2O_4$: $J_{TO} = -28.1$ K, $J_{OO} = -8.6$ K and $J_{TT} = -21$ K [60, 61]. The intersublattice interactions are stronger than those inside each sublattice, so that the spins in each sublattice align ferromagnetically, and the spins between sublattices align antiparallel. Ferrimagnetism arises from decompensation between the number of Fe ions present in each sublattice. This results in 5.3 decompensated ions per unit cell, and would correspond to a magnetic moment of about 26.5 $\mu_B/_{unitcell}$, i. e. 2.5 $\mu_B/_{Fe_2O_3}$. The measured saturation magnetization of bulk maghemite is slightly lower than the expected values: 2.2 $\mu_B/_{Fe_2O_3}$, which corresponds to 76 emu/$g_{Fe_2O_3}$ [62].

The Mössbauer spectrum of magnetite for $T < T_C$ consists of one sextet, indicating that B_{hf} of both octahedral and tetrahedral site are very similar. As a consequence, Mössbauer

spectroscopy is one of the most important tools to distinguish between maghemite and magnetite [38].

1.4 Magnetic nanoparticles in nanocomposites

Relevant properties of the magnetic nanoparticles can be controlled by incorporating them in a nanocomposite. This includes the incorporation of the nanoparticles into a matrix or template or the coating of the nanoparticles. Among the properties that can be controlled are structural properties as size, size dispersion, shape, organization, and interface. As one might expect, changing structure affects the magnetic properties of nanoparticles. On the other hand, synergy between nanoparticles and matrix leads to new properties, different from those of both components. For instance, the interface interaction between nanoparticles and coating materials results in a decrease of the magnetic moment [63, 64]. Nanoparticles templates and coatings include protein cages [43, 65, 66, 67, 68], inorganic materials [69, 70] including sol-gel derived organo-silica glasses [71], polymers (see review in [72]), and more recently organic-inorganic hybrids [73].

1.4.1 Synthesis

Different synthesis routes can be used depending on desired magnetic and structural parameters, and final form of the material (ex. powder, film, suspension)[72]. Relevant structural parameters include particles size, size distribution, shape, ordering, and particles-matrix interaction. These are better controlled using bottom-up approaches. These approaches include the formation of matrix or coating network, the precipitation of the magnetic component, and the mixture of both. This can occur in several ways that can be summarized in: i) separate formation of both components followed by their mixture; ii) precipitation of the magnetic component, mixture with the matrix/coating precursors and formation of the composite; iii) formation of the matrix/coating with the magnetic nanoparticles precursors embedded, followed by in-situ precipitation; iv) mixture of the precursors of both components followed by simultaneous formation of nanoparticles and matrix/coating [72]; and v) novel routes explore the possibility of using living organisms as bacteria and virus to produce high quality magnetic nanocomposites [74], through a biomimetic synthesis.

A step common to routes i) and ii) is the precipitation of the magnetic component. Iron oxides can be precipitated in aqueous solutions by the hydrolysis of iron salts, as described in Sec. 1.3. Another route for the formation of iron oxides is the decomposition of iron carbonyl compounds in the presence of a mild oxidant [75]. This route is quite suitable to form metal and metal alloy nanoparticles [76]. Such nanoparticles are also obtained by redox reactions, both by chemical agents or electrochemical methods. In route i), nanoparticles and matrix/coating are putted together in solution and then evaporated, spin-cast of freeze-dried.

In route ii) the mixture is made prior to the formation of the matrix/coating. For instance, this method is suitable when using insoluble polymers, since monomers are far less viscous [72]. Route ii) is also suitable to form coated nanoparticles. Typically, the nanoparticles are grown in a micellar template followed by the polymerization of the coating, as in polypyrrole-maghemite nanocomposites [77]. Route iii) is suitable for the production of films and bulk materials, as those reported in this thesis. In this way, the particles growth is controlled by the matrix, leading to narrow size and shape distribution. The nanoparticles precursor can be either adsorbed by the matrix, deposited in a porous matrix or dissolved with the matrix precursor. After this, the precipitation of the nanoparticles is achieved by one of the above described methods. Examples include the mentioned in-situ precipitation of iron, manganese and uranium oxides in ferritin protein cages [65, 66, 67, 68], the precipitation of maghemite in silica [69] and organo-silica glasses [71], polymers [72], and sol-gel derived organic-inorganic hybrids [73]. In route iv) the formation of the matrix and the nanoparticles occurs at the same time. This yields high homogeneity and provides stronger matrix-nanoparticle interactions.

Biomimetic synthesis, route v), tries to follow the steps and concepts of biomineralization. These steps are supramolecular preorganization, interfacial molecular recognition (templating) and cellular processing [78]. The final step is responsible for achieving particles with new crystallographic structures and morphologies. These new structures have unusual textures and shapes, with structural order at different lengthscales. Using routes i) to iv) templating is achieved but controlling long-range architectures is still a challenge [78].

1.4.2 Applications

The interest in magnetic nanoparticles has experienced a dramatic growth in the last decade [72]. Nowadays, the research comprises issues from basic research to applications, extending to biology, medicine and many other areas. In biology and medicine magnetic nanocomposites are used as contrast agents in magnetic resonance imaging (MRI) (see review in Ref. [79]), drug targeting [80], diagnostics [80, 81], immunoassays [82], proteins and cell immobilization/separation [83, 84, 85] and hyperthermia therapy [79, 86]. Application in other areas include magnetooptics [87, 88], magnetoresistance sensors [89] and high density recording media [90, 76, 91]. As one might expect, in biology, magnetic nanocomposites are used in the form of suspensions. In magnetooptical, sensor, actuators, and recording applications magnetic nanocomposites are used as films and multilayers and fibers.

As the MRI technique developed, it became clear that contrast agents greatly improve the diagnostic value. The first generation of contrast agents was based on Gd^{3+}, while more recently, magnetite nanoparticles embedded in dextran corona have been used [79]. Nowadays magnetite and maghemite nanoparticles coated with carboxydextran, chitosan, starch, heparin, and albumin are approved for clinical application or trials [79]. The advantage of nanoparticles is their higher magnetic moment and therefore relaxivity. Relaxivity is the

ability of magnetic ions and particles to increase the relaxation rates of the surrounding water protons. The advantage of using ferrimagnetic iron oxides relies on their low toxicity comparing to metallic nanoparticles. Another advantage is the size dependent distribution in tissues. However, a situation where an agent accumulates highly and specifically in a tumor is still far from reality [79]. Changes in the relaxation times of neighboring water molecules can be used to design biocompatible magnetic nanosensors. These nanosensors are able to detect molecular interactions in biological media. In particular, they can been designed to detect specific mRNA, proteins, enzymatic activity, and pathogens as virus. In practice, the formation of nanoparticles/molecules clusters, result in a quick and significant decrease in the spin relaxation times [82]. Biosensors using magnetic nanoparticles have applications in diagnoses, as for instance in targeting telomerase [81]. Telomerase is an enzyme concerned with the formation, maintenance, and renovation of the ends of chromosomes, which regulates the proliferative capacity of human cells. Elevated telomerase levels are found in many malignancies, offering an attractive target for therapeutic intervention and diagnostic or prognostic purposes [81]. After targeting molecules, magnetic nanoparticles can separate them from the surrounding media. For instance, phospholipid-coated colloidal magnetic nanoparticles are shown to be effective ion exchange media for the recovery and separation of proteins from protein mixtures. Protein and particles are readily recovered from the feed solution using high-gradient magnetic filtration. Such particles have high surface areas per unit volume and minimal transport resistances owing to the small diffusional distances between particles [85]. Hyperthermia is now used to treat a variety of tumors in both experimental animals and patients [92]. The most used method is capacitive heating using a radiofrequency electric field [86]. However, with this method is difficult to heat just the tumor region and not normal tissues. Intracellular hyperthermia is used to overcome the difficulty of uniformly heating only the tumor region to the required temperature (41-46°C or 46-56 °C) [86]. Intracellular hyperthermia is based on the principle that a magnetic particle can generate heat by hysteresis loss under an alternating magnetic field. This was first proposed in 1979 by Gordon et al. [93], using dextran magnetite nanoparticles. Nowadays, hyperthermia by using magnetic nanoparticles is in the stage of preclinical trials. To put it forward, efforts are being made to increase the power heating of the magnetic materials and on depositing the particles inside the tumor or in its arterial supply [79].

Magnetooptics applications include the use of the Faraday and/or Kerr rotation effect [87]. Another optical property that can be manipulated through magnetic particles is the refractive index. This can be done at refractive indexes and wavelengths of importance in optical fiber communication. The refractive index can be further tuned with externally varying fields [88]. Magnetoresistance materials are of great importance for sensor applications [94] and they are widely used in magnetic storage systems as reading heads. Advantages of polymer nanocomposites include the elimination of eddy-current losses and protection from oxidation [72].

Concerning applications in recording media, the industry of is moving towards the scenario where 1 bit is stored in one particle. This requires highly ordered arrangements of narrow size- distributed ferromagnetic nanoparticles. This can be achieved by the use of organic [76], inorganic [91], and biological [90] templates. The nanoparticles consist of FePt and CoPt alloys, since they have higher moments and coercivity. Enhanced coercivity can be obtained by the use of nanowires [91].

Chapter 2

Magnetic properties of nanoparticles

2.1 General considerations

The magnetism of nanoparticles, also designated as fine/ultrafine magnetic particles, has been studied in the last 50 years. These systems are inherently complex and have important deviations to canonic bulk behavior. At the same time, it is rather difficult to understand which factor is dominant in the deviation and how to approach the problem. There are two general approaches to study the static and dynamic properties of magnetic nanoparticles: i) one-spin particle (OSP) and ii) many-spin particle (MSP) [95]. OSP is a macroscopic approach that models one nanoparticle as a single magnetic moment, assuming coherent rotation of all atomic moments. This approach is useful to describe dynamics and interparticle interaction effects, either by using analytical descriptions or computational methods, as Monte Carlo and micromagnetic modeling. MSP is a microscopic approach that considers all atomic moments and their degrees of freedom. With MSP, surface and disorder effects are easily taken in to account but modeling dynamics is still a challenge. Since it is a complex multiple-body problem, MSP approach is used with computational methods.

In this chapter we describe magnetic properties of nanoparticles based on a OSP analytical approach. This approach is based on the Néel-Brown superparamagnetic theory and complementary models used to take into account deviations to the main theory. In some cases the results given by this approach are compared to those from OSP and MSP computational methods.

2.2 Superparamagnetism

2.2.1 General theory

Magnetic nanoparticles are often described in the framework of superparamagnetism, as proposed by Néel [96] and Brown [97]. The basic idea is that each particle is a single domain so that it can be represented by one 'giant' classic magnetic moment. Here, classic means that it can have an arbitrary direction in space, by opposition to an atomic moment whose projection in the field direction is quantized. This moment can fluctuate between minima of the energy profile, depending on the value of the measurement time of the specific experimental technique (τ_m) compared to the characteristic relaxation time associated with the energy barriers to overcome (τ).

The single domain configuration arises from the balance between exchange, anisotropy and magnetostatic energies, as recognized in the early works of Montgomery [98] and Elmore [99, 100]. Superparamagnetism theory was developed for materials with ferromagnetic interactions, i. e. those where the exchange energy tends to keep the moments (within each particle) aligned in the same direction. Exchange energy is a short-range interaction, while the magnetostatic energy, of dipolar origin, is a long range interaction that tends to break the system into parts (domains) so that the total macroscopic magnetization is zero. These domains are separated by Bloch walls, whose thickness depends on the balance between exchange and anisotropy energies. As the size of the system decreases, the total energy becomes dominated by the short-range exchange term, so that the system turns into a single magnetic domain; i. e. the system enters the superparamagnetic regime. The size below which typical magnetic materials become single domains is in the 20-800 nm range, depending on the spontaneous magnetization (that determines the magnetostatic energy intensity), and on exchange and anisotropy energies [101]. If the particles size is too small, of the order of 2 nm according to Ref. [101], the superparamagnetic approach breaks down, since surface effects become dominant.

If the particles magnetic moment is able to fluctuate across the energy barrier the system is said unblocked; otherwise the system is blocked. The fluctuations have been modeled by Brown, supposing a magnetic moment precessing around the anisotropy direction, a thermally activated damping, and a random field $h(t)$ averaging zero [101, 97]:

$$\frac{d\vec{\mu}}{dt} = \gamma_0 \vec{\mu} \times \left[-\frac{\partial E}{\partial \vec{\mu}} - \eta \frac{d\vec{\mu}}{dt} + \vec{h}(t) \right] \tag{2.1}$$

where γ_0 is the electronic gyromagnetic ratio, η is the damping constant and E the energy barrier.

As mentioned, the fact that the system is blocked or unblocked depends on the relation between τ_m and τ. The latter depends on the barriers "size" E_a, on the temperature T, and

on an attempt time τ_0, expressed by thermally activated process (Arrhenius law):

$$\tau = \tau_0 \exp\left(\frac{E_a}{k_B T}\right) \tag{2.2}$$

where k_B is the Boltzmann constant. τ_0 can be approximated by [101, 97]:

$$\tau_0(T) = \frac{\sqrt{\pi}}{4}\frac{\mu(0)}{E_a \gamma_0}\left(\frac{1}{\eta_r} + \eta_r\left(\frac{M(T)}{M(0)}\right)^2\right)\left(\frac{E_a}{k_B T}\right)^{-1/2}\left(1 + \frac{k_B T}{E_a}\right) \tag{2.3}$$

$\mu(0)$ is the modulus of the particle magnetic moment at 0 K and $M(0) = \mu(0)/V$ the corresponding magnetization. η_r represents damping effects in a dimensionless form: $\eta_r = \eta\gamma_0 M(0)$. For systems constituted by non-interacting particles, η_r is around 0.1, while in Fe interacting particles $\eta_r \sim 1$ [102]. On the other hand, in bulk materials $\eta_r \sim 0.01$ [103]. Usually, τ_0 is considered constant with temperature, being of the order of 10^{-9}- 10^{-13} s [102]. In a given experiment, where a relevant parameter is measured as a function of T, the system is blocked below a blocking temperature T_B, given by Eq. 2.2, for $\tau = \tau_m$, such that:

$$T_B = \frac{E_a}{k_B \ln(\tau_m/\tau_0)} \tag{2.4}$$

In the context of dc magnetic measurements, τ_m is typically of the order of 10 s. Taking $\tau_0 = 10^{-10}$ s, $E_a = 25 k_B T_B$.

For the simple case of particles with uniaxial anisotropy, the moment experience two minima, separated by an anisotropy energy given by:

$$E_a = K_a V \tag{2.5}$$

where K_a is the anisotropy constant, characteristic of the material, and V is the particle volume. The former equation can be generalized to systems with other anisotropy sources considering an effective anisotropy constant, K_{eff} (see table 2.1):

$$E_a = K_{eff} V \tag{2.6}$$

The uniaxial anisotropy energy has an angular dependence given by[1]:

$$E_{a\,uniax}(\theta) = -K_a V \cos^2\theta \tag{2.7}$$

where θ is the angle between the anisotropy axis (easy axis) and the particle moment (see Fig. 2.1). The material is constituted by a set of particles where the anisotropy axis of each particle may have different directions, leading to systems with different configurations.

[1] this formulation is equivalent to: $E_a(\theta) = K_a V \sin^2\theta$

Examples of these configurations are axis with random orientation and axis aligned in the same direction.

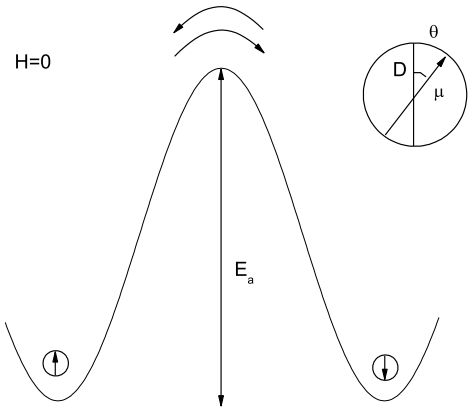

Figure 2.1: Scheme of the energy barrier profile for uniaxial anisotropy at zero external field. D is the direction of the easy axis.

2.2.2 Deviations to superparamagnetism

Real materials are far more complex than this description and it is often necessary to consider other factors. Deviations include the existence of different sources for anisotropy, size distribution, surface effects and interparticles interactions [101]. These can be dipolar and exchange interactions, which give important contribution to the total anisotropy energy. Broken symmetry at surface results in a strong magnetic surface anisotropy and weakened exchange coupling. This results in the decrease of the order temperature with respect to the bulk one. Surface disorder leads to spin canting and the consequent reduction of magnetization comparing to bulk. The particles magnetic moment has also a temperature dependence that can be different from bulk. This moment can also depend on the magnetic field, since the field can modify the surface moments configuration [102]. Another question intensively addressed during the last decade of the 20^{th} century was the quest for evidence of macroscopic quantum spin tunneling in nanoparticles (see, for instance Ref. [67, 104, 105, 106]). Most of the work was centered on analyzing deviations to the relaxation time predicted by Eq. 2.2, in particular, on finding temperature independent relaxation. These studies were inconclusive as tunneling may be relevant only at very low temperatures. Moreover, this quest triggered the detailed study of deviations to the canonic superparamagnetic behavior, some of them described in this text.

In the following sections a more detailed description of superparamagnetism and some theoretical models accounting for these deviations will be presented. At the same time, an extension of superparamagnetism to particles with antiferromagnetic interactions will also be presented and discussed.

2.3 Magnetization under an applied field above T_B

2.3.1 The Langevin law

The energy of a classic free magnetic moment in an external applied field is given by:

$$E_m = -\mu H \cos(\theta) \tag{2.8}$$

where here, θ is the angle between μ and H. The probability of having a moment with energy E_m at a temperature T is given by the Boltzmann statistics: $\exp(E_m/k_BT)$. The average magnetization M of a system with N non-interacting moments (in the present context particles) with moment μ can be expressed by the Langevin law:

$$M(H,T) = \int_0^{\pi} M = N\mu \left(\coth\left(\frac{\mu H}{k_B T}\right) - \frac{k_B T}{\mu H} \right) \tag{2.9}$$

usually written as: $M(H,T) = N\mu L(x)$, with $x = H\mu/k_BT$. M is defined as the magnetic moment per volume, and in this case N is the number of moments per volume. The saturation magnetization M_S is equal to $N\mu$. The Langevin law is commonly used to describe the $M(H,T)$ curves of non-interacting superparamagnetic particles. It is interesting to notice that Eq.(2.9) scales with H/T or with $\mu(T)H/T$, considering the μ temperature dependence. This means that $M(H)$ measurements taken at different temperatures merge into a single curve in the mentioned scales.

Magnetic moments of isolated atoms or ions, as Fe^{3+}, are better described considering the quantization of the projection of the moment in the field direction [107], i. e. by the Brillouin law, expressed by:

$$M(x) = Ng\mu_B J B_J(x) \tag{2.10}$$

with:

$$B_J(x) = \frac{2J+1}{2J} \coth\left(\frac{(2J+1)x}{2J}\right) - \frac{1}{2J} \coth\left(\frac{x}{2J}\right) \tag{2.11}$$

being g the Landé factor, μ_B the Bohr magneton, J the angular momentum quantum number, and $x = g\mu_B JH/k_BT$. For $J \gg 1$, the Brillouin law approaches the Langevin law.

2.3.2 Effect of anisotropy

Taking into account the anisotropy energy term E_a, which is always present in a superparamagnetic system, the energy experienced by the magnetic moment of a superparamagnetic particle is then described by:

$$E = E_m + E_a \tag{2.12}$$

with

$$E_m = -\mu H[\cos(\theta)cos(\alpha) + \sin(\theta)\sin(\alpha)\cos(\phi)] \tag{2.13}$$

where the angles are defined in Fig. 2.2 and xyz correspond to particle referential. E_a can

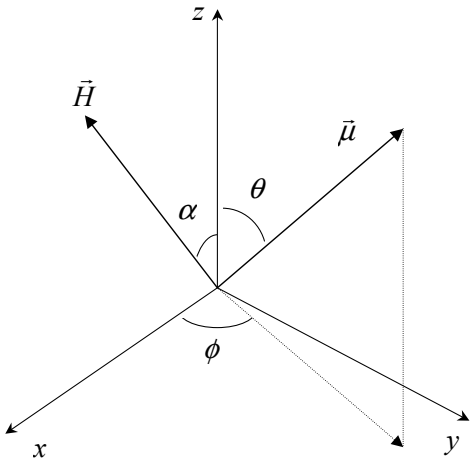

Figure 2.2: Definitions of the angles used in the calculation of the magnetization considering the anisotropy energy.

have different origins, in particular can be a shape, surface or magnetocrystalline anisotropy, and is often a mixture of these terms. To describe the effect of anisotropy one has to consider the symmetry of E_a, regardless its origin. First order uniaxial E_a term is given by Eq. 2.7. This term describes the magnetocrystalline of systems with uniaxial symmetry as, for instance, Co and shape anisotropy of cylindrical, ellipsoidal ($K_a > 0$) and disc-like particles ($K_a < 0$). The first 3 terms of E_a of systems with cubic symmetry are given by [101]:

$$\begin{aligned} E_{a\,cubic} &= K_0 + \\ &+K_1(\cos^2\theta\sin^2\theta\sin^2\phi + \cos^2\theta\sin^2\theta\cos^2\phi + \sin^2\theta\sin^2\phi\sin^2\theta\cos^2\phi) + \\ &+K_2(\cos^2\theta\sin^2\theta\sin^2\phi\sin^2\theta\cos^2\phi) \end{aligned} \tag{2.14}$$

The relation between K_1 and K_2 (sometimes designated as K_2 and K_4, respectively) determines the shape of the energy surface (see, for instance Ref. [108]) and therefore the easy axes of the system (Tab. 2.1). At the same time, the effective anisotropy constant, K_{eff} also depend on the relation between K_1 and K_2, as described in Tab. 2.1.

In a system with a given E_a, the magnetization of a particle whose z axis and $\vec{H}$ make an angle α can be calculated applying the Boltzmann statistics:

$$m(H,T,\alpha) = \frac{\int_{\theta=0}^{\pi}\int_{\phi=0}^{2\pi}(\partial E_m/\partial H)\exp(-E/k_BT)\sin\theta\, d\phi\, d\theta}{\int_{\theta=0}^{\pi}\int_{\phi=0}^{2\pi}\exp(-E/k_BT)\sin\theta\, d\phi\, d\theta} \tag{2.15}$$

The magnetization of a system of particles with a random distribution of anisotropy directions with respect to the applied field is then given by the average:

$$M(H,T) = -0.5N\int_0^{\pi} m(H,T,\alpha)\sin\alpha\, d\alpha \tag{2.16}$$

This expression can be used to perform a numerical calculation of the equilibrium $M(H,T)$ curves. Other methods, which do not involve the direct calculation of the energy in all directions and subsequent integration, are presented by Garcia-Palacios [109] and Cregg and Bessais [110]. These methods were developed for systems with uniaxial anisotropy and are based on the relation between the magnetization and the partition function. Their use requires the calculation of $M(H)$ with a low H step. From a practical point of view, this is more time consuming than the direct calculation of the energy when calculating just a few $M(H)$ values, as in a fit procedure.

Deviations from the Langevin law introduced by E_a with uniaxial symmetry can be observed in Fig 2.3, for $T = 100$ K, and $\mu = 1000\ \mu_B$. We considered $E_a = 25k_BT_B$, as estimated from Eq. 2.4 for the case of typical dc measurements. For a given temperature,

Table 2.1: Easy axes and effective anisotropy constant, K_{eff} for different relation between K_1 and K_2, according to Ref.[101]

relation between K_1 and K_2	Easy Axes	K_{eff}
$K_1 > 0$		
$K_2 > -2K_1$	[001]	$K_1/4$
$3K_1 < K_2 < -2K_1$	[001]	$-\frac{K_1^2}{K_2^2}(K_1+K_2)$
$-9K_1 < K_2 < -3K_1$	[001]	$-\frac{K_1^2}{K_2^2}(K_1+K_2)$, or $-\frac{1}{K_2^2}\left(K_1+\frac{K_2}{3}\right)^3$ (approximation)
$K_2 < -9K_1$	[111]	$-\frac{1}{K_2^2}\left(K_1+\frac{K_2}{3}\right)^3$ or $-\frac{K_1^2}{K_2^2}(K_1+K_2)$ (approximation)
$K_1 < 0$		
$K_2 > (-9/4)K_1$	[110]	$-\frac{K_1}{4K_2^2}(2K_1+K_2)^2$ (approximation)
$-2K_1 < K_2 < -(9/4)K_1$	[111]	$-\frac{1}{K_2^2}\left(K_1+\frac{K_2}{3}\right)^3$ or $-\frac{K_1^2}{4K_2^2}(K_1+K_2)$ (? approximation)
$K_2 < -2K_1$	[111]	$-\frac{K_1}{12}-\frac{K_2}{27}$

.

a departure from the Langevin law due to anisotropy becomes relevant for $T_B \gtrsim 0.1\,T$, and increases as T_B approaches T. The differences are more pronounced in the middle field region, while the low field (susceptibility) region does not depend on anisotropy.

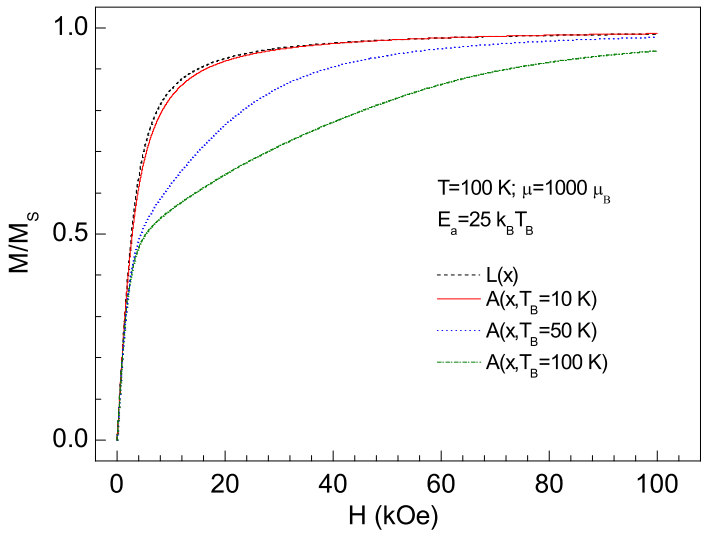

Figure 2.3: $M(H)$ curves at $T = 100$ K and $\mu = 1000\ \mu_B$, obtained using the Langevin function (L(x), Eq. 2.9) and considering the influence of the intensity of E_a (A(x), Eq. 2.16 and 2.7). E_a is expressed in terms of T_B using Eq. 2.4 and considerations described in the text.

2.3.3 Effect of distributions

Another deviation to the Langevin law results from the existence of a distribution of μ. This distribution can be a direct consequence of a distribution of volumes and/or be consequence of differences within particles, such as different degrees of disorder. The importance of considering distributions was recognized since the pioneering works of Elmore [100]. As $M(H,T)$ curves probe magnetic moments is preferable to express the magnetization in terms of a μ distribution (and not volume), as follows:

$$M(H,T) = N \int_{\mu_{min}}^{\mu_{max}} \mu L(x) f(\mu) d\mu \tag{2.17}$$

where $f(\mu)$ is a normalized distribution function. The lognormal function is often used to describe these distribution and is given by:

$$f(\mu) = \frac{1}{\mu s\sqrt{2\pi}} \exp - \left[\frac{(\log(\mu/n))^2}{2s^2}\right] \tag{2.18}$$

The mean particle moment $\langle\mu\rangle$ is equal to $n\sqrt{w}$ and the standard log-normal deviation, σ is equal to $n\sqrt{w(w-1)}$, with $w = \exp(s^2)$ [111].

Deviations to the Langevin law introduced by a lognormal moment distribution can be observed in Fig. 2.4, for $s = 1$. As s increases the deviations become more apparent. Since real systems are always distributed to a certain state, it is important to evaluate the limits where a non-distributed Langevin law can be considered as a good approximation, and the implication of ignoring the distribution in the obtained parameters. To elucidate this question we have generated sets of Langevin curves with a lognormal moment distribution (Eq. 2.17). We have used the typical values $\mu = 500\ \mu_B$, $N = 1$ (both constant with temperature), a maximum field $H_{max} = 50$ kOe, temperatures between 10 and 1000 K, and s between 0.5 and 2. Then, we used these curves as hypothetical results and we fit them to a non-distributed Langevin function (Eq. 2.9). The results in Fig. 2.5 are striking: the fit parameters μ and

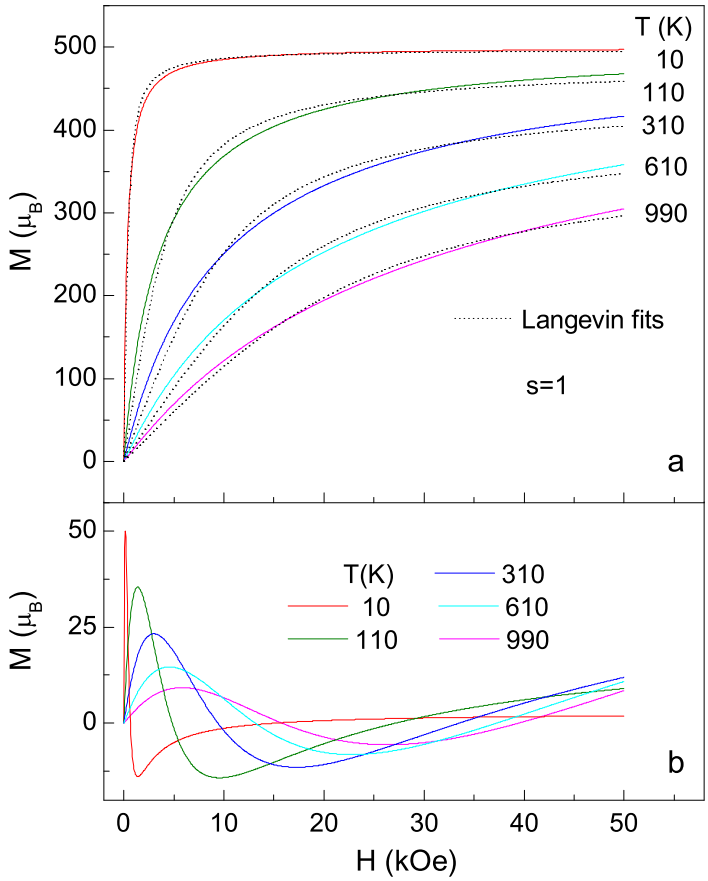

Figure 2.4: a. $M(H,T)$ curves simulated with the Langevin distributed function with $s = 1$ (Eq. 2.17) using a lognormal function (Eq. 2.18) for different temperatures (continuous lines). Fits of these curves to a non distributed Langevin function (Eq. 2.9) and fit residues (b.) are also shown.

$M_s = N\mu$ increase and decrease with temperature, respectively, even for the lower standard deviations. As s increases the relative changes of the fit parameters with temperature are more severe. Also, these dependencies are fairly linear. The fitted values tend to the real

value as the temperature decreases. Therefore, a non-distributed Langevin function can be used to estimate parameters but extreme care must be taken when analyzing their variation with temperature when dealing with distributed systems. One example is the care that must be taken on finding experimental evidence of thermoinduced moment in antiferromagnetic nanoparticles based on non-distributed fits to $M(H,T)$ curves [112] (see Sec. 2.7.6). We also

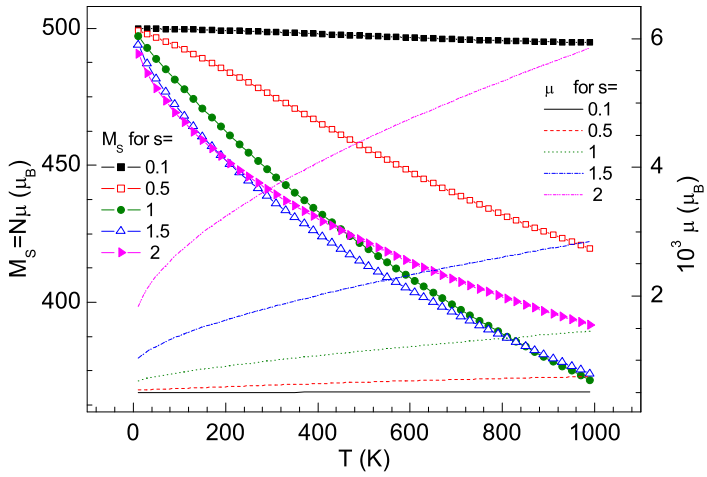

Figure 2.5: Parameters μ and $M_S = N\mu$ yielded from the fit shown in the previous figure as a function of temperature, for different standard log-normal deviations

notice that the $M(H,T)$ curves are not very sensible to Gaussian distributions. In fact, even with a function as wide as $\sigma = 3\langle\mu\rangle$ the Langevin and Langevin distributed functions have maximum differences just of the order of 3%.

2.3.4 Effect of inter-particle interactions

In many systems, the particles are sufficiently close so that dipolar interactions are relevant. A first approach is to model dipolar effects as a change in the effective energy barrier of the particle with respect to the isolated one [101]. On the other hand, collective phenomena descriptions, as those of critical slowing down spin-glass-like behavior, have been used to model dipolar effects [113, 114]. Both approaches focus on ac susceptibility measurements and will be discussed in Sec. 2.5.2. Concerning the description of $M(H)$ curves, Allia and co-workers [115] have proposed a phenomenological model that considers dipolar interactions as a perturbation to superparamagnetism. They have used the Langevin function (Eq. 2.9 or 2.17) with an effective temperature:

$$M = N\mu L\left(\frac{\mu H}{k_B(T+T^*)}\right) \tag{2.19}$$

The use of an effective temperature rather than an effective field (as used to model ferro- and antiferromagnetic interactions) was justified since dipolar interactions introduce disorder rather than order [115]. T^* is related to the root-mean-square (rms) dipolar energy as:

$$\varepsilon_D = \frac{\alpha\mu^2}{d^3} = k_B T^* \tag{2.20}$$

where d is the average interparticle distance. The proportionality constant α depends on the particles distribution in space and on short distance correlation, typically varying between units and some tens. Eq. 2.19 is in fact a Langevin equation with modified moment and particle density, such that [115]:

$$M = N_a \mu_a L\left(\frac{\mu_a H}{k_B T}\right) \tag{2.21}$$

with:

$$\mu_a = \frac{\mu}{1 + T^*/T} \qquad N_a = (1 + T^*/T)N \tag{2.22}$$

Similar relations are obtained for distributed systems. This emphasizes the fact that dipolar interactions may not substantially change the shape of the magnetization curves and therefore may not be apparent if the derived μ and N values are not compared to reliable data about particles size. We also note that ignoring interactions leads to an artificial increase of μ (taken as μ_a) and decrease of N (taken as N_a) with temperature. However, $M_S = N_a\mu_a$ will be constant with temperature and correctly estimated, unlike that found in the case of ignoring a distribution. In fact, the effect of a distribution and the effect of interactions can be distinguished, since in the former case the Langevin distributed function scales with H/T (for $\langle\mu\rangle$ and s constants), while in the latter the Langevin interacting function does not.

Allia et al. [115] have proposed the determination of T^* based on the temperature dependence of the low field magnetization (dc susceptibility). In fact, the low field approximation of Eq. 2.19 is equivalent to the Curie-Weiss law (Eq. 2.46) , discussed in Sec. 2.5.2:

$$\left(\frac{M(T)}{H}\right)_{H\to 0} = \left(\frac{N\mu^2}{3k_B(T + T^*)}\right) \tag{2.23}$$

since for $x \ll 1$, $\coth(x)$ can be expanded as $1/x + x/3$. This approach of modeling interactions was successfully applied to granular Cu-Co alloys [115] and iron-based nanoparticles [116]. In the latter, the model was applied to quite narrow distributed particles with mass densities covering 3 decades, and T^* was found to increase with concentration.

The effect of interactions was also addressed by computational methods. Chantrell et al. [117] have used Monte Carlo simulations to model M(H) curves [2] and notice a decrease of the susceptibility with the increase of interactions, but this decrease was not quantified or

[2] and also susceptibility as described in sec. 2.5.2

compared with phenomenological models. However, we notice that the evolution of the low field magnetization with temperature for different interaction strengths found in Ref. [117] is compatible with Eq. 2.23.

2.3.5 Surface effects and disorder

Up to this point the particles were described as a single magnetic moment. Deviations to this occur due to surface effects and/or core disorder. Experimental techniques and computer simulations have demonstrated that the incomplete coordination of superficial ions and the likely occurrence of surface structure defects have an important role in the magnetic properties of small particles (see for instance Ref. [118, 60, 61]). Some authors mention the existence of spin-glass like effects [3] due to surface spins [119]. These defects can lead to a magnetically disordered layer of a given thickness. MSP approach using Monte Carlo and other computational techniques are of great importance on modeling the shape of $M(H,T)$ at low temperature, in particular the dependence of the coercive field H_C and M_S with temperature, particles size, and disorder parameters, as described in the next section. However, until now, they failed when modeling the magnetic properties of superparamagnetic systems for $T_B < T < T_C$. An interesting work is being developed by H. Kachkachi and E. Bonet whose approach is to search for relations between MPS and OSP models [95]. They found that the energy profile due to a surface anisotropy approaches the one due to a cubic anisotropy. Therefore such a surface effect can be well described by a cubic anisotropy, resulting in an enhancement of K_1 compared to bulk.

Simple analytical models can be developed following the seminal work of Coey [120], where surface effects have been explained with a core-shell model. This considers the particle constituted by a bulk-like core and a magnetically 'dead' surface. In the case of $M(H,T)$ measurements, the surface is often considered as constituted by single paramagnetic and/or aniferromagnetic ions, which contribution to M is linear in field. In this core-shell model, M_S is proportional to the volume fraction of the core, as recently noticed by Millan et al. [121]:

$$M_S = M_{S0}\left(\frac{(D/2)-d}{D/2}\right)^3 \tag{2.24}$$

where M_{S0} is the bulk saturation magnetization, D the particles mean size and d the layer thickness. This simple model has been successfully applied to describe the dependence of M_S with D in different sets of maghemite nanoparticles, as seen in Fig. 2.6. Since the $M_S^{1/3}$ vs. $2/D$ plot is quite linear in different series of maghemite nanoparticles, it was concluded that the disordered layer d is almost constant in a 3 to 15 nm diameter range [121]. A linear fit yields $d = 1$ nm and M_{S0}=73 emu/g$_{Fe_2O_3}$, which is close to the bulk value and confirms the coherence of the model [121].

[3] this term is also use to describe systems with interacting superparamagnetic particles, see sec 2.5.2.

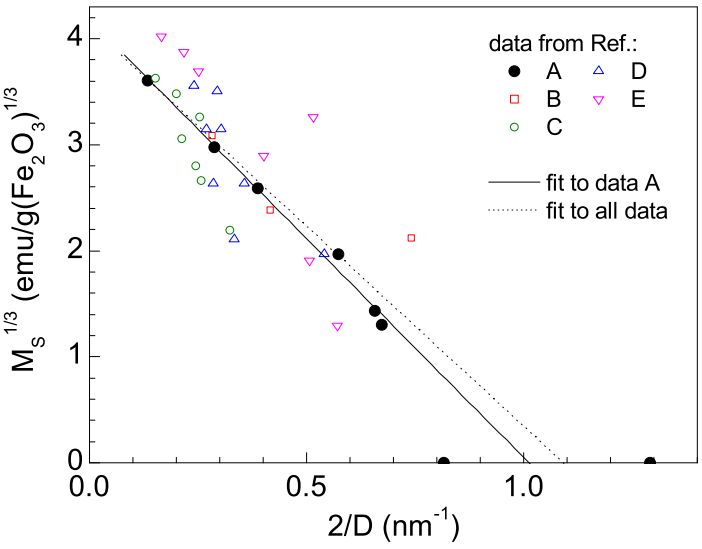

Figure 2.6: Linearization of the saturation magnetization M_S according to Eq. 2.24 ($M_S^{1/3}$ vs. $2/D$ plot) (from Ref. [121]). Data A, B, C, D and E is presented in Ref. [121], [122], [123], [124] and [125], respectively. The full line corresponds to the fitting of the data in Ref. [121] and the dashed line to the overall fitting of data.

2.4 Magnetization under an applied field below T_B

2.4.1 The Stoner-Wohlfarth model

Below T_B, the $M(H,T)$ curves show irreversibility. Stoner and Wohlfarth [126] have shown that this irreversibility can arise from competition between the anisotropy and the Zeeman energies (E_a and E_m, respectively). The Stoner-Wohlfarth model considers $T = 0$. The first step is the determination of the energy minima, maxima, and inflection points from $\partial E/\partial M_Z$ and $\partial^2 E/\partial M_Z^2$. The results depend on the angle between anisotropy axis and field. In systems with random oriented particles, the remanent magnetization is half of the saturation $M_r = M_S/2$ and H_C is of the order of $K_{eff}/2M_S$. This gives an idea of the order of magnitude for the irreversibility effects.

2.4.2 Deviations from the canonic behavior

Deviations to the Stoner-Wohlfarth model and the evolution of the hysterisis loops with temperature have been modeled by analytical and computational techniques. Usov and Peschany [127], and García-Otero and co-workers [108] have studied the influence of a cubic anisotropy in the hysteresis loops by analytical and Monte Carlo techniques, respectively. Both found that H_C is lower than the value obtained in uniaxial systems and the cycles are more 'rectangular shaped'. Differences are also observed for $K_1 < 0$ and $K_1 > 0$, with H_C being higher in the latter case. The way of decrease of H_C and M_r with temperature

depends critically on the sign of K_1 but no analytical description is given. The influence of both K_1 and K_2 on the curves was also addressed in Ref. [108]: when K_1 and K_2 are positive changes are small, while when the signs are opposite changes are relevant. The most critical case occurs for $K_1 < 0$, since in this case the anisotropy energy topology is more sensitive to changes of K_2 and to the K_1/K_2 ratio.

2.4.3 The field and volume dependence of H_C

A dependence of H_C with the particles size and temperature was first given by Kneller and Luborsky [128] and Bean and Livingston [129], for particles with uniaxial anisotropy. The energy barrier for reversal of the magnetization can be expressed as:

$$E_a = K_a V \left(1 - \frac{H M_S}{2K_a}\right)^2 \tag{2.25}$$

E_a must be sufficiently reduced by H so that the magnetization reversal occurs during the measuring time, t. Considering $E_a = 25 k_B T$ (i. e. neglecting the effect of the field in τ_0), the coercive field is such that:

$$25 k_B T = K_a V \left(1 - \frac{H_C M_S}{2K_a}\right)^2 \tag{2.26}$$

$$H_C(T) = \frac{2K_a}{M_S}\left(1 - (T/T_B)^{(1/2)}\right) \qquad V = constant \tag{2.27}$$

$$H_C(V) = \frac{2K_a}{M_S}\left(1 - (V_B/V)^{(1/2)}\right) \qquad T = constant \tag{2.28}$$

where the blocking temperature is given by Eqs. 2.2 and 2.5: $T_B = V K_a/(25 k_B)$. The blocking volume corresponds to the volume above which a system with anisotropy K_a and at a temperature T becomes blocked: $V_B = 25 k_B T/K_a$.

Eqs. 2.27 and 2.28 can be generalized by substituting the exponent (1/2) by α [130]. Simulations and experimental results show that α depends on the anisotropy, distribution of sizes, and mainly on interparticle interactions [130, 131]. Concerning interactions, Kechrakos and Trohidou [132] performed Monte Carlo simulations and observed that, at temperatures much lower that T_B both magnetization and coercivity are substantially reduced comparing to the non-interacting case. On the contrary, approaching T_B, M_r and H_C have a much slower decay, conserving the blocked character up to temperatures above the non-interacting T_B. This is in agreement with experiments reviewed in Ref. [101] and other Monte Carlo studies [117], as discussed in Sec. 2.5.2.

2.5 Ac and dc susceptibility

2.5.1 Non interacting systems

Susceptibility above the blocking

The low-field $M(H,T)$ dependence of the Langevin and Langevin with anisotropy laws is given by the well-known Curie law:

$$\chi = \frac{M(H_{app},T)}{H_{app,H\to 0}} = \frac{N\mu^2}{3k_BT} = \frac{C}{T} \tag{2.29}$$

where C is the Curie constant. In the case of distributed systems the Curie law takes the form:

$$\chi = \frac{N\langle\mu^2\rangle}{3k_BT} \tag{2.30}$$

The Curie law holds for temperatures where all moments are able to fluctuate across the anisotropy energy barrier, and for non-interacting particles with a random distribution of easy axis with respect to the applied field. Below a certain temperature, where some moments are blocked, the susceptibility depends on the history of the system, as described below. On the other hand, μ depends on temperature and this dependence becomes more severe as temperature approaches T_C. This decrease can be modeled with the help of expressions developed for bulk materials, in particular by the mean field law:

$$\mu(T) = \mu(0)\left(1 - \frac{T}{T_C}\right)^{1/2} \tag{2.31}$$

or by the magnons (Bloch) law for ferromagnets:

$$\mu(T) = \mu(0)\left(1 - BT^{3/2}\right) \tag{2.32}$$

Other dependencies of μ with temperature are found for surface spins and antiferromagnetic nanoparticles (see Sec. 2.7.5). Surface spins were found to decreases linearly with temperature as T approaches the order temperature, by Mössbauer [133] and by low-energy electron diffraction data [134].

Dc zero-field-cooled experiments

A typical experimental procedure for measuring susceptibility is the zero-field cooled (zfc) procedure. The sample is cooled down to the lowest measured temperature in the absence of the field, starting on a temperature where all particles are unblocked. A low field is then applied and the magnetization measured. In non-distributed systems there is a well defined temperature at which the moments become unblocked and where the susceptibility changes

drastically to the value expected from the Curie law (Eq. 2.29). This theoretical situation was modeled with Monte Carlo simulations by Dimitrov and Wysin [135]. As the temperature increases, χ also increase up to a maximum usually defined as the blocking temperature T_B, that depends on τ_m, E_a and H_{app}. Several authors reserve the term "blocking" for the maximum in the canonic situation, i. e. when it just depends on τ_m and E_a. In real situations, with a finite H_{app}, effects of distributions, interaction and other effects, the term "peak" or "maximum" temperature (denoted T_g or T_{max}) is rather used. In this thesis we just use the designation T_B, while trying to keep the context clear.

In E_a distributed systems and below the blocking temperature, the magnetization can be considered the sum of a Curie term associated to the fraction of particles that remain unblocked, and a term containing the contribution of the unblocked particles [136, 137, 138]:

$$\chi_{zfc} = \int_0^{E_{a\,blq}} \chi_{eq}(E_a, T) f(E_a)\, dE_a + \frac{2}{3} \int_{E_{a\,blq}}^{\infty} \chi_{\perp}(E_a, T) f(E_a)\, dE_a \tag{2.33}$$

and

$$\chi_{\perp}(E_a, T) = N \frac{\mu^2}{2K_{eff}V} \tag{2.34}$$

$\chi_{eq} = (2/3)\chi_{\perp} + (1/3)\chi_{\parallel}$ is the equilibrium susceptibility, and $\chi_{\perp}$ and $\chi_{\parallel}$ are the equilibrium zero-field susceptibilities along directions perpendicular and parallel to the anisotropy axis, respectively. When $K_{eff}V \gg k_BT$, χ_{eq} is given by the Curie law (Eq. 2.29). $E_{a\,blq}$ depends on temperature and corresponds to the activation energy that makes τ (given by Eq. 2.2) equal to the characteristic time of measurement, τ_m:

$$E_{a\,blq} = k_BT \ln\left(\frac{\tau_m}{\tau_0}\right) \tag{2.35}$$

The former susceptibility equations are written in terms of a E_a distribution, since a susceptibility measurement is probing such distributions. $f(E_a)$ is then the fraction of volume occupied by particles having the activation energy E_a. This is related to another distribution (of volumes, sizes, or moments) $g(x)$ by:

$$g(x) = f(E_a)\frac{dE_a}{dx} \tag{2.36}$$

Dc field-cooled experiments

The field-cooled experiments (fc) are similar to zfc, except that the sample is cooled under H_{app}. In a fc experiment χ decrease monotonously with temperature and is given by [136, 137]:

$$\chi_{fc} = \int_0^{E_{a\,blq}} \chi_{eq}(E_a, T) f(E_a)\, dE_a + \frac{2}{3} \int_{E_{a\,blq}}^{\infty} \chi_{eq}(E_a, T_B) f(E_a)\, dE_a \tag{2.37}$$

where $\chi_{eq}(E_a, T_B)$ is the equilibrium susceptibility of a particle with energy E_a calculated at the corresponding T_B. As expected, the difference between fc and zfc curves is due to the blocked particles: in the zfc curves their major contribution arises from the transverse component while in fc curves their susceptibility is the one obtained at T_B. The zfc and fc curves merge at a temperature T_F that depends on μ distribution. In fact it is possible to estimate the width of a lognormal μ distribution s (for $0.1 < s < 1.2$) as shown by Hansen and Mørup [137]:

$$s = 0.624 + 0.397 \ln\left(\frac{T_F}{T_B} - 0.665\right) \tag{2.38}$$

Here, T_B is defined as the temperature where the zfc curve show the peak and T_F as the temperature at which the difference $\chi_{fc} - \chi_{zfc}$ equals 10% of $\chi_{zfc}(T_B)$. The above equation is phenomenological and was obtained after using the lognormal distribution function in Eq. (2.33) and Eq. (2.37) and testing different s values.

Ac zero-field-cooled experiments

Susceptibility measurements in an alternate field with typical frequencies f in the 0.1-10^3 Hz range are a very useful tool for studying dynamical properties of magnetic systems, and in particular of superparamagnetic particles. Ac susceptibility can probe a large time window by using different frequencies and has the advantage of using a very low field h (about 10 times lower than the used in dc experiments) [101]. The result of a zfc ac experiment has some similarities to that of a dc experiment: above the irreversibility the in-phase susceptibility χ' curves follow, approximately a Curie law and the curves have a maximum at T_B. However an ac experiment yields more information, since different field frequencies correspond to different time windows, i. e. different τ_m. In an ac experiment, the onset of the irreversibility corresponds to the frequency dependence of χ' and to the onset of the out-of-phase component χ''. This onset occurs since the particles are not able to follow the alternate field (i. e. to cross the energy barrier) below a characteristic temperature. T_B will be frequency dependent, and in the canonic approximation will follow the Arrhenius law (Eq. 2.2), often verified using the linearization:

$$\ln(\tau) = \frac{E_a}{k_B T_B} + \ln(\tau_0) \tag{2.39}$$

considering that in the blocking temperature $\tau = \tau_m = 1/f$. This relation is used to determine E_a and τ_0 of superparamagnetic systems.

Lundgren et al. [139] have modeled the in- and out-of-phase components of a system constituted by magnetic entities with a relaxation time τ_i, a magnetic moment μ_{0i} at $t = \infty$, and a broad distribution of $\ln(\tau_i)$. Here we suppose that every τ_i corresponds to a given moment and a given volume, with no a priori relation between them. We also notice that χ'' is directly probing τ_i and not moments or volumes. In an alternating field $h(t) = h\sin(\omega t)$

(being h small and $f = 2\pi\omega$), the dynamics of a magnetic entity with a moment μ_{0i} is given by:

$$\tau_i \frac{d\mu_i}{dt} + \mu_i = \mu_{0i}(\tau_i)\sin(\omega t) \tag{2.40}$$

with solution:

$$\mu_{0i}(\tau_i) = \frac{1}{1+(\omega\tau_i)^2}\sin(\omega t) - \frac{\omega\tau_i}{1+(\omega\tau_i)^2}\cos(\omega t) \tag{2.41}$$

The in-phase ac susceptibility, $\chi'(\omega, T)$ of an anisotropy energy distributed superparamagnetic system is described by an equation identical to Eq. 2.33 regarding that when determining $E_{a\,blq}$ $\tau_m = 2\pi/\omega$ [136, 138].

From Eq. 2.41, χ'' of a system with a distribution f of $\ln\tau_i$ can be written as:

$$\chi''(\omega, \ln\tau_i) = -\frac{1}{h}\int_0^\infty \mu_{0i}(\ln\tau_i) f(\ln\tau_i) \frac{\omega\tau_i}{1+(\omega\tau_i)^2}\, d\ln\tau_i \tag{2.42}$$

The term $\frac{\omega\tau_i}{1+(\omega\tau_i)^2}$ is peaked at the characteristic time of measurement $\tau_i = \tau_m = 2\pi/\omega$ and thus, the integrand has its most important terms around $\tau_i = \tau_m$. In this region, $m_{0i}(\ln\tau_i)f(\ln\tau_i)$ is fairly constant and equal to $m_{0m}f(\ln\tau_m)$, so that it can be brought outside the integral:

$$\chi''(\omega, \tau_m) \simeq -\frac{\mu_{0m}}{h} f(\ln\tau_m)\int_0^\infty \frac{\omega\tau_i}{1+(\omega\tau_i)^2}\, d\ln\tau_i \tag{2.43}$$

Since the remaining integral is equal to $\pi/2$:

$$\chi''(\omega, \tau_m) \simeq -\frac{\pi}{2}\frac{\mu_{0m}}{h} f(\ln\tau_m) \tag{2.44}$$

This can be written in terms of energy as:

$$\chi''(\omega, E_{a\,blq}) \simeq -\frac{\pi}{2}\frac{\mu_{0m}}{h}\frac{E_{a\,blq}}{\ln(\tau_m/\tau_0)} f(E_{a\,blq}) \tag{2.45}$$

so that a plot χ''/T *vs.* $E_{a\,blq}$ is frequency independent and is a measure of $E_a f(E_a)$ [136, 105, 140, 141]. Since in non interacting superparamagnetic nanoparticles with ferromagnetic interactions the relation between E_a and V is well known, Eq. 2.45 is often written as a function of volume [136, 105, 141]. The term μ_{0m}/h is the parallel susceptibility that can be fairly replaced by χ_{eq} for K sufficiently large, so that $\chi_\perp \approx 0$ [142, 143]. As noticed by Svedlindh et al [143], the shape of χ''/T does not depend on the exact description used for μ_{0m}/h, since it is temperature independent.

2.5.2 Effect of interactions

Dc susceptibility

Several works have been devoted to model the effect of interactions in the dc susceptibility of magnetic nanoparticles systems, including analytical methods [144, 145, 146, 147] and Monte Carlo simulations, [117]. One of the first approaches to model the susceptibility above the blocking temperature was to assume that interactions could be represented by a Curie-Weiss law:

$$\chi(T) = \frac{C}{T - T_0} \tag{2.46}$$

where T_0 is an ordering temperature. The magnitude of T_0 is considered to reflect the strength of the interaction and the sign its type (i. e. ferromagnetic for $T_0 > 0$ and antiferromagnetic for $T_0 < 0$). This Curie-Weiss approach is in accordance with the interactions model proposed by Allia et al. [115], as noticed in section 2.3.4. The Curie-Weiss law is also the low particles concentration limit of the Onsager and Lorentz models [101]. El-Hilo et al.[146] analyzed the use of Eq. 2.46 and concluded that T_0 has two contributions with different weights in the temperature range. One contribution is negative and arises from moment distribution, being more important as T approaches T_B. The other is positive and arise from dipolar interactions. These are found to increase the height of the energy barrier for rotation, leading to an effective T_B higher than that of the isolated particles [146, 102]. T_0 is often evaluated as the extrapolation to $y = 0$ in a $1/\chi(T)$ plot. In this plot, different extrapolations are possible depending on the chosen temperature range, in accordance with the idea of an onset of a negative contribution for T close to T_B. Therefore conclusions about interactions based on T_0 must be drawn carefully [146]. We further remark that such procedure of determining T_0 may also lead to errors since the existence of a small diamagnetic contribution (χ_0, essentially constant with temperature) leads to a curvature in the $1/\chi(T)$ plot with the same trend as the imposed by the variation of T_0. Another fact that should not be disregarded is the temperature variation of μ that also introduces a curvature in the $1/\chi(T)$ plot [101].

Another question regarding the susceptibility of interacting systems is the effect of dipolar interactions in T_B. This question is still not clear, since an increase of T_B was found by Dormann et al. [102] and Luo et al. [148], while Mørup and Tronc observed a decrease of T_B in dense samples, supported by a random field model [149].

Some of the effects predicted by the susceptibility analytical models were compared to Monte Carlo calculations by Chantrell et al. [117], as follows. The model considers particles described by a single magnetic moment experiencing an energy given by Eq.(2.12), where E_a is given by Eq.(2.7) and E_m is given by Eq.(2.8). The total field acting on each particle is the sum of the applied field and the dipolar filed arising from the neighboring particles. Relevant parameters were studied as a function of the particles packing density ε. The results of El-Hilo et al. [146] regarding T_0 were not confirmed. On the contrary, as ε increases the

systems appears to have $T_0 < 0$, with increasing magnitude. T_0 was also shown to by strongly dependent on the long-range interactions. The effect of an increase of T_B with ε was also apparent in the Monte Carlo simulations, in accordance with experimental results reported in Ref. [102, 148]. Moreover a relation $T_B \propto \varepsilon^{1/2}$ was proposed. At the same time, the effect of interactions give rise to a dramatic reduction in χ as ε increases, together with a significant broadening of the peak [117]. Here we remark that this broadening is not consistent with the narrowing effect found by Dormann et al. for maghemite nanoparticles with different ε from diluted to powder samples [150]. We speculate that the narrowing effect can be due to an increase of a collective effect resembling that of spin-glass systems, which is probably not modeled by the ingredients used in the Monte Carlo simulation of Ref. [117]. Such collective effect was found in the most concentrated (powder) sample studied in Ref. [150] and may be also present in lower concentrated systems. With the increase of ε, the fc susceptibility drastically decreases comparing to the non-interacting case, showing a peak near T_B for higher concentrations. This occurs even at low ε values $(0.1 - 0.2)$ and low H_{app} and was interpreted in terms of an increase in the width of the effective energy barrier distribution as a result of a dispersion in the local interaction field. This effect is more dramatic than that experimentally found by Dormann et al. for maghemite nanoparticles [101], but agrees with the peak observed in the fc curve of ferrihydrite powders [151].

Dc/ac experiments: $T_B(H_{app})$

Since the seminal work of Mørup's group on $Fe_{1-x}C_x$ ferrofluids [152] that T_B vs. H_{app} measurements are used to probe deviations to superparamagnetism, in particular interactions and quantum tunneling. The effect of H_{app} on T_B can be regarded as follows. In the case of uniaxial anisotropy and $H_{app} = 0$, the energy (Eq. 2.7) has two equal minima. For $H_{app} \neq 0$ the energy is given by Eq. 2.13 and the minima are no longer equal. Thus, two different probabilities of jumping across minima, τ_- and τ_+ must be defined and the observed relaxation time is:

$$\frac{1}{\tau} = \frac{1}{\tau_-} + \frac{1}{\tau_+} \tag{2.47}$$

The evolution of T_B with H_{app} will therefore reflect the changes in the energy profile induced by the field and the concomitant changes in τ. To the best of our knowledge there is no approximate analytical formulation for τ_- and τ_+ under H_{app} [101].

Hanson et al. [152, 153] have calculated susceptibility curves at different H_{app}, considering a Langevin distributed function instead of the Curie law, and considering that the contribution of the blocked particles is zero. From these calculations, they observed an increase of T_B with field due to the existence of a moment distribution. In the same reports, [152, 153] interactions were considered to be responsible for a decrease of T_B with H_{app}. On this last point, Monte Carlo simulations by Chantrell et al. [117] showed no apparent differences in tend of $T_B(H_{app})$, when comparing interacting and non-interacting systems. In latter re-

ports, Luo et al. [148] and Sappey et al. [154] noted a nonmonotonic field dependence of T_B in magnetite and in maghemite particles dispersed in silica and ferritin, respectively. Again, they have shown that this measure is very sensitive to the distribution, since it is related to a $V^2 f(V)$ term that enhances the contribution of the larger particles. Unlike Hanson et al., F. Luis and co-workers [105], have taken into account the contribution of the blocked particles. Computing the characteristic data of ferritin on Eq. (2.33) they found a non-monotonic dependence in a qualitative agreement with experimental data. These results brought severe doubts on the possibility of probing resonant tunneling of magnetization in distributed macroscopic systems as ferritin [104, 153], and also on the fact that a nonmonotonic field dependence of T_B with field is due to dipolar interactions.

Ac experiments: $T_B(f)$

As the particles concentration increases, the interparticles dipolar interactions become relevant, as discussed, and their effect appears in ac experiments. In systems with interactions, the blocking temperature seems to follow the relation 2.2 (equivalent to 2.39) as the non-interacting systems. However, the extrapolated τ_0 increases with the interactions up to physically unacceptable values. The effect of the interactions in the dynamics, as seen by $T_B(f)$ have been modeled by two approaches: i) the statistical model of Dormann et al. [101, 102, 155] and ii) the super spin-glass description of the Mørup's and Hansen's group [113, 149, 114]. These approaches are somewhat contradictory and so are some experiments, as pointed out in Ref. [113]. Approach i) models interactions as changes in E_a while approach ii) looks for collective dynamics. On the other hand, different superparamagnetic interacting systems may have different intrinsic properties and the models may even coexist but none of the groups strictly applied the others model to their samples[4]. In a more recent report, model i) was associated to low/medium interactions, while approach ii) was associated to strong dipolar interactions [150].

The statistical model i) takes into account dipolar interactions of a disordered assembly of particles with a volume distribution [101, 102, 155]. Even for strong interacting systems, and in the frequency range probed by the ac susceptibility, this model predicts that $\ln(\tau)$ remains linear with $1/T_B$. In a first approximation, (useful to derive qualitative information) the extrapolation of $1/T_B$ to 0, in this case denoted by τ_0*, is given by: $\tau_0* = \tau_0 \exp(n_1)$, where n_1 is the number of first neighbors [102]. Here, the effect of the n^{th} neighbors, and the variation of μ and of τ_0 with temperature are neglected. At the same time, the energy barrier has a component due to the particle alone, $E_p = K_{eff}V$, and a component due to interactions. The latter depends on n_1, on the particles magnetic moment and volume and on $a_1 = \langle V \rangle / d_1^3$, where d_1 is average 1^{st} neighbors interparticle distance and $\langle V \rangle$ the average particles volume. Considering the approximation of the Langevin function for high x values,

[4] although the Dormann group partially did it.

$L(x) = 1 - 1/x$, the dependence of τ with the temperature is given by [155]:

$$\tau = \tau_0(T) \exp(n_1) \exp\left(\frac{K_{eff}V + n_1 M^2(T) V a_1}{k_B T}\right) \tag{2.48}$$

In a more precise approach, the variation of the magnetization $M(T)$ and the variation of τ_0 with temperature (given by Eq. 2.3) should be taken into account. In this model, this variation will result in the non linearity of $\ln(\tau)$ with $1/T_B$ for low $1/T_B$ (and $\ln(\tau)$) values, which can only be observed when T_B obtained from Mössbauer experiments is plotted with T_B from the ac experiments [102, 155]. $M(T)$ depends on the studied system, being given, for instance, by a mean field (Eq. 2.31) or by a Bloch law (Eq. 2.32). This model was successfully applied to a set of maghemite nanoparticles with different concentrations [101, 155]. Further refinement of this model includes considering the n^{th} neighbors. We notice that the factors a_j and n_j can be constrained by geometrical considerations [156]: $a_j = a_1/j^3$ and $n_j = n_1 j^2$. Considering j shells of neighbors and no approximation to the Langevin law, Eq. 2.48 can be rewritten as:

$$\tau = \tau_0(T) \exp\left(\frac{K_{eff}V + \sum_j n_j M^2(T) V a_j L(M^2(T) V a_j / kT)}{k_B T}\right) \tag{2.49}$$

Approach ii) looks for a phase transition to a super spin-glass phase at finite temperature due to a collective behavior in an interacting particle assembly. The frequency dependency of T_B can be modeled with a Vogel-Fulcher law [157]:

$$\tau = \tau_0 \exp\left(\frac{E_a}{k_B(T - T_0)}\right) \tag{2.50}$$

where T_0 would correspond to a transition temperature. However, Dormann et al. noticed that when fitting to real data several sets of parameters can be used and no clear conclusion is drawn [102]. In approach ii), ac susceptibility and IRM dc experiments (see Sec. 2.6) are used to determine the relaxation time, τ as a function of temperature. Unlike in most of the work concerning SP, τ is not associated to the maxima of the susceptibility curve but to the temperature where $\chi(T)/\chi_{eq} = 0.98$. χ_{eq} is taken as the extrapolation of $\chi(T)$ above the irreversibility using a Curie-Weiss law 2.46. $\tau(T)$ is then analyzed in a spin-glass framework:

$$\tau = \tau_* \left(\frac{T}{T_g} - 1\right)^{-z\nu} \tag{2.51}$$

where τ_* is a relaxation time associated to the individual particle, T_g is the transition temperature and $z\nu$ is a critical exponent. Evidence of critical slowing-down is obtained from

the frequency dependency of $\chi^{''}/w\chi^{'}$:

$$\chi^{''}/w\chi^{'} \propto \tau^{1-\beta/z\nu} \propto \left(\frac{T}{T_g}-1\right)^{-z\nu+\beta}, \qquad \tau \to 0 \tag{2.52}$$

where β is the order parameter critical exponent, of the order of 0.6-0.8 in spin-glasses [113]. The existence of a spin-glass-like transition can also be investigated by the nonlinear susceptibility static response [114]. The method consists on the determination of the magnetization at different low dc fields H (in the 0.1-24 Oe range, in the example given in Ref. [114]) and at a much lower ac field (∼0.05 Oe) and temperatures around T_B. The nonlinear susceptibility, χ_{nl} is defined as the deviation of M/H to the linear susceptibility χ_0, given in powers of H:

$$\chi_{nl} = -3\chi_2 H_0^2 - 5\chi_4 H_0^4 - \cdots \tag{2.53}$$

The coefficients χ_2 and χ_4 can be related to critical exponents. This approach ii) was successfully applied to narrow distributed amorphous $Fe_{1-x}C_x$ particles of about 4.7 nm, and the existence of a divergent behavior and low temperature spin-glass-like phase in interacting magnetic nanoparticle systems was claimed [113, 114]. Nevertheless, Dormann et al. [101] notice that the existence of nonlinear terms may arise from the non Curie-Weiss thermal dependence of χ_0, that can also be expressed in a power series of H. In fact, García-Otero et al. [158] performed Monte Carlo simulations of single-domain distributed particles with dipolar interactions and found no evidences of a spin-glass-like transition.

Nowadays, it is generally accepted that the statistical model is useful to investigate the effect of interactions in ac susceptibility results of low/moderate interacting systems, while the spin-glass approach is useful to model strong interacting systems [150]. However, a true transition temperature due to dipolar interactions in superparamagnetic systems is still a matter of debate. A dipolar interactions-driven transition was found in other magnetic systems as rare-earth salts [159, 160] and more recently in molecular magnets [161]. At the same time it is not clear if there is a crossover of properties between the low interaction regime and the glass collective state, or if the changes are gradual [150].

2.6 Magnetic relaxation

As discussed in Sec. 2.4, below T_B (as seen in a dc measurement) and after the application of a magnetic field, superparamagnetic systems display a remanent magnetization M_r at $H = 0$. This magnetization is then a function of time as the system approaches the equilibrium via a thermally activated process. Different states can be prepared before starting the measurement of the (remanent) magnetization as a function of time $M(t)$. Typical examples are the thermoremanent magnetization (TRM) and isothermal remanent magnetization (IRM). In TRM, the field is applied at $T > T_F$ and the sample is then cooled down to the

measuring temperature where the field is removed and $M(t)$ measured. In IRM, the sample is cooled from $T > T_F$ down to the measuring temperature at zero field and then the field is applied and subsequently removed [101].

In a TRM measurement, here designated as magnetic relaxation measurement, the magnetization of a single particle has an exponential decay [101]:

$$m(t, E_a) = m(0) \exp(-t/\tau(E_a)) \tag{2.54}$$

such that the time dependence of a set of particles can be written as:

$$M(t, E_a) = \int_0^\infty M(0) \exp(-t/\tau(E_a)) f(E_a) dE_a \tag{2.55}$$

or

$$M(t, E_a) = \int_0^\infty M(0) p(t, E_a) f(E_a) dE_a \tag{2.56}$$

defining $p(t, E_a)$ as [162]:

$$p(t, E_a) = \exp\left(-\frac{t \exp(-E_a/k_B T)}{\tau_0}\right) \tag{2.57}$$

$M(0)$ is the magnetization at $t = 0$, $\tau(E_a)$ follows an Arrhenius law in the case of canonic systems (Eq. 2.2) and $f(E_a)$ is the normalized anisotropy energy distribution. For a given time t, $p(t, E_a)$ can be approximated by a step function, changing from 0 to 1 at $E_a = E_c(t) = k_B T \ln(t/\tau_0)$, and thus [162]:

$$M(t, E_a) = \int_{E_c}^\infty M(0) f(E_a) dE_a \tag{2.58}$$

After integration over E_a, $M(t, E_a)$ is a function of $E_c(t) = k_B T \ln(t/\tau_0)$. Therefore $M(t, E_a)$ scales with $T \ln(t/\tau_0)$ [162], the time-temperature correspondence characteristic of activated processes following the Arrhenius law. The scaling is valid as long as $p(t, E_a)$ can be approximated by a step function. This approximation holds since the width of $p(t, E_a) \approx k_B T e$ (being e the base of the natural logarithm) is lower that the width of $f(E_a)$ (typically for $T < T_B$)[162]. The magnetic viscosity, S, is defined as the change in magnetization with $\ln(t)$ of a system held in a constant applied magnetic field, H:

$$S \equiv \frac{\partial M}{\partial \ln t} = -k_B T M(0) f(E_a) \tag{2.59}$$

and thus S/T is proportional to $f(E_a)$ and to χ''/T (Eq. 2.45). In fact in noninteracting systems, S/T and χ''/T are probing similar energy barriers at different characteristic times, and are proportional in a E_a scale, as found for maghemite nanoparticles with an average diameter of 7 nm [141].

2.7 Antiferromagnetic systems

2.7.1 Bulk antiferromagnetic systems

The variation of the magnetization of antiferromagnetic bulk materials with the field is linear in the medium and low field range and for $T < T_N$ (see, for instance Ref. [163]). For high fields (typically > 200 kOe) a spin-flop transition occurs and the linear relation breaks down. An antiferromagnetic susceptibility can be therefore defined as $\chi_{AF} = M/H$. χ_{AF} has perpendicular and parallel components with respect to the sublattice magnetization direction, whose variation with temperature is depicted in Fig. 2.7. For a random distribution of D directions with respect to the external field χ_{AF}=2/3$\chi_{\perp}$+$\chi_{\parallel}$. In a bulk material χ_{AF} increases with temperature up to $T = T_N$, decreasing for $T > T_N$ following a Curie-Weiss law:

$$\chi_{AF}(T_{T>T_N}) = \frac{C}{T + T_N} \tag{2.60}$$

where C is the Curie constant.

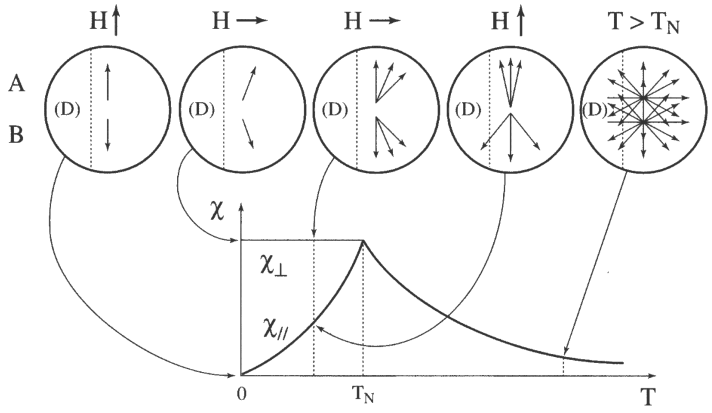

Figure 2.7: Temperature dependence of the magnetic susceptibility of a bulk antiferromagnetic material (from Ref. [163]). D is the antiferromagnetic coupling direction. Changes in the moments induced by parallel and perpendicular external fields are also depicted.

2.7.2 Antiferromagnetic nanoparticles

The magnetic properties of antiferromagnetic nanoparticles differ from the bulk ones, as noticed since the seminal works of Néel, [164, 165, 166, 167, 168] and are still matter of debate. As size decreases, antiferromagnetic particles start to evidence some characteristics typical of the superparamagnetic particles. In particular, for $T < T_N$ antiferromagnetic particles exhibit relaxation phenomena in ac and dc susceptibility and in Mössbauer spectroscopy measurements [48], while $M(H,T)$ curves evidence some degree of saturation with field [169]. The emergence of these characteristics has been attributed to uncompensated/canted moments μ_{un} coming out at the surface and/or in volume due to disorder and finite-size effects

[170, 169]. In fact, μ_{un} arises even in systems without disorder, due to particles with an odd number of "active planes" [164, 165] (an active plan contains atoms of just one of the antiferromagnetic sublattices). The relation between μ_{un} and the total number of spins n depends on the origin of the uncompensated moments. μ_{un} is proportional to n^p with $p = 1/2$ for moments randomly distributed in the volume, 1/3 for moments randomly distributed in the surface, and 2/3 for moments distributed throughout the surface in active planes [164]. Kodama et al. [170] have shown by calculations of equilibrium spin configurations that the bulk sublattice ordering is drastically affected due to finite size effects, and the system (NiO) adopt multiple sublattice spin ordering, leading to an increase of μ_{un}.

The uncompensated moments of the antiferromagnetic nanoparticles experience an energy barrier due to coupling to the antiferromagnetic moments, such that a relation similar to Eq. 2.2 holds:

$$\tau = \frac{1}{\nu} \exp\left(\frac{w}{k_B T}\right) \tag{2.61}$$

were w is though to be proportional to the volume, decreasing to zero as T approaches T_N, and ν is of the order of w/h, h being the Planck constant [164].

2.7.3 Magnetization under an applied field in the $T_B < T < T_N$ range

Early models

For temperatures between T_B and T_N, magnetization is usually modeled as the sum of a pure antiferromagnetic linear term and a Langevin function (Eq. 2.9) to describe the behavior of μ_{un}:

$$M(H,T) = \chi_{AF} H + N\mu_{un} L\left(\frac{\mu_{un} H}{k_B T}\right) \tag{2.62}$$

A similar equation is obtained if one considers the parallel and transverse antiferromagnetic susceptibilities together with an uncompensated moment that just experiences the influence of the applied field. The energy is given by [165, 171]:

$$E = -1/2\chi_{\parallel} H^2 \cos^2\alpha - 1/2\chi_{\perp} H^2 \sin^2\alpha - \mu H \cos\alpha \tag{2.63}$$

and, for low and medium fields, i. e. $H < \mu/\chi$, the magnetization is given by [171]:

$$M(H,T) = \chi_{\parallel} H + N\left(\mu_{un} + \frac{2(\chi_{\perp} - \chi_{\parallel}) k_B T}{\mu_{un}}\right) L\left(\frac{\mu_{un} H}{k_B T}\right) \tag{2.64}$$

We notice that this equation is similar to Eq. 2.62 considering an equivalent particle density that depends on μ and T: $N^* = N/(1 + 2(\chi_{\perp} - \chi_{\parallel}) k_B T/\mu^2)$. Therefore, the distinction between Eqs. 2.64 and 2.62 benefits from the knowledge of N based on other experimental techniques.

The Néel model

Néel has noticed that μ_{un} experiences the antiferromagnetic direction D, with an associated energy E_D, so that in a first approximation μ_{un} lies in that direction rather than being free to rotate as considered in the Langevin law [168]. In this approximation μ_{un} has two energy states:

$$E_0 = -\mu_{un}\cos\alpha H - E_D; E_\pi = +\mu_{un}\cos\alpha H - E_D \tag{2.65}$$

The partition function is then:

$$z(\alpha) = \exp\left(\frac{\mu_{un}\cos\alpha H + E_D}{k_B T}\right) + \exp\left(\frac{-\mu_{un}\cos\alpha H + E_D}{k_B T}\right) \tag{2.66}$$

and therefore the magnetization due to μ_{un} of a particle having an angle α between D and the field H is:

$$m_{un}(H,T,\alpha) = -k_B T\frac{\partial}{\partial H}(\ln z(\alpha)) = k_B T\frac{\frac{\mu_{un}\cos\alpha}{k_B T}\sinh\frac{\mu_{un}H\cos\alpha}{k_B T}}{\cosh\frac{\mu_{un}H\cos\alpha}{k_B T}} \tag{2.67}$$

The magnetization of a set of particles with a random distribution of directions D is:

$$M_{un}(H,T) = N\mu\frac{1}{2}\int_0^\pi \cos\alpha\sin\alpha\tanh\frac{\mu_{un}H\cos\alpha}{k_B T}d\alpha \tag{2.68}$$

or in another way:

$$M_{un}(H,T) = N\mu G(x) \tag{2.69}$$

The total magnetization of an antiferromagnetic nanoparticle system is the sum of this component and a linear term:

$$M(H,T) = N\mu G(x) + \chi_{AF}H \tag{2.70}$$

The function $G(x)$ scales with H/T, has the same susceptibility as $L(x)$, and saturates at $1/2$, while $L(x)$ saturates at 1 (Fig. 2.8). Eq. 2.70 was successfully applied to describe the magnetization as a function of field and temperature of artificially reconstructed ferritin cores [54]. The use of $G(x)$ was supported by hight-field Mössbauer spectroscopy results: at 70 kOe and 4.2 K, the Mössbauer spectra can still be modeled considering a random orientation of the moments, showing that μ_{un} remain close to the antiferromagnetic axis D.

Relation between the Néel, Langevin and uniaxial anisotropy models

The differences between the Néel, Langevin and uniaxial anisotropy models can be observed in Fig. 2.8, where these functions are plotted for a given μ_{un}, H and E_a, at different temperatures. The Langevin law (Eq. 2.9) can be regarded as a limit case of the uniaxial anisotropy model, where the anisotropy is negligible, i. e. $E_a \ll k_B T$. On the other hand,

we emphasize, to the best of our knowledge for the first time, that the Néel model is a limit case of the uniaxial anisotropy model when $E_a \gg k_B T$ and $E_a \gg \mu H$. Therefore the validity of $G(x)$ is confined to a H, T range, given by the above condition, which holds until $E_a \approx 10 k_B T$, as seen in Fig. 2.8. When analyzing magnetization measurements performed up to $H = 50 - 100$ kOe and at different temperatures above the blocking temperature T_B this condition is not fulfilled and anisotropy should be considered. An important difference between both models is the fact that the uniaxial anisotropy does not scale with H/T, unlike $G(x)$. We also notice that, depending on E_a, H and T, the uniaxial anisotropy curve can be erroneously regarded as a $L(x)$ or a $G(x)$ curve with a linear term [5]. Work to find experimental evidence of the relevance of uniaxial anisotropy in antiferromagnetic nanoparticles is still in progress.

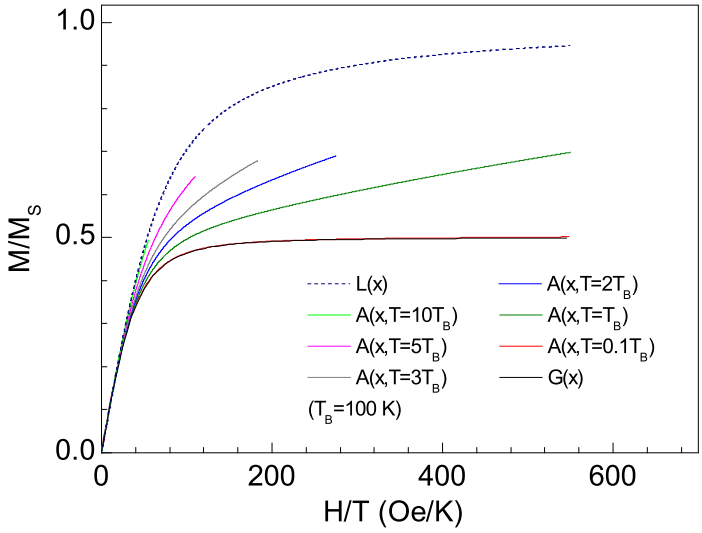

Figure 2.8: M(H/T) curves obtained using the Langevin function (L(x), Eq. 2.9) and considering the influence of the uniaxial anisotropy energy at different temperatures (A(x), Eq. 2.16 and 2.7). The Néel function G(x) is also shown.

2.7.4 Magnetization under an applied field below T_B

The magnetization of antiferromagnetic nanoparticles display hysteresis below T_B, with open cycles up to fields at least of the order of 50 kOe, large coercivity (up to ∼10 kOe), training effects, and shifted loops when the samples are cooled under an applied field [51, 60, 118, 173, 174]. Based on a formulation introduced by Mørup [175], Gilles et al. [174] have developed a Stoner-Wohlfarth-like description for antiferromagnets. This model does not reproduces some of the effects observed in antiferromagnetic nanoparticles, as high field

[5] this hypothesis was proposed in a recently released article [172]. This section was written before this article came to our knowledge.

irreversibility, shifted loops, and some particular features of the loops at low fields, including 'strangulated-like' loops. Stoner-Wohlfarth-like descriptions just produce shifted loops in the case of minor loops or when a specific exchange interaction term is used.

Concerning hysteresis loops, important insight is gained with computational models. Kodama and co-workers developed an atomic-scale model [170, 60] and applied it to simulate $M(H)$ curves of ferri- and antiferromagnetic nanoparticles. They showed that surface spin disorder and roughness are key ingredients to generate large coercivity and high field irreversibility, which is not achieved just with surface anisotropy [60].

2.7.5 Susceptibility

The susceptibility of antiferromagnetic nanoparticles is described as the sum of a superparamagnetic contribution and a pure antiferromagnetic contribution. Above blocking:

$$\chi = \chi_{SP} + \chi_{AF}(T) \tag{2.71}$$

where χ_{SP} is given by the Curie law (Eq. 2.30). In fact, Eq. 2.71 corresponds to the low field approximation of the Néel, Langevin and anisotropy models. Similarly, the description of the ac and dc results can also be made adding a $\chi_{AF}(T)$ term to the equations presented for superparamagnetic particles. A difference between χ_{SP} of antiferromagnetic and superparamagnetic nanoparticles may arise in the dependence of μ_{un} with temperature. While a good description of μ of ferromagnetic-superparamagnetic nanoparticles is given by the mean-field (Eq. 2.31) or the ferromagnetic magnons law (Eq. 2.32), the dependence of μ_{un} with temperature in antiferromagnetic nanoparticles can be given by the antiferromagnetic magnons law:

$$\mu(T) = \mu(0)\left(1 - \alpha T^2\right) \tag{2.72}$$

where α is a constant related to the value of T_N, as one might expect. This dependence was in fact found for artificially reconstructed ferritin cores [174].

Antiferromagnetic susceptibility

The origin of χ_{AF} in nanoparticles is not clear and its temperature dependence was not yet modeled. An enhancement of χ_{AF} compared to bulk is often reported, as well as a puzzling decrease with temperature [51, 151, 176, 174]. One reason for this enhancement is a pure finite size effect predicted by Néel called superantiferromagnetism [165]. Superantiferromagnetism is related to particles with an even number of active reticular planes, and becomes relevant as size decreases and the relative number of these planes increase. In a bulk antiferromagnetic, when the applied field is perpendicular to the antiferromagnetic axis D, the moments rotate in the field direction, while D is supposed to remain in the same direction. Superantiferromagnetism is due to a rotation of D in the outer planes, which is

essentially an effect of broken symmetry, that propagates with decreasing 'intensity' to the inner ones [165, 166]. Néel has first developed a discrete model, latter used by Gilles et. al [174], and then a continuous model [167]. The magnetization due to a fully compensated particle, perpendicular to the applied field can be written as:

$$m_{AF} = (\chi_\perp + n\chi_a)H \tag{2.73}$$

where $\chi_\perp$ is the bulk perpendicular susceptibility, χ_a an additional susceptibility due to the active planes and n the number of active planes, such that:

$$\chi_\perp = \frac{n}{4\lambda_1} \tag{2.74}$$

$$\chi_a = \frac{1}{4\lambda_1}\left(1 + 2\rho + 2\rho^2\left(3 - \frac{4}{n}\right) + ...\right) \tag{2.75}$$

with

$$\rho = \frac{\lambda_2}{\lambda_1 - \lambda_2} \tag{2.76}$$

λ_1 and λ_2 are the exchange coupling constants with the first and second neighbors. The magnetization has another term due to a localized surface effect [167], independent of n, negligible for n grater than some tens.

Gilles et al [174] applied the discrete Néel model to ferritin and found evidence of this enhanced susceptibility at high fields and low temperatures. At the same time, they have described the temperature dependence of the antiferromagnetic susceptibility as $\chi_{AF}(T) \propto T^{-1/2}$ [174].

2.7.6 Thermoinduced effect

Recently, Mørup and Frandsen proposed the existence of an intrinsic increase of μ_{un} with temperature in antiferromagnetic nanoparticles, due to the excitation of the uniform spin-precession mode [177]. In antiferromagnets, the spin-precession occurs in both sublattices with slightly different angles and therefore a non-zero moment arises. At the same time this angular difference increases with temperature leading to the increase of μ_{un}.

Considering two sublattices A and B, the relation between the angles is approximately:

$$\frac{\sin\theta_A}{\sin\theta_B} \approx 1 \pm \delta \tag{2.77}$$

where $\delta \approx (2H_a/H_E)^{1/2}$ and H_a and H_E are the anisotropy and exchange fields. The net magnetic moment associated to this angular difference is then:

$$\mu = M_S V|\cos\theta_B - \cos\theta_A| \approx M_S V\delta\frac{\sin^2\theta_B}{\cos\theta_B} \tag{2.78}$$

The thermal average of μ can be calculated using Boltzmann statistics, considering the energy associated to θ_A equal to the one of θ_B and given by Eq. 2.7. Considering also that $k_BT \ll K_aV$:

$$\langle\mu\rangle \approx M_S V\delta\frac{k_BT}{K_aV} \tag{2.79}$$

$\langle\mu\rangle$ is thought to be of the order of 200 μ_B at room temperature, i. e., of the same order of magnitude of the moment due to uncompensated moments.

Several studies of the magnetization curves analyzed with Eqs. 2.62 and 2.64 show an increase of μ_{un} with temperature [173, 151, 178, 179]. Such results were presented as an evidence of the thermoinduced effect by Mørup and Frandsen [177]. However, as we showed in Sec. 2.3.3, ignoring the existence of a moment distribution can lead to an artificially increase of μ_{un}. We believe that this is the case of ferrihydrite [178, 151], since the increase of μ_{un} is followed by the decrease of $M_S = N\mu_{un}$, which would imply a strong decrease in the particles density N. In fact, the thermoinduced effect does not have an experimental evidence until now.

Following the problems concerning find experimental evidences for the thermoinduced effect, Brown et al. [180] performed Monte Carlo simulations of fully compensated antiferromagnetic nanoparticles with even sublattices. These calculations show the increase of the magnetization in the anisotropy axis direction as predicted by Mørup and Frandsen [177]. At the same time, they found that $\langle\mu\rangle$ depends on the particles volume. The dependency can be expressed by: $\langle\mu\rangle \propto V^p$ where p depends on the anisotropy constant K_a. In the limit of low K_a/λ_1, p approaches 1, in accordance to Eq. 2.79.

2.8 Ferrimagnetic systems

2.8.1 Bulk ferrimagnetic systems

Ferrimagnetism occurs is systems with antiferromagnetic interactions, where the magnetic moments of the sublattices have different magnitudes (as in magnetite) or/and where the number of moments in the sublattices are different (as in maghemite). An analytical description of the susceptibility above the order temperature is possible in simple cases, as in the example given below (see, for instance Ref. [163]).

Lets consider the case of two sublattices A and B, with antiferromagnetic interactions between moments of A and B, and ferromagnetic interactions within moments of A and within those of B. In a mean-field approach, the field created by the moments of each sublattice can be expressed as:

$$\begin{aligned} H_A &= -\lambda M_B + \alpha\lambda M_A \\ H_B &= -\lambda M_A + \beta\lambda M_B \end{aligned} \tag{2.80}$$

where λ corresponds to the A/B interactions, $\alpha\lambda$ corresponds to those of A/A, and $\beta\lambda$ to those of B/B. In the paramagnetic phase (i. e. above the order temperature), the sublattices magnetization M_A and M_B can be written as:

$$\begin{aligned} M_A &= \chi_A(H_{app} + H_A) = \frac{C_A}{T}(H_{app} - \lambda M_B + \alpha\lambda M_A) \\ M_B &= \chi_B(H_{app} + H_B) = \frac{C_B}{T}(H_{app} - \lambda M_A + \beta\lambda M_B) \end{aligned} \tag{2.81}$$

where H_{app} is the external applied field. Putting together the terms in M_A and in M_B it is possible to write:

$$\chi = \frac{M_A + M_B}{H_{app}} = \frac{(C_A + C_B)T - (2 + \alpha + \beta)\lambda C_A C_B}{T^2 - T\lambda(\alpha C_A + \beta C_B) - \lambda^2 C_A C_B(1 - \alpha\beta)} \tag{2.82}$$

The inverse of the susceptibility is therefore:

$$\frac{1}{\chi} = \frac{T + \theta_p}{C_A + C_B} - \frac{\gamma}{T - \theta} \tag{2.83}$$

being θ_p and θ characteristic temperatures and γ a constant given by:

$$\begin{aligned} \theta &= (2 + \alpha + \beta)\lambda \frac{C_A C_B}{C_A + C_B} \\ \theta_p &= \lambda \frac{2C_A C_B - \alpha C_A^2 + \beta C_B^2}{C_A + C_B} \\ \gamma &= \lambda^2 \frac{C_A C_B((1 + \alpha)C_A - (1 + \beta)C_B)^2}{(C_A + C_B)^3} \end{aligned} \tag{2.84}$$

The inverse of the susceptibility is an hyperbola having θ and θ_p as asymptotes (Fig. 2.9).

Below the transition temperature, the dependence of the magnetization with the temperature can have different shapes depending on the dependence of the sublattices magnetization with the temperature. Some typical examples are shown in Fig. 2.9.

2.8.2 Nanoparticle ferrimagnetic systems

Ferrimagnetic nanoparticles are often treated in the framework of superparamagnetism as ferromagnetic nanoparticles. Examples of this include susceptibility and magnetization measurements in maghemite and magnetite (see, for instance Ref. [101]). Nevertheless, the ferrimagnetic character of these oxides is apparent in Mössbauer spectroscopy [181]. Other deviations to the superparamagnetic theory in maghemite and magnetite, that might be related to ferrimagnetism, include the possible existence of an antiferromagnetic-like linear component in the $M(H, T)$ curves [182, 183]. In fact, the existence and the order of magnitude of such component is still a matter of debate.

Studies in ferrimagnetic nanoparticles made outside the superparamagnetic framework

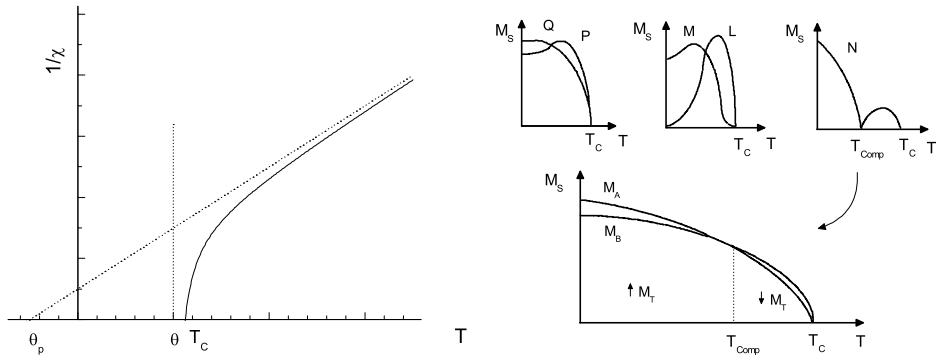

Figure 2.9: Temperature dependence of the inverse of the susceptibility in ferrimagnetic materials above T_C and magnetization of different types of ferrimagnetic materials. The temperature dependence of the two sublattices is given for case N (based on Ref. [163]).

include simulation of hysteresis loops [60, 118, 61, 184]. These simulations concern the effect of finite-size, and surface and bulk disorder in the loops. In fact, the loops of ferrimagnetic nanoparticles have high field irreversibility and shifted loops, as those of the antiferromagnetic nanoparticles. In both ferrimagnetic and antiferromagnetic nanoparticles, the onset of the loop shift and high field irreversibility are associated to "freezing" of disordered surface spins [118]. These spins can freeze in clusters that reversal together, leading to an increase of the high field irreversibility. The formation of these clusters and the consequent enhancement of irreversibility is favored in the case of ferrimagnets containing atoms with different moments, which can be observed comparing $NiFe_2O_4$ to γ-Fe_2O_3 [60].

Iglesias and Labarta have studied finite and surface effects of non-interacting maghemite nanoparticles by Monte Carlo simulations [61, 184]. The model assumes the unit cell and interaction constants of maghemite, and no other disorder than the random distribution of vacancies characteristic of maghemite [61]. They have found that the order temperature T_C decreases as the size decrease, as predicted by a finite-size scaling theory [61]:

$$\frac{T_C(bulk) - T_C(D)}{T_C(bulk)} = \left(\frac{D}{D_0}\right)^{-1/\nu} \tag{2.85}$$

with $\nu = 0.5$ and where D_0 is a microscopic length scale. At the same time, the spontaneous magnetization and the coercive fields also decrease as the size decreases. The decrease of the spontaneous magnetization was found proportional to the ratio surface/core spins. The decrease of H_C is in contrast to the experimentally observed increase. Therefore, such increase is probably not caused by finite-size or surface effects, but by a surface anisotropy enhancement, as shown in Ref. [184]. At last, none of the above mentioned effects seems responsible for the experimentally observed shifted loops.

2.9 Mössbauer spectroscopy

The recoilless emission of photons from nuclei was discovered by Rudolf Mössbauer in 1957. For this discover and subsequent explanation he has awarded the Nobel prize in 1961. Presently, the Mössbauer effect is very important in high resolution spectroscopy, in particular applied to magnetism, since ^{57}Fe is simultaneously one of the most interesting nucleus for Mössbauer spectroscopy and one of the most important magnetic element. In the following section we present some aspects of Mössbauer spectroscopy that can be found in many text books, as for instance in Ref. [185].

2.9.1 Background and experimental technique

A nucleus, atom or molecule emitting any type of radiation (photon of frequency ν) must recoil in order to conserve energy and momentum. The energy difference between the initial and final state energy levels and the emitted-photon energy, i. e., the recoil energy, is approximately:

$$\Delta\left(h\nu\right) \approx \frac{\left(h\nu\right)^2}{mc^2} \tag{2.86}$$

where m is the mass of the source and c is the speed of light. If then this photon is absorbed by another nucleus, atom or molecule, another recoil must occur, with the recoil energy being also given by Eq. 2.86, as expected. The possibility of occurring emitting and absorption phenomena between similar energy levels in neighboring nucleus, atom or molecule depends on the relation between the energy shift imposed by the recoil (two times $\Delta\left(h\nu\right)$) and the characteristic line widths of the emission and absorption spectra. If the line widths are at least of the order of $\Delta\left(h\nu\right)$ emission and absorption between the same levels "resonance absorption" will occur. This is the case of optical transitions, but not exactly the case of nuclear transitions. In particular, a transition of interest, between levels of ^{57}Fe nucleus, have an energy of $1.44{\times}10^4$eV. Since in the free iron atom mc^2 is $\approx 5 \times 10^{10}$ eV, we obtain $\Delta \approx 4 \times 10^{-3}$ eV, while the line width due to the Heisenberg Uncertainty Principle is about 4×10^{-8}eV. The observation of resonance absorption is therefore dependent on further enhancement of the line width and/or decrease of the recoil energy. The latter event occurs in solids and corresponds to the Mössbauer effect.

Because of a strong bonding of the atomic nucleus to the lattice, the recoil energy of the atom is taken up and distributed in the entire lattice as lattice vibrations. These lattice vibrations, ω_E, are quantized and thus occur in discrete amounts only. According to the Einstein model, atoms in the solid oscillate harmonically and in an isotropic but uncorrelated manner, with a single frequency ω_E (Einstein-frequency). Therefore, the radiating atom may not be able to transfer its recoil energy to an excited state of the lattice. In this case, the entire crystal recoils as a whole, with the recoil being given by Eq. 2.86, where m is now the crystal mass. This corresponds to a decrease of the recoil energy of the order of 10^{24}, making

resonance absorption possible. The Lamb-Mössbauer-factor f represents the fraction of the recoil-free transitions in comparison with the total number of transitions. It is possible to determine a function dependence for f and demonstrate the conditions for the occurrence of the Mössbauer effect: i) strong attachment to the lattice (which means a large value for ω_E) and ii) low temperature.

The transition from the $I = 3/2$ excited state to the $I = 1/2$ ground state of ^{57}Fe, is the most used concerning the application of the Mössbauer effect to magnetism. This transition is produced by the decay of an excited state of ^{57}Fe at 136.32 keV, which in turn is the result of electron capture from ^{57}Co, as depicted in Fig. 2.10.

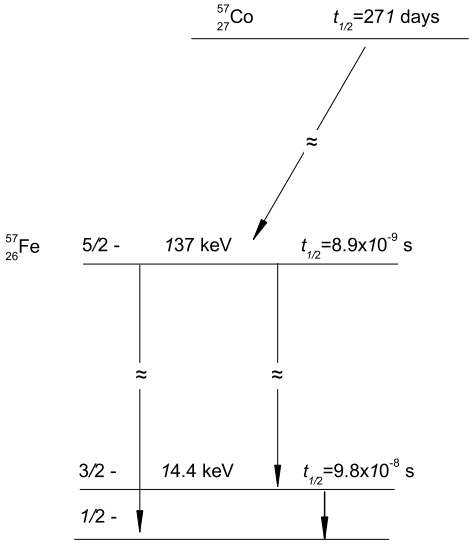

Figure 2.10: Decay scheme of ^{57}Co and Mössbauer transition of the iron nucleus.

The $I = 3/2$ and $I = 1/2$ states of the ^{57}Fe nucleus experience electrical and magnetic interactions with the electron shells surrounding it (hyperfine interactions), that can be probed by Mössbauer spectroscopy. To probe the nucleus-electron interactions it is necessary to shift the energy of the photons. This is done by moving the source relative to the sample, creating a Doppler shift in the energy of the photons. A velocity of 1 mm/s towards the sample results in an increase of 4.8×10^{-8} eV ($14.4{\times}10^3 \times v/c$). The region of interest is covered by moving the sample at a constant acceleration to a maximum velocity of about $\pm$10 mm/s. In a transmission geometry, a detector measures the transmitted photons as a function of the velocity (Fig. 2.11).

Concerning hyperfine interactions, the first here described are electrostatic interactions between the nucleus and its electrons. This interaction is different in the $I = 3/2$ and $I = 1/2$ states, and depends also on the difference of the electron charge density at the nucleus. If the interactions in the source are different from those in the absorber, an isomer shift will appear in the Mössbauer spectra, such that absorption will occur at $v \neq 0$. The isomer shifts

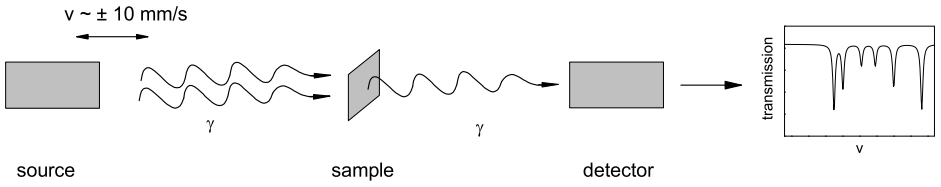

Figure 2.11: Schematic Mössbauer setup in a standard transmission experiment.

are essentially independent of temperature. The second interaction here described results in quadrupole splitting. Any nucleus with a spin quantum number greater than $I = 1/2$ has a nonspherical charge distribution, resulting in an inhomogeneous electrical field at the position of nucleus. A quadrupole splitting happens through the effect of the quadrupole interaction between the electrical nuclear quadrupole moment eQ and the electric field gradient. The sign depends on the shape of the deformation. A negative quadrupole moment indicates that the nucleus is oblate or flattened along the spin axis, whereas for a positive moment it is prolate or elongate. A third important hyperfine interaction is the nuclear Zeeman effect, that occurs if there is a non-zero magnetic field at the nucleus. The field can either be internal due to unpaired electrons or externally applied. Under one of these conditions, state $I = 1/2$ will split in two energy levels with $M_I = \pm 1/2$, and state $I = 3/2$ will split in four energy levels with $M_I = \pm 1/2$ and $M_I = \pm 3/2$. There are 6 allowed transitions between these levels, corresponding to the selection rule $\Delta M_I = 0, \pm 1$, as depicted in Fig. 2.12. This figure summarizes the qualitative effects procured by the hyperfine interactions above described in the $I = 3/2$ and $I = 1/2$ states of the ^{57}Fe nucleus, and how they affect the Mössbauer spectrum.

2.9.2 Application to iron-based nanoparticles

Mössbauer spectroscopy has been applied in different contexts of magnetism, including iron-based nanoparticles. First of all, Mössbauer spectroscopy is used for phase identification. The iron- based phases have known spectra and the different phases and phase mixture can be identified. An important example is the determination of mixtures of maghemite and magnetite, or the degree to which magnetite is nonstoichiometric. Another example is the determination of mixtures of weakly-magnetic and strong magnetic phases, as magnetite and hematite: magnetization experiments will be dominated by magnetite while in a Mössbauer spectrum all Fe atoms are "treated equally".

Mössbauer spectroscopy is also used to determine the blocking temperature, T_B associated to the characteristic time of the experiment ($\tau_m = 10^{-8}$–10^{-9} s), since the spectrum changes from a doublet to a sextet at T_B. Above the blocking temperature the particles are able to cross the anisotropy energy barrier within the characteristic time of measurement so that the local magnetic field averages zero and the Mössbauer spectrum shows a doublet. Below the

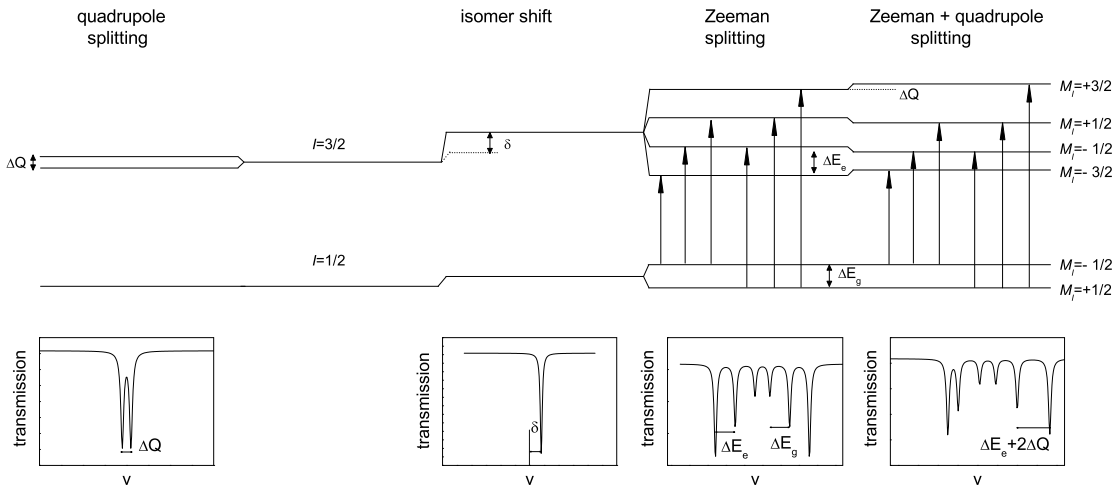

Figure 2.12: Scheme showing the isomer shift, quadrupole splitting, Zeeman splitting, and combined effect of quadrupole splitting and Zeeman splitting, The qualitative effect of the splitting in the Mössbauer spectrum is also shown.

blocking temperature the local field is non zero and the Mössbauer spectrum displays the characteristic sextet. Mössbauer spectroscopy is also used to probe dipolar interactions, since they have influence in the spectrum at temperatures around T_B (see Sec. 3.4.4 for details).

The application of an external magnetic field gives further information about the nanoparticles. Pankhurst and co-workers [48, 181] have shown that the nature of the interactions (antiferro or ferrimagnetic) can be deduced by in-field Mössbauer spectroscopy. This was particularly useful in studying 2- and 6-line ferrihydrite, as described in Sec. 1.3.1. The application of an external field is also used to decide whether the transition from a doublet to a sextet corresponds to a blocking or an ordering temperature. This question arises since both unblocked superparamagnetic and paramagnetic states yield a doublet. The application of a magnetic field above the characteristic temperature will promote a partial reappearance of the sextet in the case of superparamagnetism, while the doublet will remain in the case of paramagnetism [186].

Differences between surface and core atoms are investigated by Mössbauer spectroscopy, since it can probe the local environment of the iron ions. This was the case of ferrihydrite, where no evidence of Fe with tetragonal coordination was found by Mössbauer spectroscopy, while some early XRD models included them [42].

2.10 Magnetic property experimental techniques

The ac and dc susceptibility and magnetization measurements reported in the following chapters were performed in Quantum Design superconducting quantum interference device (SQUID) magnetometers (Quantum Design Inc.). This is an integrated device, containing a

superconducting magnet in helium bath and magnet control system, a temperature control system (from 1.8 to 400 K), and SQUID-based dc magnetometer and ac susceptometer. Here we briefly describe the dc magnetometer and ac susceptometer used in this device, in accordance with Ref. [187, 188, 189].

The results presented in the following chapters are in gaussian (cgs) units, often used in the magnetism literature. Hence, the magnetic field is expressed in oersted (Oe; 1Oe=$10^3/4\pi$ A/m) and the magnetic moment in electromagnetic units, emu=erg/gauss. As said, the magnetization M is defined as the magnetic moment per volume. However, in the following the term magnetization is also used to designate the magnetic moment per mass unit.

2.10.1 Dc measurements

The dc magnetometer uses an extraction method, by moving the sample through the detection coils in a series of discrete steps. As the sample moves through the coils, the magnetic moment of the sample induces an electric current in the superconducting detection coils. The coils have a second-derivative configuration: an upper coil turned clockwise, two central coils turned counter-clockwise and a bottom coil turned clockwise. This configuration cancels the constant field produced by the magnet. The current is then converted to a voltage by the SQUID-rf device. A SQUID device consists of a closed superconducting loop including one or two Josephson junctions, which functions as a highly linear current-to-voltage convertor. This voltage is recorded at each of the sample positions, being the raw data of the dc measurement. The raw data is then demeaning and detrending before it is further analyzed. Demeaning is the removal of a constant offset and detrend is the removal of a linear drift. The data is then treated according to the scan type: full scan, linear regression and iterative regression. The full scan takes a root mean square of the sum of the voltages and scales it to get the magnetization value. The linear regression fits the signal to the ideal dipole signal. The iterative regression is similar to the previous one with an additional parameter that corrects the sample center (within $\pm$5 mm). This last scan type is the more effective in analyzing very small signals and was used in the measurements here reported. The longitudinal SQUID calibration factor is used to convert the measured voltage to the magnetic moment. The resolution is of the order of 10^{-7}- 10^{-8} emu. A scheme of the detection circuit and the typical obtained data is shown in Fig 2.13.

2.10.2 Ac measurements

The ac susceptibility measuring system is constituted by superconducting detection coils in a second-derivative configuration, the ac drive system and drive coils, the SQUID system, the feedback system, and the ac digitizer (Fig. 2.13). Details about these different elements can be found in Ref. [189]. The frequency independent coupling between magnetic flux and induced currents in SQUID allows the use of ac frequencies and drive fields many orders of

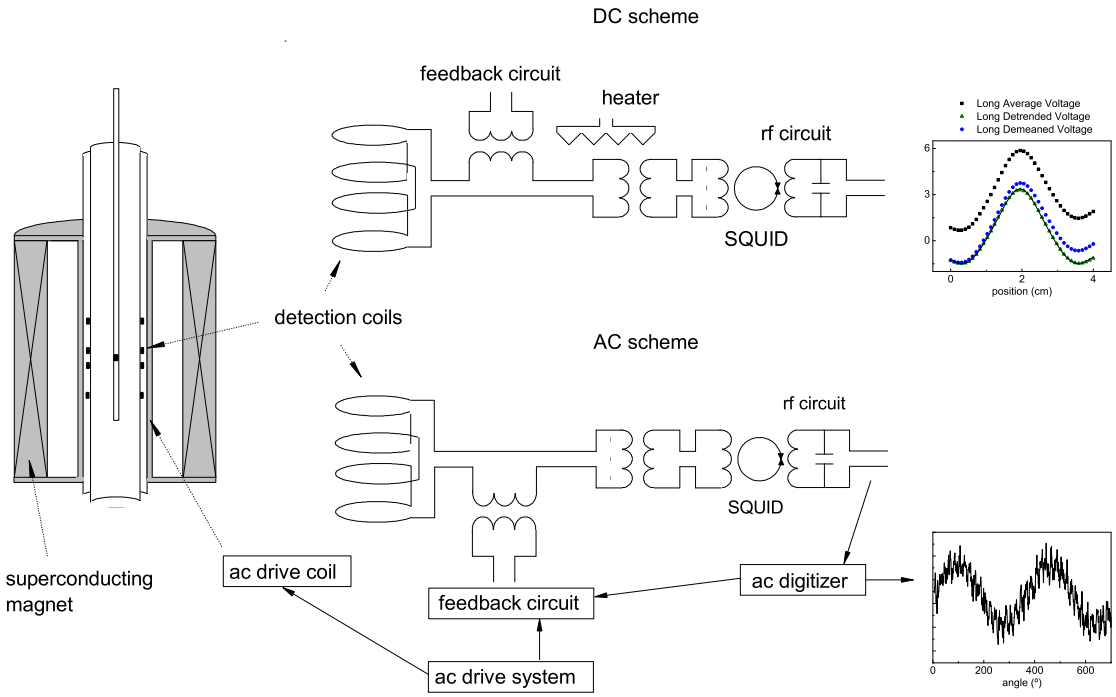

Figure 2.13: Scheme showing the dc and ac measurements system and their integration in the cryostat. The main components of the dc system are the superconducting detection coils circuit and circuit heater, the feedback system, and the SQUID-rf circuit. Typical response, demeaning and detrending curves are shown. The main components of the ac system are the superconducting detection coils circuit, the feedback system, the ac drive coil and system, the ac digitizer, and the SQUID-rf circuit. Typical response of M as a function of time is shown.

magnitude lower than those of other ac systems. In an ac measurements, the high SQUID sensitivity is combined to the noise rejection inherent in ac techniques.

A standard ac measurement comprises two separate measurements: one in the lower detection coil and one in the center coils. The sample is first moved into the lower coil, where the system null any noise and removes the dc offset and the signal of the sample itself. This is done by sending the appropriated current to the feedback transformer. The removed noise includes 50 Hz line noise and residual signal from the ac drive field, caused by the inevitable imbalance in the detection coils. The signal is nulled to a level approximately equal to that of the sample itself, to allow the SQUID electronics to be set to their maximum sensitivity. The remanent signal in the bottom coil, M_b, is then measured during a period of time specified by the user. The sample is then moved into the center of the detection system and the signal M_c measured. The moment of the sample is calculated by:

$$M = N\frac{M_c - M_b}{f(c) - f(b)} \tag{2.87}$$

where N is an overall normalization factor and $f(x)$ is the normalized response function of

the ideal dipole in the detection coils at position x. Further phase adjustment is made to correct any instrument phase shifts. A typical ac response is displayed in Fig. 2.13.

Chapter 3

Ferrihydrite/hybrid matrix nanocomposites

3.1 Overview

This chapter is devoted to the structural and magnetic properties of several groups of ferrihydrite/di-ureasils nanocomposites with different iron content. Structural studies include X-ray diffraction, small-angle X-ray scattering, and Fourier-Transform infrared and nuclear magnetic resonance spectroscopy measurements. Detailed transmission electron microscopy (TEM) studies are also presented for one of the samples. Magnetic studies include dc and ac susceptibility, magnetization as a function of field, temperature and time, and Mössbauer spectroscopy. Different models having in consideration magnetic and structural properties, and comparing the different samples are discussed. In particular, the determination of the saturation and antiferromagnetic components, the evolution of the dipolar interactions with the iron content, and the relevance of the magnetic moment distribution are addressed.

In strict terms, only one group of samples here studied (group I) contain 6-line ferrihydrite nanoparticles. The subsequent groups here presented contain iron oxyhydroxynitrate phases, which are precursors of ferrihydrite. The groups are sequentially presented such that their properties are progressively different from those of ferrihydrite. Further iron oxyhydroxynitrate phases, with properties significantly different from those of ferrihydrite, are presented in chapter 5.

3.2 Synthesis

The synthesis of the ferrihydrite/di-ureasils nanocomposites was first described in Ref. [190]. The preliminary step of the nanocomposites preparation involves the synthesis of a cross-linked hybrid precursor. This is achieved by the formation of urea linkages between the terminal NH_2 groups of a doubly functional amine (α, ω-diamine poly(oxyethylene-co-

oxypropylene)) and the isocyanate group of an alkoxysilane precursor (3- isocyanatepropyltriethoxysilane, ICPTES, Fluka), in tetrahydrofuran (THF, Merck) at room temperature (RT). This preliminary step is equal to the one used in the synthesis of undoped di-ureasils [25]. In this step, diamines having poly(oxyethylene-cooxypropylene)) chains with different molecular weight (M_w) can be used. Here we have used the commercially available Jeffamine ED-2001® and Jeffamine ED-900® (Fluka) with M_w=2000 and 900, respectively. The iron(III) nitrate nonahydrate ($Fe(NO_3)_3.9H_2O$, Aldrich) was incorporated in the second step of the synthetic procedure. In the case of the preparation of the d-U(2000)-based materials, an appropriate amount of this salt was dissolved in a mixture of ethanol and water (molar proportion ICPTES/CH_3CH_2OH/H_2O=1:4:1.5). This solution was added to the non-hydrolyzed hybrid precursor prepared in the first stage. The resulting mixture was then stirred in a sealed flask for a few minutes at RT. After this, the solution was cast into a mould and gelation took place immediately. The mould was then transferred to an oven at ca. 40°C for a period of 7 days. The samples were obtained after aging for 3 weeks at ca. 80°C. This last treatment is crucial to form mechanically stable films and to precipitate the ferrihydrite nanoparticles.

The studies presented in the first part of this chapter were performed on two groups of samples, labeled I and II. In both groups the matrix is the d-U(2000) di-ureasil. Each group is composed of samples with different iron concentrations, up to $\sim 6\%$ in weight, prepared under similar conditions (see Tab. 3.1). The designation of the samples include their matrix, their iron content, and their group. Although both groups were prepared following the same procedure, some differences became apparent during their characterization. In Sec. 3.5 we will present the synthesis of other groups of samples. The iron content of group II samples was determined by Inductively Coupled Plasma (ICP) spectrometry in LCA, Universidade de Aveiro, while in the other samples was determined by Atomic absorption spectrometry (AAS) in Departamento de Química da Universidade de Trás-os-Montes e Alto Douro.

3.3 Structural properties

3.3.1 XRD and SAXS

X-ray diffraction (XRD) measurements were performed at RT with a Philips X'Pert - MPD diffractometer using monochromated CuK_α radiation (λ = 1.541 Å) in the 1.5 - 70° 2θ range at 0.05° resolution, and 35 s acquisition per step.

The powder XRD patterns of U2Fe group I nanohybrids (Fig. 3.1) show the existence of 6- line ferrihydrite particles [49] (see Fig. 1.5 page 18). The XRD patterns have also a broad peak located at 2θ=21° associated to order within the siliceous domains [34] (not shown). The patterns of the nanohybrids with lower iron concentration ($< 2\%$) show also a set of peaks (the most intense at ca. 19.2° and 23.4°) associated to crystalline poly(oxyethylene)

(POE) chains (not shown). Despite the fact that some of these peaks are superposed to those of ferrihydrite, it is possible to infer the presence of ferrihydrite by the presence of a broad peak at ca. 62°. Further confirmation of the existence of ferrihydrite is achieved performing a thermal treatment at 100-150°C, such that the poly(oxyethylene-co-oxypropylene) chains become amorphous. In fact, after this treatment the ferrihydrite peaks (indicated with '$\star$' at ca. 36° and 62°) become visible.

The powder XRD patterns of the two most concentrated samples of group II have some differences relatively to those of group I. In particular, in group II, the relative intensity of the double peak at 60-65° is the opposite than that of group I and expected for ferrihydrite. At the same time, the shoulder appearing at 33° in samples of group I (see arrows in Fig. 1.5) is not present in samples of group II. Therefore, while the XRD patterns of the most concentrated samples of group I have the characteristic features of ferrihydrite, those of group II have characteristic features of an iron oxyhydroxynitrate phase, precursor of 6-line ferrihydrite (see Fig. 1.5 page 18). We anticipate that these differences are not so marked as those found in other iron oxyhydroxynitrate phases presented in Sec. 3.5 and 5.2.

There are several methods to determine the characteristic size of the entities which are diffracting (crystallites) based on characteristics of the peaks, as the width and the integral breadth. The latter was defined by Wilson as an "integral breadth apparent size" [192]:

$$L = \frac{\lambda K I}{A \cos\theta} \tag{3.1}$$

where L is the coherence length over which the crystalline order extends, I is the peak intensity and A its area. K is a constant which depends on the particle morphology and

Table 3.1: Particles size of the d-U(2000)/ferrihydrite nanohybrids. The XRD values correspond to the coherence length L determined using Eq. 3.1 on the peak at 2θ=36°. The SAXS values correspond to the double of the gyration radius, obtained by fitting SAXS curves to Eq. 3.2 [191]. The particles density, N_p, was estimated based on TEM (sample U2Fe2.1(I)), SAXS (other samples of group I), and XRD (group II samples), as described in Sec.3.3.2.

name	%Fe (w/w)	particles diameter (nm)			particles density, N_p
		XRD	SAXS	TEM	(10^{17}particles/cm^3)
group I					
U2Fe1.2(I)	1.2	~ 2	4		1
U2Fe2.1(I)	2.1	2	-	4.7	0.8
U2Fe3.9(I)	3.9	3	6		0.9
U2Fe5.8(I)	5.8	5	7		0.8
group II					
U2Fe1.7(II)	1.7	~ 2	-		2×10
U2Fe3.8(II)	3.8	3	-		1×10
U2Fe6.5(II)	6.5	4	-		1×10

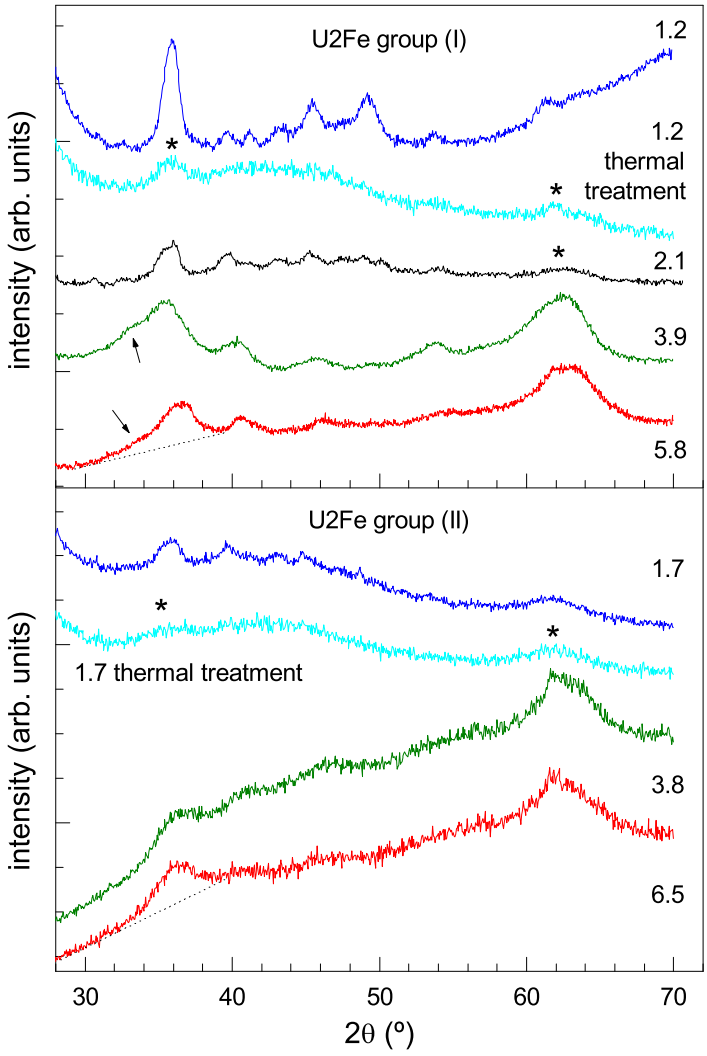

Figure 3.1: X-ray diffraction (XRD) patterns of U2Fe group I (above) and group II (below) samples. The XRD patterns obtained after a thermal treatment to the lower concentrated samples are also shown. In these patterns, the ferrihydrite features are signed with ($\star$).

varies from 0.89 to 1.39 rad. We used $K = 1$, which corresponds to an average volume of the apparent size L independently of the particular morphology. The peaks of the samples with lower iron content are too broad and the application of Eq. 3.1 gives just a crude estimation of L. However, it is possible to observe that L increases with the iron content in both sets of samples (Tab. 3.1).

Small angle X-ray scattering (SAXS) is a valuable technique to estimate the size of nanoparticles dispersed in solution or in a solid matrix (see, as examples, Ref. [116] and [193], respectively). SAXS is sensible to the low-resolution structure of the system, i. e. to the electron density fluctuations in the nanometer scale, regardless the details of the crystalline structure. SAXS measurements had been previously performed in some samples of group I

[191]. The results were modeled with a two electron density model: N isolated ferrihydrite nanoparticles with volume V and electron density ρ_p embedded in an homogeneous matrix with an electron density ρ_m. The size of nanoparticles was obtained after fitting SAXS data to the Beaucage model [194]. This model considers the scattered intensity as the sum of a Guinier law to a power law:

$$I(q) = G\exp\left(\frac{-q^2R_g^2}{3}\right) + B(q^*)^P \qquad q^* = \frac{q}{(erf(qR_g/6^{1/2}))^3} \tag{3.2}$$

where $G = N(\rho_p - \rho_m)^2V^2$ and $B = 2\pi(\rho_p - \rho_m)^2S$, S being the interface area between the particles and the matrix. P is an exponent that depends on the particles surface and equals 4 for smooth surfaces. R_g is a gyration radius, defined as $R_g = 1/V\int r^2dV$. For spherical particles the radius R is related to R_g as $R^2 = (5/3)R_g^2$. In the samples of group I, R_g increases with the iron concentration, in accordance with the XRD measurements (Tab. 3.1). This is also observed in other systems as, for example, maghemite nanoparticles grown in a polyvinylpyridine matrix [183]. The sizes determined by SAXS are systematically higher than those obtained by XRD, as one expects for poor crystallized particles, where coherence does not extends to the entire particle.

3.3.2 TEM and STEM/EDS studies

Detailed imaging studies were made on sample U2Fe2.1(I). The studies include TEM, high resolution TEM (HRTEM), and dispersion X-ray spectroscopy (EDS) in a scanning TEM (STEM). These measurements and analysis were performed by B. Rodríguez-González and Prof. L. M. Liz-Marzán of the Departmento de Quimica Fisica, Universidade de Vigo, Spain. Samples were prepared by grinding a small piece of the hybrid with a mortar, in the presence of n-butanol, then sonicating the resulting dispersion in a glass vial for 10 min, and finally depositing and drying a droplet with a pipette on a copper grid covered with a carbon-coated, holey formvar film. Microanalysis and imaging were performed on sample fragments located on holes, so that the electron beam is transmitted through the sample only. Images were obtained using a JEOL JEM 2010 FEG transmission electron microscope, operating at an acceleration voltage of 200 kV, equipped with a slow scan digital camera, a STEM unit, and an Oxford Inca Energy 200 energy dispersive X-ray spectrometer. Image Fourier filtrations were obtained from HRTEM images by windowing the Fourier transform (FT). STEM images were recorded using a bright field detector, while for elemental mapping the STEM unit was coupled to the microanalysis system. Image analysis was carried out with Digital Micrograph software by Gatan. The analysis of the particles size was performed

using the free UTHSCSA ImageTool program[1]. The discussion here presented is reported for ferrihydrite powders [195].

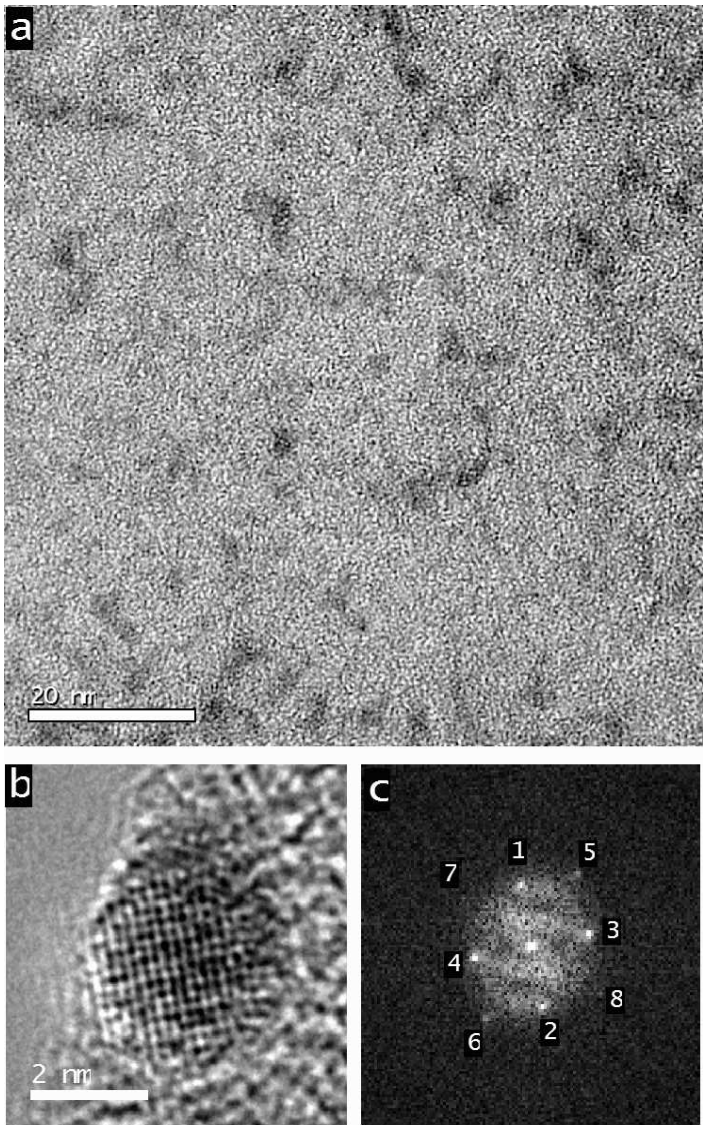

Figure 3.2: a. Bright field TEM image of ferrihydrite nanoparticles within a hybrid ureasil matrix; b. high resolution image of a particle located at the edge of the sample; c. Fourier transform of the area shown in b. The obtained spots are labelled and the data displayed in Tab. 3.2.

In Fig. 3.2a., a representative TEM bright field image of the U2Fe2.1(I) sample is shown[2], in which particles with various sizes within an amorphous matrix can be distinguished. TEM images from various regions within the samples almost invariably show isolated nanoparticles

[1]developed at the University of Texas Health Science Center at San Antonio, Texas and available from the Internet by anonymous FTP from ftp://maxrad6.uthscsa.edu

[2]other pictures can be found in appendix B

and no signs of coalescence. Since the particles are small and the particles/matrix contrast is rather low, the edges of the particles cannot be clearly discerned. However we do get sufficient contrast to confirm the presence of nanosized particles. In Fig. 3.3a., for instance, the particle edges are better defined, probably because the thickness of the film is lower than that in Fig. 3.2a.. A particles size histogram was obtained analyzing 208 particles, which are in the 1 to 15 nm range. Lognormal distribution function is often used to describe particle size distributions, particularly in the case of non symmetric distributions showing an important fraction of sizes much higher than the average [196, 197]. The size distribution of sample can be described by a lognormal function, with a diameter of 4.7±0.2 nm and deviation $s = 0.43 \pm 0.05$ (Fig. 3.3b.). This diameter is larger than that estimated from the analysis of the XRD peaks, as expected for low crystalline systems, where coherence does not extends throughout the whole particle. The obtained particle sizes and morphology (particles with non-facetted and rather fuzzy edges) are of the same order of magnitude of those previously reported in Ref. [45].

Considering the iron content ($2.1\%\mathrm{w}_{Fe}/\mathrm{w}_{sample}$), the matrix and ferrihydrite densities (respectively 1.2 and 3.96 g/cm^3 [42]), the mean ratio between the mass of ferrihydrite and the mass of iron ($\mathrm{M}_{ferrihydrite}/\mathrm{M}_{iron}$=1.75, according to the empirical formulas of ferrihydrite given in Tab. 1.1, page 15), and the mean particles volume derived with TEM, it is possible to estimate the particles density (number of particles per sample volume), N_p:

$$N_p = \frac{V_{all\,particles}}{V_{one\,particle}} = \frac{(M_{ferrihydrite}/M_{sample})\rho_{sample}}{\rho_{ferrihydrite}V_{one\,particle}} \tag{3.3}$$

In sample U2Fe2.1(I), N_p is of the order of $0.8\pm0.3\times10^{17}$ particles/cm^3. Thus, the mean interparticle distance is about 20-30 nm, in agreement with the observed the TEM images. Similar calculations can be performed for the other samples considering the size determined by SAXS (other samples of group I) or the size determined by XRD (see values in Tab. 3.1). It is possible to observe that, within each group N_p is fairly constant. This is characteristic of heterogeneous nucleation, where the number of particles is mainly dependent on the number of nucleation points rather than the iron concentration. Thus, we conclude that the existence of more iron ions in the system results in larger particles and not in an higher density of particles. The differences between the values of N_p of samples of group I and II may be attributed to the underestimation of the size obtained from the XRD patterns.

Another parameter of interest that can be estimated is the total number of Fe ions in a particle with the average size. According to the model of Drits *et al.*, [49, 50], ferrihydrite is constituted by defective and defective-free structures with unit cell volumes of 3.54×10^{-2} and 7.08×10^{-2} nm^3, respectively [50]. In this model, the number of Fe ions per unit cell of the defective and defective-free structures is 0.96 and 1.56, respectively, and the volume ratio of the structures is typically about 1:1 [50]. Therefore, the number of Fe ions in a spherical

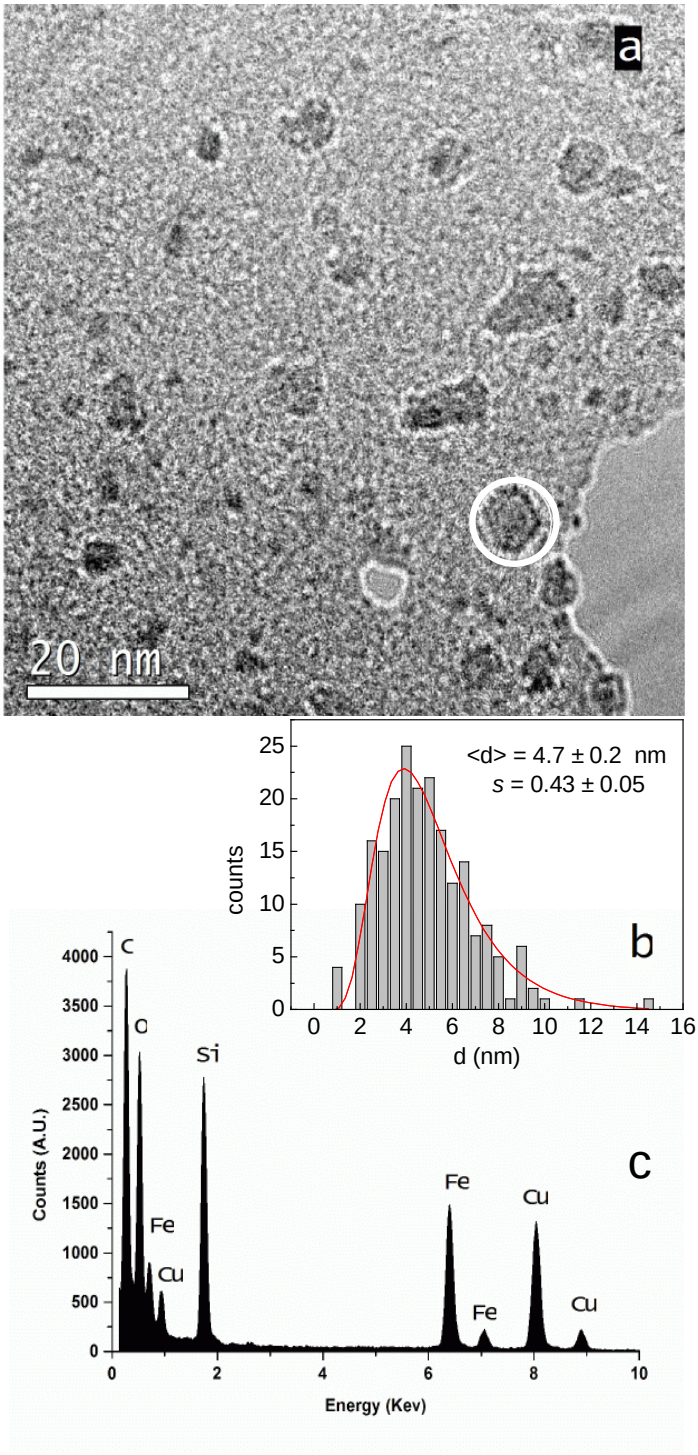

Figure 3.3: a. Bright field TEM image of ferrihydrite nanoparticles within sample U2Fe2.1(I); b. particles size histogram and lognormal distribution fit; c. microanalysis measured in the area within the circle drawn in a.

particle with an average diameter of 4.7 nm, N_t, is about 1300. Particles with full defective and defective-free structures would have $N_t \approx 1200$ and 1500 ions, respectively. Considering other models for ferrihydrite structure, namely the Eggleton and Fitzpatrick [46] and the Towe and Bradley models [39], one obtains similar N_t values. Thus, in further analysis of sample U2Fe2.1(I) we will consider $N_t = 1300 \pm 200$ ions.

The high resolution image in Fig. 3.2b. was taken on a particle located right on the edge of the sample, so that the sample is thin enough to acquire a lattice image of the particle. In this image, we can see that the particle is crystalline, with a diameter of ca. 4 nm and surrounded by the amorphous hybrid matrix. The corresponding Fourier transform is shown in Fig. 3.2c., with up to 8 high intensity spots, from which the corresponding interplane distances were calculated. The experimental values are displayed in Tab. 3.2 and compared to the closer d_{hkl} from both 6-line and 2-line ferrihydrite. From this comparison, we conclude that this particle is a 6-line ferrihydrite, since it presents a d_{hkl} of 0.20 nm, which is only possible in such a ferrihydrite. In fact, 6-line ferrihydrite usually appears after a synthesis procedure similar to that used here, i. e. thermal treatment of an iron nitrate solution at low pH, while 2-line ferrihydrite is often the product of the basic treatment of an iron nitrate solution [44].

Table 3.2: d_{hkl} values obtained after Fourier transform of Figure 3.2(b) and typical d_{hkl} values of 2-line and 6-line ferrihydrite.

spot	Fig. 3.2(b) d_{hkl} (nm)	6l Fh d_{hkl} (nm)	2l Fh d_{hkl} (nm)
1 & 2	0.20	0.20	-
3 & 4	0.19	0.20	-
5 to 7	0.14	0.15	0.15
8	0.13	0.15	0.15

The elemental distribution within the matrix and the nanoparticles was obtained by means of EDS. In Fig. 3.3c. we show the EDS spectrum measured from the area within the circle drawn in Fig. 3.3a., comprising almost exclusively a single particle with a diameter of 10 nm. The spectrum confirms the presence of iron in the particle, as well as carbon and silicon, which were expected for the matrix. The peak of oxygen, which is expected to appear in the particle and in the matrix is also present. As usual, copper peaks are also measured from the supporting grid. Since EDS provides information from the whole area, we decided to use a higher resolution analytical technique to confirm that iron is located in the particles, not in the matrix.

We used the compositional image technique through EDS in STEM. An example of the results is displayed in Fig. 3.4 and more examples can be found in appendix B. The figure includes a STEM image of several particles generated with the bright field detector (Fig.

3.4a.), and an elemental distribution mapping of Fe, generated from the Fe K_α emission line (Fig. 3.4b.), for the same area of the STEM image. In the STEM image we can see in dark contrast the particles and with brighter contrast the matrix itself. In this image we see small particles as well as larger particles, which can arise from superposition of particles at various heights, with a range between 2 nm and 10 nm. Again, the particles are not perfectly discerned because of the matrix around them. As shown in Fig. 3.4, the detection maxima within the mapping of Fe coincide with the darker areas within the STEM image, which are expected to correspond to ferrihydrite particles. The quality of the mapping is hindered by the exposure time, which is in turn limited by the image drift induced by the electron beam, but even with this limitation we see a good agreement. The Fe signal is only observed in the areas with particles, within the resolution of the technique.

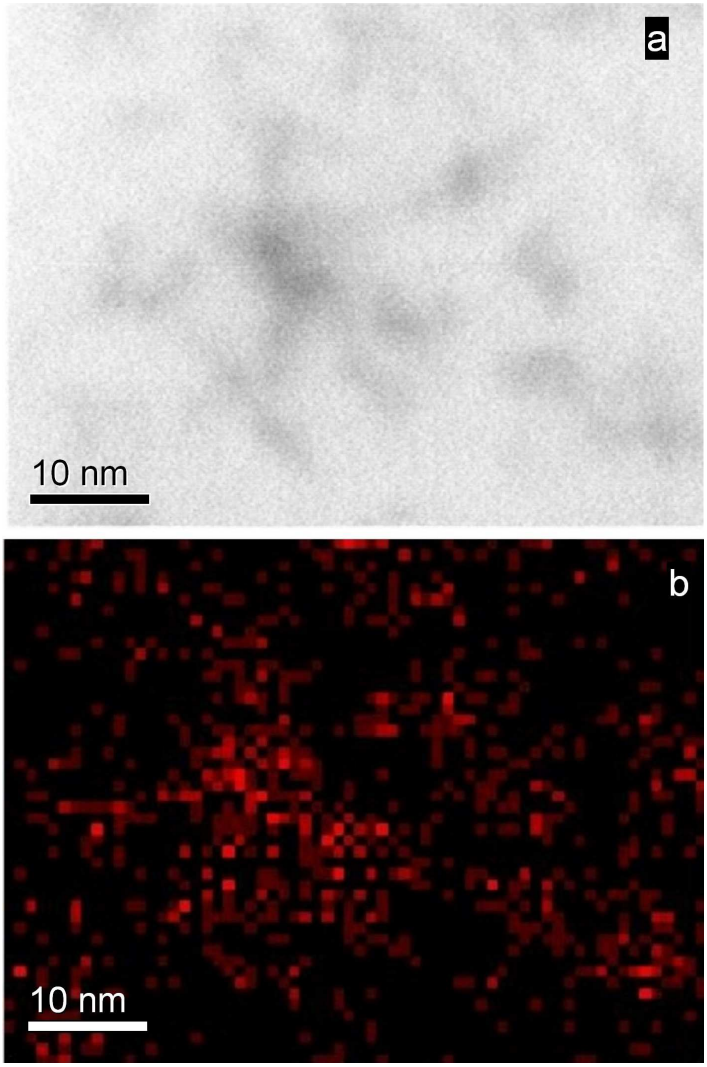

Figure 3.4: a. STEM image obtained with a bright field detector; b. elemental distribution mapping of Fe obtained using the K_α iron line.

3.3.3 FT-IR spectroscopy

Mid-infrared spectra were acquired at RT using a Bruker 22 FT-IR spectrometer (model Vektor) placed inside a glove-box with dry argon gas atmosphere. The spectra were collected over the range 4000-370 cm^{-1} by averaging at least 150 scans at cm^{-1} spectral resolution. The compounds (ca. 2 mg) were finely ground, mixed with approximately 175 mg of dried potassium bromide (Merck, spectroscopic grade) and pressed into pellets. To prevent the presence of water in the samples, the discs were dried at 90 °C under vacuum (10^{-1} mbar) for several days in the Buchi oven placed inside the same glovebox. The measurements and discussion reported in this section were performed by Denis Ostrovskii, from the Department of Experimental Physics, Chalmers University of Technology, Göteborg, Sweden, and Sílvia C. Nunes and Prof. Verónica de Zea Bermudez, Departamento de Química da Trás-os-Montes e Alto Douro, Vila Real, Portugal. The results described in this section are reported in Ref. [73].

The FT-IR analysis focus on two regions: the amide region (1850-1570 cm^{-1}) that probes the organic-inorganic cross-link of the matrix and a region that probes the COC groups of the polymer chain (1200-1040) cm^{-1}. Measurements were performed in group I samples. The interaction of the particles with the polyether chains may be probed by FT-IR in the skeleton COC stretching (Fig. 3.5b). The FT-IR spectrum of the d-U(2000) matrix exhibits a broad band centered at ca. 1110 cm^{-1} and a shoulder at ca. 1148 cm^{-1} (Fig. 3.5b). These are ascribed to COC stretching (νCOC) mode and to the coupled vibration of the νCOC and CH_2 rocking modes, respectively [25]. Since the intensity and frequency of both features remains practically unchanged in the presence of ferrihydrite nanoparticles, we conclude that the Fe^{3+} ions of the particles do not coordinate to the ether oxygen atoms of the POE chains over the whole range of iron concentration.

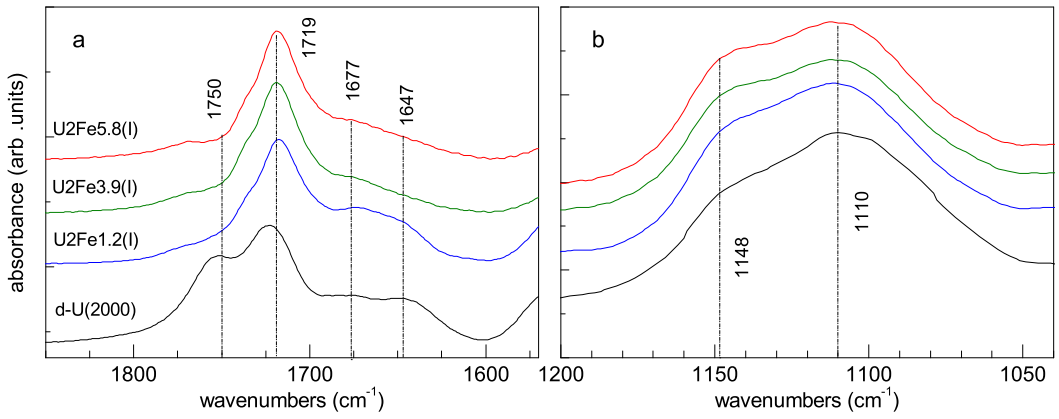

Figure 3.5: a. FT-IR spectra of the "amide I" envelope for d-U(2000) matrix and U2Fe(II) samples; b. FT-IR spectra in the νCOC region of the same samples. Frequencies are indicated for the spectrum of the most concentrated hybrid.

The "amide I" region of the FT-IR spectra of the di-ureasil with ferrihydrite nanoparticles provides insight into the role played by the urea crosslinks in the particles/matrix interaction. The "amide I" mode is a complex vibration that receives a major contribution from the νC=O vibration [198]. The "amide I" envelope is hydrogen bonding sensitive and may be resolved into several components which correspond to different environments of C=O groups. The components are known as hydrogen-bonded associations, aggregates or structures [198, 199]. Figure 3.5a shows that the profiles of the "amide I" envelope of the di-ureasil with ferrihydrite nanoparticles are dramatically different from that of the non-doped di-ureasil matrix [25], and essentially independent of the Fe^{3+} concentration. Upon introduction of the iron nitrate salt and subsequent growth of the ferrihydrite particles, a drastic decrease of the intensity of the component associated with "free" urea cross-links (ca. 1750 cm^{-1}) occurs. At the same time, it is observed the increase of the intensity of the components produced by hydrogen-bonded POE/urea structures of low degree of disorder [25] (ca. 1719 cm^{-1}). In contrast, the total spectral intensity of the features due to ordered POE/urea structures and self-assembled urea-urea aggregates [25] (ca. 1677 and 1647 cm^{-1}, respectively) seems to be almost unaffected by the presence of iron (Fig. 3.5b).

Two relevant facts arise from this analysis: i) the non-bonded urea carbonyl oxygen atoms available in the non-doped matrix are now interacting in the particles/matrix nanocomposites, and ii) these interactions do not depend on the iron content. These results indicate that a significant fraction of urea carbonyl oxygen atoms existent in the matrix are interacting with the Fe^{3+} ions at the surface of the ferrihydrite nanoparticles. This means that the non-coordinated POE chains are massively requested to form hydrogen bonds of different strength with the N-H groups of the cross-links as a result of the formation of the ferrihydrite nanoparticles. The fact that the features are independent of the iron concentration is consistent with the growth of the nanoparticles exclusively at the organic/inorganic interface. This means heterogeneous nucleation: N_p does not depend critically on the iron concentration but on the number of nucleation points, which is primarily related to the number of urea carbonyl oxygen atoms available. This is in accordance to SAXS and XRD results, where N_p was found constant (see Tab. 3.1).

3.3.4 NMR spectroscopy

The ^{29}Si magic-angle spinning (MAS) and ^{13}C cross-polarization (CP) MAS NMR spectra were recorded on a Bruker Avance 400 (94 kOe) spectrometer at 79.49 and 100.62 MHz, respectively. ^{29}Si MAS NMR spectra were recorded with 2 μs (equivalent to 30°) rf pulses and a recycle delay of 2 s and 5 kHz spinning rate. ^{13}C CP/MAS NMR spectra were recorded with a 4 μs 1H 90° pulse, 2 ms contact time, a recycle delay of 4 s, and a spinning rate of 6-7 kHz. Chemical shifts are quoted in ppm from tetrametilsilano. These measurements were performed in Departamento de Química da Universidade de Aveiro and analyzed in

collaboration with Prof. J. Rocha. Here we analyze samples from group II. The results were presented in Ref. [73].

The ^{13}C CP/MAS NMR spectrum of the non-doped d-U(2000) matrix is shown in Fig. 3.6a. The three peaks centered at about 10, 24, and 43 ppm are attributed to the three carbon atoms of the -N$(CH_2)_3$Si- groups (see Fig. 1.2, page 14). The peaks observed near 18 and 70 ppm are ascribed to the few terminal propyl CH_3 groups and to the middle oxyethylene CH_2 groups of the organic chains, respectively (see Fig. 1.2, page 14). At last, the resonance at ca. 159 ppm is assigned to the carbon atom of the C=O group of the urea linkage. The growth of ferrihydrite nanoparticles in the di-ureasil host results in a considerable broadening of all NMR resonances Fig. 3.6a. For example, the full-width-at-half- maximum (FWHM) of the strongest peak, at ca. 70.5 ppm, increases fourfold from ca. 50 to 200 Hz. This is due to the through-space interaction between the magnetic ferrihydrite particles and the ^{13}C NMR nuclei. Thus, some polymeric chains are in close spatial proximity of the nanoparticles. Another important observation is that the signal-to-noise ratio of the spectra decreases considerably as the iron concentration increases from 0 to 6.5 %. This occurs despite the fact that the number of accumulated transients was doubled, and suggests that NMR detects only a fraction of the total ^{13}C present. As a matter of fact, the resonances given by polymeric chains very close to the ferrihydrite nanoparticles are probably broadened beyond detection. Interestingly, the resonance of the carbonyl group of the urea bridges is absent from the spectra of all iron-doped materials. However, it is not clear whether this is due to the coordination of carbonyl groups to iron atoms at the nanoparticles surface or, simply, because the carbonyl resonance broadens considerably upon doping and is buried in the baseline noise.

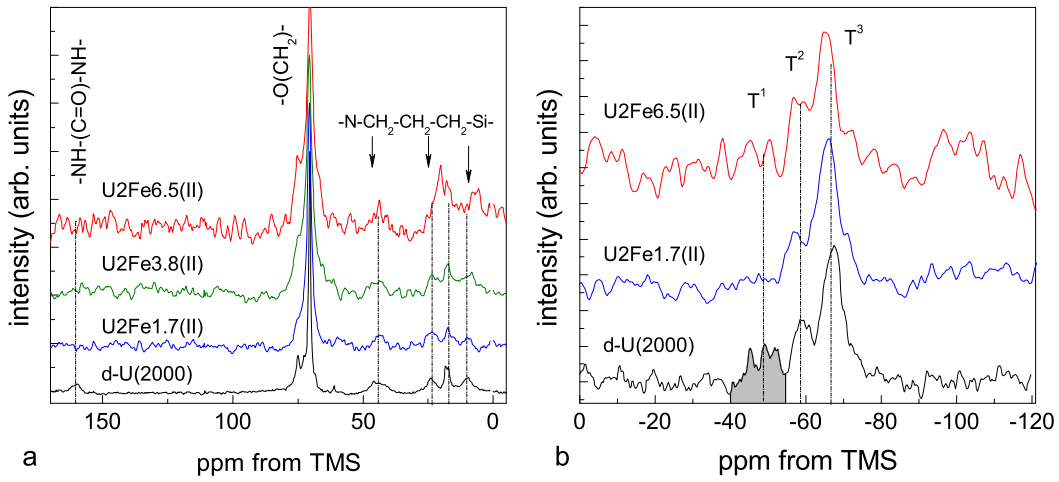

Figure 3.6: a. ^{13}C CP/MAS NMR spectra (MAS 6-7 kHz) of the d-U(2000) and U2Fe(II) samples; b. ^{2}9Si MAS spectra (MAS 5 kHz) of d-U(2000) and some of group II samples.

The ^{29}Si MAS NMR spectra of the undoped d-U(2000) di-ureasil material is shown in

Fig. 3.6b. The spectra display three relatively sharp peaks in the −40 to −55 ppm region, attributed to $RSi(O)(OH)_2$ (T^1) terminal groups. The resonances at ca. –59 and –68 ppm are assigned to $RSi(O)_2(OH)$ (T^2) and R-$Si(O)_3$ (T^3) sites of the siliceous domains, respectively. Upon the growth of the nanoparticles the T^1 signals seem to disappear from the spectra. This is not entirely clear because the signal-to-noise ratio of the spectra is poor. This is to be expected if the terminal silicon environments are in close spatial proximity of the magnetic ferrihydrite nanoparticles. In addition, the signal-to-noise ratio of the spectra decreases considerably as the iron concentration increase, as observed in ^{13}C NMR. Again, this happens despite the fact that the number of accumulated transients was doubled and indicates that NMR detects only a fraction of the total ^{29}Si present.

3.4 Magnetic properties

Samples ac and dc susceptibility and magnetization were measured with a Quantum Design superconducting quantum interference device (SQUID) magnetometer model MPMS2, Quantum Design Inc. Measurements were performed at IFIMUP-Universidade do Porto, ICMA-Universidad de Zaragoza, and Institute For Rock Magnetism (IRM)-University of Minnesota. Susceptibility measurements were performed on heating from 4 up to 300 K in zero-field-cooled (zfc) and field-cooled (fc) procedures under a magnetic field H= 50 Oe. Mössbauer spectroscopy was measured at selected temperatures between 4.2 K and 60 K. A conventional constant-acceleration spectrometer was used in transmission geometry with a ^{57}Co/Rh source, using a α-Fe foil at room temperature to calibrate isomer shifts and velocity scale. An external magnetic field up to 55 kOe was applied perpendicular to the direction of the γ-ray using a superconducting coil. Mössbauer measurements and analysis were performed by T. Brequó of the IRM-University of Minnesota.

3.4.1 Dc susceptibiliy

The temperature dependence of the dc susceptibility χ shows the existence of superparamagnetic particles (Fig. 3.7), accordingly to the following features. The susceptibility curves of the matrix/nanoparticles composite present irreversibility below a temperature T_F and a decrease of χ with temperature above T_F. All zfc curves except the one of the U2Fe1.2(I) sample present a maximum at $T = T_B$. This maximum increases with the iron content in all samples (Tab. 3.4). This increase agrees qualitatively with the observed size increase, since in a first approximation E_a and therefore T_B depend on size (Eqs. 2.2 and 2.6). T_F/T_B is lower in samples of group II and in the sample U2Fe2.1(I), indicating a narrower E_a distribution in these samples [137]. Using Eq. 2.38 (see Sec. 2.5.1, page 46) is possible to estimate the parameter s_{E_a} (related to the width of the distribution, considered lognormal[3]), which

[3]definition of lognormal distribution function can be found in Eq. 3.9, page 101

varies from 0.5 to 1.2. The zfc curves of samples of group II do not show a low temperature paramagnetic 'tail', as seen in samples U2Fe3.9(I) and U2Fe5.8(II). This suggests that samples of group I contain some paramagnetic free Fe ions, unlike those of group II.

Table 3.3: Blocking temperature T_B, irreversibility temperature T_F, and lognormal distribution parameter s_{E_a} obtained using Eq. 2.38 (See Sec. 2.5.1, page 46).

sample	T_B (K)	T_F (K)	s_{E_a}
U2Fe1.2(I)	< 5	25 $\pm$1	> 1.2
U2Fe2.1(I)	7.9 $\pm$0.3	15 $\pm$1	0.7
U2Fe3.9(I)	10.6 $\pm$0.5	33 $\pm$1	1
U2Fe5.8(I)	12 $\pm$1	50 $\pm$2	1.1
U2Fe1.7(II)	4.0 $\pm$0.5	9.5 $\pm$0.5	0.8
U2Fe3.8(II)	7.6 $\pm$0.2	14 $\pm$1	0.7
U2Fe6.5(II)	19.6 $\pm$0.5	29 $\pm$1	0.5

In a first approach, the susceptibility above the irreversibility was fitted to a Curie-Weiss law (Eq. 2.46) and allowing the existence of a χ_0 temperature independent term:

$$\chi(T) = \frac{C}{T - T_0} + \chi_0 \tag{3.4}$$

which accounts for diamagnetic (negative) contribution from the matrix χ_{matrix} and the sample holder, and a temperature independent antiferromagnetic positive contribution. The diamagnetic susceptibility of the di-ureasil matrix is $\chi_{matrix} = -2 \times 10^{-7}$ emu/g, almost independent of the temperature [200]. T_0 accounts for particle interactions as discussed in Sec. 2.5.2. The Curie constant C is related to the particles uncompensated moment μ_{un}, such that $C = N_p\langle\mu_{un}^2\rangle/3k_B$. Susceptibility data was fitted for $T > T_F$, with T_F being determined by ac susceptibility. The fitted parameters are displayed in Tab. 3.4. In group II samples, C (per sample mass) increases with the iron content. Since N_p was found reasonably constant, μ_{un} increases with the iron content, i. e., with the particle size. On the contrary, the dependence of C with the iron content in the group I samples is not monotonous. Again, since N_p is constant, μ_{un} and C follow the same trend. In the case of sample U2Fe5.8(I), although the average size of the particles is higher than that of sample U2Fe3.9(I), the number of uncompensated iron ions per particle is lower. Considering the values found for C and N_p and in the approximation $\mu_{un} \approx \sqrt{\langle\mu_{un}^2\rangle}$ it is possible to estimate μ_{un} for group I samples, and observe that it increases with the iron content in the first 3 samples (Fig. 3.8). Since for group II samples we just have a crude estimation of N_p we do not present and estimation of μ_{un}. The χ_0 term is zero in the lowest concentrated samples, positive in sample U2Fe5.8(I) and negative in the remaining samples. The positive value found in sample U2Fe5.8(I) indicates an important fraction of antiferromagnetically compensated ions,

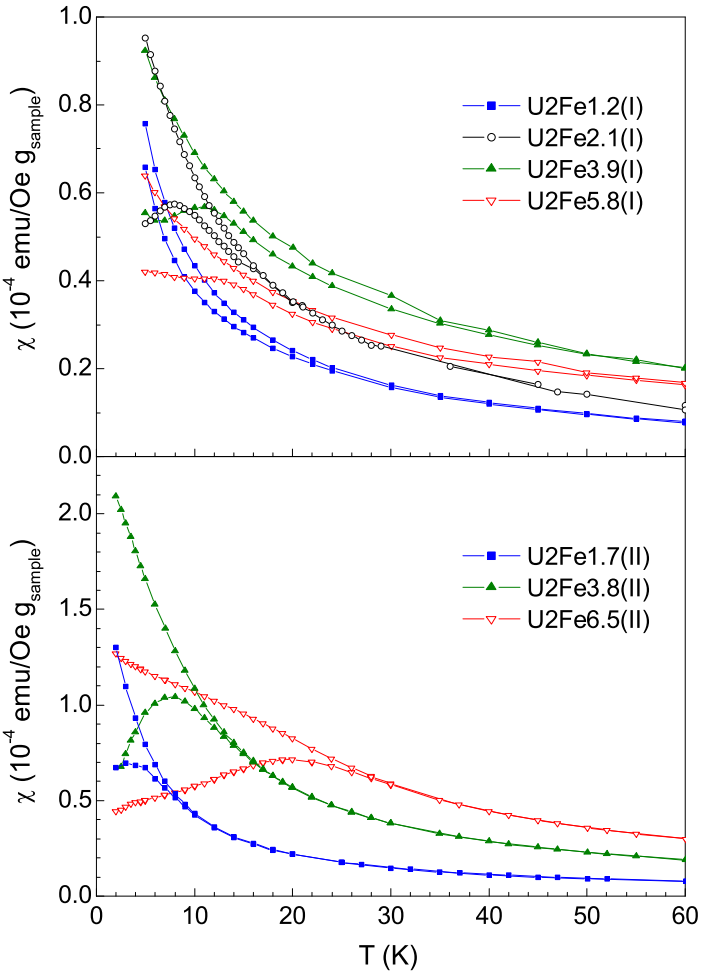

Figure 3.7: Dc susceptibility as a function of temperature, $\chi(T)$, of group I and group II samples (above and below, respectively). Lines are eye guides.

as concluded from the analysis of C. The negative values found for group II samples will be discussed later.

The increase of $|T_0|$ with the iron concentration in group II samples is the first indication of an increase of dipolar interactions with the iron content. The signal of T_0 (negative, so that the susceptibility curve extrapolates to positive temperatures) is in accordance with Monte Carlo simulations performed by Chantrell et al. [117] and disagrees with the El-Hilo et al. model [146], as described in Sec. 2.5.2. This disagreement is due the fact that in Ref. [146] the determination of T_0 is based on the analysis of $1/\chi$ plots, disregarding the existence of a diamagnetic χ_0 term. This term yields a curvature that can be misinterpreted as a temperature dependent T_0. The positive T_0 values found for the two less concentrated samples of group I are actually close to zero and a departure from this value may be due to experimental errors.

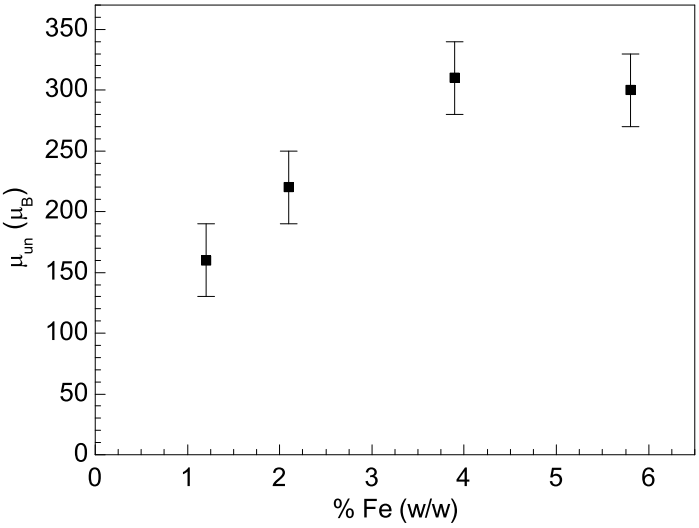

Figure 3.8: Estimation of μ_{un} for group I samples, based on C obtained from fit to Eq. 3.4.

The Curie-Weiss law was used under the presuppose that C is constant with temperature. This is true for $T \ll T_N$, which is not exactly the case here since $T_N \sim 300 - 500$ K. In fact, C must decrease down to the characteristic value of the paramagnetic iron ions as one crosses the order temperature T_N. When $T_0 = \chi_0 = 0$, the dependence $C(T)$ is directly observed

Table 3.4: Parameters resulting from fitting dc susceptibility data of group I and II samples to Eq. 3.4

sample		Eq.3.4 fit	
	C (10^{-4}emu K/Oe g_{sample})	T_0 (K)	χ_0 (10^{-7}emu/Oe g_{sample})
U2Fe1.2(I)	4.7 ±0.1	1.7 ±0.5	0.4 ±0.4
U2Fe2.1(I)	6.6 ±0.5	4 ±3	-6 ±3
U2Fe3.9(I)	13.8 ±0.7	-7 ±2	-7 ±3
U2Fe5.8(I)	11 ±1	-9 ±5	14 ±4
U2Fe1.7(II)	4.50 ±0.05	-0.6±0.1	0.2 ±0.4
U2Fe3.8(II)	12.2 ±0.1	-1.2±0.1	-8.2 ±0.5
U2Fe6.5(II)	18.9 ±0.1	-2.0±0.1	-7.1 ±0.5

sample	α		Eq.3.4/3.5 fit	
	(10^{-6}K^{-2})	C (10^{-4}emu K/Oe g_{sample})	T_0 (K)	χ_0 (10^{-7}emu/Oe g_{sample})
U2Fe1.7(II)	5±1	4.36 ±0.08	-0.3±0.2	8 ±2
U2Fe3.8(II)	1.7 ±0.2	11.7 ±0.1	-0.6±0.1	0.01 ±0.9
U2Fe6.5(II)	0.7 ±0.2	18.3 ±0.1	-1	0.5 ±0.4

in a χT plot, which is not the present case. Therefore, in a second approach we have fitted susceptibility data to Eq. (3.4), considering $C(T) = N_p\mu_{un}^2(T)/3k_B$, with $\mu_{un}(T)$ given by the magnons law:

$$\mu(T) = \mu(0)\left(1 - \alpha T^2\right) \tag{3.5}$$

This describes the dependence of the sublattices moment of bulk antiferromagnets and was also successfully applied to describe the dependence of the uncompensated moment of ferritin nanoparticles [174, 201], as shown in Sec. 4.3.3. Considering the $C(T)$ dependence improves the fit quality, in particular in the case of samples U2Fe1.7(II), U2Fe3.8(II). This is observed in the decrease of χ^2 (almost one order of magnitude), in the decrease of the residues amplitude, and in the increase of randomness (Fig. 3.9 c., d. and e.), and can be qualitatively seen in the χT plot shown in Fig. 3.9 a. In the case of sample U2Fe6.5(II), the relevance of including the $C(T)$ dependence is not obvious, since T_B is higher and thus the fit range is smaller. The susceptibility data of group I samples is too noisy to apply this second approach. In general, it is expected that the addition of fit parameters may lead to a fit improvement with no physical meaning, which is not the present case, as follows. We have compared fits with the same number of parameters: the one with the Curie-Weiss law and another considering $C(T)$ and disregarding the existence of T_0. For samples U2Fe1.7(II) and U2Fe3.8(II), the inclusion of the $C(T)$ dependence is more relevant to the fit quality than the inclusion of T_0.

The α values obtained by the fit (Tab. 3.4) lead to an extrapolated Néel temperature, T_N of 450±50 K, 770±50 K and 1150±70 K, for U2Fe1.7(II), U2Fe3.8(II) and U2Fe6.5(II) samples, respectively (from the condition $\alpha T_N^2 = 1$). These values are of the order of the one expected for ferrihydrite and, in particular, the first value is in qualitative agreement with the one found for ferrihydrite powders: 330±20 K [50]. A more accurate estimation of T_N and the determination of a possible dependence of T_N with size will depend on susceptibility measurements up to higher temperatures. At the same time χ_0 is positive, unlike that found after fitting with the Curie-Weiss law (Eq. 3.4). This is consistent with the expected for antiferromagnetic systems and reveals that the χ_{AF} contribution is higher than the diamagnetic terms, being of the order of 10^{-8} emu/g_{sample}. The fitted $|T_0|$ and C values are similar to those obtained in the first approach and their evolution with the iron content the same, so that the conclusions drawn above still hold: dipolar interactions increase with the iron content and so does μ_{un}.

Further refinement of the description of $\chi(T)$ of these systems would include the variation of χ_{AF} with the temperature, which constitutes a very small correction given the relative small temperature variation of χ_{AF} comparing to χ.

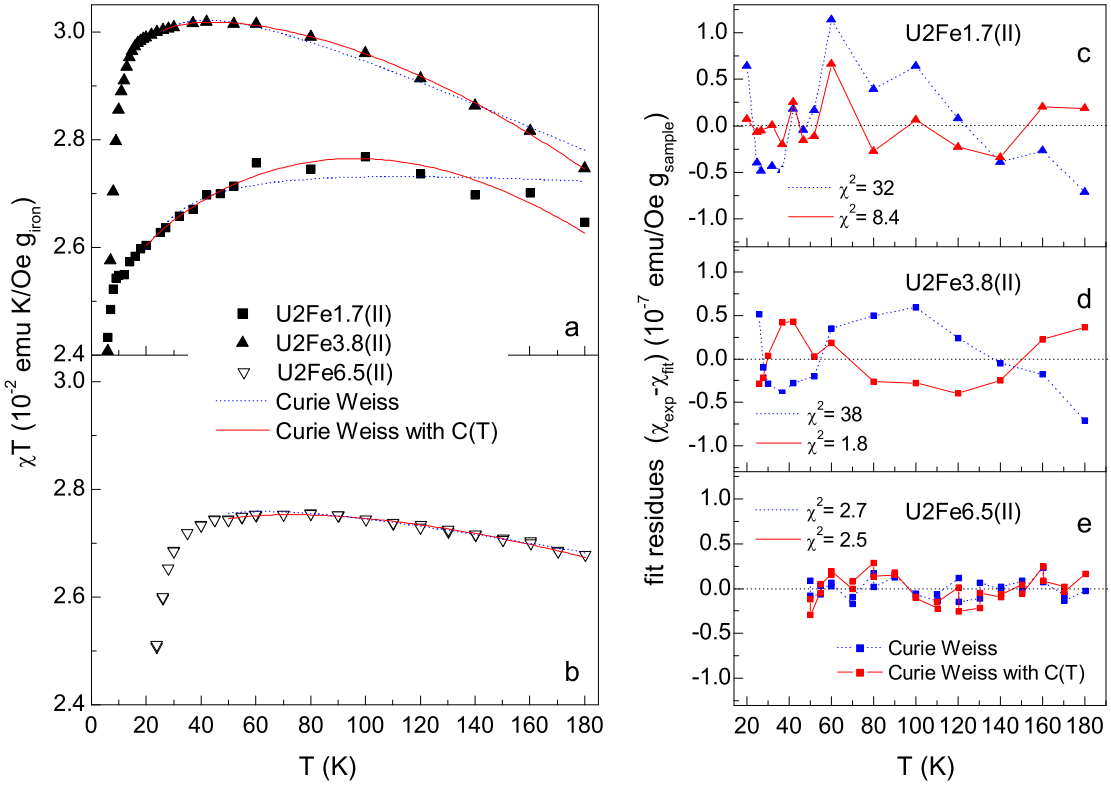

Figure 3.9: χT as a function of temperature for samples U2Fe1.7(II), U2Fe3.8(II) (panel a.) and sample U2Fe6.5(II) (panel b.); solid lines represent fits to the Curie-Weiss equation (Eq. 3.4) and Curie-Weiss considering the $C(T)$ dependence given by the magnons law (Eq. 3.5). Differences between experimental and fitted susceptibility (fit residues) for U2Fe1.7(II), U2Fe3.8(II) and U2Fe6.5(II) samples are plotted in panel c., d. and e., respectively.

3.4.2 Ac susceptibility

The in-phase χ' and out-of-phase χ'' components of the ac susceptibility of group II and group I samples are plotted in Fig. 3.10 as a function of temperature, for selected frequencies in the $f = 0.1 - 1500$ Hz range. Above $T = T_F$, χ' is independent of f and follows approximately a Curie law. That is, magnetic moments are able to cross the anisotropy energy barrier in the time scale of the experiments. For decreasing temperatures and below T_F, the particles that experience higher energy barriers become blocked. This leads to the onset of the out-of-phase susceptibility component, χ'', and to a decrease of χ' compared to that expected from Curie law. χ' exhibit a frequency-dependent maximum at a temperature T_B resulting from the balance between the decrease resulting from the blocking and the increase predicted by the Curie law. This dependence is approximately linear as expected from the Néel-Arrhenius relation Eq. (2.2) (see Fig. 3.16). A deeper analysis of the evolution of the maximum with the frequency is presented in section 3.4.5. χ' of sample U2Fe6.5(II) have maxima around $T = 25$ K and a shoulder around 8 K. These features correspond to two

maxima in the χ'' curve, indicating the existence of a bimodal energy barriers distribution. A closer look to the dc susceptibility curves of sample U2Fe6.5(II) also reveals such bimodal distribution. As found in the dc measurements, T_B increases with the iron content, as expected for systems whose particles size increases with iron content. Comparing the samples of group I and II with similar amount of iron, namely samples U2Fe3.8(II) and U2Fe3.9(I), one observes that the latter has higher T_B, which indicates that the average volume of the particles and/or the anisotropy constant are higher in sample U2Fe3.9(I).

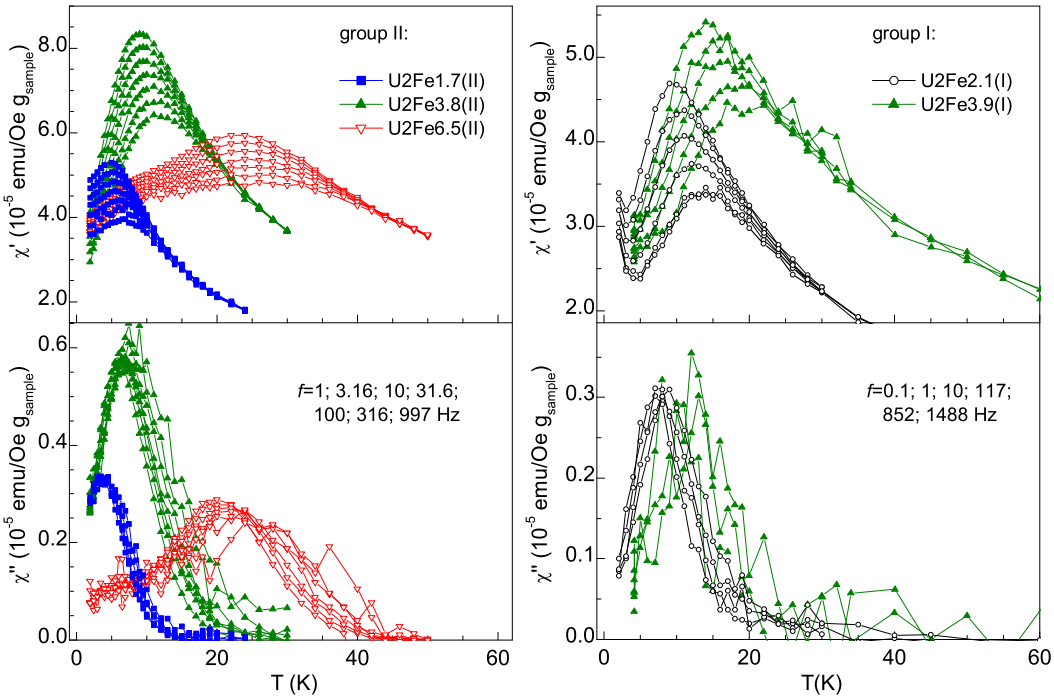

Figure 3.10: Ac susceptibility as a function of temperature of group II and group I samples at selected frequencies. Above: in-phase component $\chi'(T)$, and below: out-of-phase component $\chi''(T)$.

The out-of-phase curves obtained at different frequencies scales in a $\chi''(T, f)$ vs. $E = T * \ln(\tau_m/\tau_0)$ plot (with $\tau_m = 1/f$) (Fig. 3.11), as expected for systems where the particles contributing to χ'' at a given τ_m and T are those with energy E (see Sec. 2.5.1, page 47). Based on this plot one can determine the anisotropy energy distribution. These distributions are well described by a gamma distribution function, except in the case of sample U2Fe5.8(II) that shows a bi-modal distribution. A detailed analysis of these distributions and their comparison to size distributions is presented in Sec. 4.4.

3.4.3 Magnetic relaxation measurements $M(t, T)$

The time dependence of the magnetization was measured at different temperatures, using a TRM procedure (see Sec. 2.6, page 53). This procedure consists on cooling the samples from

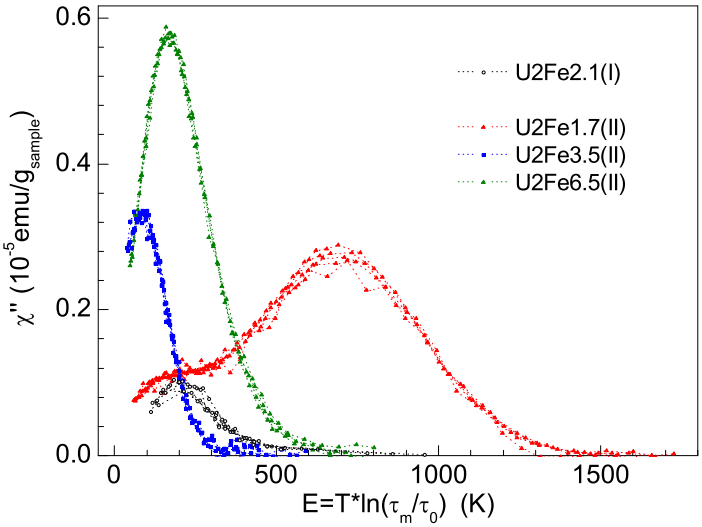

Figure 3.11: $\chi''(T, f)$ as a function of $E = T * \ln(\tau_m/\tau_0)$, with τ_0 determined by the linear extrapolation shown in Fig. 3.16.

$T > T_F$ down to the measuring temperature T at $H = 20$ kOe, decreasing the field to H =50 Oe, and measuring $M(t, T)$. Typically, t ranges from 60 to 8000 s. In the $M(t, T)$ curves of the measured samples (U2Fe2.1(I) and those of group II), the magnetization decreases according to a logarithmic approximation. As an example, $M(t, T)$ curves of sample U2Fe1.2(II) are plotted in logarithmic scale in Fig. 3.12a. The $M(t, T)$ curves were then fitted to:

$$M(t, T) = M_0 - S \ln(t + t_0) \tag{3.6}$$

where t_0 is the instant at which the field is switched off. In practice it takes about 200 s to change the field from 20 kOe to 50 Oe and the fitted t_0 lays in this time span. The obtained viscosities S values are plotted as a function of temperature in Fig. 3.12b, for the studied sample. S is close to zero at temperatures of the order of T_F and passes trough a maximum at a temperature around T_B. These maxima constitute blocking temperatures, which occur at temperatures lower than those seen in ac and dc measurements. This is expected in the framework of superparamagnetism, since in viscosity measurements particles 'have more time to relax' (i. e. the observation window is wider than that of the dc measurements) and so particles become unblocked at lower temperatures. As observed in dc and ac susceptibility measurements, the blocking temperature increases with the iron content, within samples of group II.

As described in Sec. 2.6, $S(T)$ is a measure of the anisotropy energy distribution, which will be analyzed in Sec. 4.4. Qualitatively, one observes that the $S(T)$ curve of sample U2Fe6.5(II) shows the existence of a bimodal anisotropy energy distribution, as found in dc and ac measurements.

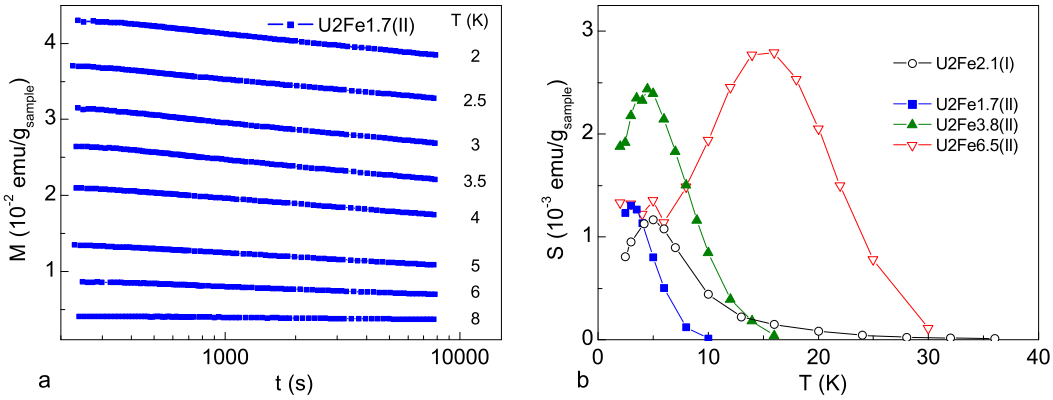

Figure 3.12: a. Magnetization as a function of time (in logaritmic scale) of U2Fe1.2(II) sample; b. viscosity, S, as a function of temperature of group II and U2Fe2.1(I) samples.

3.4.4 Mössbauer spectroscopy

The Mössbauer spectra of samples U2Fe2.1(I), U2Fe3.8(II) and U2Fe6.5(II) at selected temperatures are plotted in Fig. 3.13. For $T > T_B$ as seen in a Mössbauer experiment, the spectra presents a doublet, as expected for unblocked superparamagnetic particles. This is due to the fact that the characteristic time associated to the energy barriers overcome (τ) is lower than the characteristic time of a Mössbauer experiment, the Larmor precession time ($\tau_m = 10^{-8}$– 10^{-9} s). Thus, the fast relaxation makes the magnetic interactions to be averaged to zero, yielding a paramagnetic-like doublet. For temperatures below T_B the Mössbauer spectrum is magnetically split in a sextet. In a Mössbauer experiment, T_B can be defined as the temperature at which the contribution (integrated intensity) of the doublet equals that of the sextet. For sample U2Fe2.1(I) $T_B = 29 \pm 2$ K. As observed in the susceptibility measurements, the blocking temperature of group II samples increases with the iron content, being 25 ± 2 K and 50 ± 2 K, for samples with 3.8 and 6.5 % of iron content.

Hyperfine parameters such as magnetic hyperfine field (B_{hf}), isomer shift (IS) and quadrupole shift (QS) have been determined using the $NORMOS$ program [202], considering the spectra as the sum of a doublet and a distribution of sextets (blue and green lines in Fig. 3.13, respectively). As the temperature increases, the particles become unblocked and the sextet contribution decreases, as observed in Fig. 3.14 right plot for sample U2Fe2.1(I). In general, the hyperfine parameters at low temperature (T=4.2 K, Tab. 3.5) are characteristic of low crystalized ferrihydrite nanoparticles. In fact, a reduction of the average hyperfine field compared to that usually found for ferrihydrite is observed: B_{hf}=460-469 kOe in the present case versus 490-500 kOe of ferrihydrite [203]. Such reduction has also been assigned to surface disorder [204, 205, 206], which may also apply to the present case. In a closer look and comparing the parameters obtained for the studied samples, differences are found between U2Fe2.1(I) and U2Fe6.5(II) samples, in particular in B_{hf}, which is higher in the

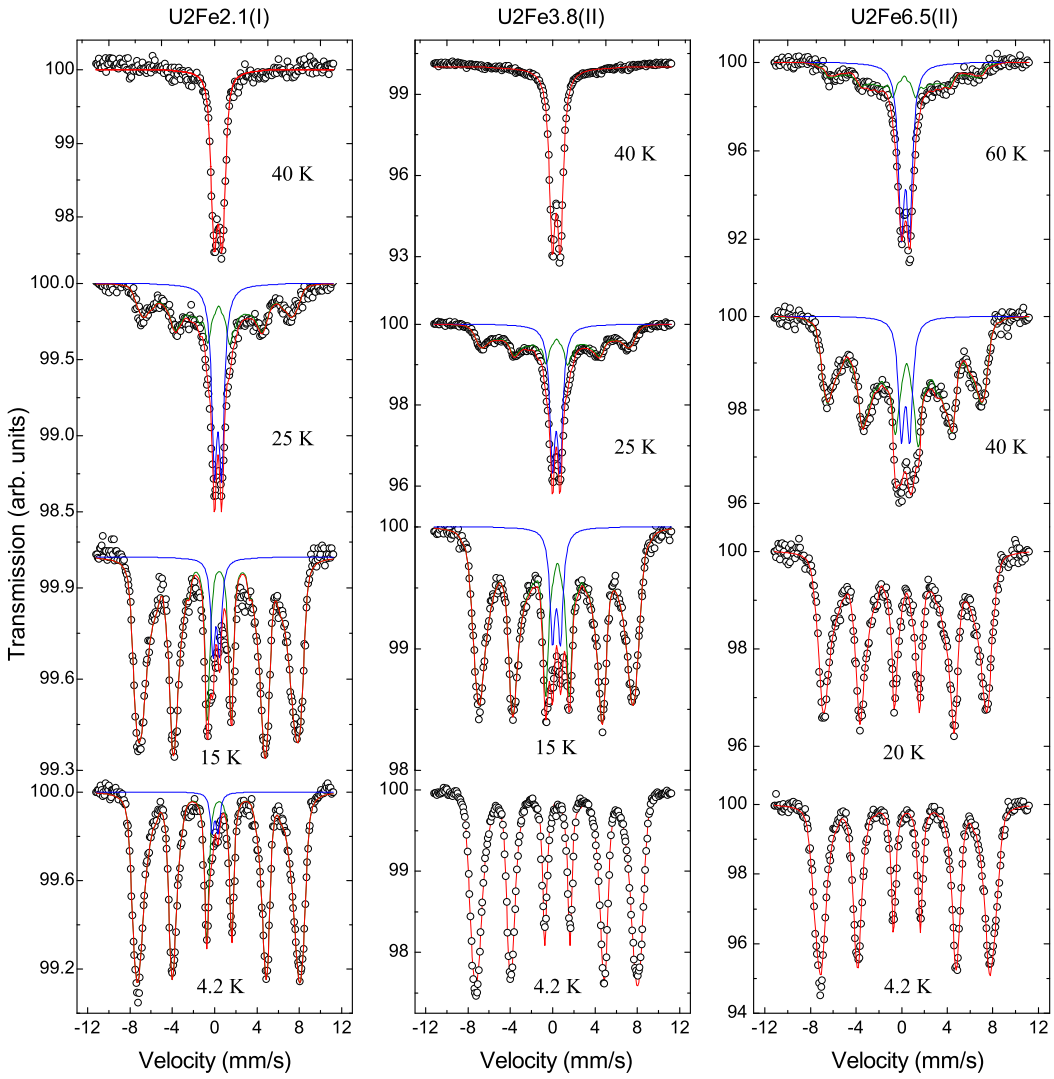

Figure 3.13: ^{57}Fe Mössbauer absorption spectra of samples U2Fe2.1(I), U2Fe3.8(II), and U2Fe6.5(II) at selected temperatures. Green line correspond to the contribution of the sextet distribution, blue line correspond to the contribution of the double and red line correspond to the sum of both contributions.

former, and in QS, which is lower in the latter sample. These differences are consistent with the idea that sample U2Fe2.1(I) has low crystalized ferrihydrite nanoparticles while sample U2Fe6.5(II) has an iron oxyhydroxynitrate phase. In fact, in sample U2Fe6.5(II) B_{hf} is between that of iron oxyhydroxynitrate phase (B_{hf}=450-460 kOe and at 4.2 K [44]) and that of ferrihydrite. On the other hand, although no QS is reported for iron oxyhydroxynitrate, the value reported for the iron oxyhydroxysulfate phase at 4.2 K is $QS = -0.37$ mm/s, [38], and so QS of sample U2Fe6.5(II) is between this value and that of ferrihydrite (-0.06 mm/s). It is expected that the hyperfine parameters of iron oxyhydroxynitrate can be similar to those of iron oxyhydroxysulfate, since their Mössbauer spectra and XRD patterns have similar

features [44] (see Fig. 1.10). The hyperfine parameters of sample U2Fe3.8(II) are closer to those of sample U2Fe2.1(I) than to those of U2Fe6.5(II). Up to this point, the differences between group II samples observed by XRD and dc susceptibility measurements could be assigned to size. Here, the differences in the hyperfine parameters may be due to size but also to different local magnetic environments.

Table 3.5: Hyperfine parameters of samples U2Fe2.1(I), U2Fe3.9(II), and U2Fe6.5(II) at 4.2 K: average hyperfine field $\langle B_{hf} \rangle$ quadrupole splitting QS and isomer shift IS.

T=4.2 K	U2Fe2.1(I)	U2Fe3.8(II)	U2Fe6.5(II)
$\langle B_{hf} \rangle$ (kOe)	469	468	460
QS (mm/s)	−0.06	−0.08	−0.14
IS (mm/s)	0.53	0.54	0.52

The hyperfine fields distribution is broad (Fig. 3.14, left plot), as expected for disordered systems, i. e. systems with a broad distribution of local fields/enviorements. Such broad distribution is usually found in ferrihydrite, being attributed to the different atomic environments of core and surface iron ions: the magnetic hyperfine fields at the nuclei of the surface iron ions are smaller than those in the particle core [64].

Mössbauer spectroscopy can be used to probe dipolar interactions, as shown by Mørup et al. [207], Dormann et al. [150], and Zhao et al. [64]. The latter authors applied Mössbauer spectroscopy to Si-doped ferrihydrite and ferrihydrite impregnated in SiO_2. For non-negligible dipolar interactions and at temperatures around T_B the spectrum shows a collapsed magnetic hyperfine field pattern (V-shaped pattern), as observed in the spectra of the U2Fe6.5(II) sample at 40 K (Fig. 3.13). On the contrary, the spectrum of U2Fe2.1(I) sample does not show evidence of a collapsed pattern, indicating that dipolar interactions are negligible. The evolution of such interactions with the iron content is presented in the following section.

As mentioned above, in the superparamagnetic unblocking temperature region, the fast relaxation makes the magnetic interactions to be averaged to zero, yielding a paramagnetic-like doublet. The superparamagnetic situation can be distinguished from the paramagnetic one by the application of an external field: in superparamagnetic systems the split is partially recovered. This can be observed in Fig. 3.15: at 40 K and 55 kOe the Mössbauer spectrum of sample U2Fe2.1(I) shows partial splitting.

3.4.5 Influence of the iron concentration: dipolar interactions

The dependence of the blocking temperature with the characteristic measuring time, $T_B(\tau_m)$ is an excellent tool to investigate dipolar interactions. The effect of these interactions can be understood in the framework of the statistical model, as shown by Dormann et al.

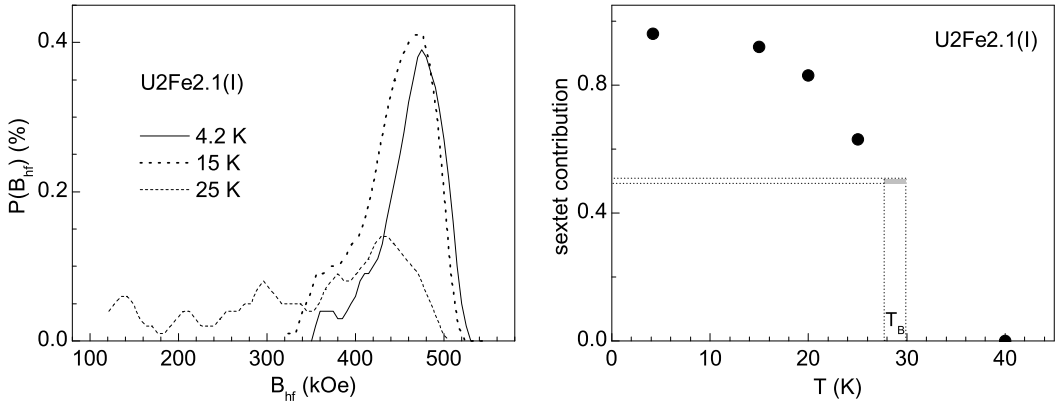

Figure 3.14: Hyperfine field distribution (left) and thermal variation of the relative intensity of the sextet contribution (right). The blocking temperature $T_B \simeq 29$ K corresponds to half (0.5) of sextet contribution.

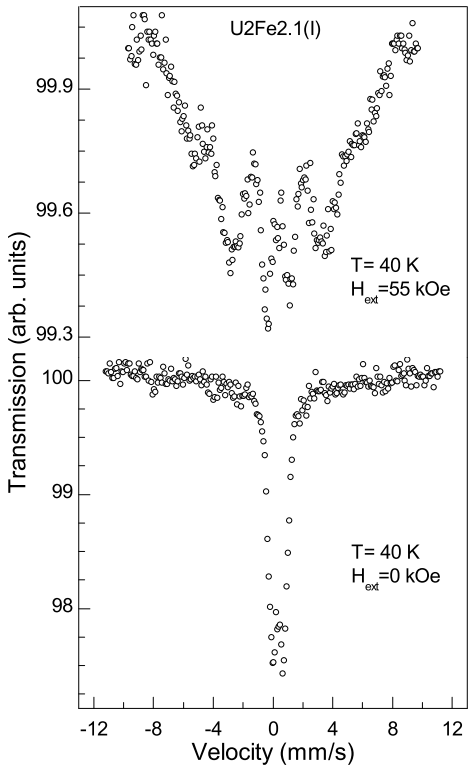

Figure 3.15: ^{57}Fe Mössbauer absorption spectra of samples U2Fe2.1(I) at 40 K at 0 and 55 kOe external field.

[101, 102, 155] (see Sec. 2.5.2, page 51). This model describes dipolar interactions as a change in the effective energy barrier experienced by the particle, which is frequency dependent. This leads to a deviation to the Néel-Arrhenius law (Eq. 2.2). The deviation becomes apparent in the $\log(\tau_m)$ vs. $1/T_B$ plot since the extrapolation of $\log(\tau_m)$ to zero, considering τ_m

values characteristic of ac measurements, yields too low τ_0 values (typically below 10^{-13} s). The dependence of $\log(\tau_m)$ with $1/T_B$ is plotted in Fig. 3.16 for U2Fe2.1(I), U2Fe3.9(I)

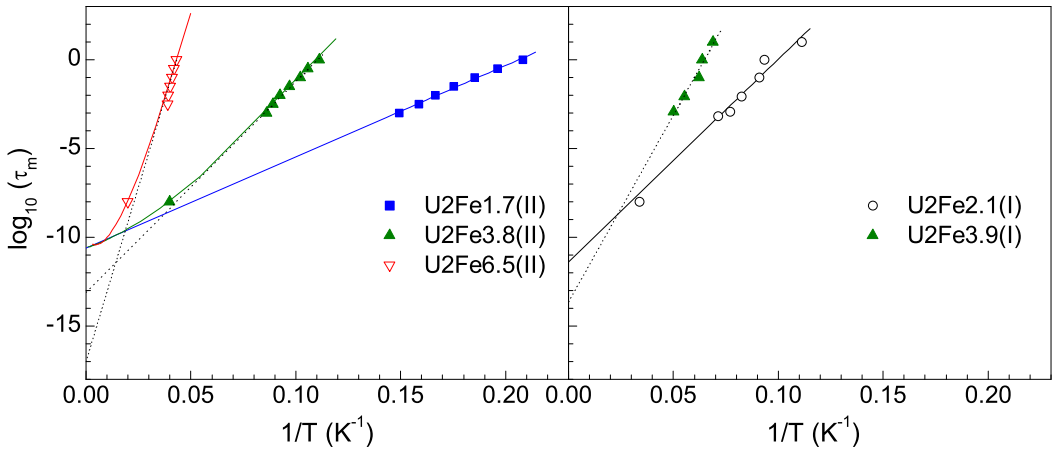

Figure 3.16: Thermal variation of the relaxation time for group II (left plot) and U2Fe2.1(I) and U2Fe3.9(I) samples (right plot). Dotted lines are linear extrapolations while solid lines represent fits to the statistical model.

and group II samples. The plot comprises T_B obtained from the in-phase component of the ac susceptibility and T_B obtained from the Mössbauer spectroscopy. Considering the ac susceptibility data, it can be observed that the extrapolated τ_0 decreases (Fig. 3.16, dotted lines) as the iron concentration increases. Such dramatic decrease leads to a physically unacceptable value of τ_0 for the most concentrated sample ($\tau_0 \approx 10^{-17}$ s). Since the samples have the same type nanoparticles, they are expected to have similar τ_0, at least within each group. Therefore, the increase of the extrapolated value is a clear indication of an increase of the dipolar interactions with the iron content, as one might expect. We recall that this increase was also observed by the increase of $|T_0|$ in dc susceptibility, and by the emergence of a collapsed Mössbauer spectra with the increase of iron content. We have applied the statistical model of Dormann to samples U2Fe3.8(II) and U2Fe6.5(II) to quantify the strength of dipolar interactions. The dependence of the uncompensated magnetic moment with temperature was described by the magnons law (Eq. 3.5), in accordance with the analysis performed in dc data and magnetization results. The constant α was fixed equal to 6.2×10^{-6} K^{-1}, in order to set the transition temperature at a value within the expected for these systems (around 400 K). We have considered 12 nearest neighbors and two nearest neighbors shells ($j = 2$), although considering $j = 1$ gives similar results, within the error bar. The ratio between the magnetic moment of the samples was taken from the dc measurements analysis. We have considered that the interactions in the most diluted samples are negligible so that $\tau_0(1/T \rightarrow 0)$ can be obtained by linear extrapolation to zero in the $\log_{10}(\tau_m)$ vs. $1/T$ plot (Fig. 3.16). The parameters of $\tau_0(T)$ in Eq. 2.3 ($\mu(0)/E_a\gamma_0$, η_r, and E_a) were constrained so that $\tau_0(1/T \rightarrow 0)$ in samples U2Fe3.8(II) and U2Fe6.5(II) was kept equal to

the value found for sample U2Fe1.7(II) (5×10^{-11} s). We have tried different η_r values within the expected range (0.1-0.6).

The results shown in Fig. 3.16 and Tab. 3.6 were obtained for $\eta_r = 0.1$ and $\eta_r = 0.6$ in sample U2Fe3.8(II) and U2Fe6.5(II), respectively, according to that found in Ref.[155] for weakly and strongly interacting systems. The choice of these values is somewhat arbitrary but, by choosing different η_r values, the qualitative results are the same. All these assumptions were made so that only two parameters were left free, which is essential to the fit convergence. The free parameters are the particles anisotropy energy E_p and first neighbors interaction energy, M^2Va_1. As qualitatively observed, the interaction energy increases with the iron content in group II samples. This increase is followed by the particles anisotropy energy increase, as expected since both size and magnetic moment increase.

Table 3.6: Statistical model (Eq. 2.49) fit parameters: particles anisotropy energy E_p and first neighbors interaction energy, M^2Va_1. Details are given in the text.

	U2Fe2.1(I)	U2Fe1.7(II)	U2Fe3.8(II)	U2Fe6.5(II)
$E_p = K_{eff}V$ (K)	260±30	52±2	190±15	210±20
M^2Va_1 (K)	~ 0	~ 0	12±2	56±3

From E_p one can determine the effective anisotropy constant K_{eff}, considering that $E = K_{eff}V$, where V is the particle volume. For sample U2Fe2.1(I), $K_{eff} = 4 \times 10^5$ erg/cm^3, (considering spherical particles) in agreement with the value found in artificially reconstructed ferritin cores: $(3-6) \times 10^5$ erg/cm^3 [54].

3.4.6 $M(H,T)$ measurements

Hysteresis cycles

Below $T \approx T_F$, the $M(H,T)$ curves of the ferrihydrite/di-ureasil nanocomposites show irreversibility, that depends on the sample history. In particular, in antiferromagnetic and ferrimagnetic nanoparticles the curves depend on the cooling field, having and exchange bias field H_E if cooled under an applied field. We have measured hysteresis cycles at 3 different temperatures, in samples U2Fe1.7(II) and U2Fe3.8(II). Samples were cooled from $T > T_F$ down to 2 K at $H_{app} = 5$ kOe and cycled between $H = 50$ kOe and $H = -50$ kOe. The subsequent cycles were measured by increasing the temperature up to the measurement temperature with $H_{app} = 50$ kOe. Cycles measured at 2 K are shown in Fig. 3.17.

The hysteresis cycles of both samples are closed but far from saturation. The cycles have linear and saturation components, with the former being more visible in sample U2Fe3.8(II). Both samples exhibit coercive (H_C) and exchange (H_E) fields, that rapidly decrease to zero as T approaches T_F, as seen in Fig. 3.18. Actually, the decrease of H_C is more severe

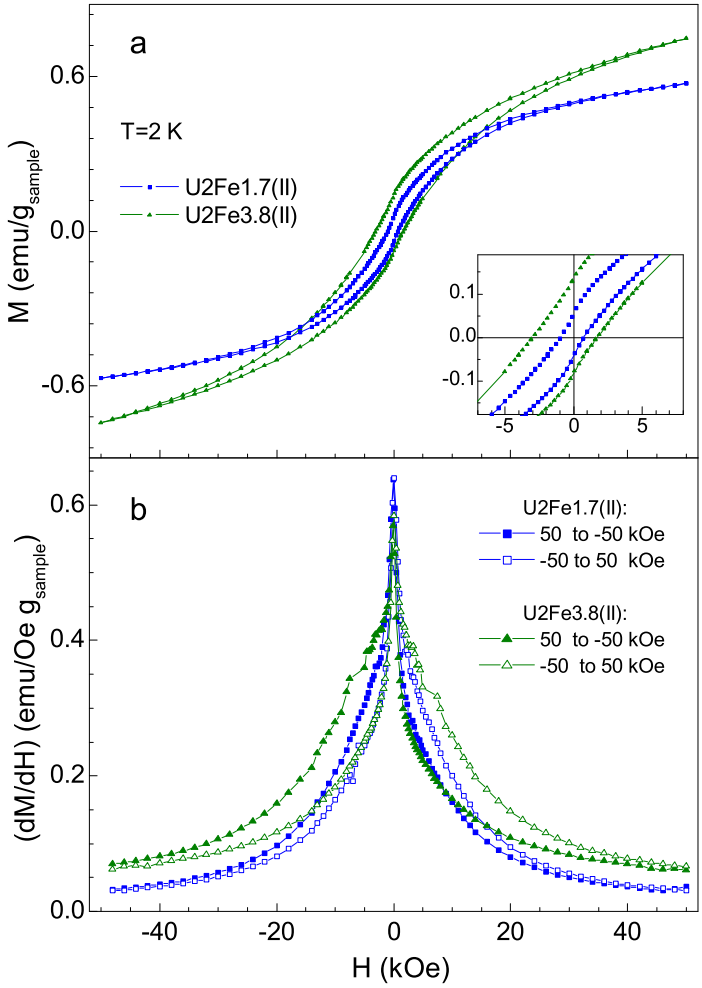

Figure 3.17: a. Hysteresis curves measured at T=2 K in samples U2Fe1.7(II) and U2Fe3.9(II); b. field derivative of the magnetization, dM/dH.

than the expected for superparamagnetic nanoparticles, which is given by Eq.(2.27). The dependence of H_E with temperature is not linear, as expected for of the random-field model of exchange anisotropy [208] and observed in γ-Fe_2O_3 nanoparticles [119]. However, these conclusions must be drawn with caution, since we just have 3 experimental points.

The shape of the hysteresis cycles of samples U2Fe1.7(II) and U2Fe3.9(II) is not the expected for superparamagnetic neither superantiferromagnetic particles. Superparamagnetic cycles are widest at zero field and exhibit an inflection point at the coercive field. The experimental hysteresis shows anomalous "pinched" curves at low fields, with an inflection point near zero field, as observed in the dM/dH plot (Fig. 3.17, lower panel). dM/dH has a peak at $H = 100 \pm 100$ Oe and not at the field where $M = 0$ ($H = H_C + H_E$), indicating that a considerable amount of moments follow the field near zero field. Similar dM/dH behavior is observed in ferritin [104, 209, 51] and, by the time, was associated to macroscopic reso-

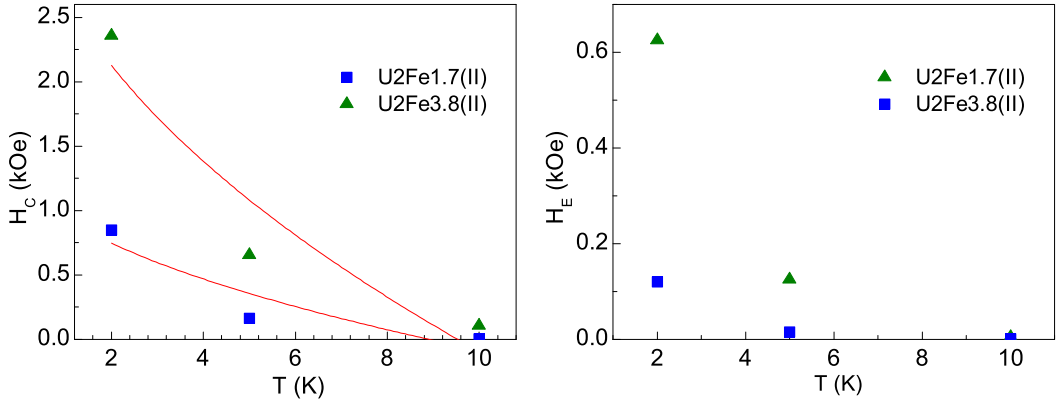

Figure 3.18: Coercive (H_C) and exchange fields (H_E) as a function of temperature, in samples U2Fe1.2(II) and U2Fe3.9(II). Lines in the H_C plot are fits to Eq. (2.27)

nant tunneling of the magnetic moment, although it is now recognized that the magnetic relaxations of ferritin in magnetic fields are dominated by classical superparamagnetic fluctuations [210]. We notice that the hysteresis cycles were recorded in steady fields and that each measurement took about 20 s so that relaxation during field stabilization and during measurements occur. This relaxation may be responsible for the occurrence of a peak in the dM/dH curves at $H \neq H_C + H_E$. Further measurements of hysteresis curves recorded in sweeping fields and different field variation velocities would be needed to clarify this point.

$M(H,T)$ above T_B

Above $T \approx T_F$, the $M(H,T)$ curves of the ferrihydrite/di-ureasil nanocomposites are reversible. At 50 kOe, the curves are not yet saturated and can be described has having linear and partial saturation components, as found for the hysteresis curves (Fig. 3.19). In a first approximation, we have fitted magnetization data to a simple Langevin function added to a linear term, as described in Sec. 2.7.3:

$$M(H,T) = N_p\,\mu_{un} L\left(\frac{\mu_{un} H}{k_B T}\right) + \chi_{AF} H \tag{3.7}$$

The Langevin function describes the partial saturation while the linear term describes the antiferromagnetic contribution. As result we have obtained an oscillatory residue (Fig. 3.20b). The fitted χ_{AF} decreases with temperature, as previously observed in antiferromagnetic [151, 179, 54, 174, 51] and ferrimagnetic nanoparticles [182]. The fitted parameters $M_S = N_p\,\mu_{un}$ and μ_{un} decrease and increase with temperature, respectively (Fig. 3.20d and c), in accordance with earlier results [178]. Similar systematic oscillatory fit was observed in ferromagnetic [211, 212, 213] and antiferromagnetic nanoparticles [151, 179, 214]. Such behavior of residues and fit parameters is also found when intrinsic distributed data are fitted

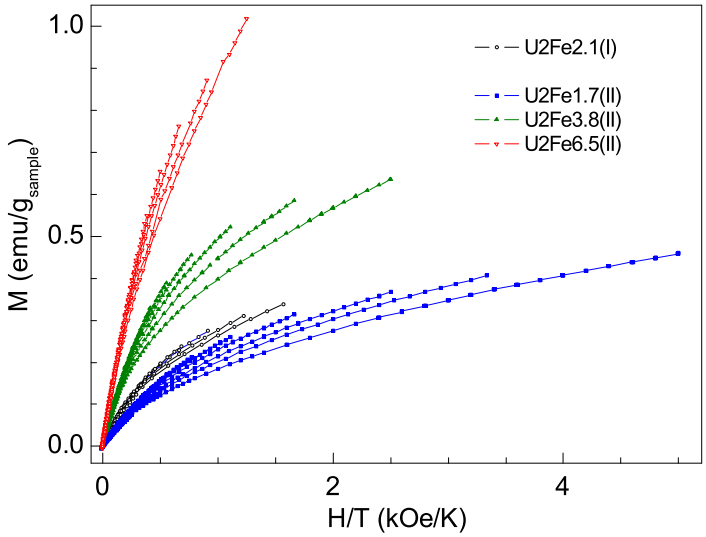

Figure 3.19: Magnetization as a function of H/T of group II and U2Fe2.1(I) samples, at selected temperatures between 10 and 250 K.

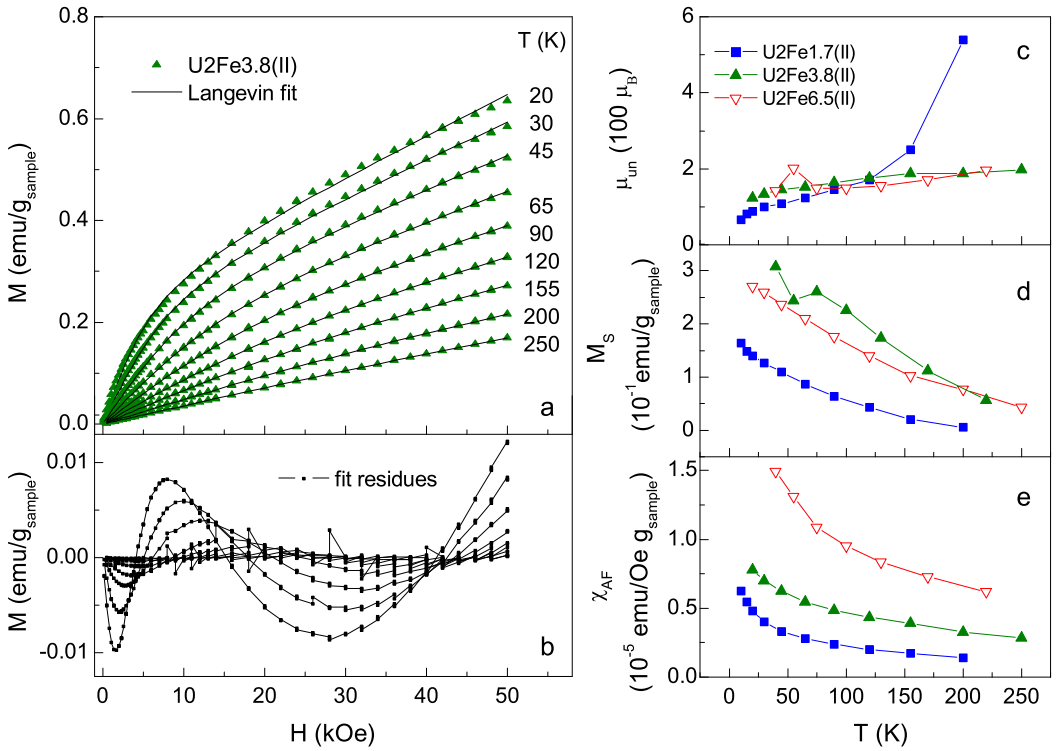

Figure 3.20: a. Magnetization of U2Fe3.5(II) as a function of H at the indicated temperatures; solid lines represent fits to the Langevin equation (Eq. 3.7); b. fit residues. Fit parameters: c. μ_{un}, d. M_S, and e. χ_{AF}.

with simple Langevin function [112] (see Sec. 2.3.3, page 38). The simultaneous increase of μ_{un} and decrease of $M_S = N_p\,\mu_{un}$ is puzzling and would imply a strong decrease of the particle density N_p, which has no physical ground.

We have also tried the Néel function (Eq. 2.70) instead of the Langevin one. This function considerers that the uncompensated moments are constrained by the antiferromagnetic component, such that they are essentially aligned in the antiferromagnetic direction (see Sec. 2.7.3, page 56). However we notice no improve in the fit quality: χ^2 is about 5% higher and similar oscillatory residues are observed. At the same time, the temperature dependence of the fitted parameters μ_{un} and M_S is similar to that of the Langevin fit.

In a second approach we have investigated the existence of a magnetic moment distribution, such that the total magnetization is expressed by:

$$M(H,T) = N_p \int_{\mu_{min}}^{\mu_{max}} \mu_{un} L(x) f(\mu_{un}) d\mu_{un} + \chi_{AF} H \tag{3.8}$$

where μ_{un} is the particle uncompensated moment and $f(\mu_{un})$ its normalized lognormal distribution given by:

$$f(\mu_{un}) = \frac{1}{\mu_{un} s\sqrt{2\pi}} \exp - \left[\frac{(\log(\mu_{un}/n))^2}{2s^2}\right] \tag{3.9}$$

The mean particle moment $\langle\mu_{un}\rangle$ is equal to $n\sqrt{w}$ and the standard lognormal deviation σ is equal to $n\sqrt{w(w-1)}$, with $w = \exp(s^2)$. In ideal ferromagnetic superparamagnetic systems, μ is proportional to the volume and the moment distribution arises only due to a volume distribution. In that case it is possible to consider volume distributions instead of moments distribution. However, in real systems, surface disorder, frustration and spin canting may contribute to moment distributions distinct from volume ones [164]. This distinction becomes more relevant in the case of antiferromagnetic or ferrimagnetic particles. A much improved fit is obtained using Eq. 3.8 and 3.9, resulting in residues of the order of data scattering (Fig. 3.21). Since the particles density N_p obtained in these individual fits is essentially the same for all curves, we performed a global fit imposing the same N_p for all data. We notice that when using the Néel function (Eq. 2.70) together with the lognormal distribution we obtain non-linear least square values of about 5% higher than using a lognormal distributed Langevin function, as found in the case of non-distributed analysis. The large contrast between $\langle\mu_{un}\rangle$ and $N_p\langle\mu_{un}\rangle$ obtained using distributions, and M_S and μ_{un} obtained from the non-distributed fit is shown in Fig. 3.22b and c.

When considering the moment distribution, the average uncompensated moment decreases with temperature unlike the increase observed when disregarding distributions. At the same time, $M_S = N_p\,\mu_{un}$ follows the same trend as $\langle\mu_{un}\rangle$ (since N_p is constant with temperature) and not the linear decrease previously found. The antiferromagnetic susceptibility decreases with temperature (Fig. 3.22a.), having values lower than those found when fitting without a moment distribution. The parameter s of the lognormal distribution is constant

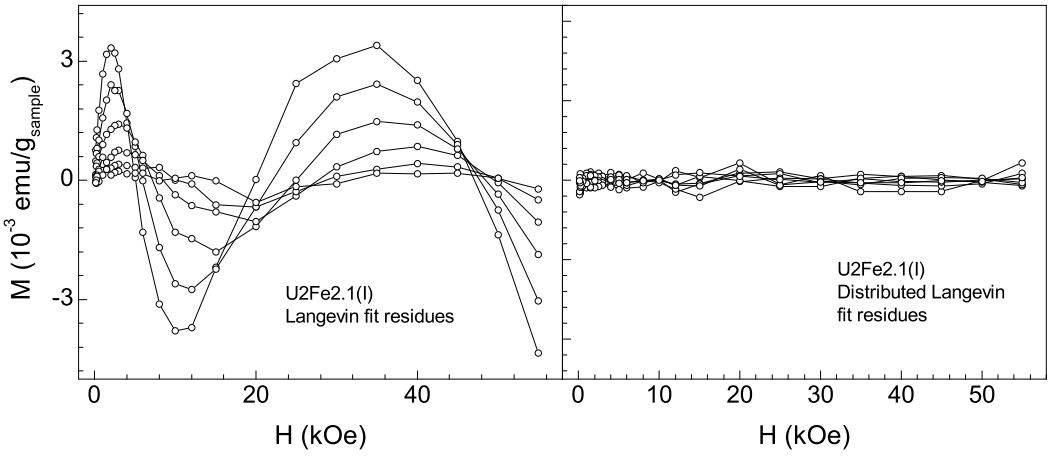

Figure 3.21: Residues after fitting magnetization of sample U2Fe2.1(I) to the Langevin law, and to the Langevin lognormal-distributed function.

with temperature, within the fit error, being 0.9 in sample U2Fe2.1(I) and 1.0, 1.2 and 0.9 in samples U2Fe1.7(II), U2Fe3.8(II) and U2Fe6.5(II), respectively. It is also possible to observe that $\langle\mu_{un}\rangle$ of sample U2Fe2.1(I) is higher than that of group II samples, while M_S and therefore N_p are lower.

The parameters extracted from the analysis of the magnetization curves can be compared to those extracted from the dc susceptibility and TEM/SAXS. N_p values derived from the magnetization curves agree qualitatively well with those derived from structural TEM/XRD measurements (Tab. 3.7), with the former being systematically higher than the latter. This agreement is apparent in the difference of almost one order of magnitude observed in both magnetization- and structural-derived N_p when comparing sample U2Fe2.1(I) and group II samples. Again, this highlight the differences between group I and group II samples. The fitted $\langle\mu_{un}\rangle$ corresponds to a mean number of fully uncompensated Fe^{3+} ions, N_{un}, of 12 in sample U2Fe2.1(I), and 3, 4, and 9 in samples U2Fe1.7(II), U2Fe3.8(II) and U2Fe6.5(II), respectively. Taking into account the value of N_t derived in Sec.3.3.2 for sample U2Fe2.1(I) (1300 ± 200 ions), we find $N_{un} = N_t^p$, with $p \approx 1/3$, which suggests that the uncompensated spins are mainly randomly distributed at the surface. We anticipate that this approximation will be refined in chapter 4, Sec. 4.4.

From $\langle\mu_{un}\rangle$ and N_p it is possible to estimate $C(O)_{M(H)} = N_p\langle\mu_{un}^2(0)\rangle/3k_B$, with $\langle\mu_{un}^2\rangle = \langle\mu_{un}\rangle^2 + \sigma^2$. $C(O)_{M(H)}$ can be compare to that obtained from the dc susceptibility, here termed $C(0)_{dc}$. The estimations of $C(O)$ are in good agreement, following the same trend with the iron content (Tab. 3.7). On the other hand, χ_{AF} obtained from $M(H)$ curves is higher than that obtained from dc susceptibility (χ_0). The observed differences indicate some deficiencies in the models applied to dc susceptibility and $M(H,T)$ curves. These may arise from ignoring the temperature variation of χ_0 and from ignoring the effect of anisotropy in the

Table 3.7: Comparison between N_p obtained from TEM/XRD results and N_p obtained from distributed fits to $M(H,T)$ curves, and comparison between $C(0)$ obtained after Eq. 3.4/3.5 fit to dc susceptibility curves $(C(0)_{dc})$ and $C(0)$ obtained from distributed fits to $M(H,T)$ curves $(C(0)_{M(H)})$.

	U2Fe2.1(I)	U2Fe1.7(II)	U2Fe3.8(II)	U2Fe6.5(II)
parameters from (TEM/XRD):				
N_p (10^{17}particles/cm^3)	0.8	2×10	1×10	1×10
parameters from $M(H,T)$:				
N_p (10^{17}particles/cm^3)	2	35	45	20
$C(0)_{M(H)}$ (10^{-4} emu K/Oe g$_{sample}$)	2.4	3.8	12	14
parameters from fit to $\chi(T)$:				
$C(0)_{dc}$ (10^{-4} emu K/Oe g$_{sample}$)	-	4.36	11.7	18.3

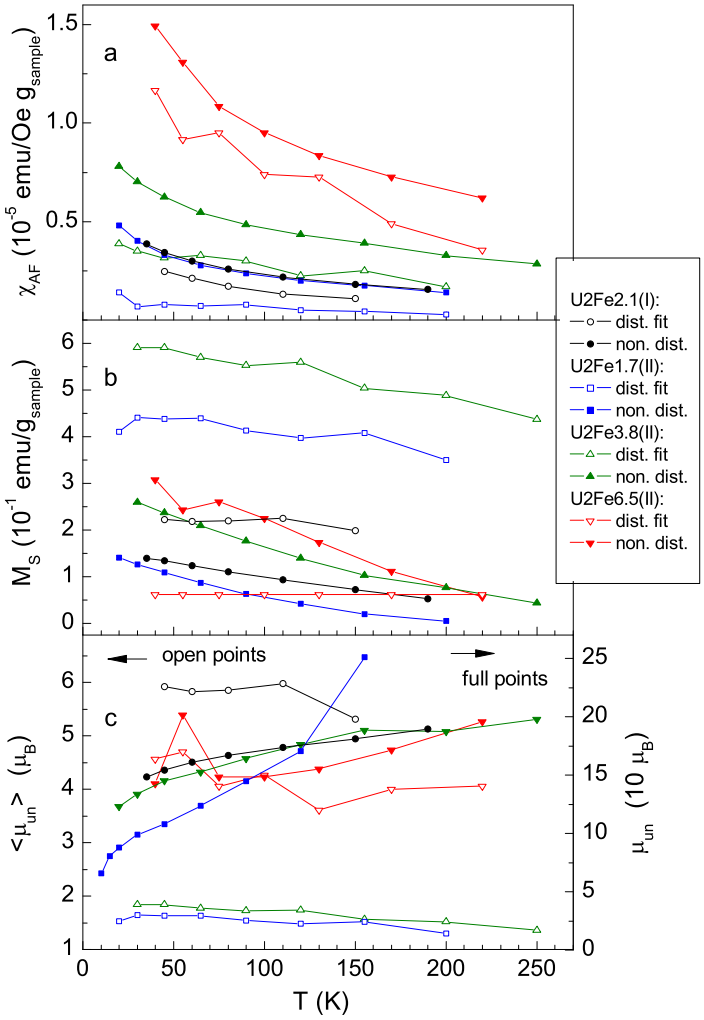

Figure 3.22: Comparison between parameters obtained after fitting magnetization curves considering the saturation component given by a non-distributed Langevin function (full points) and given by a Langevin distributed function (open points). a. anitferromagnetic susceptibility χ_{AF}; b. saturation magnetization M_S; c. uncompensated moment μ.

$M(H)$ curves. The latter issue would in fact lead to an estimation of χ_{AF} and $C(0)_{M(H)}$ by excess and defect, respectively. Improved results and modeling are expected to be obtained in magnetization measurements performed up to higher fields ($\sim 300 - 500$ kOe).

From the previous analysis we conclude that to consider a moment distribution is not just a matter of deriving more accurate parameters but it can drastically change the physical interpretation of the characteristics of superparamagnetic nanoparticles and deserves a more detailed study, as presented in chapter 4.

3.5 Influence of the chains' length and synthesis procedure in the formation of ferrihydrite: d-U(2000) vs d-U(900)

As described in Sec. 1.2.5, one of the advantages of organic-inorganic hybrids, and di-ureasils in particular, is the possibility of tuning the organic/inorganic ratio. In di-ureasils, this is achieved by changing the polymer molecular weight, i. e. the polymer chain length. In an attempt to explore this possibility, we have performed synthesis of iron/d-U(900) composites (termed U9Fe) and compared them with the d-U(2000) based ones.

The iron/d-U(900) nanocomposites were synthesized using a procedure similar to the one used to produce the d-U(2000) based composites. However, some changes were introduced in the second stage. In the case of the synthesis of the iron-doped d-U(900) compounds, ethanol and water were added to the corresponding hybrid precursor, followed by the incorporation of the iron nitrate. Moreover, the amount of ethanol added varied with salt concentration: 5, 20 and 25 ml for the iron concentrations of 3.4, 9.5 and 12%, respectively. We recall that in the d-U(2000)-based composites, the iron nitrate was first dissolved in a ethanol/water solution and the ethanol/water ratio was kept constant for all studied concentrations. The procedure here described was adopted in order to increase the amount of iron incorporated in the matrix. Following the synthesis of the U9Fe samples, this new procedure was also used to synthesize a new set of d-U(2000)/iron nanocomposites, termed U2Fe(III).

In the following sections we present a study comparing some structural and magnetic properties of these sets of samples: the d-U(2000)/ferrihydrite nanocomposites presented in the previous sections (group II samples), and the d-U(2000)/iron nanocomposites and the d-U(900)/iron nanocomposites synthesized according to the procedure described in the previous paragraph.

3.5.1 XRD

The XRD patterns of the U9Fe and U2Fe(III) samples are shown in Fig. 3.23. The patterns of the U2Fe(III)samples are similar to those expected for an ironoxyhydroxynitrate phase. In fact, the relative intensity of the double peak at 2θ= 60-65° is the opposite of the expected for ferrihydrite: the peak appearing at 61° is more intense than that at ca. 63.5°. The peak at 61° is even more sharp and (relatively) intense in the U9Fe samples, showing again the existence of an ironoxyhydroxynitrate phase. The U2Fe(III) samples can contain either a mixture of ferrihydrite/ironoxyhydroxynitrate or an ironoxyhydroxynitrate phase with a structure approaching ferrihydrite.

Analyzing the width of the peaks of U9Fe samples, we conclude that one of the characteristic length is about four times greater than the other (Tab. 3.8). This indicates that the nanoparticles present in U9Fe samples are chain-shaped. The ratio of L obtained from the peaks at 35° and 61° gives an estimation of the particles form factor.

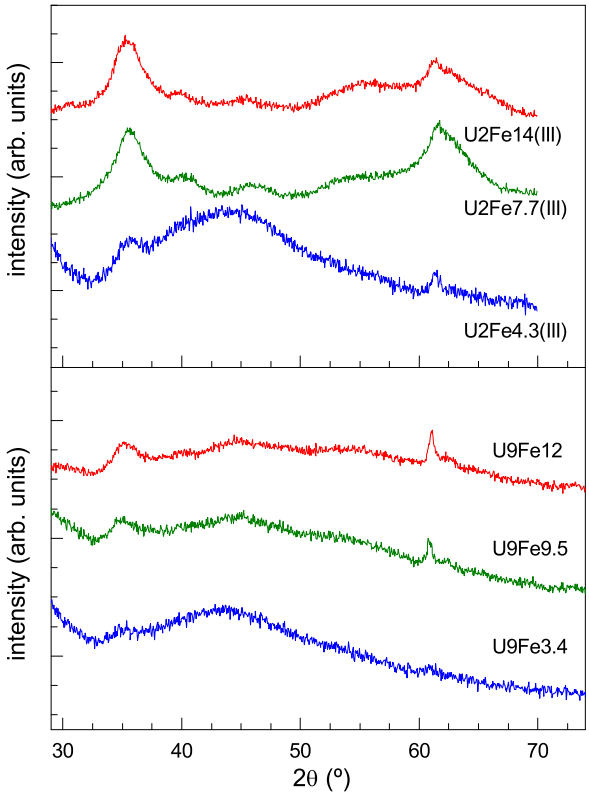

Figure 3.23: XRD patterns of the U2Fe(III) and U9Fe samples.

3.5.2 FT-IR spectroscopy

As described in Sec. 3.3.3, the amide region probes the organic-inorganic cross-link of the matrix. This region, in particular the "amide I" envelope, is strongly affected by the addition of iron nitrate to the d-U(900) host (Fig. 3.24a). The most important observation in the evolution of the "amide I" envelope with the iron content is that the changes produced are concentration dependent, in contrast with the d-U(2000)/ferrihydrite nanocomposites.

Table 3.8: Peak position an associated coherence length, L, in the U2Fe(III) and U9Fe samples

sample	peak center (2θ)	L (nm)
U9Fe9.5	60.9	13.5±0.3
	35.0	4.8 ±0.4
U9Fe12	61	17.5±0.3
	35.2	4.4±0.4
U2Fe7.7(III)	35.5	3.8±0.4
U2Fe14(III)	35.4	3.5±0.4

At 3.4 wt% of iron, the component associated with "free" urea cross-links (ca. 1750 cm^{-1}) is no longer seen, proving that the "free" C=O groups are saturated by Fe^{3+} ions. At 9.5 wt%, major modifications take place in this spectral range (Fig. 3.24a): new associations (ca. 1601 cm^{-1}) form at the expense of a massive destruction of the ordered POE/urea and urea-urea aggregates (ca. 1675 and 1642 cm^{-1}, respectively). These new associations are considerably stronger than those initially present in d-U(900). In the FT-IR spectrum of the most concentrated hybrid, the 1601 cm^{-1} feature persists and some of the hydrogen-bonded aggregates initially present are formed again. These data show that the Fe^{3+} coordination mechanism in the d-U(900) medium resembles globally that found in related POE/siloxane hybrid systems doped with other cations [215, 216, 217].

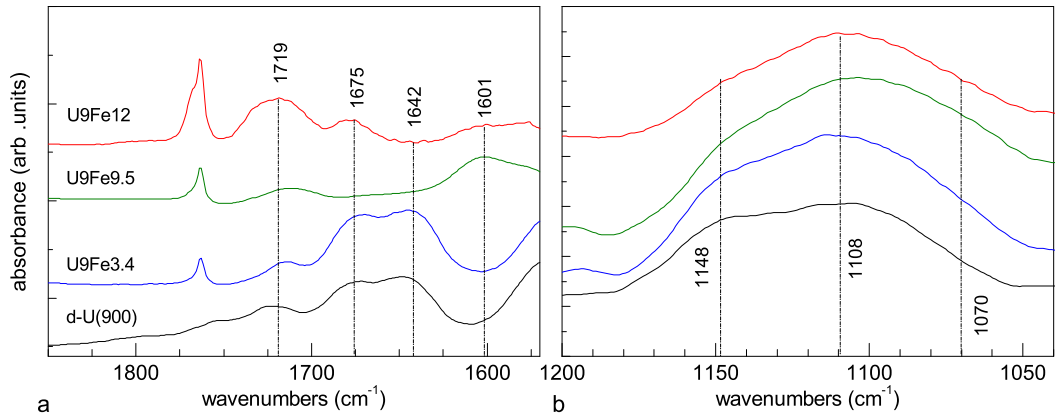

Figure 3.24: a. FT-IR spectra of the "amide I" envelope for d-U(900) matrix and U9Fe samples; b. FT-IR spectra in the νCOC region of the same samples. Frequencies are indicated for the spectrum of the most concentrated hybrid.

On the other hand, the νCOC region gives information about the interaction of the Fe^{3+} ions with the polyether chains. In the U9Fe samples we note the growth of a shoulder in the low-frequency side of the νCOC envelope, around 1070 cm^{-1} (Fig. 3.24b). This new feature is attributed to complexed polyether chains [216, 217], i.e., to the νCOC vibration of oxyethylene units coordinated to Fe^{3+} ions. Considering the relative intensity of the 1100 and 1070 cm^{-1} bands, we conclude that at the highest concentration studied (12% wt) the proportion of noncomplexed polymer chains still exceeds that of the complexed ones. The situation is different than that found in the d-U(2000)/ferrihydrite composites, where the polyether chains where almost unchanged by the presence of ferrihydrite (Sec. 3.3.3).

3.5.3 NMR spectroscopy

The ^{29}Si MAS and ^{13}C CP MAS NMR spectra were recorded accordingly to the procedure described in Sec. 3.3.4, with the following differences. The recycle delay was 60 s and the spinning rate 14.5 kHz. The ^{1}H high-power decoupled ^{13}C MAS NMR spectra were recorded

with 4 μs ^{1}H 90° pulse, a 2 μs ^{13}C 45° pulse, and 80 s recycle delay. The broadening effect on the ^{13}C CP/MAS spectra of the U9Fe samples was so important that made impossible to record such spectra. At the same time, ^{1}H high-power decoupled spectra with fast MAS (15 kHz) could be obtained but only for the sample with lower (3.4 wt%) Fe^{3+} content (Fig. 3.25a). This spectrum exhibited a 70.5 ppm peak with a FWHM of ca. 470 Hz, due to the carbon atoms of the poly(oxyethylene) chains. The ^{29}Si MAS NMR spectra of U9Fe samples was recorded only when fast (14.5 kHz) MAS was used (Fig. 3.25b). The spectra of of U9Fe samples display two peaks at ca. –59 and –68 ppm, assigned to $RSi(O)_2(OH)$ (T^2) and R-$Si(O)_3$ (T^3), respectively. These features are similar to those of U2Fe materials. The main difference is that the ^{29}Si NMR resonances in U9Fe are significantly broader.

3.5.4 Magnetic properties

Dc susceptibility

The dc susceptibility curves of the U9Fe12 sample present no irreversibility in the 5-300 K range (Fig. 3.26). The susceptibility curves of the U2Fe(III) samples present irreversibility below a temperature $T_F \approx 35$ K and a decrease of χ with temperature above T_F (Fig. 3.26). All zfc curves except the one of the U2Fe4.3(III) sample present a maximum at $T_B \approx 20$ K (see Tab. 3.9). T_B has a non-monotonic behavior with iron concentration. At low temperatures ($T < 8$ K), the susceptibility measured in the zfc procedure decreases with temperature, increasing again in the $8 < T < 20$ K range. This indicates the existence of a least two components, that can be a bimodal distribution of nanoparticles, two kinds of nanoparticles or a distribution of nanoparticles and paramagnetic Fe ions.

We have fitted susceptibility curves above $T = T_F$ to a Curie-Weiss law allowing the existence of a χ_0 temperature independent term (Eq. 3.4). Fit parameters are displayed in Tab. 3.9. U9Fe12 sample can be fitted to such law with residual T_0. The effective moment per Fe ion μ_{eff} is equal to 4.0 μ_B, lower than the expected for Fe^{3+} isolated ions: 5.32 μ_B. At the same time, χ_0 is positive, indicating that a fraction of the moments experience AF interactions. In the U2Fe(III) samples, μ_{eff} decreases with concentration, while χ_0 increases. This is an indication that the fraction of ions with antiferromagnetic interactions increases with the iron concentration. At the same time, $|T_0|$ is higher of the samples with higher Fe concentration, indicating also an increase of dipolar interactions.

Ac susceptibility

The in-phase and out-of-phase components of the magnetic susceptibility of U2Fe14(III) and U9Fe12 samples are plotted in Fig. 3.27 as a function of temperature, for selected frequencies in the $f = 0.1 - 1500$ Hz range. In the U2Fe14(III) sample, χ' is independent of f above $T_F \approx 80$ K. The χ' and χ'' curves of the U2Fe14(III) sample show the existence

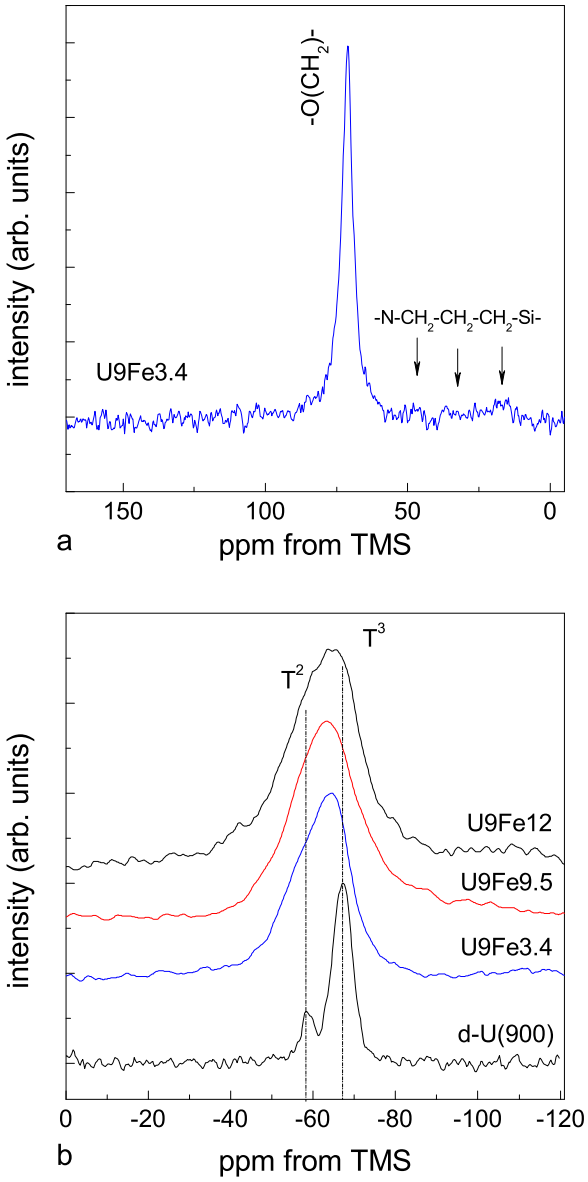

Figure 3.25: a. ^{1}H high-power decoupled ^{13}C MAS NMR spectrum (MAS 15 kHz) of d-U(900) and U9-Fe samples; b. ^{29}Si MAS (MAS 14.5 kHz) of the same samples.

of two maxima, one at $T \approx 8$ K and another at $T \approx 30$ K, as seen in the dc susceptibility measurements. These can be either due to a bimodal distribution or to the existence of two phases.

The χ' curves of the U9Fe12 sample are frequency dependent and χ'' becomes non-zero below 7 K. This is an evidence of the existence of some nanoparticles in the system. The maxima of the χ' curve, T_B, depends on the frequency according to the Arrhenius law (Eq. 2.2), as seen in Fig 3.27, inset. Fitting this data to Eq. 2.2 yields $\tau_0 = 10^{-13}$ s and $E_a = 50$ K. If the nanoparticles are ferrihydrite, this τ_0 implies the existence of non-negligible

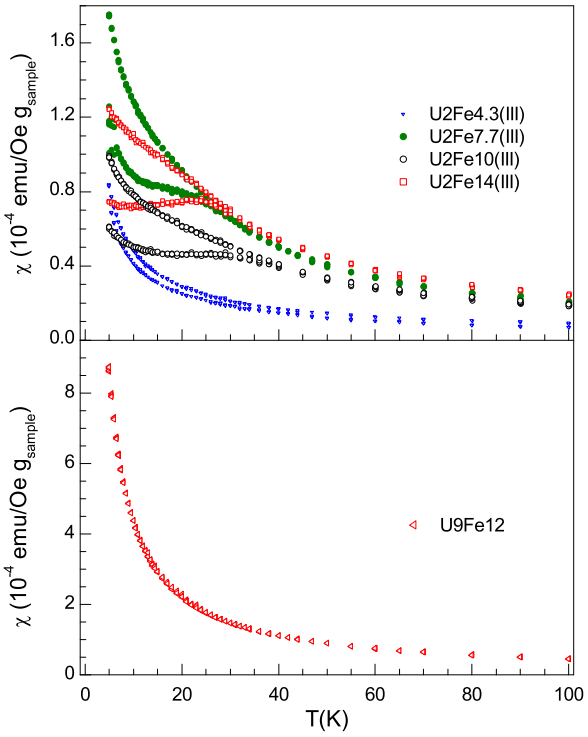

Figure 3.26: Dc susceptibility of U2Fe(III) and U9Fe samples as a function of temperature in the 5-100 K range.

interparticle interactions, since the expected value is at leat one order of magnitude higher. For non-negligible interparticle interactions E_a is an overestimation of the particle anisotropy energy, E_p. However, considering $E_p = E_a$ and the anisotropy constant of ferrihydrite equal to 4×10^5erg/cm^3 (the value found for sample U2Fe2.1(I), Sec.3.4.5), the size of the nanoparticles can be roughly estimated as 3 nm.

Table 3.9: T_B and parameters resulting from fitting dc susceptibility data of U2Fe(III) and U9Fe samples to Eq. 3.4.

sample	T_B ±1 (K)	μ_{eff} ±0.1 (μ_B)	T_0 (K)	χ_0 (emu/Oe g$_{sample}$)
U9Fe12	-	4.0	−0.01±0.02	7.4×10^{-7} $\pm5\times10^{-8}$
U2Fe7.7(III)	18	3.5	−1.5±0.3	-6×10^{-7} $\pm1\times10^{-7}$
U2Fe10(III)	25	2.7	−4.0±0.8	$+3.3\times10^{-6}$ $\pm2\times10^{-7}$
U2Fe14(III)	22	2.7	−3.0±0.7	$+3.4\times10^{-6}$ $\pm2\times10^{-7}$

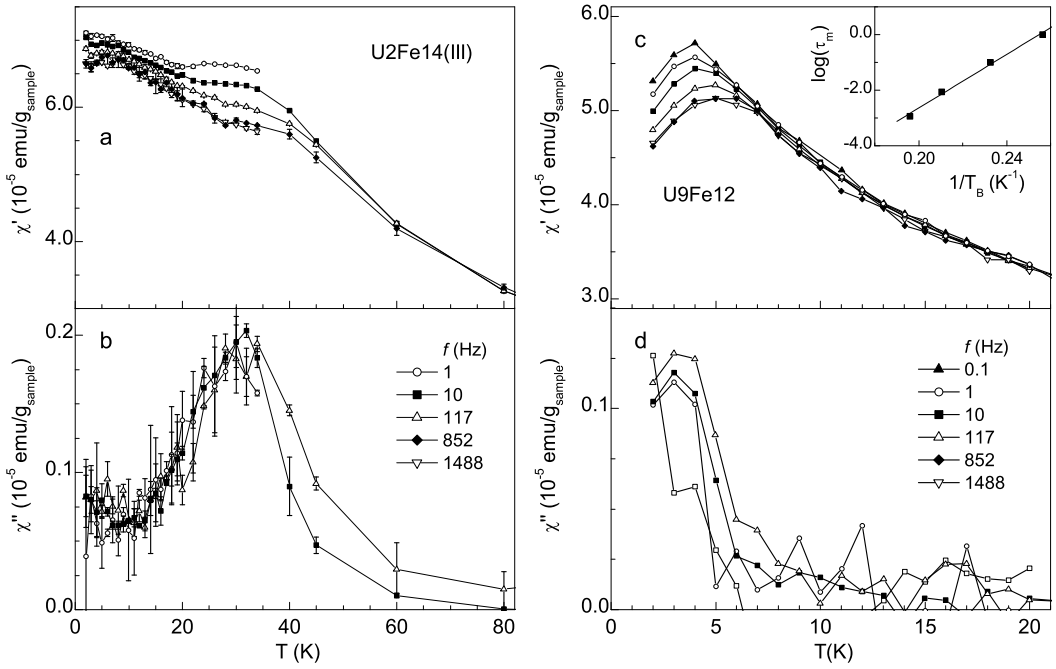

Figure 3.27: Ac susceptibility of U2Fe14(III) (a. and b.) and U9Fe12 (c. and d.) as a function of temperature. Panels a. and c.: in-phase component $\chi'(T)$, panels b. and d.: out-of-phase component $\chi''(T)$. Panel c. inset represents thermal variation of the relaxation time.

$M(H,T)$ curves

The $M(H,T)$ curves of the U2Fe14(III) sample at temperatures between 5 and 120 K do not scale in a H/T plot, as expected for nanoparticles at temperatures below or close to T_B. The curves at higher temperatures have an higher magnetization value for a given H/T value, indicating an increase of the magnetic moment and/or a decrease of the influence of the anisotropy energy compared to the thermal one. Both effects all likely to occur, since the first one is expected to occur below the irreversibility temperature, $T_F \approx 80$K, and the second is typically relevant for $T < 10T_B$ (see Sec. 2.3.2). The $M(H)$ curve at 5 K can be well fitted to a Brillouin law (Eq. 2.10), considering Fe^{3+} ions ($J = 5/2$), revealing the existence of paramagnetic Fe^{3+} ions, beyond the two sets of nanoparticles already detected. The fraction of the Fe ions of the U2Fe14(III) sample with paramagnetic behavior can also be estimated, comparing the parameter N of Eq. 2.10 (number of Fe paramagnetic ions per sample mass) with the total number of Fe ions. The Fe paramagnetic ions are about 14% of the total iron in the sample.

The $M(H,T)$ curves of sample U9Fe12 at 5, 10, and 20 K scale in a H/T plot, as expected for systems of nanoparticles where $T > 10T_B$ and isolated ions. As in the previous case, the curves can be fitted to a Brillouin law (Eq. 2.10), considering Fe^{3+} ions ($J = 5/2$) that correspond to 9% of the total iron in the sample.

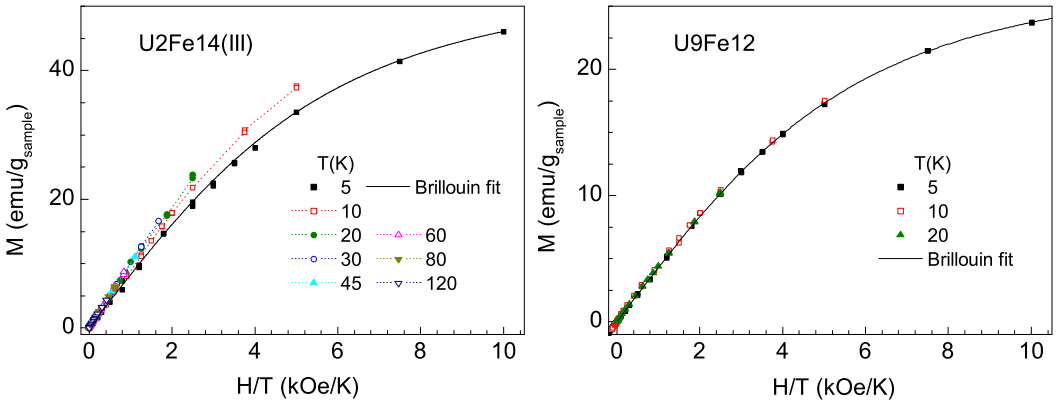

Figure 3.28: Magnetization as a function of H/T of U2Fe14(III) and U9Fe12 samples, at selected temperatures. Continuous black lines represent fits to Brillouin law (Eq. 2.10).

3.5.5 Influence of chains' length and synthesis procedure: conclusions

In the iron-doped di-ureasils, the modification of the average polymer molecular weight and the modification of the ethanol/water concentration allows obtaining different transient iron phases, from long amorphous iron oxyhydroxynitrate chains to ferrihydrite. The samples can be ordered as: iron nitrate salt, U9Fe samples, U2Fe(III), U2Fe(II), and U2Fe(I), with the last corresponding to ferrihydrite. Such order was made in accordance with the proposed mechanism of the formation of iron nanoparticles in aqueous media, at low pH (see Sec. 1.3.2). The mechanism involves the salt dissolution followed by the formation of chain-polymers constituted by octahedra sharing corners. Iron is in the center of the octahedra, while O, HO, and H_2O species occupy the corners. The chain-polymers condense forming double-chain and multi-chain polymers. These multi-chains are further condensed, since some octahedra start to share edges and faces, until the nanoparticle formation. Up to now, this process has been studied by freeze drying the iron nitrate solution at different instants of the process [44]. The use of the di-ureasil hybrid matrices and different water concentrations allows the stabilization of different transient phases and the accomplishment of structural and magnetic analysis.

The changes induced by the different chain length (d-U(2000) group I and II samples versus d-U(900) samples) are apparent in FT-IR spectroscopy and magnetic properties. FT-IR data suggest that the significant differences detected are associated to the iron local coordination and the magnitude and extension of the hydrogen-bonded urea-urea and urea-POE associations. In d-U(2000), the iron ions bond massively to the free carbonyl groups of the urea cross-links, at the organic-inorganic interface. Hence, the carbonyl-type oxygens are the preferential coordination sites, allowing the anchoring and subsequent nucleation of the ferrihydrite nanoparticles. The higher flexibility of the POE chains in the d-U(2000) di-ureasils and the faster segmental chain motions involving a larger number of repeat units

allows higher iron diffusion rates in the host. This results in efficient ferrihydrite particle growth. This flexibility enhances the ability of the polymer chains to wrap around the anchored ferrihydrite nanoparticles. The wrapping of the nanoparticles by the polymer chains and the anchor at the organic-inorganic interface is depicted in Fig. 3.29. This figure draws attention to the analogy between ferrihydrite nanoparticles incorporated in the long chain organic-inorganic di-ureasils and the protein coated ferritin cores.

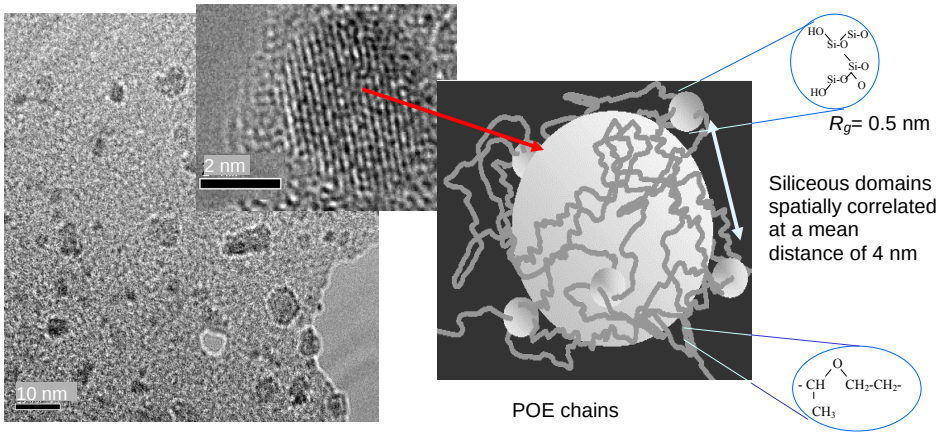

Figure 3.29: TEM and HRTEM images and schematic representation of the structure of the ferrihydrite/d- U(2000) hybrids. Small spheres depict the siliceous domains while the large sphere represents one ferrihydrite nanoparticle. The polymer chains are shown as coiled grey lines wrapping around the nanoparticle.

3.6 Summary

In this chapter we have presented structural and magnetic studies on ferrihydrite/di-ureasil nanocomposites. The formation of ferrihydrite depends on the ethanol/water ratio used during the hydrolysis and condensation of the hybrid precursor, and on the length of the organic chain. By changing these conditions, several iron oxyhydroxynitrate phases were obtained, from iron nitrate to 6-line ferrihydrite. The formation of ferrihydrite benefits from the flexibility of the longer polymer chains of the d-U(2000) matrix and from the existence of carbonyl groups that act as nucleation points, as deduced from FT-IR and NMR spectroscopies. The existence of these points leads to heterogeneous nucleation such that the incorporation of more iron leads to the formation of larger nanoparticles, in agreement with XRD, SAXS, TEM, and FT-IR spectroscopy results. The size, shape ,and size distribution of one of the samples (with 2.1% of iron) was determined by detailed TEM studies. The 6-line ferrihydrite nanoparticles have globular shape, are well dispersed in the matrix, and have an average diameter of 4.7±0.2 nm with a lognormal deviation $s = 0.43 \pm 0.05$.

The structural studies were then combined with magnetic studies in order to obtain a

deeper understanding of the composites, and on the behavior of antiferromagnetic nanoparticles. First of all, we have determined characteristic parameters as average uncompensated magnetic moment and anisotropy constant. In particular, in the sample with 2.1% of iron, the nanoparticles have an average uncompensated magnetic moment of 60 μ_B and an anisotropy constant of $K_{eff} = 4 \times 10^5$ erg/cm^3. The latter value is in agreement with values previously found in artificially reconstructed ferritin cores [54]. Comparing two different sets of samples, it was observed that the moment and anisotropy constant of 6-line ferrihydrite are higher than those of an iron oxyhydroxynitrate phase approaching ferrihydrite. Within each set, it was possible to observe the increase of dipolar interactions with the iron content, combining results from dc and ac susceptibilities, and Mössbauer spectroscopy.

The determination of parameters as the average uncompensated magnetic moment and the antiferromagnetic susceptibility is based on modeling magnetization curves. Models include saturation and linear terms, associated to the uncompensated moments and antiferromagnetic component, respectively. The saturation term can be described by a non-distributed Langevin function or by a Langevin-distributed function, for instance. We have shown that when applying these two functions to the magnetization curves of ferrihydrite, contradictory temperature dependencies of the uncompensated magnetic moment and saturation magnetization are obtained. We found that the distributed function is a better description of the system, since the use of the non-distributed function would imply an increase of the particle density with temperature.

Chapter 4

Magnetic studies in ferritin and ferrihydrite nanoparticles

4.1 Overview

This chapter is devoted to a detailed analysis of the field dependence of magnetization, and to the relation between anisotropy energy, size and magnetic moment distributions. New methods for the separation of saturation and antiferromagnetic components, and relating structural and magnetic properties based on distributions are presented. These methods are applied to the ferrihydrite nanocomposites of group I and II, presented in the previous chapter, and to ferritin, a model system for antiferromagnetic nanoparticles. From these methods it was possible to analyze the importance of disorder in ferritin and the random distribution of moments in a ferrihydrite nanocomposite.

4.2 Description of the samples

The ferritin samples used in these experiments were obtained from Sigma Chemical Company and prepared in powder samples according to Ref. [51]. A drop of ferritin solution was placed in a glass lamella and dried at RT during 24 h. The resulting film was then reduced to powder. Ferritin is a system with low interparticle dipolar fields, due to the protein shell that prevents aggregation and to the low particles net magnetic moment. In fact, Allen et al. [218] concluded about a weak interparticle interaction at 5 K, and Luis and co-workers [105] have shown negligible differences in ac susceptibility curves of ferritin samples with different concentrations, from diluted to solid samples. In addition, ferritin has a narrow size distribution (of the order of $s = 0.15$–0.20 [43, 174]) and therefore one expects a small moment distribution, that can be reasonably ignored [51, 173].

The ferrihydrite/hybrid matrix nanocomposites here described are those of group II

(U2Fe1.7(II), U2Fe3.8(II), and U2Fe6.5(II)), and one sample of group I (U2Fe2.1(I)), studied in chapter 3.

4.3 M(H,T) analysis: the scaling method

In the analysis of magnetization curves of antiferromagnetic nanoparticles one faces several problems. Firstly, these systems have an antiferromagnetic susceptibility component, which is difficult to separate from the superparamagnetic part, especially if the latter is far from saturation. One important fact is that the departure from saturation depends on the temperature and thus, an high field linear fit gives χ_{AF} in excess and, more drastically, successively distant from the accurate value as the temperature is higher. This is the reason why the method of using linear fits to the asymptotic law and high field regions, suggested by Harris et al. [171] does not avoid the errors introduced by the non-distributed Langevin fit. Consequently, when performing these linear fits one also obtains M_S and μ_{un} that decrease and increase with temperature, respectively. Secondly, in antiferromagnetic systems, the superparamagnetic component can have deviations to the canonic behavior, as described in Sec. 2.3 and 2.7.3. In particular, the superparamagnetic component can be modeled with different functions: the Langevin function (Eq. 2.9), a Langevin function with a modified N_p (Eq. 2.64), a function that considers anisotropy (Eq. 2.16), or the Néel function (Eq. 2.70). Considering these questions, we have developed a method to derive qualitative and quantitative information about the variation of μ_{un} and χ_{AF} with temperature. This information is obtained independently of the magnetization and magnetic moment distribution functions. We first apply the method to ferritin samples, since ferritin is considered a model for non-interacting and mono-dispersed antiferromagnetic nanoparticles. Using ferritin one benefits from the extensive work performed on both structural and magnetic characterization.

4.3.1 Description of the method and application to ferritin

In the case of antiferromagnetic nanoparticles with $\langle\mu_{un}\rangle$ constant with temperature and with negligible interparticle interactions, the superparamagnetic component scales with H/T, independently of the existence of a moment distribution and of the law that describes that component. This statement excludes systems with an anisotropy energy of the order of $\langle\mu_{un}\rangle H/T$. The antiferromagnetic component, $\chi_{AF}H$ would scale with H/T only if χ_{AF} obeyed to a Curie law (Eq. 2.29). This is not expected to occur, and therefore the first derivative of the magnetization with respect to the field multiplied by temperature has a component that collapses in an H/T scale and another component, associated with χ_{AF}, which does not, in accordance with:

$$\left(\frac{\partial M}{\partial H}\right)_T T = F\left(\frac{H}{T}\right) + \chi_{AF}T \tag{4.1}$$

where F is an unknown function of H/T. Thus, a constant difference between the magnetization data obtained at different temperatures will appear in an $(\partial M/\partial H)_T T$ vs. H/T plot, as shown in Fig. 4.1a for ferritin. This difference is better evaluated in a

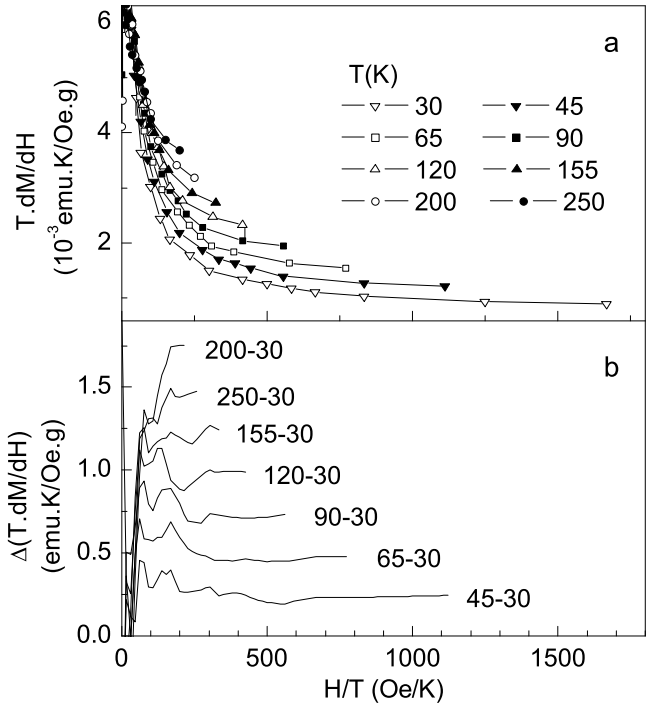

Figure 4.1: a. Representation of $(\partial M/\partial H)_T T$ as a function of H/T for horse spleen ferritin; b. difference between each of the above curves and the $T = 30$ K curve as a function of H/T.

$(\partial M/\partial H)_T T - (\partial M/\partial H)_T T_0$ vs. H/T representation, where T_0 is the lowest temperature. In the case of native horse-spleen ferritin, considering $T_0 = 30$ K, we can observe a region where $(\partial M/\partial H)_T T - (\partial M/\partial H)_T T_0$ can be considered constant with H/T (Fig. 4.1b), as expected from Eq. 4.1. The increment of $\chi_{AF} T$ in relation to a given temperature T_0 (in Fig. 4.2a for ferritin), can be determined considering the values of $(\partial M/\partial H)_T T - (\partial M/\partial H)_T T_0$ in the high H/T region, since:

$$\chi_{AF}(T)T = (\partial M/\partial H)_T T - (\partial M/\partial H)_T T_0 + \chi_{AF}(T_0)T_0 \tag{4.2}$$

$\chi_{AF}(T)$ can be determined after knowing $\chi_{AF}(T_0)$. This can be estimated from the extrapolation to zero of $(\partial M/\partial H)_T$ as a function of T/H, and for ferritin: $\chi_{AF}(T_0) = 2.6 \times 10^{-5}$ emu/Oe g_{sample}. Finally, we find that χ_{AF} decreases with temperature (Fig. 4.2b).

The superparamagnetic component of the magnetization curve of antiferromagnetic particles (M_{SP}) can then be easily obtained by subtracting $\chi_{AF}(T)H$ to the total magnetization. M_{SP} is plotted in Fig. 4.3a for ferritin. As noticed, the variation of $(\partial M/\partial H)T - (\partial M/\partial H)T_0$ is not constant with H/T in all range and therefore the curves do not superimpose in H/T.

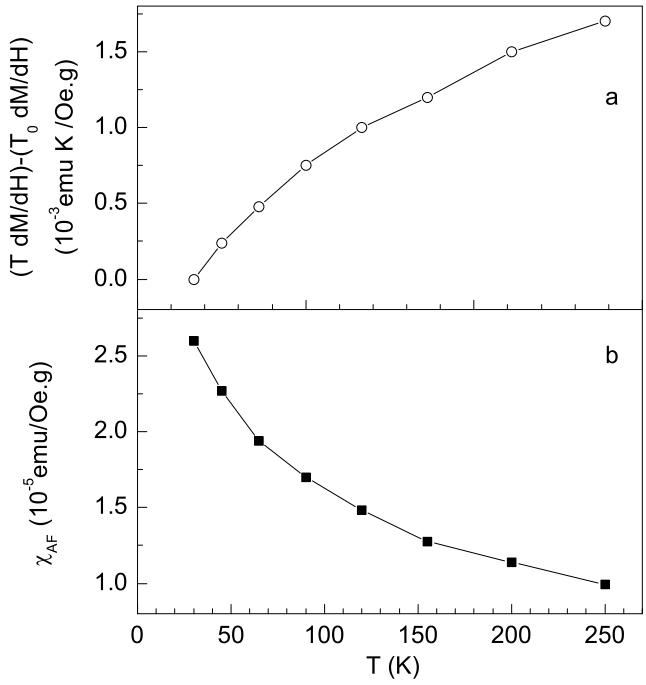

Figure 4.2: a. Representation of $(\partial M/\partial H)_T T - (\partial M/\partial H)_T T_0$ as a function of T for horse spleen ferritin; b. $\chi_{AF}(T)$ calculated accordingly to Eq. 4.2.

This is an indication that $\langle \mu_{un} \rangle$ varies with temperature. An important observation is that the curves saturate successively at higher H/T values as the temperature of measurement is higher. We can therefore conclude that in ferritin $\langle \mu_{un} \rangle$ decreases with temperature. This conclusion is drawn without any assumption of a particular function or distribution. In a general case, if the M_{SP} curves scale, a single fit to all temperatures can be performed and several laws and distribution functions can be tested. This test is performed avoiding the $\chi_{AF}H$ component and knowing beforehand that $\langle \mu_{un} \rangle$ and N are constant with temperature. In antiferromagnetic systems where $\langle \mu_{un} \rangle$ is found to be temperature dependent, as in ferritin, one can still determine the relative variation of $\langle \mu_{un} \rangle$ with temperature, under certain conditions. The conditions are the existence of a narrow μ_{un} distribution, or the existence of a small variation of $\langle \mu_{un} \rangle$ with temperature, compared to the distribution deviation. In one of these two situations there is a scaling factor for each curve such that dividing M_{SP} and multiplying H/T by this same factor scales all curves. In other words, it is possible to find a $M_{SP}/\mu(T)$ vs. $H\mu_{un}(T)/T$ scaling plot. This scaling factor is the relative variation of $\langle \mu_{un} \rangle$ with temperature. Strictly speaking, in ferritin magnetization curves there are no such scale factors and thus a distribution function cannot be ignored. However, ferritin approaches the case where the variation of $\langle \mu_{un} \rangle$ with temperature is small compared with the distribution deviation. Accordingly, a good scaling (Fig. 4.3b) and an estimation of the $\mu_{un}(T)/\mu_{un}(30)$

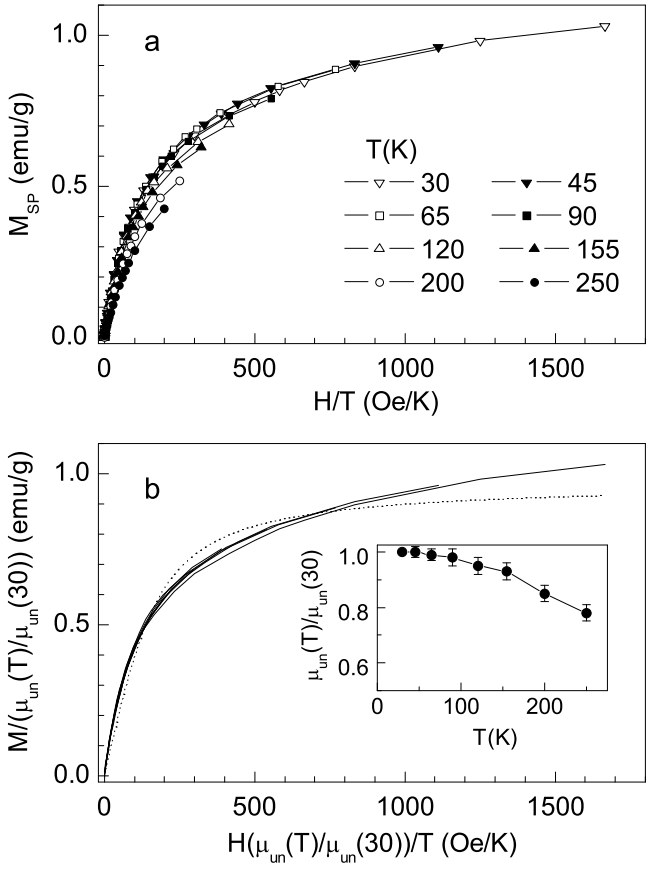

Figure 4.3: a. Ferritin superparamagnetic (saturation) component M_{SP} as a function of H/T; b. M_{SP} in the scaling plot $M_{SP}/(\mu_{un}(T)/\mu_{un}(30))$ vs. $H(\mu_{un}(T)/\mu_{un}(30))/T$. The non-distributed Langevin fit is shown as dotted line. Inset shows the relative $\langle\mu_{un}\rangle$ temperature variation.

ratio (inset of Fig. 4.3b) are obtained. The $\langle\mu_{un}\rangle$ decrease ratio is 0.78±0.03 when the temperature increases from 30 to 250 K.

In summary, without knowing the particular distribution function nor the individual particle magnetization law, this method gives information about the χ_{AF} and $\langle\mu_{un}\rangle$ temperature dependence. The absolute scale of $\chi_{AF}(T)$ and $\langle\mu_{un}(T)\rangle$ are determined by knowing χ_{AF} and μ_{un} at the reference temperature T_0. The subsequent ferritin magnetization curves analysis is therefore enlightened by the information here derived, namely that a distribution function cannot be ignored and that $\langle\mu_{un}\rangle$ decreases with temperature. All this analysis is based on the assumption that the superparamagnetic component of the magnetization scales with H/T.

4.3.2 Application to ferrihydrite/hybrid matrix nanocomposites

We have further applied the scaling method to U2Fe2.1(I) and group II samples and found results similar to those found in ferritin. $(\partial M/\partial H)_T T$ does not scale with H/T and so U2Fe2.1(I) and group II samples have a relevant χ_{AF} contribution, as expected for antiferromagnetic nanoparticles. This can be observed in Fig 4.4a for sample U2Fe2.1(I). The difference between $(\partial M/\partial H)_T T$ curves is not as constant as that found for ferritin (Fig 4.4b), in particular at higher temperatures. However, $\chi_{AF}(T)$ can still be estimated for lower temperatures (see Fig. 4.6). The superparamagnetic component obtained after subtracting $\chi_{AF}(T)$ does not scale with H/T, due to a variation of $\langle \mu_{un} \rangle$ with temperature, as observed in Fig 4.4c and d for sample U2Fe2.1(I). The variation of $\langle \mu_{un} \rangle$ with temperature obtained for group II samples is plotted in Fig. 4.6. The overall trend is a decrease of $\langle \mu_{un} \rangle$ with temperature as found for ferritin.

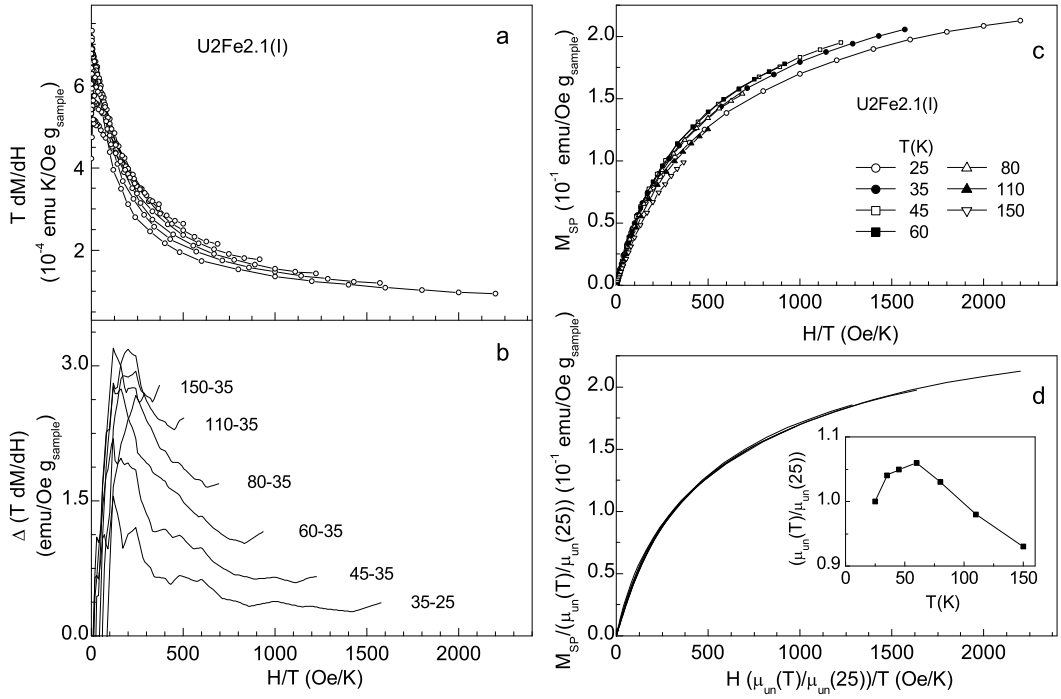

Figure 4.4: a. Representation of $(\partial M/\partial H)_T T$ as a function of H/T for sample U2Fe2.1(I); b. difference between each of the above curves and the $T = 25$ K curve as a function of H/T; c. U2Fe2.1(I) superparamagnetic (saturation) component M_{SP} as a function of H/T; d. M_{SP} in the scaling plot $M_{SP}/(\mu_{un}(T)/\mu_{un}(30))$ vs. $H(\mu_{un}(T)/\mu_{un}(30))/T$. Inset shows the relative $\langle \mu_{un} \rangle$ temperature variation.

4.3.3 Comparison between scaling method and fitting results

An agreement between the $\chi_{AF}(T)$ and $\langle \mu_{un}(T) \rangle$ variation obtained with the fit using a distributed Langevin function and the scaling method is observed both in ferritin (Fig. 4.5)

and in ferrihydrite/di-ureasil samples (Fig. 4.6). In fact, the scaling method gives a smoother variation at higher temperatures. In both procedures we observe a decrease of the average magnetic moment with temperature. Such decrease was already found by Gilles et al. for artificially reconstructed ferritin cores, using the Néel (Eq. 2.70) and lognormal functions [54]. This was done imposing the size distribution obtained by TEM and a power-law relation between magnetic moment and volume. Based on the scaling and on the distributed fits we conclude that $\langle \mu_{un} \rangle$ decreases with temperature and that ignoring the existence of a moment distribution is the cause of the artificial increase of $\langle \mu_{un} \rangle$ and decrease of M_S previously reported in ferritin [51, 173]. The decrease of M_S was also found by several authors in other anitiferromagnetic particles systems as ferrihydrite [151, 178], ferrihydrite doped with Ni, Mo and Ir [176], and NiO [179, 51] and was tentatively associated to a surface moments intrinsic behavior. Our results show that care must be taken to ensure that such an M_S variation has physical meaning and does not come from ignoring a magnetic moment distribution.

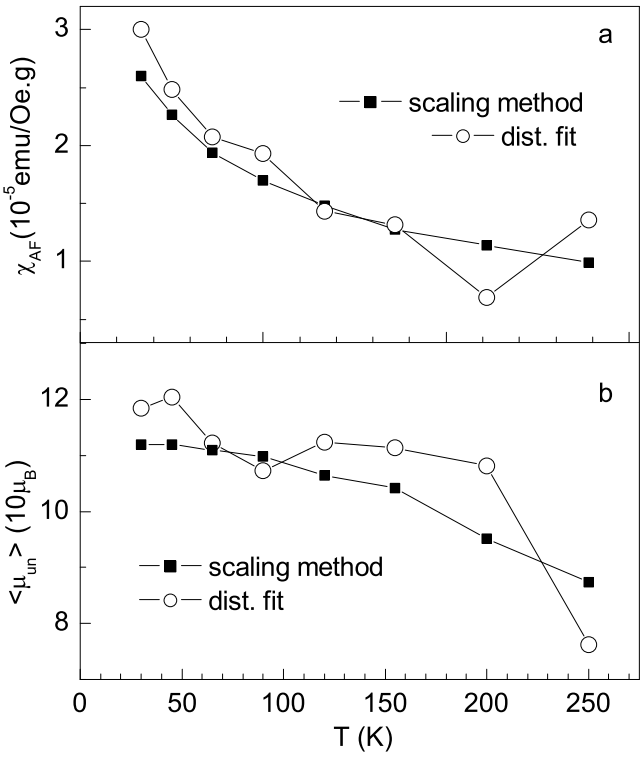

Figure 4.5: χ_{AF} (a.) and $\langle \mu_{un} \rangle$ (b.) obtained with Eqs. 3.8 and 3.9 for ferritin, compared with the values obtained with the scaling method.

On the other hand, the increase of μ_{un} with temperature based on a non-distributed analysis was also observed in artificial ferritin with different core mean sizes [171] and ferrihydrite particles [151, 178]. A closer look reveals that the strongest variations reported take place in powder ferrihydrite samples [151] and in the smaller artificial ferritins [171], where a wider

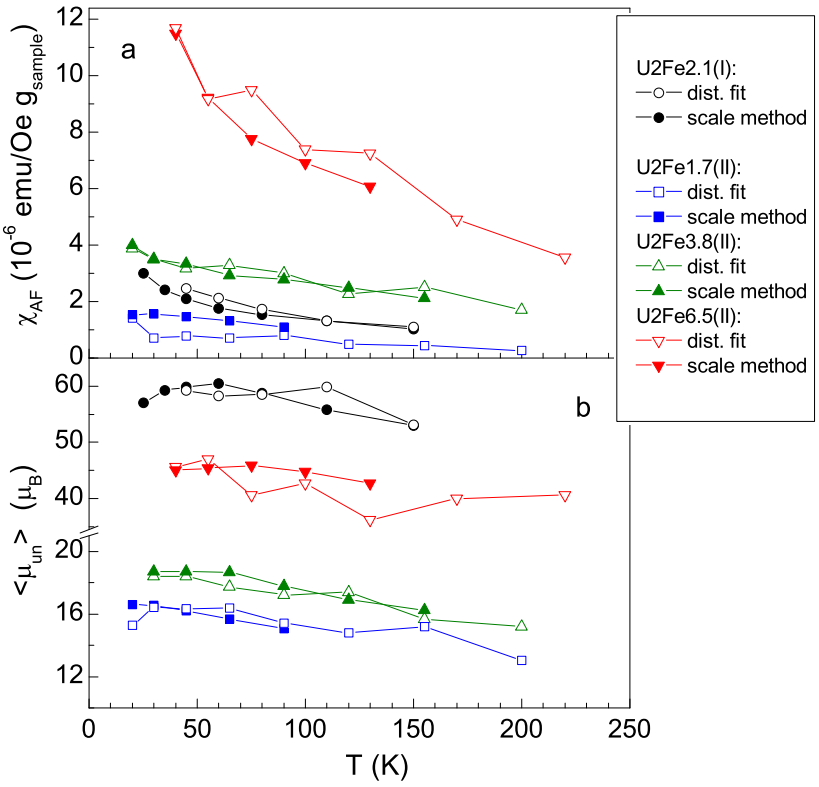

Figure 4.6: $\chi_{AF}(T)$ (a.) and $\langle\mu_{un}(T)\rangle$ (b.) of of group II and U2Fe2.1(I) samples obtained with Eqs. 3.8 and 3.9 compared with the values obtained with the scaling method.

volume and thus $\langle\mu_{un}\rangle$ distribution are likely to occur. Such apparent temperature assisted onset of magnetic moments was associated with interparticle interactions [151], weaker exchange, strong radial anisotropy, frustration, and multiple sublattices (see Ref. [171] and references therein). In addition, recent work interprets this anomalous behavior as dynamic thermoinduced magnetization [177]. Despite the possible contribution of all these features in the referred systems, we show that the existence of a μ_{un} distribution leads to an analogous $\langle\mu_{un}\rangle$ artificial temperature variation that must be carefully analyzed (see also Ref [112]). Thus, the structure information [151, 178, 179, 51], the spin arrangements [51], the thermoinduced magnetization [177], and deviations from the Curie law [219] derived based on that increase raise severe doubts.

Since the mean magnetic moment results from the uncompensated/canted moments of the antiferromagnetic configuration, we may expect that, in a first approximation, $\langle\mu_{un}(T)\rangle$ follows the bulk antiferromagnetic magnons law (Eq. 3.5). Such relation was already observed in ferritin [174] and is also observed using $\langle\mu_{un}(T)\rangle$ derived with the scaling method, as shown in Fig. 4.7. Extrapolating to $\langle\mu_{un}(T^2)\rangle = 0$ one obtains an estimation of the Néel temperature, $T_N \sim 500$ K, in accordance with the value derived in Ref. [174]. Recent neutron diffraction investigations performed on 2.8 nm diameter ferrihydrite powder particles show

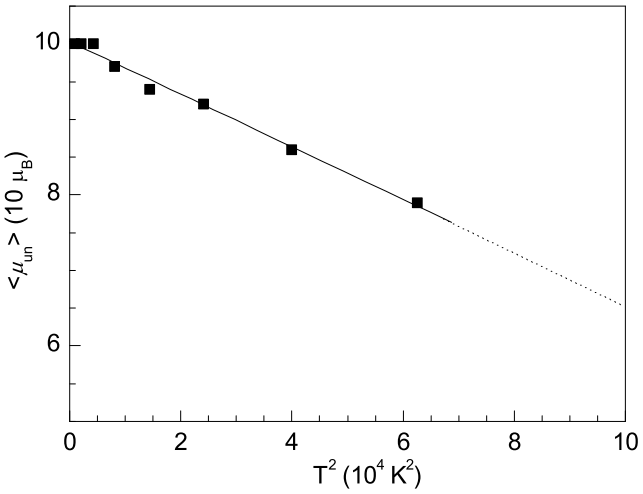

Figure 4.7: Plot of $\langle \mu_{un} \rangle$ against T^2 for ferritin, where the agreement with an antiferromagnetic magnons law (Eq. 3.5, solid line) can be observed.

that $T_N = 330 \pm 30$ K [50]. The difference between this value and our T_N estimation may be due to the difference in the particles size (our ferritin sample has a diameter up to 5 nm) since is likely that T_N decreases as the size decreases. At the same time, 500 K is probably an overestimation of T_N, because the T^2 law is not expected to hold up to such high temperature.

4.4 Relation between size, anisotropy energy and moment investigated by distributions

One of the goals of this chapter is to investigate relations between structural and magnetic properties, which are not clearly established for antiferromagnetic nanoparticles. In particular, there is no a priori established relation between V and μ_{un}. As a consequence, E_a and V can also be not proportional. One may however expect that, in general:

$$\begin{aligned} \mu_{un} &= KV^p \\ E_a &= K'V^q \end{aligned} \tag{4.3}$$

where p and q can be lower than 1. As described in Sec. 2.7, p gives information about the origin of the uncompensated moments, as summarized in Tab. 4.1. In a similar way, E_a can be proportional to volume, to surface, or to a mixture of both, depending on the origin of anisotropy.

In a given situation where $\langle V \rangle$ and $\langle \mu_{un} \rangle$ of one sample are known it is impossible to simultaneous determine K and p, the same being true for $\langle V \rangle$ and $\langle E_a \rangle$. Their determination

is usually done comparing samples with different $\langle V \rangle$, considering that K and p are constant in all samples. This approach is limited by the possibility of synthesizing identical systems with different average volumes, that usually covers less that one order of magnitude. An alternative approach was developed to take advantage of the existence of size distributions. A wide distributed sample can be regarded as one system containing a set of different average sizes. Distributions were qualitatively used by Luis and co-workers for the determination of the origin of magnetic anisotropy in gaussian size-distributed Co nanoparticles [136]. They concluded that surface anisotropy has an important contribution, since the E_a distribution is narrower than the V distribution. The effect of size distributions on the magnetic properties was later used to study two-dimensional Co structures by Rusponi et al. [220]. The idea was based on the fact that the shape of χ' was critically dependent on the chosen distribution, namely surface, perimeter, and perimeter plus surface distributions. The authors concluded that perimeter atoms were those relevant to the reversal process in the Co structures, i. e., E_a depends on the perimeter. Gilles and co-workers have also tried to use susceptibility curves to obtain the relation between μ_{un} and V in ferritin [54]. However, they found that their experimental curves were not very sensitive to the particular shape of distribution nor the value of p [54].

In this section, we show that comparing distributions is quite effective in probing relations between properties. Two general properties are behind this analysis: i) when two variables are directly related by an algebraic expression, the relation between their distributions has valuable information about that expression, and ii) when a variable A is related to two other variables B and C, the distribution of A is a convolution of distributions B and C. Property i) will be described in Sec. 4.4.1 and applied for finding the relation between anisotropy energy and size in sample U2Fe2.1(I) (Sec.4.4.2), and property ii) is in the base of the analysis of size and moment distribution in ferritin.

4.4.1 Relation between lognormal distributed physical quantities

Lets consider two distributed quantities y and x, such that:

$$y = ax^b \tag{4.4}$$

Table 4.1: Relation between the power p and the different origins of μ_{un}.

moments:	in volume	randomly distributed in volume	a surface layer	randomly distributed in surface
$p =$	1	1/2	2/3	1/3

The distribution of y, $g(y)$ is related to the distribution of x, $g(y)$ by:

$$g(y) = f(x)/(dy/dx) \tag{4.5}$$

If $f(x)$ is a lognormal distribution function with parameters s_x and n_x defined as:

$$f(x) = \frac{1}{x s_x \sqrt{2\pi}} \exp - \left[\frac{(\log(x/n_x))^2}{2 s_x^2} \right] \tag{4.6}$$

then $g(y)$ is given by:

$$g(y) = \frac{1}{ab(E/K)^{(b-1)/b}} \frac{1}{(y/a)^{(1/b)} s_x \sqrt{2\pi}} \exp - \left[\frac{[\log((y/a)^{(1/b)}/n_x)]^2}{2 s_x^2} \right] = \\ = \frac{1}{y s_y \sqrt{2\pi}} \exp - \left[\frac{(\log(y/n_y))^2}{2 s_y^2} \right] \tag{4.7}$$

with:

$$n_y = a\, n_x^b \tag{4.8}$$

and

$$s_y = b\, s_x \tag{4.9}$$

This means that if a physical quantity x is lognormal distributed, all other physical quantities that can be related to x by a power relation are also lognormal distributed. More important, when comparing two related physical quantities, the proportion between the distribution parameters s is a direct measure of the power b, while the relation between n gives information about a. Therefore, the relation between V and E, and between V and μ_{un} in one sample can be derived knowing the lognormal distribution of V, E and μ_{un}.

The relations expressed in Eqs. 4.7, 4.8, and 4.9 are a particular case of reproductive properties of the lognormal distribution function [111]. In general, if X_i are independent random variables having lognormal distribution functions with parameters n_i and s_i (as defined in Eq. 4.6), their product $Y = c \prod X_i^{b_i}$ (with b_i and $c > 0$ being constants) is also lognormal distributed, with $s_Y = \sum b_i s_i$ and $n_Y = c \sum n_i^{b_i}$ [111]. In general, reproductive properties can be used in the analysis of an output whose inputs are lognormal distributed, as for instance in quantitative analysis of human information processing during psychophysical tasks [221]. For the best of our knowledge, this is the fist time that they are used in the context of the magnetic properties of nanoparticles.

Although many physical properties of interest as size are often lognormal distributed many others are better characterized by other functions. This is the case of the anisotropy energy, which is often described by a gamma distribution [142, 141, 143, 105]. The gamma

function can be expressed by:

$$f(x) = \frac{B^{-A}x^{A-1}}{\Gamma(A)} \exp - \left(\frac{x}{B}\right) \tag{4.10}$$

with the average of x given by AB and the variance $\sigma = AB^2$. For $A > 1$, the gamma distribution is similar to the lognormal function, so that the the use of the latter function even in the case where the gamma distribution is more suitable may be a good approximation. Therefore the use of Eqs. 4.8 and 4.9 may also be a good approximation to find the parameters a and b. These parameters may also be found in the general case of a different or an unknown distribution, as follows. It is possible to calculate y' and $g(y')$ from experimental measurements of $f(x)$ using Eqs. 4.5 and 4.4, and seed a and b values. Then is possible to find suitable a and b values so that $|g(y') - g(y)|$ is minimum. This can be made by searching for a scaling plot or numerically with a minimization algorithm.

4.4.2 Size and energy distributions

As described in Sec. 2.5.1 and 2.6, χ''/T and S/T constitute a direct measure of the anisotropy energy distribution, observed in different time scales. This is true for non-interacting systems, as found for U2Fe2.1(I) sample, based on ac susceptibility and Mössbauer spectroscopy. In fact, the shape of $S(T)$ changes with the particles concentration, due to dipolar interactions, as shown by Fiorani et al. for maghemite nanoparticles [222]. In Fig. 4.8 we can observe that the distribution obtained from χ''/T and S/T fairly superimpose, meaning that Eq. 2.45 and 2.59 are good approximations. Both χ''/T and S/T curves are well fitted by a gamma distribution function, with A=3.3 and B=53 K (Fig. 4.8). As expected for $A > 1$, both data can also be satisfactorily fitted to similar lognormal functions, with $s_{\chi''/T} = 0.61 \pm 0.02$ and $n_{\chi''/T} = 170 \pm 4$ K, and $s_{S/T} = 0.65 \pm 0.02$ and $n_{S/T} = 176 \pm 4$K, respectively. We therefore consider $s_{E_a} = 0.63 \pm 0.04$ from the average of $s_{\chi/T}$ and $s_{S/T}$. Since $s_D = 0.43 \pm 0.05$, and using Eq. 4.9 we obtain the power relation between E and D $q' = 1.5 \pm 0.2$, so that:

$$E_a = K''D^{3/2} \qquad (K) \tag{4.11}$$

Using $n_{\chi''/T}$ and $n_{S/T}$ on Eq. 4.8 we can determine the proportionality between E_a and $D^{3/2}$, $K'' = 18$ K nm$^{-3/2}$. As expected from Eq. 4.11, we observe that the distribution of $(\chi''/T)^{2/3}$ and $(S/T)^{2/3}$ superimpose to the diameter distribution (Fig. 4.9). This is a confirmation that describing χ/T and S/T by a lognormal function is a good approximation regarding finding q and K''. Eq. 4.11 can be rewritten in terms of the particles volume as:

$$E_a = K'V^{1/2} \tag{4.12}$$

Here we recall that the relation between volume and the uncompensated moments is

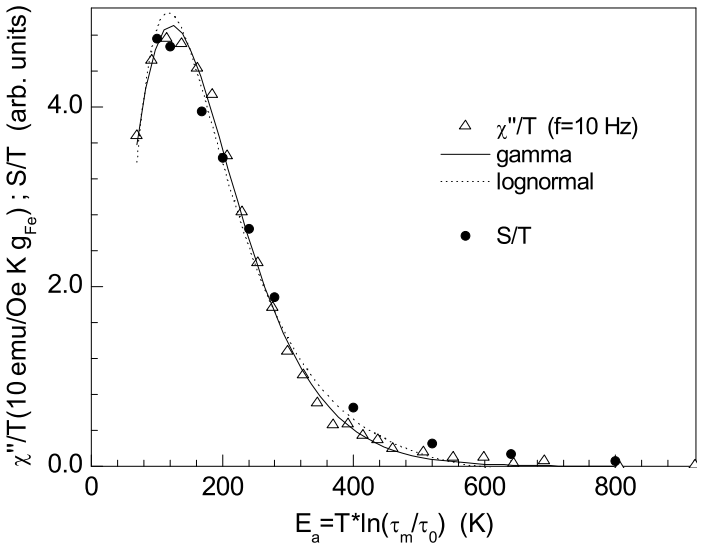

Figure 4.8: Anisotropy energy distribution of sample U2Fe2.1(I) obtained by the out-of-phase component of ac susceptibility (χ''/T) and viscosity (S/T) measurements. Lognormal and gamma distribution fits to χ''/T data are shown.

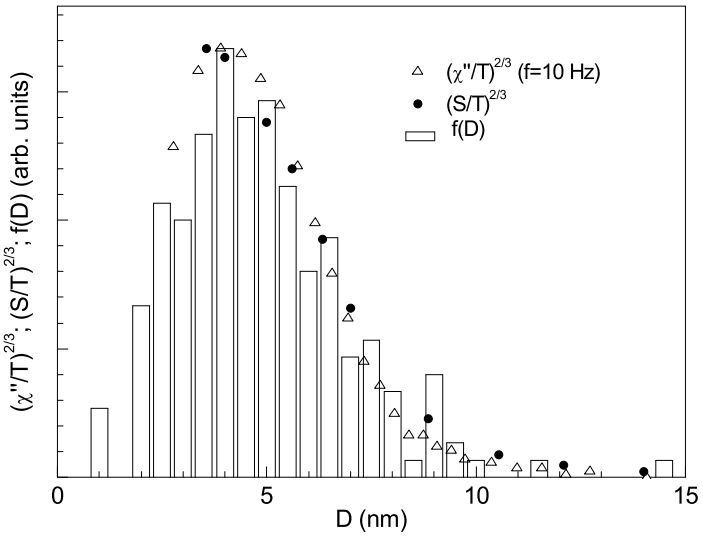

Figure 4.9: Diameter distribution determined by TEM compared to the anisotropy energy distributions obtained by (χ''/T) and (S/T) raised to the power $1/q' = 2/3$, showing the scaling between $E_a^{2/3}$ and D, in sample U2Fe2.1(I). Using other powers such as 3, 2 or 1 gives unsatisfactory scaling.

$\mu_{un} \propto V^{1/2}$, when these are randomly distributed in volume. Such relation was proposed for antiferromagnetic nanoparticles by Néel [164] and is consistent with magnetization measurements performed on ferritin [51, 201]. Thus, it is tempting now to attribute the anisotropy energy to the uncompensated moments of the nanoparticle. In fact, these are the moments

contributing to the Curie-like ac susceptibility and experience the blocking phenomena associated with the onset of χ'' and S. Therefore uncompensated moments should be those relevant in determining the relation between E_a and V. Within this framework, $V^{1/2}$ can be regarded as the equivalent volume that contains the ferromagnetic-like uncompensated moments.

4.4.3 Size and moment distributions

In ferritin, the value of $\langle\mu_{un}(30K)\rangle$=120 μ_B obtained with the distributed Langevin fit is about 5 times lower than the value obtained using a non-distributed Langevin function (Eq. 3.7) and about 0.8 of the value obtained in Ref. [174]. This corresponds to a mean number of fully uncompensated Fe^{3+} ions N_{un} of 23. The number of Fe^{3+} ions involved in the superparamagnetism is obviously higher, as a range between fully compensated and fully uncompensated configurations is expected. Since the mean horse-spleen ferritin core has a total number of Fe ions N_t of about 2000-3000 [43], N_{un} is of the order of N_t^p with $1/2 < p < 1/3$. This suggests that the uncompensated spins are not only at the surface but also randomly distributed through the volume. On the other hand, one would expect to derive p based on Eq. 4.9. The lognormal moment deviation s_μ obtained with the fit procedure varies from a 0.9 at 30 K, to 1.3 at 65 K, and to 1.0 at 250 K. These values are about 10 times higher than the typical value of the ferritin diameter distribution (max. $s_D = 0.2$ [174]). Therefore, $s_V = 0.6$ and $p = 1/0.6 = 1.7$, which has no physical ground, since we should have $p \leq 1$. We find two possible explanations for this disagreement: the $M(H)$ analysis is not suitably describing the system, yielding an overestimation of s_μ and/or the estimation of s_μ is correct and has contributions other than the size distribution. Putting this last explanation in other words: an important magnetic moment distribution exists even in a case where the size distribution is of minor importance. This points out the existence of particles with approximately the same size but different degrees of inner or surface structure/magnetic disorder. The uncompensated moment distribution would then be the convolution of the size and "disorder distribution".

For sample U2Fe2.1(I) the scenario is different: from $M(H)$ analysis we obtain $s_\mu = 0.9$ (similar to the value found for ferritin), while $s_D = 0.43 \pm 0.05$ and thus $s_V = 1.3 \pm 0.2$. This implies $p = 0.7 \pm 0.1$, that can be addressed as $p \approx 2/3$. It is clear that here disorder does not play such an important role as in the case of ferritin. This does not mean that here disorder is lower than in ferritin but just that now the size distribution is broader than the "disorder distribution", so that the convolution of both is dominated by size. Yet, the existence of disorder may bring inaccuracy to the determination of p. We note that p here derived is different than that found comparing the average values of N_{un} and N_t ($p = 1/3$, see Sec. 3.4.6). It is interesting to note that both p values are obtained based on the same analysis made on the $M(H)$ curves. The only difference is the approach of deriving p: using

average values of the uncompensated moment and size or using the information about the distribution of both. This is an example of how the use of averages may lead to inaccurate estimations, since the pre-factor of the power law is also involved.

The exponent p must also be compared to the results of the analysis of the relation between anisotropy energy and volume (Sec. 4.4.2). We have found $E_a \propto V^{1/2}$ and argued that this corresponds to the volume that contains uncompensated moments randomly distributed in volume. In this framework, p would be equal to $1/2$, while in the previous paragraph we found $p \approx 2/3$. We believe that this difference may reflect problems in determining p, which does not results from direct measurements as q, but from modeling $M(H)$ curves.

4.5 Summary

In this chapter, we have presented a method to separate saturation and linear components of magnetization of antiferromagnetic nanoparticles, and extract qualitative and quantitative information about the average uncompensated magnetic moment, the antiferromagnetic susceptibility, and their temperature dependence. This method was successfully applied to ferritin, a model for antiferromagnetic nanoparticles, and to the ferrihydrite/di-ureasil nanocomposites. The antiferromagnetic susceptibility and the uncompensated magnetic moment were found to decrease with temperature, with the latter following a magnons law. Extrapolating this dependence we have estimated a Néel temperature of about 500 K.

We have also shown how distributions can be used to investigate basic properties of the nanoparticles. These basic properties cannot be obtained by comparing average values, and include the determination of the origin of the magnetic moment and anisotropy energy (i. e. if the magnetic moment has volume, surface, or random origin, for instance). The concept of using distributions is based on reproductive properties of the lognormal distribution function and can be generalized to other functions. We have applied this concept to ferritin and concluded that an important role played by disorder in the magnetic properties becomes visible, as the size distribution is narrow. By using distributions it was also concluded that the anisotropy energy is proportional to the square root of the volume of the nanoparticles, indicating that the uncompensated moments, being responsible for the anisotropy, are randomly distributed in volume.

Chapter 5

Iron oxyhydroxynitrate/hybrid matrix composites

5.1 Overview

In this chapiter we present the synthesis of low crystalline and crystalline iron oxyhydroxynitrate phases inside di-ureasil matrices, using solvolysis routes. The evolution of structural and magnetic properties of low crystalline iron oxyhydroxynitrate phases with thermal treatment is studied based on XRD and ac susceptibility measurements. Magnetization, dc susceptibility and Mossbaüer spectroscopy studies of a crystalline iron oxyhydroxynitrates phase are also presented.

5.2 Low crystalline iron oxyhydroxynitrates

As seen in Sec. 3.5 of the last chapter, some amount of amorphous iron oxyhydroxynitrate is formed for higher ethanol/water ratios. Following this result, we have further reduced the amount of water present in the system by using solvolysis sol-gel route instead of the hydrolysis one.

5.2.1 Synthesis

As in the synthesis of the ferrihydrite/di-ureasils nanocomposites, the preliminary step of the nanocomposites preparation involves the synthesis of a cross-linked hybrid precursor. As described, this is achieved by the formation of urea linkages between the terminal NH_2 groups of a doubly functional amine (α, ω-diamine poly(oxyethylene-cooxypropylene)) and the isocyanate group of an alkoxysilane precursor (3- isocyanatepropyltriethoxysilane, ICPTES, Fluka) in tetrahydrofuran (THF, Merck) at room temperature (RT). At this step, diamines having poly(oxyethylene-cooxypropylene)) with different molecular weight (M_w)

can be used. In this study we have used the commercially available Jeffamine ED-2001 ® (Fluka) with M_w=2000. The iron(III) nitrate nonahydrate ($Fe(NO_3)_3.9H_2O$, Aldrich) was incorporated in the second step of the synthetic procedure. Samples were prepared, containing iron nitrate corresponding to a theoretically amount of Fe in the final material of 5% wt. The salt was dissolved in a mixture of ethanol, water and acetic acid (molar proportion ICPTES/CH_3CH_2OH/Ac=1:4:3). This solution was added to the non-hydrolyzed hybrid precursor prepared in the first stage. The resulting mixture was then stirred in a sealed flask for a few minutes at RT. After this, the solution was cast into a mould and gelation did not took place immediately. The mould was covered with Parafilm with needle holes and dried at ambient conditions for several days until gelation occurred. We must stress that gelation did not occur in the case of samples that were not doped with salts and were kept up in a nitrogen atmosphere for about 10 days [32]. Di-ureasil xerogels were thus formed by exposure of the corresponding sols to ambient humidity and probably to iron salt coordination water. The mould was then transferred to an oven at ca. 40 °C, for a period of 7 days. The final material is a mechanically stable and orange-red transparent film. These samples were synthesized by Doctor Lianshe Fu.

Different samples were then obtained by successively heating the sample with 5% Fe wt and M_w=2000 at 50°, 60°, 70° and 80°C, during 48 hours at each temperature. With the thermal treatment, samples became opaque and their color changed to brown. Samples were labeled U2Fe5AA40, U2Fe5AA50, U2Fe5AA60, U2Fe5AA70 and U2Fe5AA80.

5.2.2 XRD

The XRD patterns of U2Fe5AA40 U2Fe5AA50,U2Fe5AA70 and U2Fe5AA80 samples are shown in Fig. 5.1. The pattern of the U2Fe5AA40 sample display a bump centered at $2\theta \simeq 46°$, associated to the siliceous domains of the di-ureasil matrix [32]. After heating the sample at 50°C, peaks associated to an iron oxyhydroxynitrate phase become apparent. The most relevant of these peaks are labeled as a. and b. in Fig. 5.1. In the case of schwermannite, peak a. and b. correspond to plans (212) and (004), respectively [44]. Since this iron oxyhydroxynitrate phase and schwermannite have similar XRD profiles (see Fig. 1.10(a)) and are thought to have similar structure, it is plausible that peaks a. and b. correspond to similar plans.

When the temperature is further increased, some new peaks, at $2\theta \simeq 33$, 38, 47 and 58°, appear. As described in Ref [44], in water solution, the iron oxyhydroxynitrate transforms into ferrihydrite and then to hematite. However, the peaks found at $2\theta \simeq 33$, 38, 47 and 58° do not correspond to hematite (see Fig. 5.1) nor to any other common iron phase. At the same time, the peaks do not seem to be due to the crystalline iron oxyhydroxynitrate reported by Pelloquin et al. [59]. The peaks may therefore correspond to another iron phase containing nitrate ions, here generally termed as iron oxyhydroxynitrate. It is expected that

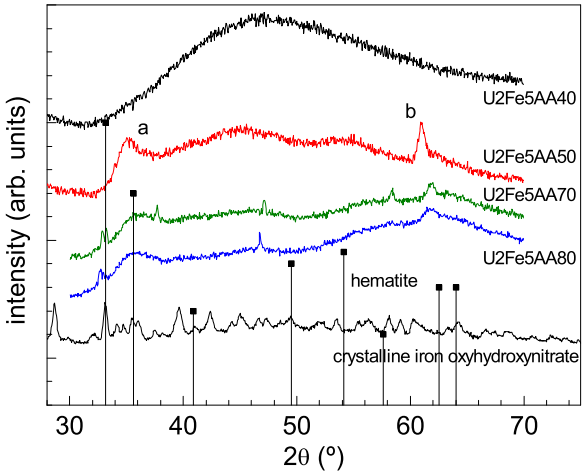

Figure 5.1: XRD patterns of U2Fe5AA40, U2Fe5AA50, U2Fe5AA70 and U2Fe5AA80 samples. The XRD pattern of the crystalline iron oxyhydroxynitrate phase (see Sec. 5.3) and the position of hematite peaks are also shown for comparison.

at sufficiently high temperatures a more thermodynamically stable phase such as hematite or goethite is obtained. However, in the di-ureasil matrix the pathway to obtain these phases does not seem to include ferrihydrite but a set of iron oxyhydroxynitrate phases.

As described in Sec. 3.3.1, the coherence length L over which the crystalline order extends can be estimated using Eq. 3.1. The values of L found for the peaks labeled a. and b. (L_a and L_b) are given in Tab. 5.1. One observes that L decreases with increasing temperature of sample treatment. Considering the peak attribution discussed in the previous paragraph, L_b corresponds to the z direction, while L_a has an important component in perpendicular directions. Therefore, the differences between L_a and L_b show that the iron oxyhydroxynitrate phase is constituted by elongated nanoparticles. Moreover, the evolution of L_a and L_b with the thermal treatment shows that the initial stages correspond to the formation of more elongated nanoparticles. The nanoparticles volume, estimated as $V = L_a^2 \times L_b$, decreases with the thermal treatment, which is consistent with a condensation process leading to the formation of more close-packed iron oxyhydroxynitrate phases.

Table 5.1: Coherence lengths L_a and L_b associated to the peaks at $2\theta = 35°$ and $61°$, respectively. The volume of the particles was estimated considering a parallelepiped with dimensions $L_b \times L_a \times L_a$.

sample	$L_b \pm 1$ (nm)	$L_a \pm 1$ (nm)	$V = L_b \times L_a^2$ (nm^3)
U2Fe5AA50	13	5	325
U2Fe5AA70	12	3	108
U2Fe5AA80	9	2	36

5.2.3 Ac susceptibility

The in-phase χ' and out-of-phase χ'' components of the magnetic susceptibility of U2Fe5AA50, U2Fe5AA60 and U2Fe5AA70 samples are plotted in Fig. 5.2 as a function of temperature (in the 2-35 K range), for selected frequencies in the $f = 0.1 - 1500$ Hz range. χ' is almost independent of f, while χ'' is almost zero. A small onset of χ'' is observed in sample U2Fe5AA70.

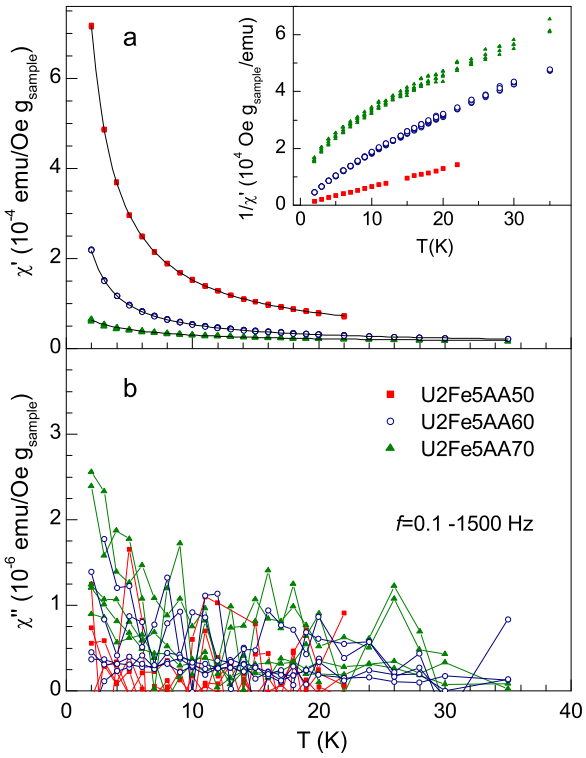

Figure 5.2: Ac susceptibility as a function of temperature of samples U2Fe5AA50, U2Fe5AA60 and U2Fe5AA70. a. in-phase component $\chi'(T)$, b. out-of-phase component $\chi''(T)$. The field frequencies are 0.1, 1, 10, 117, 852 and 1488 Hz. Continuous lines are fits to Eq. 3.4. Inset of panel a. show the inverse of $\chi'(T)$ as a function of temperature.

We have fitted χ' curves to a Curie-Weiss law added to a χ_0 temperature independent term (Eq. 3.4). Fit parameters are displayed in Tab. 5.2. The Curie constant, C, decreases with the temperature of treatment, while T_0 and χ_0 increase. Considering that the amount of iron does not change with the thermal treatment, we observe that the effective moment, μ_{eff} decreases with the heat treatment temperature. This is true since any relative weight lost is much lower than the changes observed in C. Therefore the thermal treatment is promoting the establishment of antiferromagnetic interactions. As a result of these interactions χ_0 increases. The observed increase of $|T_0|$ is usually associated to an increase of dipolar interactions. The origin of such increase is not clear, since the average interparticle distance

is supposed to remain constant with the treatment and, at the same time, the magnetic moment of the particles decreases with the treatment. One possible explanation is the onset of some blocking within the studied temperature range. Such blocking seems to occur, since χ'' is different from zero, at least in samples treated at higher temperatures. If such blocking exists, as temperature decreases, χ' is successively lower than the expected from the Curie law, leading to the appearance of a T_0 value without a physical meaning.

Table 5.2: Curie constant, C, T_0 and χ_0 parameters resulting from fitting ac susceptibility data of U2Fe5AA samples to Eq. 3.4. The effective moment μ_{eff}, was estimated considering Fe=5% wt.

sample	C (10^{-4} emu K/Oe g_{sample})	μ_{eff} ($\pm 0.3\ \mu_B$)	T_0 (K)	χ_0 (10^{-6} emu/Oe g_{sample})
U2Fe5AA50	14.9 ± 0.1	3.6	-0.09 ± 0.01	5.2 ± 0.4
U2Fe5AA60	4.54 ± 0.02	2.0	-0.17 ± 0.01	9.0 ± 0.2
U2Fe5AA70	2.2 ± 0.1	1.4	-2.7 ± 0.3	11.0 ± 6

5.3 Crystalline Iron oxyhydroxynitrate

The iron ions of the samples treated at 40° are not in a stable configuration, even at room temperature. In fact, with time the composites changes their color and become opaque, as described below.

5.3.1 Synthesis

As in the previous synthesis, the preliminary step of the nanocomposites preparation was the preparation of a cross-linked hybrid precursor using, in this case, Jeffamine ED-600 ® (Fluka). The iron(III) nitrate nonahydrate ($Fe(NO_3)_3.9H_2O$, Aldrich) was incorporated in the second step, corresponding to a theoretical amount of Fe in the final material of 10% wt. The salt was dissolved in a mixture of ethanol, water, and acetic acid (molar proportion ICPTES/CH_3CH_2OH/Ac=1:4:3) and added to the non-hydrolyzed hybrid precursor. The resulting mixture was then stirred in a sealed flask for a few minutes at RT. The mould was covered with Parafilm with needle holes and dried at ambient conditions for several days until gelation occurred. The mould was then transferred to an oven at ca. 40 °C, for a period of 7 days. The final material was a mechanically stable and orange-red transparent film.

After a few months in ambient conditions, the color of the samples changed from red-orange to red-brick and they became opaque. This indicates a slow condensation of the iron octahedra towards the formation of an iron phase. The transformation time is about 1 year and the sample was termed U6Fe10AA1yr. These samples were synthesized by Doctor Lianshe Fu.

5.3.2 XRD

The XRD pattern of U6Fe5AA1yr sample is shown in Fig. 5.3. The pattern displays narrow peaks associated to the crystalline iron oxyhydroxynitrate described by Delgado et al. [58, 59]. There is a systematic difference between the peaks of the U6Fe5AA1yr sample and those of Ref. [59]. This difference is of about 0.3°, constant with 2θ, being associated to an error in the zero position, rather than a change in the cell parameters. The coherence length L associated to this phase is 25 nm. The pattern shows also broad peaks at $2\theta = 22$ and 45°, due to the siliceous domains of the di-ureasil matrix [32].

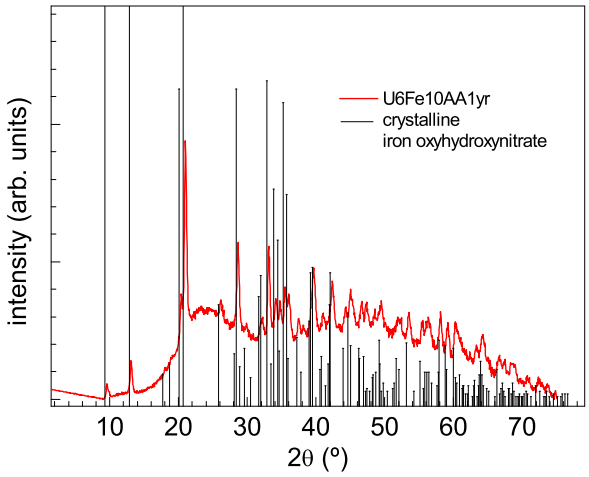

Figure 5.3: XRD pattern of U6Fe10AA1yr sample. The peak position of the reported crystalline iron oxyhydroxynitrate phase are also shown for comparison (Ref. [59], PDF 01-089-6191).

5.3.3 SEM

SEM images were obtained at 25 kV on a Hitachi Field Emission S-4100 microscope. The sample was coated with a carbon film. A typical SEM image of the di-ureasil/crystalline iron oxyhydroxynitrate composite is shown in Fig. 5.4. The image shows the existence of micrometer particles or aggregates, with a rough surface. The existence of iron in the particle was not confirmed by EDS. However, the particle can be clearly associated to the iron oxyhydroxynitrate phase since such micrometer particles do not appear in the SEM images of non-doped and rare-earth doped di-ureasils studied up to now. The particles are about one order of magnitude larger than the characteristic size determined by XRD, showing that the micrometer particle is constituted by several crystallites.

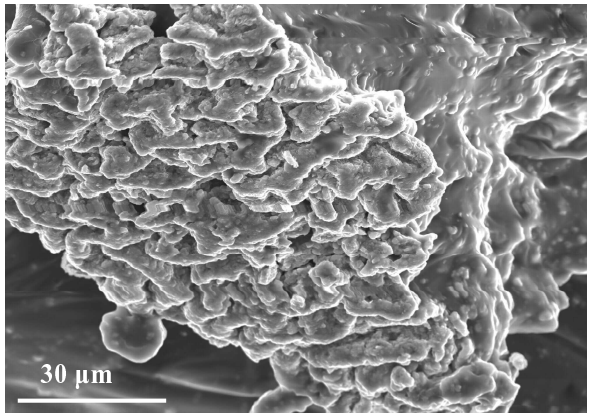

Figure 5.4: SEM image of U6Fe10AA1yr sample.

5.3.4 Magnetic properties

Magnetization

The magnetization curves of U6Fe10AA1yr sample are show in Fig. 5.5, as a function of the field (a) and as a function of H/T (b). At the lowest temperature (10 K) the magnetization shows partial saturation, associated to isolated Fe^{3+} ions, similar to the case of Fig. 3.28, Sec. 3.5.4. However, unlike the latter case, the curves to not scale with H/T, showing that the U6Fe10AA1yr sample contains also non-isolated Fe^{3+} ions, i. e., ions that experience interactions. Another important observation is that the system has no remanent magnetization ($M_r = 0 \pm 2 \times 10^{-5}$ emu/g$_{sample}$).

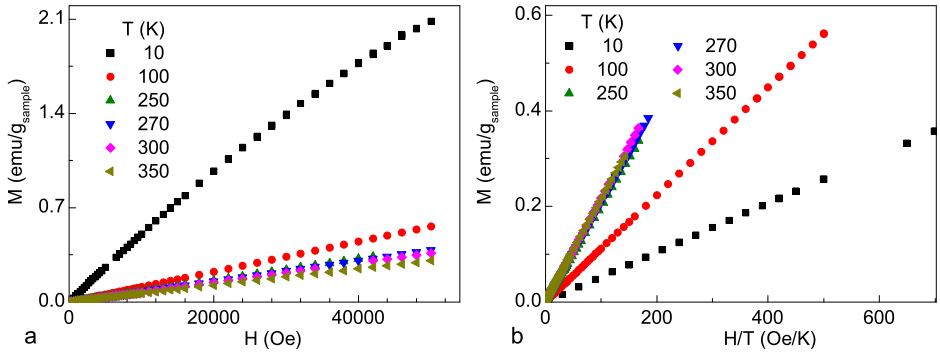

Figure 5.5: a. Magnetization of U6Fe10AA1yr sample as a function of field at selected temperatures; b. same data plotted as a function of H/T.

Dc susceptibility

Since no remanent magnetization was found in the $M(H,T)$ curves, the inverse of the dc susceptibility can be used to investigate the type of interactions present in the system. The $1/\chi(T)$ curve (Fig. 5.6b) resembles that of a ferrimagnetic material. Fitting $1/\chi(T)$ to the two sublattice mean field model for ferrimagnets (Eq. 2.83) we obtain a transition temperature of the order of 1 K and an high temperature extrapolation $\theta_p = -1700 \pm 100$ K. Considering just a linear extrapolation on obtains $\theta_p = -720$ K, which is closer to the characteristic values found in iron oxides.

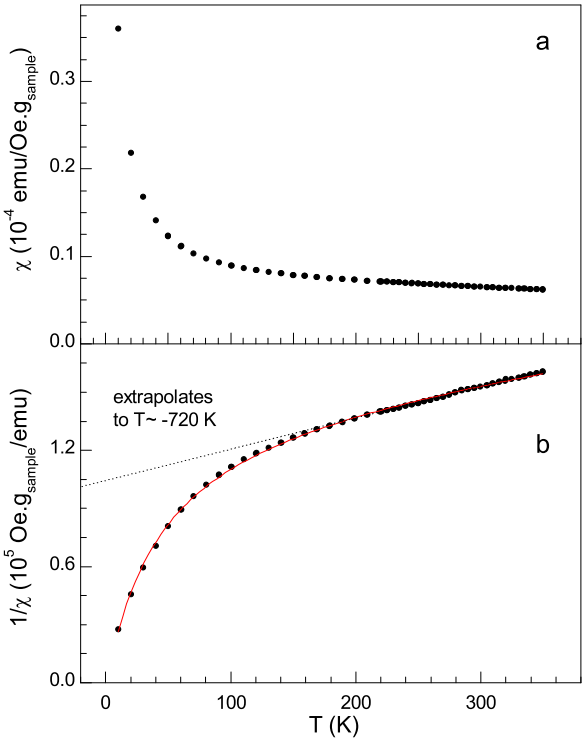

Figure 5.6: a. Dc susceptibility of U6Fe10AA1yr sample, recorded with H=50 Oe as a function of temperature; b. inverse of dc susceptibility of U6Fe10AA1yr sample as a function of temperature. Line represent fit to Eq. 2.83.

5.3.5 Mössbauer spectroscopy

Mössbauer spectroscopy results of the U6Fe10AA1yr sample performed at 4.2 K are shown in Fig. 5.7. Qualitatively it may be observed that the spectrum is constituted by a doublet superimposed to a sextet. This shows that part of the Fe^{3+} ions are in the paramagnetic or superparamagnetic state and another part is in an ordered state or superparamagnetic/blocked state. Since the dc susceptibility and magnetization measurements show no evidence of superparamagnetism but the existence of isolated ions and ions with interactions, the Mössbauer

spectroscopy results must be interpreted as being due to paramagnetic and ordered Fe^{3+} ions. Further studies will include the variation of the spectrum with temperature and the spectrum obtained with an external applied field.

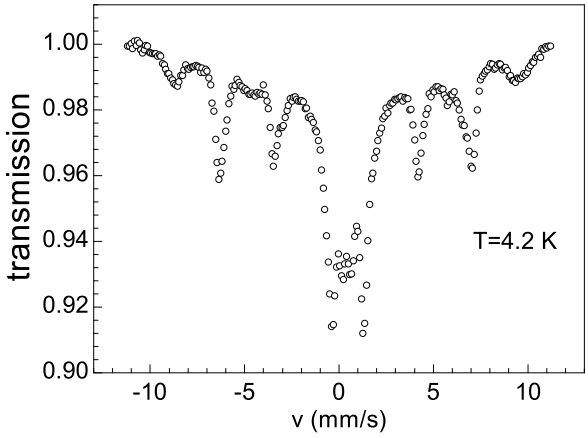

Figure 5.7: Mössbauer spectroscopy measurements of the U6Fe10AA1yr performed at 4.2 K.

5.4 Summary

In this chapter we explored the formation of iron oxyhydroxynitrate particles in di-ureasil matrix. This was performed using a solvolysis sol-gel route, after the observation of iron oxyhydroxynitrate in di-ureasils synthesized with larger amounts of ethanol, as reported in the previous chapter, Sec. 3.5. The low crystalline iron oxyhydroxynitrate phases reported in that section are probably precursors of ferrihydrite, similar to those previously reported by Schwertmann and co-workers [44] (represented in Fig. 5.8 as a blue hexagon). Using the solvolysis route it is possible to grow low crystalline iron oxyhydroxynitrate phases that, after thermal treatment inside the di-ureasil matrix do not transform into ferrihydrite but to other iron oxyhydroxynitrate phases. These are represented in Fig. 5.8 as an orange hexagon. The di-ureasil matrix can be therefore used either to capture different intermediate states of ferrihydrite or to serve as a non-aqueous reactor where new iron oxyhydroxynitrate phases are formed. In fact, the di-ureasil matrix is better described as a reactor than as a "freezing agent", since the most unstable phases are able to evolve with time. In particular, a crystalline iron oxyhydroxynitrate phase is formed in one of the di-ureasil/iron nitrate samples treated at 40°C (sample U6Fe10AA) after about one year at room temperature (represented in red in Fig. 5.8). The possible inter-transformation between these phases (dotted arrows in Fig. 5.8) and their possible transformation into other common iron oxides requires future studies.

The low crystalline iron oxyhydroxynitrate phases reported in this chapter have anti-

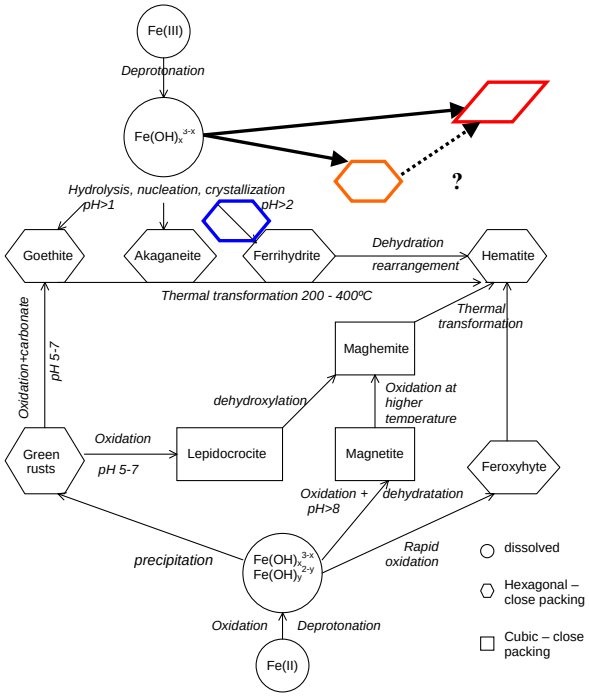

Figure 5.8: Schematic representation of formation and transformation pathways of the iron oxyhydroxynitrates phases, in the framework of the formation and transformation of common iron oxides as proposed in Ref. [38]. Blue hexagon correspond to iron oxyhydroxynitrates which are precursors of ferrihydrite (Sec. 3.5), the orange hexagon corresponds to the low crystalline iron oxyhydroxynitrate phase discussed in Sec. 5.2, and the red lozenge corresponds to the crystalline iron oxyhydroxynitrate phase discussed in Sec. 5.3.

ferromagnetic interactions, as deduced from magnetometery studies. The number of iron ions antiferromagnetically coupled increase as the iron oxyhydroxynitrate phase transforms from chain-shaped nanoparticles to more condensed ones. The crystalline iron oxyhydroxynitrate phase here reported has a fraction of paramagnetic iron ions and another fraction experiencing interactions. Based on dc susceptibility measurements the crystalline iron oxyhydroxynitrate phase is better described as a ferrimagnet, with a transition temperature of the order of 1 K.

Chapter 6

Maghemite and magnetite/hybrid matrix nanocomposites

6.1 Overview

In this chapter we describe some approaches to synthesize maghemite and magnetite nanoparticles in organic-inorganic matrices, inspired by the in situ growth of such particles in polymers. Magnetic measurements show the existence of weakly interacting superparamagnetic nanoparticles. From ac susceptibility measurements it was possible to determine the anisotropy energy and estimate the characteristic size of the nanoparticles. A first study on the influence of the density of binding points in the formation of maghemite nanoparticles is presented.

6.2 Synthesis

Both ferrihydrite and iron oxyhydroxynitrate nanoparticles can be formed at about the same pH of formation of the di-ureasil matrix (pH$<$ 7). This contributes to the success of growing such phases in di-ureasils. This is not the case of the ferrimagnetic iron oxides maghemite and magnetite, which are formed in basic conditions (see Fig. 1.4, and Sec. 1.3.4 and 1.3.3). Therefore, a basic treatment which is not part of the di-ureasil synthesis will have to be introduced in the procedure. In the following paragraphs, some approaches to the synthesis of maghemite and magnetic nanoparticles in the di-ureasil matrix are presented. The general approach is an in-situ precipitation of the nanoparticles, inspired in the synthesis of maghemite in polyvinylpyridine [183]. The samples here studied were synthesized in collaboration with Doctor Lianshe Fu and Prof. Angel Millan.

6.2.1 Maghemite

As above described, the synthesis of maghemite at low temperature must include a basic treatment. Unfortunately, it was observed that the matrix is not stable under base treatment with |NaHO|=1 M, commonly used in the synthesis of maghemite. This is particularly severe in the case of the di-ureasils with longer poly(oxyethylene) chains, as the d-U(2000). Therefore a weaker base was used: $|NH_4OH|$=1 M. Another important question related to the synthesis of maghemite is the existence of Fe^{2+}, which is crucial to the nucleation of the particles.

The first set of di-ureasil/maghemite composites was produced using pre-prepared d-U(600) matrices (using the procedure described in Sec. 1.2.5). These matrices were placed into a solution of $|FeBr_2|$=0.5 M and $|FeBr_3|$=1 M, at room temperature during 24 h. The 0.5 M $FeBr_2$ 1 M $FeBr_3$ solution was prepared as follows. An appropriated amount of $FeBr_2$ and $FeBr_3$ salts (Aldrich) is dissolved in water, with stirring at room temperature. The solution is then decanted in the presence of a permanent magnet and filtered to separate any iron colloids or small nanoparticles. The matrices with the incorporated Fe^{2+} and Fe^{3+} ions were then treated with 1 M NH_4OH solution (Aldrich)during 1 h, washed with water, and dried at ca. 40°C for a period of 24 h [223]. One of these samples, whose characterization is presented below, was termed U6Maghem.

The procedure described in the previous paragraph was also applied using di-ureasil matrices with longer chains, namely d-U(900) and d-U(2000) matrices. However, the Fe^{2+} and Fe^{3+} ions were not coordinated to the matrix with sufficient strength, so that migration was observed during the basic treatment. This migration caused inhomogeneity in the system. To overcome the migration another synthesis procedure was tested. In this second procedure, the 0.5 M $FeBr_2$/1 M $FeBr_3$ solution was added to the hybrid precursor to trigger the hydrolysis and condensation of the matrix. The amount of Fe was calculated so that the final concentration was 3% wt. Hybrid precursors with different chain length were used, namely those obtained from Jeffamine ED-2001 ®, Jeffamine ED-900 ® (Fluka), Jeffamine ED-600 ®, Jeffamine ED-400 ® and (Fluka) Jeffamine ED-250 ®. The samples were then dried at 40°C during 15 days. The dried samples were treated with 1 M NH^4OH solution during 24 h. The sample obtained from Jeffamine ED-2001 ® dissolved in the basic solution and therefore no film was obtained. This was not the case of samples obtained from other Jeffamines, where no migration or surface precipitation was observed. The samples were washed and dried at 60°C during 2 days. Samples were termed U9Fe3(1:2)Maghem, U6Fe3(1:2)Maghem, U4Fe3(1:2)Maghem and U3Fe3(1:2)Maghem. In the following sections a preliminary study on sample U6Fe3(1:2)Maghem will be presented. As usual, "U" designates the urea cross-linkage, "6" is an indication of the polymer chain length, "(1:2)" is the proportion of organic/inorganic precursors (Jeffamine/ICPTES), and "Maghem" indicates the existence of maghemite nanoparticles.

Aiming a better coordination of the Fe ions by the di-ureasil matrix a third procedure was tested. The idea is to perform the synthesis of the hybrid precursor with excess of ICPTES (inorganic precursor), so that some isocyanate (-N-C=O) groups do not react with the NH_2 groups of Jeffamine, being able to act as extra coordination points. Hybrid precursors with Jeffamine/ICPTES ratios of 1:4 and 1:2 (control sample, without excess of ICPTES) using Jeffamine ED-600® were prepared. The hybrid precursor was then used to grow maghemite nanoparticles according to the procedure described in the previous paragraph. Samples were termed U6Fe3(1:2)Maghem and U6Fe3(1:4)Maghem.

6.2.2 Magnetite

The synthesis of di-ureasil/magnetite nanocomposites is analogous to the one described for the first set of di-ureasil/maghemite samples. The di-ureasil/magnetite nanocomposites were produced after the immersion of an undoped d-U(600) matrix in a solution of ammonium iron(II) sulfate hexahydrate $(NH_4)_2Fe(SO_4)_2 \cdot 6H_2O$, Aldrich) during 24 h. The material was treated with 1 M NH_4^+ solution during 1 h at 100°C, washed with water and dried at ca. 40°C for a period of 24 h. The sample here studied was termed U6Magne.

6.3 XRD

The XRD patterns of U6Maghem and U6Magne samples (shown in Fig. 6.1) exhibit peaks characteristic of spinel structures. The XRD pattern of U6Maghem sample is dominated by the two most intense peaks of the spinel structure (labeled with ∘), whereas the pattern of U6Magne sample display a more ordered structure (peaks labeled with ⋆). The application of Eq. 3.1 formula gives coherence lengths L of the order of 10 and 2 nm for magnetite and maghemite nanoparticles, respectively.

Both patterns display also a broad peak centered at $2\theta \simeq 21°$, associated to the siliceous domains of the di-ureasil matrix [32]. The pattern of U6Magne sample shows also a broad peak at ca. $2\theta = 3.2°$, due to an interference effect between siliceous domains, spatially correlated at an average distance of 2.7 nm [35, 32] (see Sec 1.2.5). This shows that the growth of the magnetite nanoparticles does not disrupt the nanostructure of the matrix.

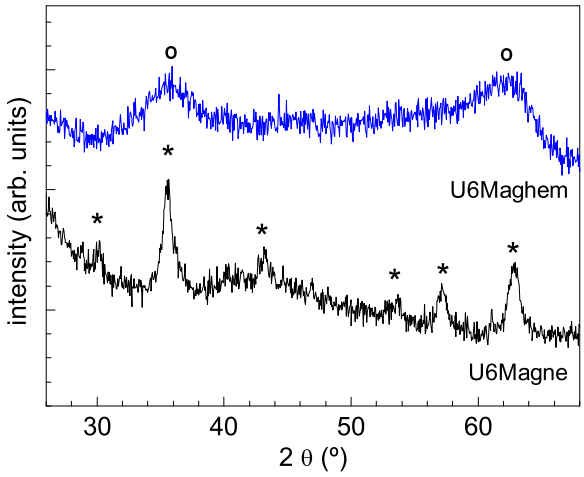

Figure 6.1: XRD patterns of U6Maghem and U6Magne samples. Peaks attributed to the spinel structure of maghemite and magnetite are labeled with ∘ and ⋆, respectivelly.

6.4 Ac susceptibiliy

6.4.1 Maghemite

The in-phase χ' and out-of-phase χ'' components of the magnetic susceptibility of U6Maghem sample are plotted in Fig. 6.2 as a function of temperature (in the 2-260 K range), for selected frequencies in the $f = 0.1 - 1000$ Hz range. χ' is frequency dependent in all temperature range with the concomitant non-zero value of χ'', showing frequency dependent maxima at temperatures of the order of 25 K. As seen in the previous chapters, this is expected for superparamagnetic nanoparticles that became blocked at a given temperature, depending on the characteristic time of the measurement (see Sec. 2.2). The maxima of χ' follows a Néel-Arrhenius law (Eq. 2.2), as observed in the inset of Fig. 6.2. The extrapolated τ_0 is of the order of 10^{-12} s, characteristic of non-interacting/low interacting maghemite nanoparticles [102, 155], and the anisotropy energy E_a is 720±25 K. Considering the typical values of K_{eff} found of maghemite nanoparticles (3.9×10^5 erg/cm^3 [155]), we can estimate the characteristic diameter of spherical particles as 8 nm. Since $L \approx 2$ nm it is expected that each particle has more than one crystallite with 2 nm and/or an important fraction of amorphous material. Further SAXS and TEM studies may clear this point and alow an estimation of K_{eff}.

6.4.2 Magnetite

The dependence of χ' and χ'' with frequency and temperature is characteristic of non-interacting (blocked) superparamagnetic nanoparticles (Fig. 6.3). In fact, the maxima of the χ' curves follow a Néel-Arrhenius law (Eq. 2.2), as observed in the inset of Fig. 6.3. At

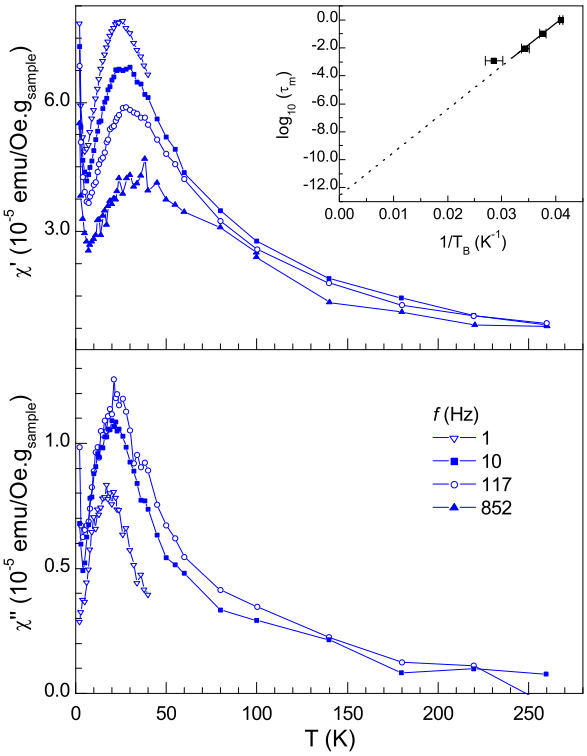

Figure 6.2: Ac susceptibility as a function of temperature of sample U6Maghem. Above: in-phase component $\chi'(T)$, and below: out-of-phase component $\chi''(T)$. Inset shows the thermal variation of the relaxation time as $\log(\tau_m)$ vs. $1/T_B$.

the same time, the extrapolated τ_0 is of the order of 10^{-11} s, as expected for non-interacting nanoparticles. The nanoparticles anisotropy energy E_a is 3500±370K. Considering K_{eff} of bulk magnetite (1.9×10^5erg/cm^3 [224]), which is also found in nanoparticles [225], the diameter of the particles can be estimated as 17 nm. Again, this value is higher than L which may indicate that the particles have an important fraction of amorphous material.

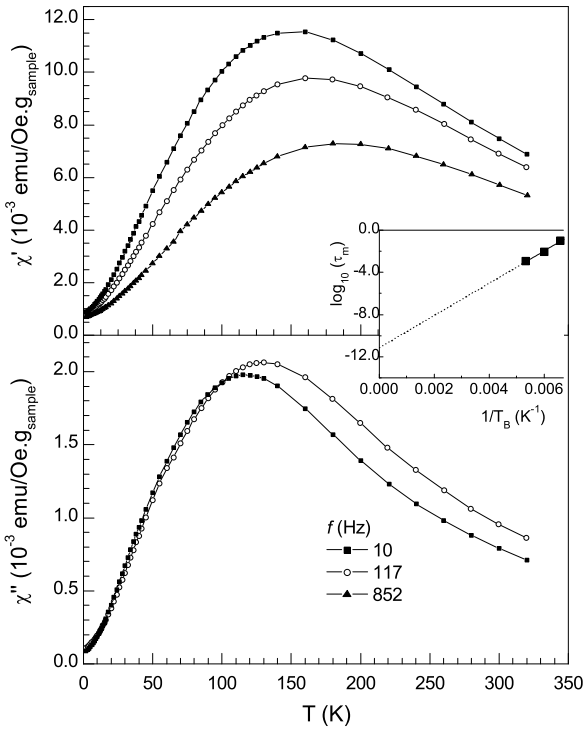

Figure 6.3: Ac susceptibility as a function of temperature of sample U6Magne. Above: in-phase component $\chi'(T)$, and below: out-of-phase component $\chi''(T)$.

6.5 M(H,T) measurements

6.5.1 Maghemite

The magnetization curves of U6Maghem sample are show in Fig. 6.4, as a function of the field (a) and as a function of H/T (b), for selected temperatures between 30 and 300 K. The magnetization shows partial saturation. This can either be attributed to the existence of an antiferromagnetic component or to anisotropy. In fact anisotropy makes saturation occur at fields higher than those expected from the Langevin law (see Sec. 2.3.2 for details). Clearly, the curves do not follow the Langevin law, since they do not superimpose in a H/T scale (Fig. 6.4b). It is puzzling that the curves seem to saturate at lower magnetization values as temperature increases, and at the same time they scale in H/T when looking to the susceptibility region (inset of Fig. 6.4b.). The reason for this behavior is not clear and the issue deserves further attention.

6.5.2 Magnetite

The magnetization of U6Magne sample reaches saturation at fields lower than those of U6Maghem (Fig. 6.5). This is consistent with the fact that the magnetic moment of the

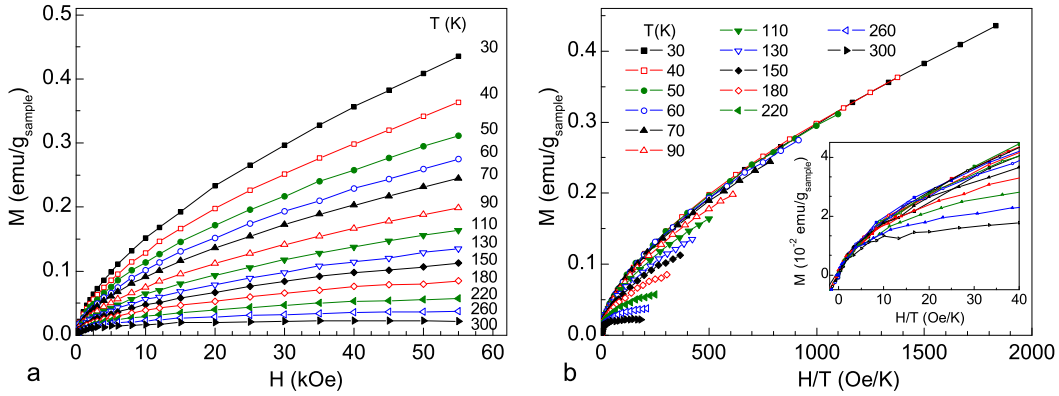

Figure 6.4: a. Magnetization of sample U6Maghem as a function of field at selected temperatures; b. same data plotted as a function of H/T and zoom over the low field (susceptibility) region.

magnetite nanoparticles is higher than that of maghemite and/or the anisotropy constant is lower. The higher magnetic moment of the magnetite nanoparticles is clearly due to the greater size of magnetite nanoparticles, as observed by XRD, and to the expected higher magnetization per volume of magnetite. The anisotropy constant might in fact be lower as found in literature [224, 225, 155].

As in U6Maghem, the magnetization curves of U6Magne sample do not scale in H/T (Fig. 6.5b.). In this case, the low field susceptibility increases as the temperature increases up to 200 K, due to an increase of the number of unblocked nanoparticles (Fig. 6.5b., inset). For $T > 200$ K the saturation magnetization decreases with temperature, as expected when approaching the transition temperature.

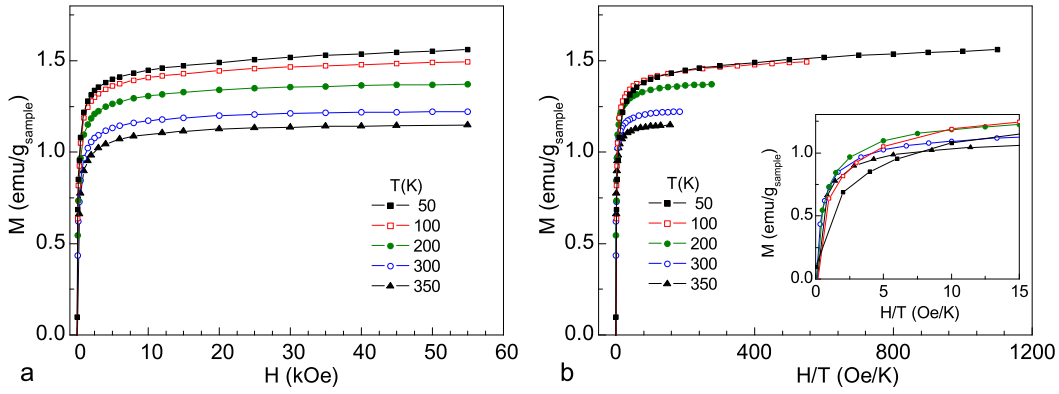

Figure 6.5: a. Magnetization of sample U6Magne as a function of field at selected temperatures; b. same data plotted as a function of H/T and zoom over the low field (susceptibility) region.

6.6 Influence of the isocyanate groups in the formation of maghemite

As described in Sec. 6.2.1 a second set of samples was prepared, where the iron ions were incorporated into the matrix in the beginning of the sol-gel process. Moreover, samples with excess of inorganic precursor were synthesized. This excess leads to the existence isocyanate ((-N-C=O) groups that do not react with the terminal amine groups of Jeffamine. In the following we compare samples obtained using Jeffamine ED-600® (Fluka) and Jeffamine/ICPTES ratios of 1:2 and 1:4 (termed U6Fe3(1:2)Maghem and U6Fe3(1:4)Maghem).

6.6.1 Dc susceptibility

The dc susceptibility curves show the existence of superparamagnetic particles (Fig. 6.6, above). Measurements were performed on heating from 2 up to 340 K in zero-field-cooled (zfc) and field-cooled (fc) procedures with a magnetic field of 20 Oe. The susceptibility curves present irreversibility below a temperature $T_F = 8$ and 3.5 K, for sample U6Fe3(1:2)Maghem and U6Fe3(1:4)Maghem, respectively. Sample U6Fe3(1:2)Maghem seems to have a maximum at ca. $T_B = 2$ K. On the other hand, it is possible that the sample with excess of ICPTES (U6Fe3(1:4)Maghem) has a maximum at $T_B < 2$ K. This means that the anisotropy energy of the nanoparticles present in sample U6Fe3(1:2)Maghem is higher than that of sample U6Fe3(1:2)Maghem. Considering that K_{eff} is the same in both samples (i. e. both samples have nanoparticles with the same phase, the phase have similar crystallinity, and surface and shape anisotropy are similar), nanoparticles of sample U6Fe3(1:2)Maghem have higher volume. Despite this considerations, it is clear that the excess of isocyanate groups favors the formation of nanoparticles with different physical properties, which is an indirect indication of interaction between those groups and Fe ions. This interaction can either be regarded as a coordination or a change in the local reaction conditions via pH, redox conditions or others.

Considering that interparticle interactions are negligible in both samples and above T_F, the plot χT vs. T (Fig. 6.6b.) is a measure of the temperature dependence of the effective magnetic moment squared. In addition, a term constant with temperature, χ_0 (either diamagnetic or antiferromagnetic) will appear in that plot as a linear contribution. In the case where χ_0 is negligible $\sqrt{\chi T}$ is proportional to the effective moment. The increase of χT with temperature for $T < 10$ K (Fig. 6.6b.), corresponds to the increase of the Curie constant due to the unblocking of the nanoparticles. For $10 < T < 100$K, the increase of χT is less intense, in particular in sample U6Fe3(1:2)Maghem. For $T > 100$K, χT decreases in sample U6Fe3(1:2)Maghem. This decrease is in agreement with the expected decrease towards zero in bulk maghemite when approaching the transition temperature (at about 900 K). The intermediate region ($10 < T < 100$ K) observed in sample U6Fe3(1:2)Maghem may correspond to a spurious antiferromagnetic phase, to a disordered surface where antiferro-

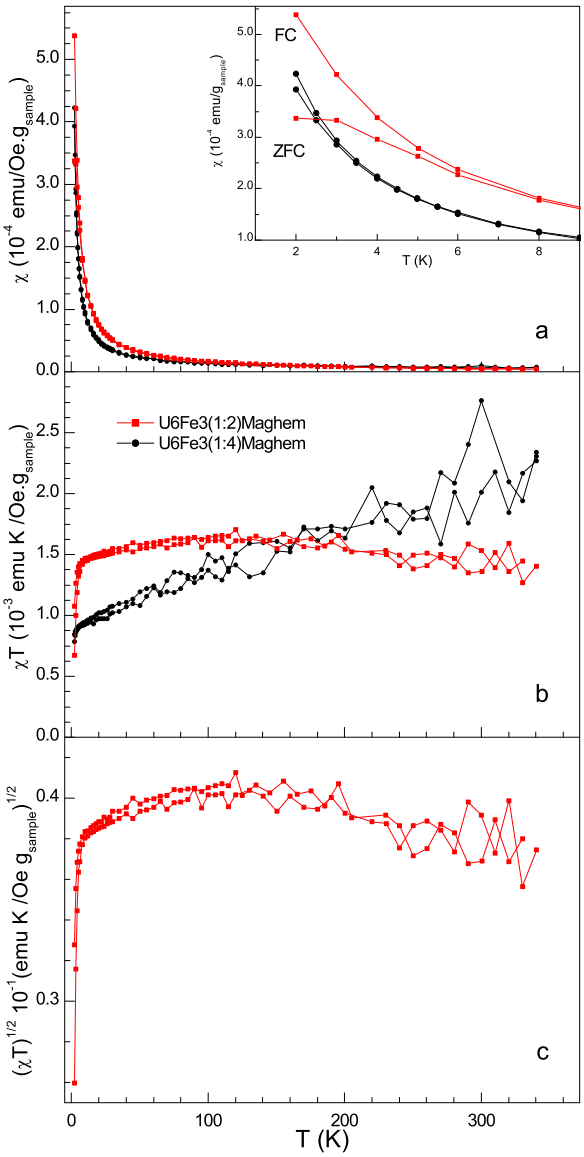

Figure 6.6: a. Dc susceptibility curves of samples U6Fe3(1:2)Maghem and U6Fe3(1:4)Maghem as a function of temperatures; inset: zoom over the low temperature region; b. effective Curie constants χT determined from the above shown dc susceptibility curves; c. effective magnetic moment $\sqrt{\chi T}$ of sample U6Fe3(1:2)Maghem as a function of temperature.

magnetic interactions are dominant, or to a pure finite size effect. This finite size effect is evident in Monte Carlo simulations performed by Iglésias and Labarta [61]: bulk maghemite has a monotonous temperature dependency, while a set of spherical particles with a diameter of 3 unit cells has a non-monotonous temperature dependency, due to surface atoms. On the other hand, the χT temperature dependence observed in sample U6Fe3(1:2)Maghem can be an intrinsic (volume) ferrimagnetic behavior, due to a different temperature dependence of the magnetization of the two magnetic sublattices. As described in Sec. 1.3.4, maghemite has

tetrahedral and octahedral sublattices with 8 and $13+1/3$ Fe ions, respectively. The spins in each sublattice align ferromagnetically, while the spins between sublattices align antiparallel. Qualitatively, the $\sqrt{\chi T}$ curve of sample U6Fe3(1:2)Maghem (Fig. 6.6c. would correspond to a faster decrease of the magnetization of the tetrahedral sublattice for $10 < T < 100$ K (so that the net magnetic moment increases) and faster decrease of the magnetization of the octahedral sublattice for $T > 100$ K. This corresponds to the ferrimagnets of type P or M shown in Sec. 2.8.1, Fig. 2.9.

As in sample U6Fe3(1:2)Maghem, the linear increase observed in sample U6Fe3(1:4)Maghem may correspond to a spurious antiferromagnetic phase, to a disordered surface, an enhanced finite size, or intrinsic ferrimagnetic effect. It is expected that χT starts to decrease with temperature for some temperature above 340 K, unless in the scenario of the existence of an antiferromagnetic phase.

6.7 Summary

In this chapter, we have presented the successful formation of maghemite and magnetite nanoparticles in di-ureasil matrix. The particles are precipitated by a basic treatment after the incorporation of Fe^{3+}/Fe^{2+} ions, in the case of maghemite, and Fe^{2+} ions in the case of magnetite. Two sets of samples were prepared, with the Fe ions being incorporated in the beginning and in the end of the sol-gel process. Another set of samples was prepared with an excess of isocyanate groups.

The ac susceptibility shows that both maghemite and magnetite behave as non-interacting/weakly interacting superparamagnetic nanoparticles, as expected for low concentrated and well dispersed systems. The anisotropy energy of the magnetite nanoparticles derived from the ac susceptibility is higher than that of maghemite nanoparticles. Considering the expected values for K_{eff}, we estimate that magnetite nanoparticles are larger than maghemite nanoparticles, as expected from the coherence lengths derived from the XRD patterns. The sizes estimated from the energy barriers are higher than the coherence lengths, which might indicate that the nanoparticles are partially amorphous. The magnetization of maghemite and magnetite show departures from Langevin behavior. These departures are however distinct than those found for ferrihydrite and further analysis is in progress.

In the maghemite/di-ureasil sample prepared with the Fe ions being incorporated in the beginning of the sol-gel process and no excess of isocyanate groups a non-monotonic dependency of χT was observed. This was attributed to a non-monotonic dependency of the magnetic moment, possible due to finite-size, surface effects, or intrinsic ferrimagnetic behavior. It is also shown that the isocyanate groups interact with the Fe ions, leading to nanoparticles with different magnetic properties than those of the sample without excess of isocyanate groups. In particular different irreversibility temperatures and different χT

dependence are observed. These differences are compatible with the existence of smaller particles in the sample with excess of isocyanate groups.

Chapter 7

Conclusions

7.1 Summary and conclusions

In this thesis we have studied and analyzed the relation between structural and magnetic properties of ferrihydrite, iron oxyhydroxynitrate phases, maghemite, and magnetite nanoparticles grown in organic-inorganic matrices.

Ferrihydrite is an antiferromagnetic iron oxide hydroxide, present in cold-water springs and recent bottom sediments of some lakes and soils, and in the core of ferritin protein [42]. Ferrihydrite is often the first product of the hydrolysis of iron nitrate salt, and in this process it is possible to identify different precursors, generally termed iron oxyhydroxynitrate [44]. Magnetite and maghemite are ferrimagnetic iron oxides with an inverse spinel structure. In magnetite, ferrimagnetism arises from the different moment of the Fe^{3+} and Fe^{2+} ions, while in maghemite ferrimagnetism arises from the different number of Fe^{3+} ions present in two sublattices with antiferromagnetic interactions [38]. The matrices are termed di-ureasils, being composed of nanometric siliceous-rich regions and polymer (POE) chains of different lengths [25]. Changing the POE chains length and doping di-ureasils with ions allows to tune mechanical, conductivity and luminescence properties [226, 26].

The general approach used in this thesis to the nanocomposites formation is the synthesis of the hybrid matrix in the presence of iron salts, and the subsequent precipitation of the nanoparticles. The precipitation is achieved by thermal treatment at low pH, in the case of ferrihydrite and iron oxyhydroxynitrate phases, and by basic and thermal treatment in the case of maghemite and magnetite. The formation of these different phases across the iron oxides phase diagram (Fig 7.1) benefits from the flexibility of the sol-gel process used in the synthesis of di-ureasils, that allows different synthesis conditions, the use of different organic and inorganic precursors, and the possibility of incorporating different salts. The di-ureasil matrix is a useful template to grow well dispersed nanoparticles with different sizes. This matrix is a non-aqueous reactor where transient oxyhydroxynitrate phases can be captured, and new oxyhydroxynitrate phases can be formed. By using different Fe^{2+}/Fe^{3+} ratios in

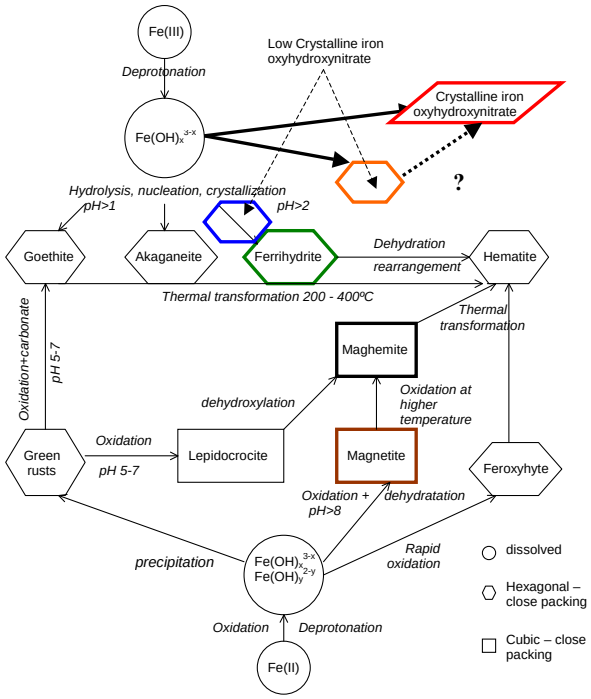

Figure 7.1: Schematic representation of formation and transformation pathways of the iron phases studied in this thesis: ferrihydrite, iron oxyhydroxynitrate phases, maghemite, and magnetite (after Ref. [38]).

the iron salt and by changing the temperature of the basic treatment it is possible to obtain magnetite or maghemite. The magnetic properties of the maghemite nanoparticles can be changed by introducing non-reacted isocyanate groups, such that the existence of more groups probably imply the formation of smaller particles. By changing the ethanol/water ratio used during the formation of the matrix, and the length of the organic chains, it is possible to grow ferrihydrite and different iron oxyhydroxynitrate phases from iron nitrate to ferrihydrite. The formation of ferrihydrite benefits from the flexibility of the longer polymer chains of the d-U(2000) matrix and from the existence of carbonyl groups that act as nucleation points, as deduced from FT-IR and NMR spectroscopies. The existence of these points leads to heterogeneous nucleation such that the incorporation of more iron implies the formation of larger nanoparticles, in agreement with XRD, SAXS, TEM, and FT-IR spectroscopy results.

Phase identification and a preliminary estimation of the nanoparticles size (determination of the coherence length L) was performed by XRD. The estimated sizes range from 2 nm in maghemite and in the smaller ferrihydrite nanoparticles, to the 10 nm in magnetite and 25 nm in the crystalline iron oxyhydroxynitrate phase. The low crystalline iron oxyhydroxynitrate phases have elongated particles that condense in smaller particles of other iron oxyhydroxynitrate phases by thermal treatment, or in smaller ferrihydrite nanoparticles when using larger amounts of H_2O. A detailed TEM study was performed in one of the

samples containing ferrihydrite nanoparticles (sample U2Fe2.1(I)). The nanoparticles have globular shape, are well dispersed in the matrix, and have an average diameter of 4.7±0.2 nm with a lognormal deviation $s = 0.43 \pm 0.05$.

These structural studies were then combined with magnetic studies in order to obtain a deeper understanding of the composites and on the magnetic behavior of the nanoparticles. From the dc susceptibility measurements it was possible to observe the increase of the Curie constant with the iron content in the ferrihydrite/di-ureasil nanocomposites and its decrease with the thermal treatment in the low crystalline iron oxyhydroxynitrate/di-ureasil nanocomposites. In the first case this was an indication of the increase of the uncompensated moment of the nanoparticles, while in the second case this was an indication of the increase of the number of antiferromagnetic coupled moments. From the ac susceptibility measurements it was possible to determine the energy barrier of the ferrihydrite nanoparticles ($E_a = 52 \pm 2$ K in the nanocomposite with 2.1% of iron), in the maghemite/di-ureasil nanocomposite ($E_a = 720 \pm 25$ K), and in the magnetite/di-ureasil nanocomposite ($E_a = 3500 \pm 370$ K). Since in the case of ferrihydrite the size of the nanoparticles was determined, is was possible to estimate the anisotropy constant ($K_{eff} = 4 \times 10^5$ erg/cm^3), in agrement with the values found in literature [54]. Comparing iron oxyhydroxynitrate and ferrihydrite samples, it was observed that the moment and anisotropy constant of ferrihydrite are higher than those of an iron oxyhydroxynitrate phase approaching ferrihydrite. Within each set, it was possible to observe the increase of dipolar interactions with the iron content, combining results from dc and ac susceptibilities and Mössbauer spectroscopy. The magnetization curves of ferrihydrite include linear and saturation components, due to the antiferromagnetic and uncompensated moments, respectively. The magnetization curves of maghemite also include two components, with a more pronounced decrease of the linear component with temperature. In the magnetization curves of magnetite the linear component is negligible and the curves are dominated by the saturation of the ferrimagnetic moments. Despite the antiferromagnetic interactions found in the iron oxyhydroxynitrate phases approaching ferrihydrite (group III samples), the magnetization curves are dominated by the paramagnetic ions, which are about 10% of the total ions.

Concerning modeling magnetization curves, we have presented a method to separate linear and saturation components and extract qualitative and quantitative information about the average uncompensated magnetic moment, the antiferromagnetic susceptibility, and their temperature dependence. We have applied this method to ferritin and to the ferrihydrite/di-ureasil nanocomposites. The antiferromagnetic susceptibility and the uncompensated magnetic moment were found to decrease with temperature, with the latter following a bulk antiferromagnetic magnons law. Extrapolating this dependence we have estimated an order temperature of about 500 K. With reference to modeling the relation between magnetic moment anisotropy energy and volume, we have presented a method based on distributions. The idea is based on reproductive properties of the lognormal distribution function and can

be generalized to other functions. This method makes use of broad size distributed samples, which are often regarded as less interesting samples. By using distributions we concluded that, in the ferrihydrite nanoparticles here studied, the anisotropy energy is proportional to the square root of the volume. This indicates that the uncompensated moments being responsible for the anisotropy are randomly distributed in volume. We have also applied this method to ferritin and concluded that an important role played by disorder in the magnetic properties becomes visible, since the size distribution is narrow.

7.2 Future perspectives

Modeling the magnetization properties of nanoparticles will benefit from combining one spin and multiple spin particle techniques and comparing findings with experimental results. In some cases, the distinction between different models is only possible by knowing structural parameters as particles size and density, and so structural and magnetic characterization must be performed. As one might expect, experimental results should come from very well characterized samples, with controlled parameters, and sets of samples where parameters are independently varied. Further advances will be the result of combined efforts in synthesis, experimental techniques and modeling.

Concerning the samples presented in this thesis, it will be interesting to continue their structural and magnetic characterization, in order to clarify their properties and some of the issues described in the previous paragraphs. In particular TEM and SAXS studies should be performed in all samples, opening the possibility of studying the evolution of the anisotropy constant with size, and anisotropy energy distribution with size distribution. This will also open the possibility of observing a qualitative relation between the evolution of the local field distribution and size distribution with the iron content. The magnetic properties of the iron oxyhydroxynitrate phases may also be subject of further magnetic and structural characterization in order to understand some basic properties, as the formation conditions and transformation pathways between phases. Magnetic characterization may proceed with magnetization measurements at high fields ir order to study the approach to saturation and the exchange bias phenomena in ferrihydrite and maghemite nanoparticles. It would also be interesting to perform small angle neutron scattering (SANS), in order to determine the average structural and magnetic size of the nanoparticles as a function of the magnetic field. Magnetic and structural measurements in ferrihydrite nanocomposites with an applied pressure will be performed. The pressure will change the average interparticle distance and may change the stability of the sublattices, in particular at the surface.

Concerning specific structural and magnetic studies, it would be desirable to synthesize new materials, designed to take advantage of a given technique. In particular, it would be interesting to grow nanoparticles in matrices with lower X-ray and neutron scattering intensities, in order to improve SAXS and SANS analysis. Nanoparticles with the selective

introduction of ^{57}Fe ions can be synthesized, to selective highlight surface and core properties in SANS and Mössbauer experiments. It would also be interesting to synthesize systems with low particle density and particles with different sizes, from 1 to 20 nm, in order to have low dipolar interactions and pursue studies on the influence of anisotropy and on the relation between anisotropy energy, magnetic moment and size.

Concerning open questions related to the magnetic properties of nanoparticles, we highlight the influence of anisotropy in magnetic properties, the relation between an equivalent anisotropy and surface effects, and the existence for a smearing of the influence anisotropy due to dipolar interactions. Regarding dipolar interactions, one may expect finding a dipolar ordering temperature in superparamagnetic nanoparticles and the clarification about the possible gradual transition between a noninteracting to a collective state as concentration increases. An ordering temperature may be found in systems of concentrated particles with low size distribution and ordered spatial arrangement. In antiferromagnetic nanoparticles, the temperature dependence and enhancement of susceptibility compared to bulk are issues that deserve further investigation. This is also the case of the temperature dependence of the uncompensated moment and its relation to volume. The origin of the exchange bias in antiferromagnetic and ferrimagnetic nanoparticles should also be further investigated and compared to related findings in multilayer films. Another interesting issue is the possibility of controlling the stability of the surface nanoparticles sublattice with an applied pressure. In ferrimagnetic nanoparticles it will be important to clarify which properties are equivalent to those of ferromagnetic nanoparticles and which are specific of the ferrimagnetic spin arrangement. Specific properties might be the existence of an antiferromagnetic susceptibility and surface-related properties. The evolution of the saturation magnetization with size and the properties of systems with different degrees of disorder should also be analyzed.

Appendix A

MatLab routine for moment distributed Langevin M(H,T) fit

A.1 Routine LagFitLNdes

```
%%%% ROUTINE FIT TO LANGEVIN LOGNORMAL DISTRIBUTED FUNCTION
%%%% ADDED TO AN ANTIFERROMAGNETIC COMPONENT
%%%% N. J. O. Silva, nunojoao@fis.ua.pt, Aveiro 2004

format long e
clear

%%%%loading data
%%%%field on 1st column, magnetization on the others
load D:\Magnetismo\U2Fe3n40ExpFit.DAT
%%%%change according to data file name
hexp=U2Fe3n40ExpFit(:,1);
%%%%change according to the number of magnetization columns
mexp=U2Fe3n40ExpFit(:,2)

%%%%initial guess (change according to the number of magnetization columns )
t=[45]; %%%% temperature
m0i=0.02; %%%% particles density
nmedi=[7]; %%%% number of uncompensated Fe ions
si=[0.9]; %%%% lognormal "deviation" parameter
chii=[2.5e-6]; %%%% antiferromagnetic linear component

%%%% starting is a vector with the initial guesses
starting(1)=m0i;
```

```
starting(2)=si;
starting(3)=nmedi;
starting(4)=chii;

%%%% iterations number
options=optimset('MaxIter',2000);

%%%% information going to the sub routine:
%%%% starting, options, experimental data and temperature
estimate=fminsearch('LagFitLNdessub',starting,options,hexp,mexp,t);

%%%%OUTPUT

%%%%output fit parameters displayed on screen
m0=estimate(1)
s=estimate(2)
nmed=estimate(3)
chi=estimate(4)

%%%% constants
mibor=9.2740154e-21; %erg.G-1
k=1.380658e-16; %erg.K-1
mife=5;

%%%%building the fitted function

ni=0.001;
nf=5000;
dn=(nf-ni)/100000;
n=[ni:dn:nf]';

mm=[];hh=[];
for i=1:length(hexp)
h=hexp(i);
algo3=mife*mibor*(n.p̂)*h/(k*t);
fdis=(exp(-(log(n/nmed)).2̂./(2*s2̂))./(sqrt(2*pi)*s.*n));
func_inte_depois=m0*(n.p̂).*fdis.*((coth(algo3))-(1./algo3));
plot(n,func_inte_depois)
drawnow
mtotal=chi*h+trapz(func_inte_depois)/trapz(fdis);
hh=[hh;h];
```

```
mm=[mm;mtotal];
end plot(hexp,mexp,'o',hh,mm)


%%%% saving fit parameters
para=estimate;
save D:\parametrosLangLNfit.dat para/ascii;
```

A.2 Sub-routine LagFitLNdessub

```
%%%% SUB-ROUTINE:
%%%% FIT TO LANGEVIN LOGNORMAL DISTRIBUTED FUNCTION
%%%% N. J. O. Silva %%%% Aveiro 2004

%%%%'parametros' is a vector with the initial guesses
%%%%'hexp' and 'mexp' are vectors with data and 't' is the temperature

function chi2=LagFitLNdessub(parametros,hexp,mexp,t)

%%%% parameters: 'm0' correspond to the particles density,
%%%%'s' is related to the deviation of the lognormal distribution function,
%%%% 'nmed' corresponds to the number of Fe uncompensated ions %%%%(each Fe ions has a moment of 5 bohr magnetons) and
%%%%'chi' is the antiferromagnetic susceptibility
m0=parametros(1);
s=parametros(2);
nmed=parametros(3);
chi=parametros(4);

%%%% constants
mibor=9.2740154e-21; %%%%erg.G-1
kb=1.380658e-16;%%%%erg.K-1
mife=5;

%%%%integration limits (in number of Fe uncompensated spins)
ni=0.001; nf=5000;
%%%%integration step (linear in logaritmic scale)
dnl=((log(nf)-log(ni))/10000);
%%%%vector with the all the integration points
nl=[log(ni):dnl:log(nf)]'; %%%%column in log scale
n=exp(nl); %%%%column in linear scale
```

```
%%%%temperature cycle (index k)
for k=1:length(t)
%%%%matrices where the theoretical magnetization (and field) values %%%% are going to be placed
mm=[];hh=[];

%%%% fields cycle
for i=1:length(hexp)
h=hexp(i);

%%%% algo3 is a vector with the Langevin function arguments (miu*H/kT) %%%% corresponding to each particles moment
%%%% particle moment=Fe magnetic moment*Bohr magneton*number of Fe ions
algo3=mife*mibor*n.*h/(kb*t(k));
%%%%distribution function
fdis=(exp(-(log(n/nmed(k))).^2./(2*s(k)^2))./(sqrt(2*pi)*s(k).*n));
%%%% function to be integrated
fdis_Lang=n.*fdis.*((coth(algo3))-(1./algo3));

%%%%2 options to see the distribution function
%plot(n,func_inte_depois)
%drawnow

%%%%integration
%%%%mt is the total magnetization (due to the uncompensated ions) for a given field
mt=0;
area=0;
%%%% sum over all moments
for j=1: (length(n)-1)
lj=0.5*(n(j+1)-n(j))*(fdis_Lang(j)+fdis_Lang(j+1));
mt=mt+lj;
aj=0.5*(n(j+1)-n(j))*(fdis(j)+fdis(j+1));
area=area+aj;
end

%%%% option to control the value of 'area'(that should be close to 1)
%area

%%%%the antiferromagnetic component is added at this point
mtotal=chi(k)*h+(m0*mt/area);
hh=[hh;h];
```

```
mm=[mm;mtotal];
end

%%%%error is defined as the difference between the calculated
%%%%and experimental magnetizations
erro(:,k)=mm-mexp(:,k);
%%%%option to see the fit evolution

plot(hexp,mexp(:,1),'o',hh,mm)
drawnow

end

%%%%the function to minimize is the square of the sum of the 'erro' matrix
chi2=sum(sum(erro.^2))
```

Appendix B

TEM and STEM/EDS images

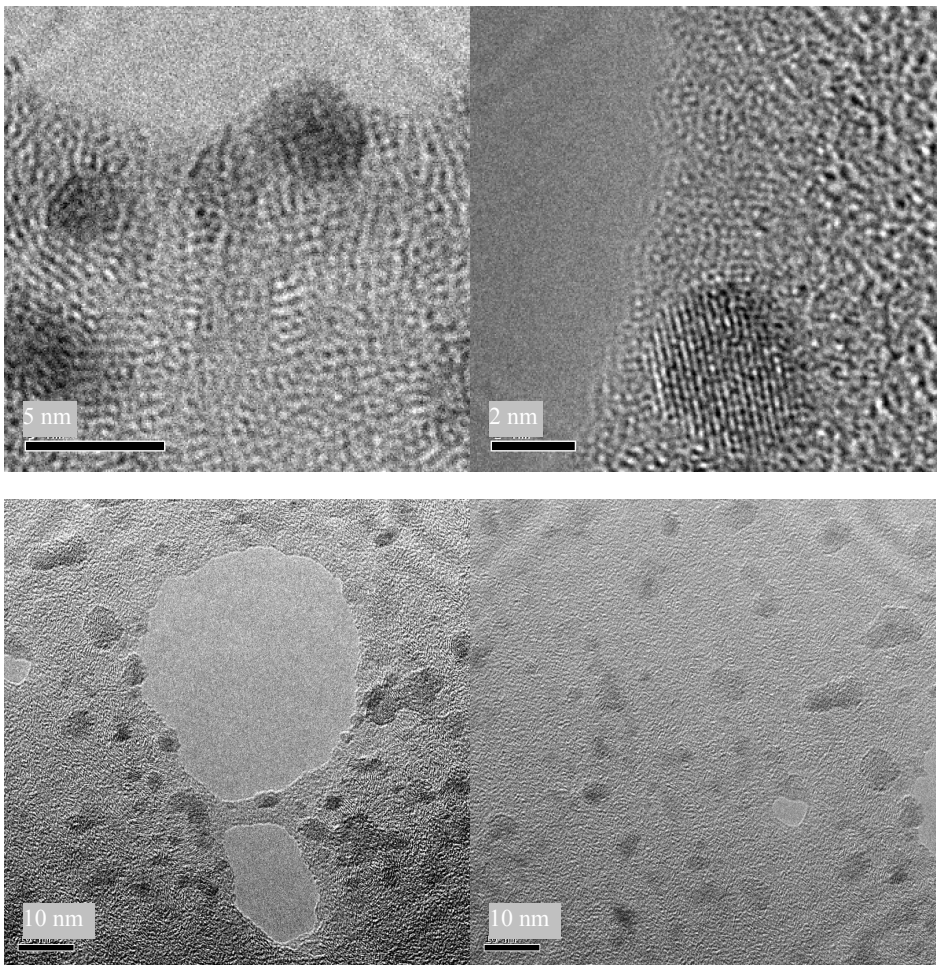

Figure B.1: Bright field TEM and high resolution TEM images of ferrihydrite nanoparticles within a hybrid ureasil matrix (sample U2Fe2.1(I)). TEM studies are presented in Sec. 3.3.2, page 75.

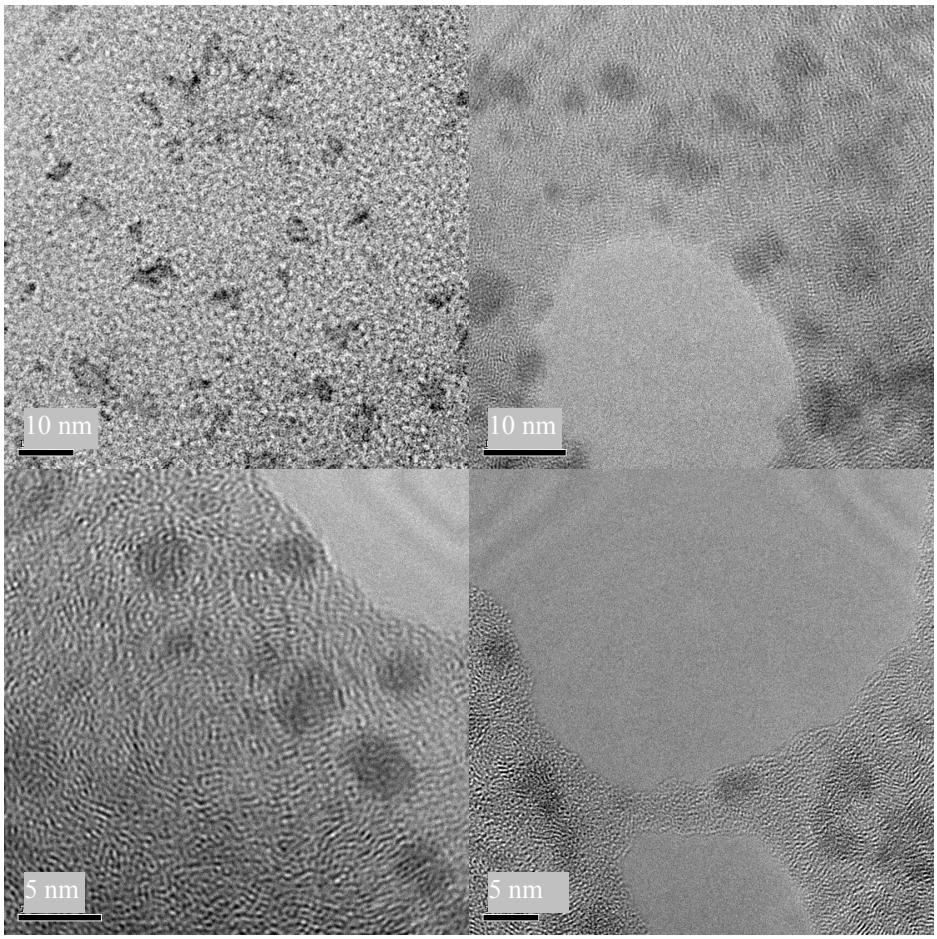

Figure B.2: Bright field TEM and high resolution TEM images of ferrihydrite nanoparticles within a hybrid ureasil matrix (sample U2Fe2.1(I)). TEM studies are presented in Sec. 3.3.2, page 75.

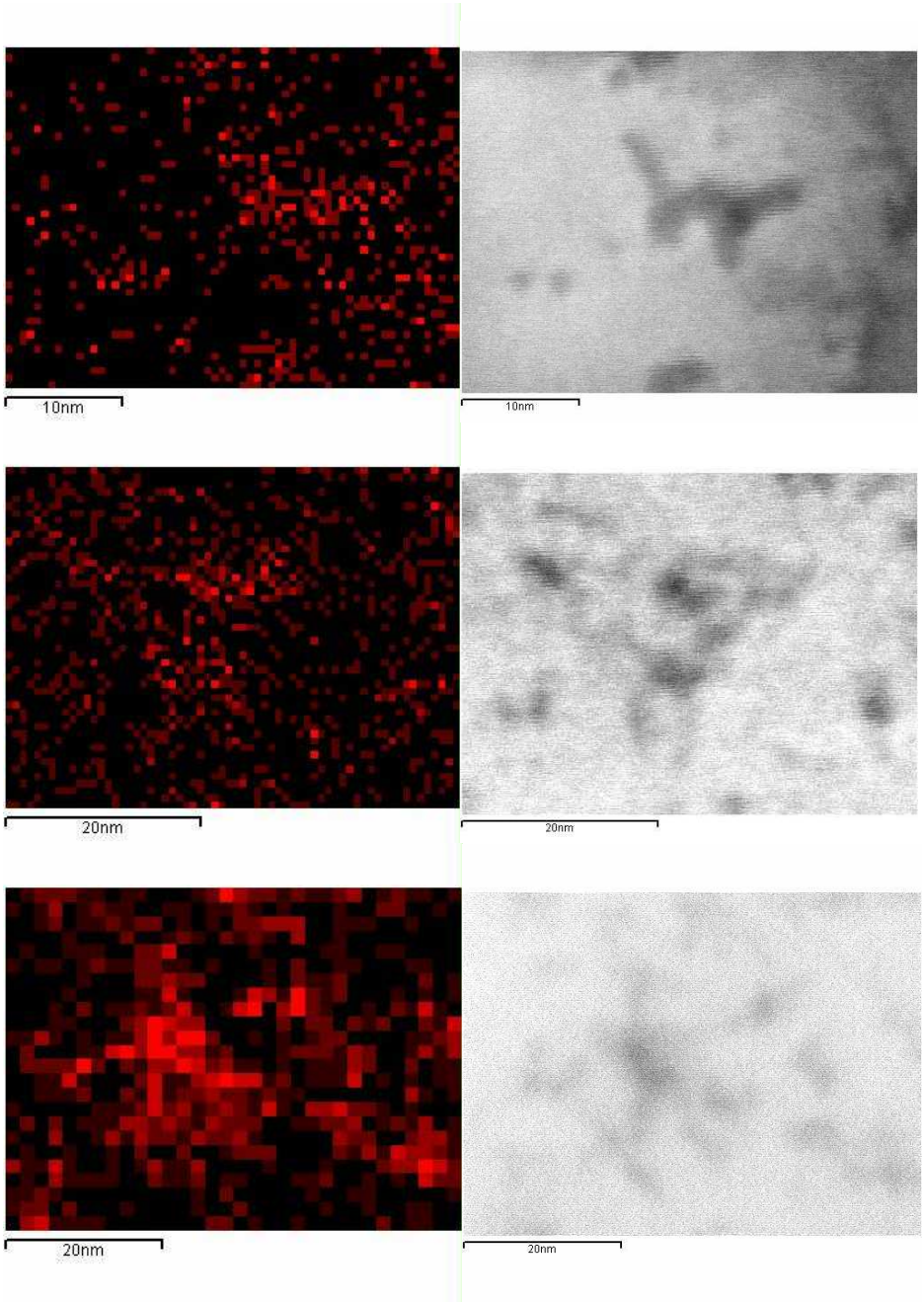

Figure B.3: STEM images obtained with a bright field detector and corresponding element distribution mapping of Fe obtained using the K_α iron line, in sample U2Fe2.1(I). These studies are presented in Sec. 3.3.2, page 75.

Appendix C

List of samples/measurements

Table C.1: List of measurements performed in the samples studied in this thesis

sample	XRD	SAXS	TEM/SEM	FT-IR	NMR	χ_{dc}	χ_{ac}	$M(H,T)$	$M(t,T)$	Mössbauer spectroscopy
group I										
U2Fe1.2(I)	✓	✓		✓		✓		✓		
U2Fe2.1(I)	✓		✓			✓	✓	✓	✓	✓
U2Fe3.9(I)	✓	✓		✓		✓	✓	✓		
U2Fe1.2(I)	✓	✓		✓		✓		✓		
group II										
U2Fe1.7(II)	✓				✓	✓	✓	✓	✓	
U2Fe3.8(II)	✓				✓	✓	✓	✓	✓	✓
U2Fe6.5(II)	✓				✓	✓	✓	✓	✓	✓
group III										
U2Fe4.3(III)	✓					✓				
U2Fe7.7(III)	✓					✓				
U2Fe10(III)						✓				
U2Fe14(III)	✓					✓	✓	✓		
group d-U(900)										
U9Fe3.4	✓			✓	✓					
U9Fe9.5	✓			✓	✓					
U9Fe12	✓			✓	✓	✓	✓	✓		
solvolysis group										
U2Fe5AA50	✓						✓			
U9Fe5AA60							✓			
U9Fe5AA70	✓						✓			
U9Fe5AA80	✓									
U6Fe10AAyr	✓		✓			✓		✓		✓
maghemite/magnetite										
U6Maghem	✓						✓	✓		
U6Fe3(1:2)Maghem	✓					✓				
U6Fe3(1:4)Maghem	✓					✓				
U6Magne	✓						✓	✓		

Bibliography

[1] C. Sanchez, F. Ribot, B. Lebeau, Molecular design of hybrid organic–inorganic nanocomposites synthesized via sol–gel chemistry, J. Mater. Chem 9 (1999) 35–44.

[2] C. Sanchez, A. A. Soler-Illia, F. R. T. Lalot, C. R. Mayer, V. Cabuil, Designed hybrid organic-inorganic nanocomposites from functional nanobuilding blocks, Chem. Mater. 13 (2001) 3061–3083.

[3] D. B. Mitzi, K. Chondroudis, C. R. Kagan, Organic–inorganic electronics, IBM J. Res. & Dev. 45 (2001) 29–45.

[4] D. Avnir, D. Levy, R. J. Reisfeld, The nature of the silica cage as reflected by spectral changes and enhanced photostability of trapped rhodamine 6g, J. Phys. Chem. 88 (1984) 5956–5959.

[5] D. Levy, S. Einhorn, D. Avnir, Applications of the sol-gel process for the preparation of photochromic information-recording materials: synthesis, properties, mechanisms, J. Non-Cryst. Solids 113 (1989) 137–145.

[6] R. J. Reisfeld, Spectroscopy and applications of molecules in glasses, J. Non-Cryst. Solids 121 (1990) 254–266.

[7] A. Shimojima, Y. Sugahara, K. Kuroda, Synthesis of oriented inorganic-organic nanocomposite films from alkyltrialkoxysilane-tetraalkoxysilane mixtures, J. Am. Chem. Soc. 120 (1998) 4528–4529.

[8] J. J. E. Moreau, L. Vellutini, M. Wong Chi Man, C. Bied, J.-L. Bantignies, P. Dieudonné, J.-L. Sauvajol, Self-organized hybrid silica with long-range ordered lamellar structure, J. Am. Chem. Soc. 123 (2001) 7957–7958.

[9] N. Liu, B. Smarsly, D. R. Dunphy, Y.-B. Jiang, C. J. Brinker, Self-directed assembly of photoactive hybrid silicates derived from an azobenzene-bridged silsesquioxane, J. Am. Chem. Soc. 124 (2001) 14540–14541.

[10] J. Alauzun, A. Mehdi, C. Reye, R. J. P. Corriu, Hydrophilic conditions: a new way for self-assembly of hybrid silica containing long alkylene chains, J. Mater. Chem 15 (2005) 841–843.

[11] H. Tang, J. Sun, J. J. X. Zhou, T. Hu, P. Xie, R. Zhang, A novel aryl amide-bridged ladderlike polymethylsiloxane synthesized by an amido h-bonding self-assembled template, J. Am. Chem. Soc. 124 (2002) 10482–10488.

[12] J. J. E. Moreau, L. Vellutini, M. Wong Chi Man, C. Bied, New hybrid organic-inorganic solids with helical morphology via h-bond mediated sol-gel hydrolysis of silyl derivates of chiral (r,r) or (s,s)-diureidocyclohexane, J. Am. Chem. Soc. 123 (2001) 1509–1510.

[13] J. J. E. Moreau, L. Vellutini, M. Wong Chi Man, C. Bied, Shape-controlled bridged silsesquioxanes: Hollow tubes and spheres, Chem. Eur. J. 9 (2003) 1594–1599.

[14] L. D. Carlos, V. de Zea Bermudez, V. S. Amaral, S. C. Nunes, N. J. O. Silva, J. R. Rute A. Sá Ferreira, C. V. Santilli, D. Ostrovskii, Nanoscopic photoluminescence memory as a fingerprint of complexity in self-assembled alkylene/siloxane hybrids, Adv. Mater.

[15] C. Sanchez, B. Julián, P. Belleville, M. Popall, Applications of hybrid organic-inorganic nanocomposites, J. Mater. Chem. 15 (2005) 3559–3592.

[16] L. L. Hench, J. K. West, The sol-gel process, Chem. Rev. 90 (1990) 33–72.

[17] E. J. A. Pope, J. D. J. Mackenzie, Sol-gel processing of silica: Ii. the role of the catalyst, J. Non-Cryst. Solids 87 (1986) 185–198.

[18] E. Stathatos, P. Lianos, B. Orel, A. S. Vuk, R. Jese, Study of acetic acid-catalyzed nanocomposite organic/inorganic ureasil sol-gel ionic conductors, Langmuir 19 (2003) 7587–7591.

[19] C. J. Brinker, Hydrolysis and condensation of silicates, J. Non-Cryst. Solids 100 (1988) 31–50.

[20] H. Schmidt, H. Scholze, A. Kaiser, Principles of hydrolysis and condensation reaction of alkoxysilanes, J. Non-Cryst. Solids 63 (1984) 1–11.

[21] H. Van Olphen, Maya blue: A clay-organic pigment?, Science 154 (1966) 645–646.

[22] B. Arkles, Commercial applications of sol-gel-derived hybrid materials, MRS Bulletin 26 (2001) 402–408.

[23] G. Schottner, Hybrid sol-gel-derived polymers: Applications of multifunctional materials, Chem. Mater. 13 (2001) 3422–3435.

[24] E. Bescher, F. Piqué, D. Stulik, J. D. Mackenzie, Long-term protection of the last judgment mosaic in prague, J. Sol-Gel Sci. Tech. 19 (2000) 215–218.

[25] V. de Zea Bermudez, L. D. Carlos, L. Alcácer, Sol-gel derived urea cross-linked organically silicates. 1. room temperature mid-infrared spectra, Chem. Mater. 11 (1999) 569–580.

[26] L. D. Carlos, Y. Messaddeq, H. F. Brito, R. A. Sá Ferreira, V. de Zea Bermudez, S. J. L. Ribeiro, Full colour phosphors from Eu(III)-based organosilicates, Adv. Mater. 12 (2000) 594–598.

[27] L. S. Fu, R. A. Sá Ferreira, N. J. O. Silva, A. J. Fernandes, I. S. Gonçalves, V. de Zea Bermudez, L. D. Carlos, Structure-photoluminescence relationship in Eu(III) α-diketonate-based organic/inorganic hybrids. influence of the synthesis method: carboxylic acid solvolysis versus conventional hydrolysis, J. Mater. Chem. 15 (2005) 3117–3125.

[28] S. C. Nunes, V. de Zea Bermudez, D. Ostrovskii, M. M. Silva, S. Barros, M. J. Smith, R. A. Sá Ferreira, L. D. Carlos, J. Rocha, E. Morales, Di-urea cross-linked poly(oxyethylene)/siloxane ormolytes for lithium batteries, J. Electrochem. Soc. 152 (2005) A429–A438.

[29] L. D. Carlos, R. A. Sá Ferreira, V. de Zea Bermudez, C. Molina, L. A. Bueno, S. J. L. Ribeiro, White light emission of Eu^{3+}-based hybrid xerogels, Phys. Rev. B. 60 (1999) 10042–10053.

[30] V. I. Boev, J. Pérez-Juste, I. Pastoriza-Santos, C. J. R. Silva, M. de Jesus M. Gomes, L. M. Liz-Marzán, Flexible ureasil hybrids with tailored optical properties through doping with metal nanoparticles, Langmuir 20 (2004) 10268–10272.

[31] C. Molina, R. A. S. Ferreira, L. D. Carlos, R. R. Gonçalves, S. J. L. Ribeiro, Y. Messaddeq, P. J. Moreira, O. Soppera, A. P. Leite, P. V. S. Marques, V. de Zea Bermudez, Planar and uv written channel optical waveguides prepared with siloxane-poly(oxyethylene)-zirconia organic/inorganic hybrids. structure and optical properties, J. Mater. Chem. 15 (2005) 3937–3945.

[32] L. S. Fu, R. A. Sá Ferreira, N. J. O. Silva, L. D. Carlos, V. de Zea Bermudez, J. Rocha, Photoluminescence and quantum yields of urea and urethane cross-linked nanohybrids derived from carboxylic acid solvolysis, Chem. Mater. 16 (2004) 1507–1516.

[33] E. Stathatos, P. Lianos, U. Lavrencic-Stangar, B. Orel, A high-performance solid-state dye-sensitized photoelectrochemical cell employing a nanocomposite gel electrolyte made by the sol-gel route, Adv. Mater. 14 (2002) 354–357.

[34] L. D. Carlos, V. de Zea Bermudez, R. A. Sá Ferreira, L. Marques, M. Assunção, Sol-gel derived urea cross-linked organically silicates. 2. blue light emission, Chem. Mater. 11 (1999) 581–588.

[35] K. Dahmouche, C. V. Santilli, S. H. Pulcinelli, A. F. Craievich, Small-angle x-ray scattering study of sol-gel-derived siloxane-peg and siloxane-ppg hybrid materials, J. Phys. Chem. B 103 (1999) 4937–4942.

[36] K. Dahmouche, L. D. Carlos, V. de Zea Bermudez, R. A. Sá Ferreira, C. V. Santilli, A. F. Craievich, Saxs study of Eu^{3+}-doped sol-gel derived siloxane-polyethyleneoxyde hybrids, J. Mater. Chem. 11 (2001) 3249.

[37] L. D. Carlos, R. A. Sá Ferreira, V. de Zea Bermudez, I. Orion, J. Rocha, Sol-gel derived nanocomposites hybrids for full colour displays, J. Lumin. 87-89 (2000) 702.

[38] R. M. Cornell, U. Schwertmann, The Iron Oxides: Structure, Properties, Reactions, Occurences and Uses, Wiley-VCH Verlag GmbH & Co. KGaA, Weinheim, 2003.

[39] K. M. Towe, W. F. Bradley, Mineralogical constitution of colloidal "hydrous ferric oxides", J. Colloid Interface Sci. 24 (1967) 384–392.

[40] F. V. Chukhrov, B. B. Zvyagin, A. I. Gorshkov, L. P. Ermilova, V. V. Balashova, Ferrihydrite, Izvest. Akad. Nauk SSSR, Ser. Geol. 4 (1973) 23.

[41] J. D. Russell, Infrared spectroscopy of ferrihydrite - evidence for the presence of structural hydroxyl-groups, Clay Miner. 14 (1979) 109–114.

[42] J. L. Jambor, J. E. Dutrizac, Occurrence and constitution of natural and synthetic ferrihydrite, a widespread iron oxyhydroxide, Chem. Rev. 98 (1998) 2549–2586.

[43] S. Mann, Inorganic Materials, Willey and Sons, Chichester, 1996.

[44] U. Schwertmann, J. Friedl, H. Stanjek, From Fe(III) ions to ferrihydrite and then to hematite, J. Coll. Interface Sci. 209 (1999) 215–223.

[45] D. E. Janney, J. M. Cowley, P. R. Buseck, Structure of synthetic 6-line ferrihydrite by electron nanodiffraction, Am. Mineral. 86 (2001) 327–335.

[46] R. A. Eggleton, Fitzpatrick, New data and a revised structural model for ferrihydrite, Clays Clay Miner. 36 (1988) 111–124.

[47] A. Manceau, V. A. Drits, Local structure of ferrihydrite and feroxyhite by exafs spectroscopy, Clay Miner. 28 (1993) 165–184.

[48] Q. A. Pankhurst, R. J. Pollard, Structural and magnetic properties of ferrihydrite, Clays Clay Miner. 40 (1992) 268–272.

[49] V. A. Drits, B. A. Sarkharov, A. L. Salyn, A. Manceau, Structural model for ferrihydrite, Clay Miner. 28 (1993) 185–207.

[50] E. Jansen, A. Kyek, W. Schafer, U. Schwertmann, The structure of six-line ferrihydrite, Appl. Phys. A: Mater. Sci. Process 74 (2002) S1004.

[51] S. A. Makhlouf, F. T. Parker, A. E. Berkowitz, Magnetic hysteresis anomalies in ferritin, Phys. Rev. B. 55 (1997) R14717–R14719.

[52] W. H. Meiklejohn, C. P. Bean, New magnetic anisotropy, Phys. Rev. 102 (1956) 1413–1414.

[53] W. H. Meiklejohn, C. P. Bean, New magnetic anisotropy, Phys. Rev. 105 (1957) 904–913.

[54] C. Gilles, P. Bonville, K. K. Wong, S. Mann, Non-langevin behaviour of the uncompensated magnetization in nanoparticles of artificial ferritin, Eur. Phys. J. B 17 (2000) 417–427.

[55] J. Rose, A. Manceau, A. Masion, J. Y. Bottero, Structural and mechanisms of formation of $FeOOH(NO_3)$ oligomers in the early stages of hydrolysis, Langmuir 13 (1997) 3240–3246.

[56] U. Schwertmann, J. Friedl, G. Pfab, A new Iron(III) oxyhydroxynitrate, J. Sol. State Chem. 126 (1996) 336.

[57] J. M. Bigham, L. Carlson, E. Murad., Schwertmannite, a new iron oxyhydroxy-sulphate from pyhasalmi, finland, and other localities, Mineral. Mag. 58 (1994) 641–648.

[58] A. López Delgado, A. García Martínez, M. Gálvez Morros, J. Therm. Anal. 34 (1988) 843–852.

[59] L. Pelloquin, M. Lou A powder diffraction study of iron oxide hydroxide nitrate, $Fe_2O(OH)NO_3.H_2O$: *ab initio* structure determination and anion exchange reactions.

[60] R. H. Kodama, A. E. Berkowitz, Atomic-scale modeling of oxide nanoparticles, Phys. Rev. B. 59 (1999) 6321–6336.

[61] O. Iglesias, A. Labarta, Finite-size and surface effects in maghemite nanoparticles: Monte carlo simulations, Phys. Rev. B. 63 (2001) 286–292.

[62] P. Weiss, R. Forrer, Ann. Phys. 12 (1929) 279.

[63] A. E. Berkowitz, J. A. Lahut, I. S. Jacobs, L. M. Levinson, D. W. Forester, Spin pinning at ferrite-organic interfaces, Phys. Rev. Lett. 34 (1975) 594–597.

[64] J. Zhao, F. E. Huggins, Z. Feng, G. P. Huffman, Surface-induced superparamagnetic relaxation in nanoscale ferrihydrite particles, Phys. Rev. B. 54 (1996) 3403–3407.

[65] M. Allen, D. Willits, J. Mosolf, M. Young, T. Douglas, Protein cage constrained synthesis of ferrimagnetic iron oxide nanoparticles, Adv. Matter. 14 (2002) 1562–1564.

[66] T. Douglas, M. Young, Host–guest encapsulation of materials by assembled virus protein cages, Nature 393 (1998) 152–155.

[67] S. Gider, D. D. Awschalom, T. Douglas, S. Mann, M. Chaparala, Classical and quantum magnetic phenomena in natural and artificial ferritin proteins, Science 268 (1995) 77–80.

[68] F. C. Meldrum, V. J. Wade, D. L. Nimmo, B. R. Heywood, S. Mann, Synthesis of inorganic nanophase materials in supramolecular protein cages, Nature 349 (1991) 684–687.

[69] C. Cannas, M. F. Casula, G. Concas, A. Corrias, D. Gatteschi, A. Falqui, A. Musinu, C. Sangregorio, G. Spano, Magnetic properties of γ-Fe_2O_3–SiO_2 aerogel and xerogel nanocomposite materials, J. Mater. Chem. 11 (2001) 3180–3187.

[70] V. Salgueiriño-Maceira, M. A. Correa-Duarte, M. Spasova, L. M. Liz-Marzán, M. Farle, Composite silica spheres with magnetic and luminescent functionalities, Adv. Funct. Mater. 16 (2006) 509.

[71] M. S. Rao, I. S. Dubenko, S. Roy, N. Ali, B. C. Dave, Matrix-assisted biomimetic assembly of ferritin core analogues in organosilica sol-gels, J. Am. Chem. Soc. 123 (2001) 1511–1512.

[72] A. Millan, F. Palacio, E. Snoeck, V. Serin, P. Lecante, Magnetic polymer nanocomposites in Polymer Nanocomposites, Woodhead Publishing Ltd, Cambridge, 2005.

[73] N. J. O. Silva, V. S. Amaral, V. de Zea Bermudez, S. C. Nunes, D. Ostrovskii, J. Rocha, L. D. Carlos, Matrix assisted formation of ferrihydrite nanoparticles in a siloxane/poly(oxyethylene) nanohybrid, J. Mater. Chem 15 (2005) 484–490.

[74] U. Heynen, D. Schuler, Growth and magnetosome formation by microaerophilic magnetospirillum strains in an oxygen-controlled fermentor, Appl. Microbiol. 61 (2003) 536–544.

[75] T. Hyeon, S. S. Lee, J. Park, Y. Chung, H. B. Na, Synthesis of highly crystalline and monodisperse maghemite nanocrystallites without a size-selection process, J. Am. Chem. Soc. 39 (2003) 12798–12801.

[76] S. Sun, C. B. Murray, D. Weller, L. Folks, A. Moser, Monodisperse FePt nanoparticles and ferromagnetic nanocystal superlattices, Science 287 (2000) 1989–1992.

[77] G. Bidan, O. Jarjayes, J. M. Fruchart, E. Hannecart, New nanocomposites based on tailor dressed magnetic nanoparticles in a polypyrrole matrix, Adv. Mater. 6 (1994) 152–155.

[78] S. Mann, Molecular tectonics in biomineralization and biomimetic materials chemistry, Nature 365 (1993) 499–505.

[79] S. Mornet, S. Vasseur, F. Grasset, E. Duguet, Magnetic nanoparticle design for medical diagnosis and therapy, J. Mater. Chem 14 (2004) 2161–2175.

[80] I. Brigger, C. Dubernet, P. Couvreur, Nanoparticles in cancer therapy and diagnosis, Adv. Drug. Deliver Rev. 54 (2002) 631–651.

[81] J. Grimm, J. M. Perez, L. Josephson, R. Weissleder, Novel nanosensors for rapid analysis of telomerase activity, Cancer Res. 64 (2004) 639–643.

[82] J. M. Perez, L. Josephson, R. Weissleder, Use of magnetic nanoparticles as nanosensors to probe for molecular interactions, Chem. Bio. Chem. 5 (2004) 261–264.

[83] A. Dyal, K. Loos, M. Noto, S. W. Chang, C. Spagnoli, K. V. P. M. Shafi, A. Ulman, M. Cowman, R. A. Gross, Activity of candida rugosalipase immobilized on γ-Fe_2O_3 magnetic nanoparticles, J. Am. Chem. Soc. 125 (2003) 1684–1685.

[84] U. T. Bornscheuer, Immobilizing enzymes: How to create more suitable biocatalysts, Angew. Chem. Int. Ed. 42 (2003) 3336–3337.

[85] S. Bucak, D. A. Jones, P. E. Laibinis, T. A. Hatton, Protein separations using colloidal magnetic nanoparticles, Biotechnol. Prog. 19 (2003) 477–484.

[86] A. Ito, H. Honda, T. Kobayashi, Cancer immunotherapy based on intracellular hyperthermia using magnetite nanoparticles: a novel concept of "heat-controlled necrosis" with heat shock protein expression, Cancer Immunol Immunother 55 (2006) 320–328.

[87] F. Royer, D. Jamon, J. J. Rousseau, V. Cabuil, D. Zins, H. Roux, C. Bovier, Experimental investigation on γ-Fe_2O_3 nanoparticles faraday rotation: particles size dependency, Eur. Phys. J - Appl. Phys. 22 (2003) 83–37.

[88] H. E. Horng, C.-Y. Hong, S. Y. Yang, H. C. Yang, Designing the refractive indices by using magnetic fluids, Appl. Phys. Lett. 82 (2003) 2434–2436.

[89] A. E. Varfolomeev, D. Y. Godovskii, G. A. Kapustin, A. V. Volkov, M. A. Moskvina, Giant negative magnetoresistance in a composite systems based on Fe_3O_4 nanocrystals on a polymer matrix, JETP Lett. 67 (1998) 39–42.

[90] J. Hoinville, A. Bewick, D. Gleeson, R. Jones, O. Kasyutich, E. Mayes, A. Nartowski, B. Warne, J. Wiggins, K. Wong, Magnetic recording at high densities on protein-derived copt nanoparticles, Mat. Res. Soc. Symp. Proc. 735 (2002) C3.1.

[91] T. Thurn-Albrecht, J. Schotter, G. A. Kastle, N. Emley, T. Shibauchi, G. K. Krusin-Elbaum, C. T. Black, M. T. Tuominene, T. P. Russell, Ultrahigh-density nanowire arrays grown in self-assembled diblock copolymer templates, Science 290 (2000) 2126–2129.

[92] J. van der Zee, Heating the patient: a promising approach?, Ann. Oncol. 13 (2002) 1173–1184.

[93] R. T. Gordon, J. R. Hines, D. Gordon, Intracellular hyperthermia a biophysical approach to cancer treatment via intracellular temperature and biophysical alterations, Med. Hypotheses 5 (1979) 83–102.

[94] K. M. H. Lenssen, et al., Robust giant magnetoresistance sensors, Sensors Actuators A 85 (2000) 1–8.

[95] H. Kachkachi, E. Bonet, Surface-induced cubic anisotropy in nanomagnets, Phys. Rev. B. 73 (2005) 224402.

[96] L. Néel, C. R. Hebd. Seances Acad. Sci. 228 (1949) 664.

[97] W. F. Brown Jr., Thermal fluctuations of a single-domain particle, Phys. Rev. 130 (1963) 1677–1686.

[98] C. G. Montgomery, The magnetic properties of nickel colloids, Phys. Rev. 39 (1932) 163–164.

[99] W. C. Elmore, Ferromagnetic colloid for studying magnetic structures, Phys. Rev. 58 (1938) 308–310.

[100] W. C. Elmore, The magnetization of ferromagnetic colloids, Phys. Rev. 54 (1938) 1092–1095.

[101] J. L. Dormann, D. Fiorani, E. Tronc, Advances in Chemical Physics, 98. Magnetic relaxation in fine-particle systems, John Willey & Sons, New York, 1997.

[102] J. L. Dormann, L. Bessais, D. Fiorani, A dynamic study of small interacting particles: superparamagnetic model and spin-glass laws, J. Phys. C 21 (1988) 2015–2034.

[103] L. Bessais, L. B. Jaffel, J. L. Dormann, Phys. Rev. B. 45 (1992) 7805–7815.

[104] J. Tejada, X. X. Zhang, E. del Barco, J. M. Hernández, E. M. Chudnovsky, Macroscopic resonant tunneling of magnetization in ferritin, Phys. Rev. Lett. 79 (1997) 1754–1757.

[105] F. Luis, E. del Barco, J. M. Hernández, E. Remiro, J. Bartolomé, J. Tejada, Resonant spin tunneling in small antiferromagnetic particles, Phys. Rev. B. 59 (1999) 094409.

[106] P. Bonville, C. Gilles, Search for incoherent tunnel fluctuations of the magnetization in nanoparticles of artificial ferritin, Physica B 304 (2001) 237–245.

[107] W. E. Henry, Spin paramagnetism of Cr^{+++}, Fe^{+++}, and Gd^{+++} at liquid helium temperatures and in strong magnetic fields, Phys. Rev. 88 (1952) 559–562.

[108] J. García-Otero, M. Porto, J. Rivas, A. Bunde, Influence of the cubic anisotropy constants on the hysteresis loops of single-domain particles: A monte carlo study, J. App. Phys. 85 (1999) 2287–2292.

[109] J. L. Garcia-Palacios, Advances in Chemical Physics, 112. On the Statics and Dynamics of Magnetoanisotropic Nanoparticles, John Willey & Sons, New York, 2000.

[110] P. Cregg, L. Bessais, Series expansions for the magnetisation of a solid superparamagnetic system of non-interacting particles with anisotropy, J. Mag. Mag. Mat. 202 (1999) 554–564.

[111] E. L. Crow, K. Shimizu, Lognormal distributions theory and applications, Marcel Dekker, New York, 1988.

[112] N. J. O. Silva, L. D. Carlos, V. S. Amaral, Comment on "thermoinduced magnetization in nanoparticles of antiferromagnetic materials", Phys. Rev. Lett. 95 (2005) 039707.

[113] C. Djurberg, P. Svedlindh, P. Nordblad, M. F. Hansen, F. Bødker, S. Mørup, Dynamics of an interacting particle system: Evidence of critical slowing down, Phys. Rev. Lett. 79 (1997) 5154–5157.

[114] T. Jonsson, P. Svedlindh, M. F. Hansen, Static scaling on an interacting magnetic nanoparticle system, Phys. Rev. Lett. 81 (1997) 3976–3979.

[115] P. Allia, M. Coisson, P. Tiberto, F. Vinai, M. Knobel, M. A. Novak, W. C. Nunes, Effect of dipolar interaction observed in iron-based nanoparticles, Phys. Rev. B. 64 (2001) 144420.

[116] J. M. Vargas, W. C. Nunes, L. M. Socolovsky, M. Knobel, , D. Zanchet, Effect of dipolar interaction observed in iron-based nanoparticles, Phys. Rev. B. 72 (2005) 184428.

[117] R. W. Chantrell, N. Walmsley, J. Gore, M. Maylin, Calculations of the susceptibility of interacting superparamagnetic particles, Phys. Rev. B. 63 (2000) 024410.

[118] R. H. Kodama, A. E. Berkowitz, E. J. McNiff Jr., S. Foner, Surface spin disorder in $NiFe_2O_4$ nanoparticles, Phys. Rev. Lett. 77 (1996) 394–397.

[119] B. Martínez, X. O. L. Balcells, A. Rouanet, C. Monty, Low temperature surface spin-glass transition in γ-Fe_2O_3 nanoparticles, Phys. Rev. Lett. 80 (1998) 181–184.

[120] J. M. D. Coey, Noncollinear spin arrangement in ultrafine ferrimagnetic crystallites, Phys. Rev. Lett. 27 (1971) 1140–1142.

[121] A. Millan, A. Urtizberea, F. Palacio, N. J. O. Silva, V. S. Amaral, E. Snoeck, V. Serin, Surface effects in maghemite nanoparticles, J. Mag. Mag. Mat. http://dx.doi.org/10.1016/j.jmmm.2006.09.011.

[122] C. Pecharromán, T. Gonzalezcarreño, J. E. Iglesias, The infrared dielectric-properties of maghemite, γ-Fe_2O_3, from reflectance measurement on pressed powders, Phys. Chem. Miner. 22 (1995) 21–29.

[123] E. M. Moreno, M. Zayat, M. P. Morales, C. J. Serna, A. Roig, D. Levy, Preparation of narrow size distribution superparamagnetic γ-Fe_2O_3 nanoparticles in a sol-gel transparent SiO_2 matrix, Langmuir 18 (2002) 4972–4978.

[124] N. Feltin, M. P. Pilen, New technique for synthesizing iron ferrite magnetic nanosized particles, Langmuir 13 (1997) 3927–3933.

[125] M. P. Morales, M. Andres-Verges, S. Veintemillas-Verdaguer, M. I. Montero, C. J. Serna, Structural effects on the magnetic properties of γ-Fe_2O_3 nanoparticles, J. Mag. Mag. Mat. 203 (1999) 146–148.

[126] E. C. Stoner, E. P. Wohlfarth, A mechanism of magnetic hysteresis in heterogeneous alloys, Philos. Trans. R. Soc. London Ser. A 240 (1948) 599–642.

[127] N. A. Usov, S. E. Peschany, Theoretical hysteresis loops for single-domain particles with cubic anisotropy, J. Mag. Mag. Mat. 174 (1997) 274–260.

[128] E. F. Kneller, F. E. Luborsky, Particle size dependence of coercivity and remanence of single-domain particles, J. App. Phys. 34 (1963) 656–658.

[129] C. P. Bean, J. D. Livingston, Superparamagnetism, J. App. Phys. 30 (1959) S120–S129.

[130] H. Pfeiffer, Determination of anisotropy-field distribution in particle assemblies taking into account thermal fluctuations, Phys. Stat. Sol. A 118 (1990) 295–306.

[131] W. C. Nunes, M. A. Novak, M. Knobel, A. Hernando, Magnetic properties in granular $Co_{10}Cu_{90}$ alloys: the effect of random anisotropy and interparticle interactions, J. Mag. Mag. Mat. 226-230 (2001) 1856–1858.

[132] D. Kechrakos, K. N. Trohidou, Magnetic properties of dipolar interacting single-domain particles, Phys. Rev. B. 58 (1998) 12169–12177.

[133] T. Shinjo, M. Kiyama, N. Sugita, K. Watanabe, T. Takada, Surface magnetism of α-Fe_2O_3 by Mössbauer spectroscopy, J. Mag. Mag. Mat. 35 (1983) 133–135.

[134] D. L. Mills, Surface effects in magnetic crystals near the ordering temperature, Phys. Rev. B. 3 (1971) 3887–3895.

[135] D. A. Dimitrov, G. M. Wysin, Magnetic properties of superparamagnetic particles by a monte carlo method, Phys. Rev. B. 54 (1996) 9237–9241.

[136] F. Luis, J. M. Torres, L. M. García, J. Bartolomé, J. Stankiewicz, F. Petroff, F. Fettar, J. L. Maurice, A. Vaurès, Enhancement of the magnetic anisotropy of nanometer-sized co clusters: Influence of the surface and interparticle interactions, Phys. Rev. B. 65 (2002) 094409.

[137] M. F. Hansen, S. Mørup, Estimation of blocking temperatures from zfc/fc curves, J. Mag. Mag. Mat. 203 (1999) 214–216.

[138] J. I. Gittleman, B. Abeles, S. Bozowski, Superparamagnetism and relaxation effects in granular Ni-SiO_2 and Ni-Al_2O_3, Phys. Rev. B. 9 (1974) 3891–3897.

[139] L. Lundgren, P. Svedlindh, O. Beckman, Measurement of complex susceptibility on a metallic spin glass with broad relaxation spectrum, J. Mag. Mag. Mat. 25 (1981) 33–38.

[140] F. Luis, J. Bartolomé, J. Tejada, E. Martínez, Ac susceptibility study of the magnetic relaxation phenomena in CrO_2 digital compact cassette magnetic tapes, J. Mag. Mag. Mat. 157-158 (1996) 266–267.

[141] T. Jonsson, J. Mattsson, P. Nordblad, P. Svedlindh, Energy barrier distribution of a noninteracting nano-sized magnetic particle system, J. Mag. Mag. Mat. 168 (1997) 269–277.

[142] M. I. Shliomis, V. I. Stepanov, frequency dependence and long time relaxation of the susceptibility of the magnetic fluids, J. Mag. Mag. Mat. 122 (1993) 176–181.

[143] P. Svedlindh, T. Jonsson, J. L. García-Palacios, Intra-potential-well contribution to the of a noninteracting nano-sized magnetic particle system, J. Mag. Mag. Mat. 169 (1997) 323–334.

[144] M. El-Hilo, K. O'Grady, R. W. Chantrell, Susceptibility phenomena in a fine particle system. I. concentration dependence of the peak, J. Mag. Mag. Mat. 114 (1992) 295–306.

[145] M. El-Hilo, K. O'Grady, R. W. Chantrell, Susceptibility phenomena in a fine particle system. II. field dependence of the peak, J. Mag. Mag. Mat. 114 (1992) 307–313.

[146] M. El-Hilo, K. O'Grady, R. W. Chantrell, The ordering temperature in fine particle systems, J. Mag. Mag. Mat. 117 (1992) 21–28.

[147] M. El-Hilo, K. O'Grady, R. W. Chantrell, Modeling of interaction effects in granular systems, J. Mag. Mag. Mat. 221 (2000) 137–148.

[148] W. Luo, S. R. Nagel, T. F. Rosenbaum, R. E. Rosensweig, Dipole interactions with random anisotropy in a frozen ferrofluid, Phys. Rev. Lett. 67 (1991) 2721–2724.

[149] S. Mørup, E. Tronc, Superparamagnetic relaxation of weakly interactiong particles, Phys. Rev. Lett. 72 (1994) 3278–3281.

[150] J. L. Dormann, D. Fiorani, R. Cherkaoui, E. Tronc, F. Lucari, F. D'Orazio, L. Spinu, M. Noguès, H. Kachkachi, J. P. Jolivet, J. Mag. Mag. Mat. 203 (1999) 23–27.

[151] M. S. Seehra, V. S. Babu, A. Manivannan, J. W. Lynn, Neutron scattering and magnetic studies of ferrihydrite nanoparticles, Phys. Rev. B. 61 (2000) 3513–3518.

[152] M. Hanson, C. Johansson, S. Mørup, Zero-field cooled magnetization of amorphous $Fe_{1-x}C_x$ particles-field dependence of the maximum, J. Phys: Condens. Matter 7 (1995) 9263–9268.

[153] M. Hanson, C. Johansson, S. Mørup, Comment on "macroscopic resonant tunneling of magnetization in ferritin", Phys. Rev. Lett. 81 (1998) 731.

[154] R. Sappey, E. Vincent, N. Hadacek, F. Chaput, J. P. Boilot, D. Zins, Nonmonotonic field dependence of the zreo-field cooled magnetization peak in some systems of magnetic nanoparticles, Phys. Rev. B. 56 (1997) 14551–14559.

[155] J. L. Dormann, F. D'Orazio, F. Lucari, E. Tronc, P. Prené, J. P. Jolivet, D. Fiorani, R. Cherkaoui, M. Noguès, Thermal variation of the relaxation time of the magnetic moment of γ-Fe_2O_3 nanoparticles with interparticle interactions of various strengths, Phys. Rev. B. 53 (1996) 14291–14297.

[156] R. F. C. Marques, C. Garcia, P. Lecante, B. Warot-Fonrose, E. Snoeck, J. Dexpert-Ghys, S. J. Ribeiro, N. J. O. Silva, V. S. Amaral, A. Millán, M. Verelst, Electroprecipitation, surface modification, and characterization of magnetite nanoparticles for bio-medical applications, submitted.

[157] S. Shtrikman, E. P. Wohlfarth, The theory of the vogel-fulcher law of spin glasses, Phys. Lett. A 85 (1981) 467–470.

[158] J. García-Otero, M. Porto, J. Rivas, A. Bunde, Influence of dipolar interaction on magnetic properties of ultrafine ferromagnetic particles, Phys. Rev. Lett. 84 (2000) 167–170.

[159] M. R. Roser, L. R. Corruccini, Dipolar ferromagnetic order in a cubic system, Phys. Rev. Lett. 65 (8) (1990) 1064–1067.

[160] S. J. White, M. R. Roser, J. Xu, J. T. van der Noordaa, L. R. Corruccini, Dipolar magnetic order with large quantum spin fluctuations in a diamond lattice, Phys. Rev. Lett. 71 (21) (1993) 3553–3556.

[161] A. Morello, F. L. Mettes, O. N. Bakharev, H. B. Brom, L. J. de Jongh, F. Luis, J. F. Fernandez, G. Aromi, Magnetic dipolar ordering and relaxation in the high-spin molecular cluster compound Mn_6, Phys. Rev. B. 73.

[162] A. Labarta, O. Iglesias, L. Balcells, F. Badia, Magnetic relaxation in small-particle systems: $T\ln(t/\tau_0)$ scaling, Phys. Rev. B. 48 (1993) 10240–10246.

[163] E. du Trémolet de Lacheisserie, Magnétisme I - Fondements, EDP Sciences, Les Ulis, 2000.

[164] L. Néel, C. R. Hebd. Seances Acad. Sci. 252 (1961) 4075–4080.

[165] L. Néel, C. R. Hebd. Seances Acad. Sci. 253 (1961) 9–12.

[166] L. Néel, C. R. Hebd. Seances Acad. Sci. 253 (1961) 203–208.

[167] L. Néel, C. R. Hebd. Seances Acad. Sci. 253 (1961) 1286–1291.

[168] L. Néel, Propriétés magnétiques des grans fins antiferromagnétiques: superparamagnétisme et superantiferromagnétisme, J. Phys. Soc. Japan 17 Sup. B 1 (1962) 676–685.

[169] A. Punnoose, H. Magnone, M. S. Seehra, J. Bonevich, Bulk to nanoscale magnetism and exchange bias in cuo nanoparticles, Phys. Rev. B 64 (17) (2001) 174420.

[170] R. H. Kodama, S. A. Makhlouf, A. E. Berkowitz, Finite size effects in antiferromagnetic NiO nanoparticles, Phys. Rev. Lett. 79 (1997) 1393–1396.

[171] J. G. E. Harris, J. E. Grimaldi, D. D. Awschalom, A. Chiolero, D. Loss, Excess spin and the dynamics of antiferromagnetic ferritin, Phys. Rev. B. 60 (1999) 3453–3456.

[172] D. E. Madsen, S. Mørup, M. F. Hansen, On the interpretation of magnetization data for antiferromagnetic nanoparticles, J. Mag. Mag. Mat. 305 (2006) 95–99.

[173] S. H. Kilcoyne, R. Cywinski, Ferritin: a model superparamagnet, J. Mag. Mag. Mat. 140-144 (1995) 1466–1467.

[174] C. Gilles, P. Bonville, H. Rakoto, J. M. Broto, K. K. Wong, S. Mann, Magnetic hysteresis and superantiferromagnetism in ferritin nanoparticles, J. Mag. Mag. Mat. 241 (2002) 430–440.

[175] S. Mørup, Spin-flop in antiferromagnetic microcrystals, Surf. Sci. 156 (1985) 888–892.

[176] A. Punnoose, T. Phanthavady, M. S. Seehra, N. Shah, G. P. Huffman, Magnatic properties of ferrihydrite nanoparticles doped with Ni, Mo and Ir, Phys. Rev. B. 69 (2004) 054425.

[177] S. Mørup, C. Frandsen, Thermoinduced magnetization in nanoparticles of antiferromagnetic materials, Phys. Rev. Lett. 92 (2004) 217201.

[178] N. J. O. Silva, V. S. Amaral, L. D. Carlos, V. de Zea Bermudez, Ferrihydrite antiferromagnetic nanoparticles in a sol-gel derived organic-inorganic matrix, J. Mag. Mag. Mat. 455-456 (2004) 569–572.

[179] M. S. Seehra, P. Dutta, H. Shim, A. Manivannan, Particle size dependence of exchange-bias and coercivity in CuO nanoparticles, Sol. State Comm. 128 (2003) 299–302.

[180] G. Brown, A. Janotti, M. Eisenbach, G. M. Stocks, Intrinsic volume scaling of thermoinduced magnetization in antiferromagnetic nanoparticles, Phys. Rev. B. 72 (2005) 140405R.

[181] Q. A. Pankhurst, R. J. Pollard, Origin of the spin-canting anomaly in small ferrimagnetic particles, Phys. Rev. Lett. 67 (2) (1991) 248–250.

[182] P. Dutta, A. Manivannan, M. S. Seehra, N. Shah, G. P. Huffman, Magnetic properties of nearly defect-free maghemite nanocrystals, Phys. Rev. B. 70 (2004) 174428.

[183] I. Gilbert, A. Millan, F. Palacio, A. Falqui, E. Snoeck, V. Serin, Magnetic properties of maghemite nanoparticles in a polyvinylpyridine matrix, Polyhedron 22 (2003) 2457–2461.

[184] O. Iglesias, A. Labarta, Role of surface disorder on the magnetic properties and hysteresis of nanoparticles, Physica B 343 (2004) 286–292.

[185] N. N. Greenwood, T. C. Gibb, Mössbauer Spectroscopy, Chapman and Hall, London, 1971.

[186] T. S. Berquó, P. Sølheid, Mössbauer revisited again: measurement in applied fields, IRM Quarterly 14 (2004) 1.

[187] Outline of Data Regression Routines, Quantum Design Inc., San Diego, 2000.

[188] M. Mc Elfresh, Fundaments of magnetism and magnetic measurements, Quantum Design Inc., San Diego, 1994.

[189] A. D. Hibbs, R. E. Sager, S. Kumar, J. E. McArthur, A. L. Singsaas, K. G. Jensen, M. A. Steindorf, T. A. Aukerman, H. M. Schneider, A squid-based ac susceptometer, Rev. Sci. Instrum. 65 (1994) 2644–2652.

[190] N. J. O. Silva, V. S. Amaral, L. D. Carlos, V. de Zea Bermudez, Magnetic properties of fe-doped organic-inorganic nanohybrids, J. App. Phys. 93 (2003) 6978–6980.

[191] N. J. O. Silva, K. Dahmouche, C. V. Santilli, V. S. Amaral, L. D. Carlos, V. de Zea Bermudez, A. F. Craievich, Structure of magnetic poe-siloxane nanohybrids doped with Fe(II) and Fe(III), J. Appl. Cryst. 36 (2003) 961–966.

[192] A. J. C., Mathematical Theory of X-ray Powder Diffractometry, Philips, Eindhoven, 1963.

[193] G. Kellermann, A. F. Craievich, Isothermal aggregation of Ag atoms in sodium borate glass, Phys. Rev. B. 70 (2004) 054106.

[194] G. Beaucage, Approximations leading to a unified exponential/power-law approach to small-angle scattering, J. Appl. Cryst. 28 (1995) 717–728.

[195] N. J. O. Silva, V. S. Amaral, L. D. Carlos, B. Rodríguez-González, L. M. Liz-Marzán, A. Millan, F. Palacio, V. de Zea Bermudez, Structural and magnetic studies in ferrihydrite nanoparticles formed within organic-inorganic hybrid matrices, J. Appl. Phys. 100 (2006) 054301.

[196] L. B. Kiss, J. Söderlund, G. A. Niklasson, C. G. Granqvist, New approach to the origin of lognormal size distributions of nanoparticles, Nanotechnology 10 (1999) 25–28.

[197] C. G. Granqvist, R. A. Buhrman, Ultrafine metal particles, J. App. Phys. 47 (1976) 2200–2219.

[198] D. J. Skrovanek, S. E.Howe, P. C. Painter, M. M. Coleman, Hydrogen-bonding in polymers - infrared temperature studies of an amorphous polyamide, Macromolecules 18 (1985) 1676.

[199] M. M. Coleman, K. H. Lee, D. J. Skrovanek, P. C. Painter, Hydrogen-bonding in polymers. 4. infrared temperature studies of a simple polyurethane, Macromolecules 19 (1986) 2149–2157.

[200] V. S. Amaral, L. D. Carlos, V. de Zea Bermudez, Magnetic probing of tunable Eu^{3+} local site in organic/inorganic nanohybrids, IEEE Trans. Magn. 37 (2001) 2935.

[201] N. J. O. Silva, V. S. Amaral, L. D. Carlos, Relevance of magnetic moment distribution and scaling law methods to study the magnetic behaviour of antiferromagnetic nanoparticles: application to ferritin, Phys. Rev. B. 71 (2005) 184408.

[202] T. S. Berquó, P. Sølheid, Improving the validity of hyperfine field distributions from metallic alloys. part i: unpolarized source., Nucl. Instr. Meth. B 28 (1987) 398–405.

[203] E. Murad, U. Schwertmann, The Mössbauer spectrum of ferrihydrite and its relations to those of other iron oxides, Am. Mineral. 65 (1980) 1044–1049.

[204] J. Z. Jiang, G. F. Goya, H. R. Rechenberg, Magnetic properties of nanostructured $CuFe_2O_4$, J. Phys.: Condens. Matter 11 (1999) 4063–4078.

[205] F. Bødker, S. Mørup, S. Linderoth, Surface effects in metalic iron nanoparticles, Phys. Rev. Lett. 72 (1994) 282–285.

[206] C. J. Serna, F. Bødker, S. Mørup, M. P. Morales, F. Sandiumeng, S. Veintemillas-Verdaguer, Spin frustration in maghemite nanoparticles, Solid State Commun. 118 (2001) 437–440.

[207] S. Mørup, C. Frandsen, F. Bødker, S. N. Klausen, P. Lindgård, M. F. Hansen, Magnetic properties of nanoparticles of antiferromagnetic materials, Hyp. Inter. 144-145 (2002) 347–357.

[208] A. P. Malozemoff, Mechanisms of exchange anisotropy, J. App. Phys. 63 (1988) 3874–3879.

[209] J. R. Friedman, U. Voskoboynik, M. P. Sarachik, Anomalous magnetic relaxation in ferritin, Phys. Rev. B. 56 (1997) 10793–10796.

[210] H. Mamiya, I. Nakatani, T. Furubayashi, Magnetic relaxations of antiferromagnetic nanoparticles in magnetic fields, Phys. Rev. Lett. 88 (2002) 0672021.

[211] B. Kalska, J. J. Paggel, P. Fumagalli, M. Hilgendorff, M. Giersig, Magneto-optics of thin magnetic films composed of co nanoparticles, J. App. Phys. 92 (2002) 7481–7485.

[212] M. A. Khadar, V. Biju, A. Inoue, Effect of finite size on the magnetization behavior of nanostructured nickel oxide, Mater. Res. Bull. 38 (2003) 1341–1349.

[213] M. Yoon, Y. Kim, Y. Kim, V. Volkov, H. Song, Y. Park, S. L. Vasilyak, I.-W. Park, Magnetic properties of iron nanoparticles in a polymer film, J. Mag. Mag. Mat. 265 (2003) 357–362.

[214] E. Quintero, R. Tovar, M. Quintero, J. Gonzalez, J. M. Broto, H. Rakoto, R. Barbaste, J. C. Woolley, G. Lamarche, A. M. Lamarche, Magnetic behaviour of $Cu_2FeGeSe_4$, J. Mag. Mag. Mat. 210 (2000) 208–214.

[215] V. de Zea Bermudez, R. A. Sá Ferreira, L. D. Carlos, C. Molina, S. J. L. Ribeiro, Coordination of Eu^{3+} ions in siliceous nanohybrids containing short polyether chains and bridging urea cross-links, J. Phys. Chem. B 105 (2001) 3378.

[216] V. de Zea Bermudez, D. Ostrovskii, M. M. Gonçaves, L. D. C. R. A. S. Ferreira, L. Reis, P. Jachobsson, Urethane cross-linked poly(oxyethylene)/siliceous nanohybrids doped with Eu^{3+} ions. part i: Coordinating ability of the host matrix, Phys. Chem. Chem. Phys. 6 (2004) 638–648.

[217] M. M. Gonçaves, V. de Zea Bermudez, D. Ostrovskii, L. D. Carlos, Ion solvation and hydrogen bonding in Eu^{3+}-doped mono-urethanesil hybrids carrying pendant short polyether chains, J. Mol. Struct. 611 (2002) 83–93.

[218] P. D. Allen, T. G. St. Pierre, R. Street, Magnetic interactions in native horse spleen ferritin below the superparamagnetic blocking temperature, J. Mag. Mag. Mat. 177-181 (1995) 1459–1460.

[219] M. S. Seehra, A. Punnoose, Deviations from the curie-law and variation of magnatic susceptibility in antiferromagnetic nanoparticles, Phys. Rev. B. 64 (2001) 11837–11846.

[220] S. Rusponi, T. Cren, N. Weiss, M. Epple, P. Buluschek, L. Claude, H. Brune, The remarkable difference between surface and step atoms in the magnetic anisotropy of two-dimensional nanostructures, Nature Mater. 2 (2003) 546–551.

[221] T. O. Kvalseth, Some informational properties of the lognormal-distribution, IEEE Trans. Inform. Theory 6 (1982) 963–966.

[222] D. Fiorani, A. M. Testa, P. Prené, E. Tronc, J. P. Jolivet, R. Cherkaoui, J. L. Dormann, M. Noguès, J. Mag. Mag. Mat. 140-144 (1995) 395.

[223] N. J. O. Silva, A. Millan, V. S. Amaral, F. Palacio, L. S. Fu, L. D. Carlos, V. de Zea Bermudez, Iron oxide and oxide-hydroxide nanoparticles in organic-inorganic matrices, Mater. Sci. Forum 514-516 (2006) 142–146.

[224] E. P. Valstyn, J. P. Hanton, A. H. Morrish, Ferromagnetic resonance of single-domain particles, Phys. Rev. 128 (5) (1962) 2078–2087.

[225] E. Lima Jr., A. L. Brandl, A. D. Arelaro, G. F. Goya, Spin disorder and magnetic anisotropy in Fe_3O_4 nanoparticles, J. App. Phys. 99 (2006) 083908.

[226] S. M. Gomes Correia, V. de Zea Bermudez, M. M. Silva, S. Barros, R. A. Sá Ferreira, L. D. Carlos, M. J. Smith, Short chain U(600) di-urea cross-linked poly(oxyethylene)/siloxane ormolytes doped with lanthanum triflate salt, Electrochimica Acta 47 (2002) 2551.